



HAL
open science

Atom interferometry using frequency comb and progress on atomic recoil measurement

Clément Debavelaere

► **To cite this version:**

Clément Debavelaere. Atom interferometry using frequency comb and progress on atomic recoil measurement. Quantum Physics [quant-ph]. Sorbonne Université, 2024. English. NNT : 2024SORUS302 . tel-04837020

HAL Id: tel-04837020

<https://theses.hal.science/tel-04837020v1>

Submitted on 13 Dec 2024

HAL is a multi-disciplinary open access archive for the deposit and dissemination of scientific research documents, whether they are published or not. The documents may come from teaching and research institutions in France or abroad, or from public or private research centers.

L'archive ouverte pluridisciplinaire **HAL**, est destinée au dépôt et à la diffusion de documents scientifiques de niveau recherche, publiés ou non, émanant des établissements d'enseignement et de recherche français ou étrangers, des laboratoires publics ou privés.

**THÈSE DE DOCTORAT
DE SORBONNE UNIVERSITÉ**

Spécialité : Physique

École doctorale n°564: Physique en Île-de-France

réalisée sous la direction de Saïda Guellati-Khélifa

au Laboratoire Kastler Brossel



présentée par

Clément DEBAVELAERE

Sujet de la thèse :

**Atom interferometry using frequency comb and
progress on atomic recoil measurement**

soutenue le 27 septembre 2024

devant le jury composé de :

M ^{me} CHAMPENOIS Caroline,	DR, PIIM,	Rapporteuse
M. COMPARAT Daniel,	DR, LAC,	Rapporteur
M LANDRAGIN Arnaud,	DR, SYRTE,	Examineur
M ^{me} PICQUÉ Nathalie,	PR, MBI,	Examinatrice
M. WESTBROOK Christoph,	DR, LCF,	Président du Jury
M ^{me} GUELLATI-KHÉLIFA Saïda,	PR, LKB,	Directrice de thèse
M CLADÉ Pierre,	DR, LKB,	Co-encadrant de thèse

Contents

Contents	iii
Introduction	5
I Frequency Comb Atom Interferometry	7
1 Introduction to Frequency comb	9
1.1 Frequency comb basics	9
1.2 Frequency comb spectroscopy	11
1.2.1 Two photon direct frequency comb spectroscopy	12
1.2.1.1 Ladder scheme	12
1.2.1.2 Lambda scheme	14
1.3 Context of this work	15
1.4 Outlook	18
2 Theory of atom-wave diffraction with a frequency comb	19
2.1 Three-level system and numerical simulation of a co-propagating transition	20
2.2 Raman diffraction induced by counter-propagating picosecond pulses	23
2.2.1 Description of the problem	24
2.2.2 Effective Hamiltonian	25
2.2.3 Discussion	27
2.3 Excitation schemes	29
3 Raman diffraction with a picosecond laser	31
3.1 Pico-second frequency comb laser and characterization	31
3.1.1 Repetition rate stabilization	33
3.1.2 Laser pulse characterization set-up	34
3.1.2.1 Spectrometer measurement	34
3.1.2.2 Intensity auto-correlation measurement	36
3.2 Cold atom source	38
3.2.1 Ultra high vacuum chamber	38
3.2.2 Trapping and cooling atoms	38
3.2.3 Time of flight detection	39
3.3 Fixed length delay line set-up	41

3.3.1	Raman transition with a frequency comb: experimental realisation	41
3.3.2	Measurement of the delay line	42
3.3.3	Counter-propagating Raman transition	45
4	First atom interferometer driven by a frequency comb	49
4.1	Theory of atom interferometry	49
4.2	Experimental results	55
4.2.1	Monte Carlo Simulation	56
4.2.2	Study of the contrast	58
4.3	Double diffraction	60
5	Moving delay line frequency comb atom interferometer	65
5.1	Moving delay line apparatus	66
5.1.1	Phase shift calculation	66
5.1.2	FPGA programming	69
5.1.3	Electronic driver of the voice coil	71
5.2	Following the mid-point of the interferometer	72
5.2.1	Monte-Carlo simulation	72
5.2.2	Results	74
5.3	Atom interferometer using spatially-localized beam splitters	77
II	Progress on atomic recoil measurement	85
6	Introduction	87
6.1	Measurement of the ratio h/m	89
6.1.1	Stimulated Raman transition	89
6.1.1.1	General considerations	89
6.1.1.2	Resonance condition	89
6.1.1.3	Raman coupling	91
6.1.1.4	Co and counter-propagating geometry	93
6.1.2	Representation free approach	94
6.1.3	Bloch oscillation	97
6.2	2020 measurement	99
6.3	Outlook	100
7	Experimental set-up and measurement of h/m	103
7.1	Vacuum cell	103
7.2	Cold atom production: from molasses to a BEC	104
7.2.1	Magneto optic trap	105
7.2.2	Optical molasses	105
7.3	BEC production	107
7.3.1	Evaporation optical setup	107
7.3.2	Evaporation sequence	108

7.4	Raman and Bloch lasers	110
7.4.1	Amplifier and SHG generation	110
7.4.2	Bloch Lasers	112
7.4.3	Raman lasers	112
7.4.4	Beam path of the science lasers	113
7.5	Measurement of \hbar/m	116
7.5.1	Temporal sequence	118
7.5.2	Four configurations	118
8	Phase shift in Raman phase lock loop	121
8.1	AOM set-up	122
8.2	Double lock scheme	126
9	The BEC problem	131
9.1	The BEC to scan the wavefront	132
9.1.1	Monte Carlo simulation	133
9.2	New collimators	134
9.2.1	Propagation of a Noisy Gaussian Beam	134
9.2.2	Study of the intensity profile	136
9.2.3	Simulation of the collimators	138
9.2.4	Numerical simulation	139
9.3	Implementation and new measurement with the BEC	139
9.3.1	New BEC measurement	140
9.3.2	Parasitic reflection	141
	Conclusion	147
	Appendices	149
A	Effective Hamiltonian, Raman Transition with a Picosecond Laser	151
A.1	System with More Than Three Levels	153
A.2	System with Three Internal Levels and an External Variable	154
	Bibliography	157

Remerciements

Au cours de ces trois années de thèse, j'ai eu l'opportunité de travailler et de rencontrer de nombreuses personnes qui m'ont permis de progresser comme je le souhaitais, m'ont aidé et soutenu. Je tiens à les remercier toutes ici.

Je souhaite tout d'abord remercier Saïda et Pierre, qui m'ont accueilli au sein de leur équipe durant ces trois années.

Merci, Saïda, de m'avoir fait confiance et de m'avoir guidé dans mes premiers pas en tant que jeune chercheur. Bien que ton emploi du temps ait souvent été chargé, tu trouvais toujours le temps de répondre à mes questions et de m'aider à avancer dans les meilleures conditions. Tu m'as appris que rien ne sert de courir, qu'il faut avant tout bien faire les choses. J'aimerais aussi souligner ton côté humain : tu as toujours été là dans les moments les plus difficiles pour moi, prêtant une oreille attentive et bienveillante lors des périodes plus compliquées. Merci également à toi, Pierre. Au-delà de tes compétences impressionnantes en informatique et électronique, c'est surtout ta manière d'aborder la physique qui m'a profondément marqué. Tu m'as permis de mieux appréhender le monde qui nous entoure. De plus, je sais désormais que beaucoup de problèmes liés à la manip' peuvent être résolus en moins de cinq minutes. Tout comme Saïda, tu as toujours été présent pour m'écouter et me conseiller. Pour tout ça, un grand merci.

Je tiens également à remercier Cyrille, avec qui j'ai fait mes premiers pas sur la manip peigne de fréquence. Tu es celui qui m'a tout appris sur l'expérimentation. Merci de m'avoir transmis ta passion et tant de connaissances. Je souhaite également souligner la personne que tu es : j'ai trouvé en toi un ami, et travailler à tes côtés a toujours été un plaisir. Bon courage pour la suite à Strasbourg !

Mes remerciements vont aussi à tous les membres de l'équipe métrologie. Merci à toi, François, avec qui discuter, que ce soit de science ou d'autres sujets, a toujours été un plaisir. Merci à toi, Pauline, pour tes conseils et ton aide précieuse dans le choix de mon post-doc.

Ce travail n'aurait pas pu aboutir sans le soutien des différents services du laboratoire. Merci à Tom d'avoir sauvé la fin de ma thèse. Merci également aux services informatique, électronique et mécanique pour leur expertise et leur disponibilité. Enfin, un grand merci à tous les membres du secrétariat pour leur bonne humeur et grâce à qui toute la vie au labo

s'est déroulée sans accroc : merci David, Laëticia, Céline et Stéphanie.

Je remercie les membres du jury de thèse. Merci à Caroline Champenois et Daniel Comparat, qui ont rapporté ce manuscrit et ont grandement contribué à améliorer sa qualité. Merci à Nathalie Picqué et Arnaud Landragin pour l'intérêt porté à ce travail et pour vos questions enrichissantes. Enfin, merci à Chris Westbrook d'avoir accepté de présider ce jury. Mes remerciements sincères pour l'intérêt porté à mes travaux et pour vos questions.

Évidemment, merci à Zhibin et Corentin, qui m'ont précédé sur l'expérience h/m. Je tiens également à remercier les doctorants actuels de l'équipe. Rayan, bon courage pour la fin de ta thèse. Tu as rendu ces années bien plus agréables grâce à ton rire et à toutes tes maladresses. Oscar, merci d'avoir animé nos repas au CROUS et d'avoir chanté avec moi en salle de manip. Tu vas y arriver avec ton MOT d'Ytterbium, j'en suis sûr ! Samuel, merci d'avoir passé des heures et des heures avec moi sur cette manip qui ne voulait pas rester stable. Nous avons partagé énormément de moments ensemble au cours de ces deux dernières années. Merci pour toutes ces séances de rigolade et ces heures de musique en manip. Courage pour la suite, si l'expérience te résiste autant c'est que tu es proche d'une grande découverte.

Un grand merci à toutes les personnes qui ont partagé le quotidien du bureau 304 (alias le poulailler) avec moi : Myrann, Kylian, Clara, Tanguy et Alix. Bien qu'à très forte densité et entropie, il a toujours été rempli de bonne humeur et d'une ambiance chaleureuse. Merci également à tous les autres doctorants que j'ai côtoyés quotidiennement, notamment P-E et Lucien, toujours partants pour une petite Chouffe au Buisson avec les collègues du bureau. Pour tous ces bons moments (au labo ou non) et ces discussions passionnées sur la physique tard le soir, un immense merci.

Ces trois années ne se résument pas uniquement à la vie au laboratoire. J'aimerais remercier mes amis pour leur soutien indéfectible et pour tous les moments passés ensemble. Merci à Caron, Léonie, Théophane, Valou, PR, Double, Piot, Céline, Tanguy. Vous avez été là pour me permettre de décrocher du laboratoire et de profiter pleinement de la vie parisienne.

De même, un immense merci à mon colocataire, Kevin, pour ces quatre années passées au 152. Vivre et travailler à tes côtés a toujours été un plaisir. Pour toutes ces discussions au Buisson, le soutien que tu m'as apporté, ta présence et tous ces moments passés à looter, je te remercie infiniment.

Je ne serais pas la personne que je suis sans ma famille. Un immense merci pour votre soutien constant, votre accompagnement et votre écoute lorsque je parlais de mon travail. Merci du fond du cœur à mes parents, Anne et Philippe, mes frères, Benjamin et Marc, ma tante, mon oncle, mes cousins et ma grand-mère.

Camille, merci d'être la personne que tu es. Tu m'as porté et supporté depuis maintenant cinq années. Pour tout ce que nous avons vécu et ce que nous vivons, merci.

À mes parents,

Introduction

At low temperatures, matter exhibits wave-like behaviour, enabling to create interferometers similar to optical ones. The first atomic interferometers were constructed in the early 1990s [19; 38]. These pioneering devices used microfabricated gratings to divide and recombine wave packets. A paradigm shift has been using laser pulses to manipulate matter waves. An atomic beam splitter based on a laser pulse creates a coherent superposition between two internal atomic states. Due to the conservation of momentum in the interaction process, the atom undergoing the transition acquires the energy of the photons and their momentum. This momentum gain allows the atoms to be in a coherent superposition of states that are spatially separated.

Since the pioneering work of Chu and Kasevich[37], light pulse atom interferometry has opened up a huge field of applications. Particularly in precision measurement domain where applications range from fundamental research and metrology [1; 10; 42; 46; 50; 62] to geophysics and navigation [13], and have reached a level of maturity sufficient for industrial exploitation. However, this technology is still far from having reached its full potential. New concepts and tools are being developed and are still to be investigated in order to push the boundaries. Among them is the improvement of the efficiency, order and coherence of large momentum beam-splitters [17; 22; 44], the implementation of optimal control and squeezing methods which promise a substantial gain in sensitivity.

The next generation of instruments, particularly very large ones, are under development. They are designed primarily to test fundamental physics (such as the equivalence principle, atomic neutrality and dark matter detection) and to detect gravitational waves. In these instruments, the free fall of atoms could last several seconds [8], or the separation between distant accelerometers could reach several hundred metres [18], and improvements in atom flux, temperature reduction and duty cycle are also key issues.

My PhD thesis work is part of this effort. On the one hand, it aims to develop a new technique to extend atom interferometry to a larger number of atomic species. On the other hand, by better understanding and controlling the systematic effects that limit the accuracy of interferometers, with a specific application to the determination of the fine structure constant.

My thesis work focuses on two research projects.

The first part concerns a new experiment that I started during my Master 2 internship: the implementation of an atom interferometer using a frequency comb laser to drive Raman transitions. The use of frequency combs opens up new possibilities for atom interferometry. In fact, due to their high peak intensity, it is possible to reach the UV-XUV region and thus study new atom species. Our initial idea was to perform a proof-of-concept experiment on rubidium atoms in the visible. The first interferometer was quickly obtained and the results were published in Physical Review Letters [54] one year later. The critical point is to control the superposition between the atom cloud and the overlap zone of the picosecond pulses. To increase the sensitivity of our interferometer, we then decided to implement a setup that would allow dynamic control of this overlap zone without adding phase noise to our lasers. This new setup also allowed us to create a new type of interferometer where we can probe each arm of the interferometer independently. Both theoretical and numerical studies highlighted the technical and fundamental limitations of our technique. We discovered that an atom interferometer driven by a frequency comb laser would be limited in its interrogation time by a dispersion in momentum transmitted to the atoms due to the finite duration of our laser pulses. These results have been published in Physical Review A [26].

The second part of my thesis focuses on the measurement of the ratio h/m between the Planck constant and the Rubidium mass. This work is part of a project that started in 1998 with François Biraben and is a direct continuation of the work of C. Carrez. The main goal is the accurate determination of the fine structure constant. My work on this experiment focused on studying and understanding the two systematic effects that limit the accuracy of the latest h/m measurement carried out by the team in 2020. We first carried out several studies on the phase shift in the Raman phase-locked loop using a new scheme for the phase-lock system and a new method to implement the frequency ramp used to compensate the gravity. We carried out an extensive study of this effect in an attempt to reduce it. An independent measurement of this effect has been carried out. It corroborates measurements with atoms. In addition, the group decided to use a colder atom source, a Bose-Einstein Condensate (BEC), to mitigate numerous systematic effects, mainly related to the transverse expansion of the atomic cloud. Using a BEC, C. Carrez's (the previous PhD student on the experiment [20]) observed that the value of h/m varies over time. I had to repeat the measurements with BEC to confirm the explanation for these fluctuations. When I took over this experiment, I first improved the phase locking of the Raman lasers, which led to nearly a 2-fold improvement in the statistical uncertainty. I then built new collimators which I characterized and installed on the experiment. This led to a review of the optical system at the entrance to the vacuum cell, including the installation of a larger PBS (polarization beam splitter cube). Measurement with BEC showed unfortunately that new PBS induces spurious reflections that mask the benefits of the new collimators. A new type of polarization beam splitter has just been installed on the experiment, and should significantly reduce these parasitic reflections.

Part I

Frequency Comb Atom Interferometry

Chapter 1

Introduction to Frequency comb

In the 1990s, frequency combs revolutionised frequency measurement by providing a direct link between optical and radio frequencies. This achievement was rewarded with the 2005 Nobel Prize, which honoured the work of T.W. Hänsch and J.L. Hall [34] for "contributions to the development of laser-based precision spectroscopy, including the optical frequency comb technique". By stabilizing the carrier-envelope offset, the laureates made it possible to avoid the often heavy and complex frequency chains in frequency measurement. Frequency combs are now widely used in many laboratories. Primarily used to obtain frequency references and thus to stabilise lasers, they have quickly found application in spectroscopy [3; 4; 27; 28; 40; 60; 61].

In this chapter, I will introduce the concept of frequency comb lasers and their application in spectroscopy. I will introduce key ideas for the rest of this thesis. This section draws heavily on the work of Piqué et al[49]. This article provides a more detailed and expert insight into frequency comb spectroscopy.

1.1 Frequency comb basics

We show the time and frequency domain representations of a frequency comb on [Figure 1.1](#). The term "frequency comb laser" is derived from the spectral shape of its emission.

In the frequency domain, its spectrum consists of regularly spaced teeth at the repetition frequency f_{rep} , hence the name "comb". The width of this spectrum is called $\delta\nu$. Due to dispersion in the cavity, there is a pulse-to-pulse phase shift $\Delta\Phi_{\text{ce}}$ between the envelope and the carrier.

In the temporal domain, coherent pulses are observed with a pulse duration of τ , where τ is inversely related to $\delta\nu$ with a typical duration in the femtosecond to picosecond range. Each pulse is separated by a duration T_r , where $T_r = 1/f_{\text{rep}}$. This interval corresponds to the time it takes a pulse to make a round trip in the cavity. Therefore, controlling the repetition rate involves controlling the cavity length. Frequency combs cover many spectral regions from the ultraviolet to the far infrared with repetition rates from 500 GHz to less than 50 MHz.

The control of the carrier envelope offset Φ_{ce} using the f - $2f$ technique (made possible by broadening the spectrum over more than a decade) was awarded the Nobel Prize in

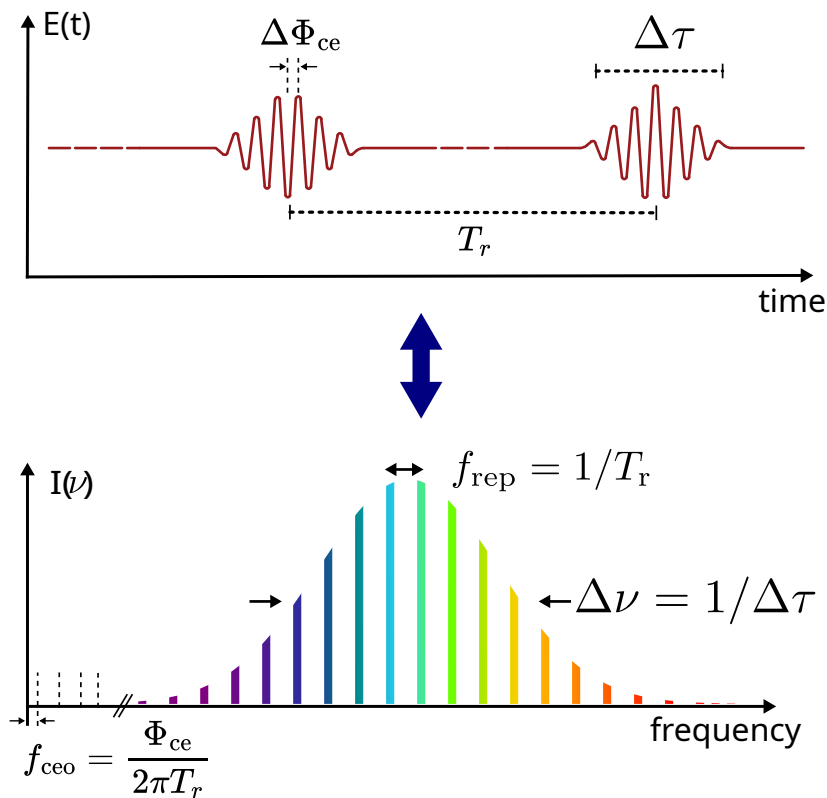


Fig. 1.1 *Frequency spectrum and time domain representation of a frequency comb laser. A Fourier transform links the temporal and frequency domain.*

2005. A detailed discussion of this technique is beyond the scope of this thesis. Suffice it to say that without this phase control, the frequency ruler represented by a frequency comb becomes ineffective, as its reference point is constantly shifting.

The [Figure 1.2](#) shows the principle of a mode-locked laser. Each longitudinal mode is in phase in the cavity in which the pulse is. However, to maintain this coherence, it is important to compensate for the group velocity dispersion. In fact, there are many modes in the cavity, and as they propagate, they experience a different velocity. Without compensation for this velocity dispersion, if the modes were in phase, then after propagation through the cavity some modes would be out of phase, resulting in a loss of coherence.

In femtosecond mode-locked lasers, this dispersion is often compensated by a pair of prisms. Conversely, for picosecond solid-state lasers, a Gires-Tournois interferometer (GTI) is often used to compensate for dispersion.

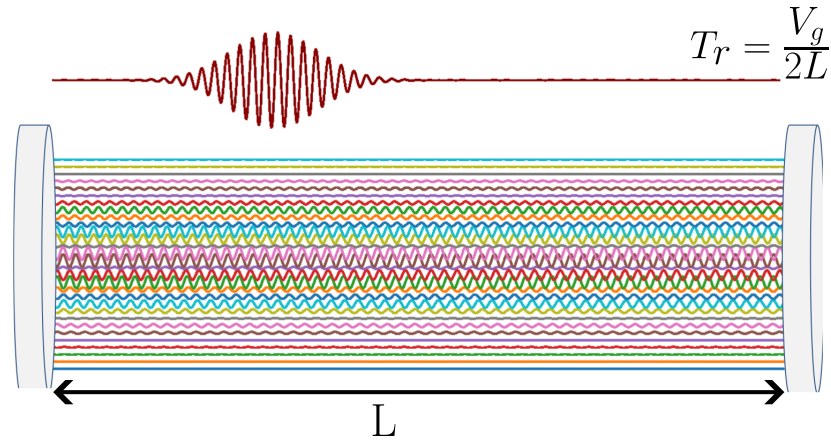


Fig. 1.2 Principle of a mode-locked cavity. Each longitudinal mode is in phase at a certain point of the cavity, building up a pulse. If the group velocity dispersion is well compensated, the pulse will bounce back and forth inside the cavity. Each time the pulse arrives at the output coupler, a part of the pulse escapes the cavity.

1.2 Frequency comb spectroscopy

We will now present some spectroscopy experiments using pulsed lasers. Frequency comb spectroscopy takes advantage of the broad spectral range and high resolution of the comb spectrum (related to f_{rep}). The technique of frequency comb spectroscopy is based on addressing a gas sample of atoms or molecules with the spectrum of a laser consisting of discrete and narrow frequency modes (frequency comb). The comb is characterised by a repetition rate f_{rep} and by the carrier-envelope frequency offset f_{ceo} . The frequencies of the comb modes can therefore be written as $f_n = n f_{\text{rep}} + f_{\text{ceo}}$ with n an integer.

The simplest method of frequency comb spectroscopy, shown on [Figure 1.3](#), involves exciting a sample via a single or multi-photon transition using a frequency comb laser. The spectrum of the frequency comb is then observed with a spectrometer. Depending on the absorption spectrum of the sample, certain comb teeth will be more or less absorbed. Therefore, by measuring the intensity of the different spectral components, the absorption spectrum of the sample can be deduced. This technique uses the broad emission spectrum of the frequency comb to measure a broad absorption band. In this method, the spectral resolution of the measurement is linked to the repetition rate. Thus, the laser source is selected with an emission spectrum that covers the absorption spectrum of the sample and a repetition rate that matches the desired spectral resolution.

More advanced methods have been developed, such as dual frequency comb spectroscopy (DFCS) [23; 49]. It involves the use of two optical frequency combs with slightly different repetition rates. They are used to measure the spectral properties of molecular samples. When the two combs are combined, they interfere to produce a time-domain signal. Due to the slightly different repetition rates, the interferogram contains beat frequencies corresponding to the differences between the comb lines of the two combs. By detecting the interferogram with a photodetector, the beat frequencies can be measured.

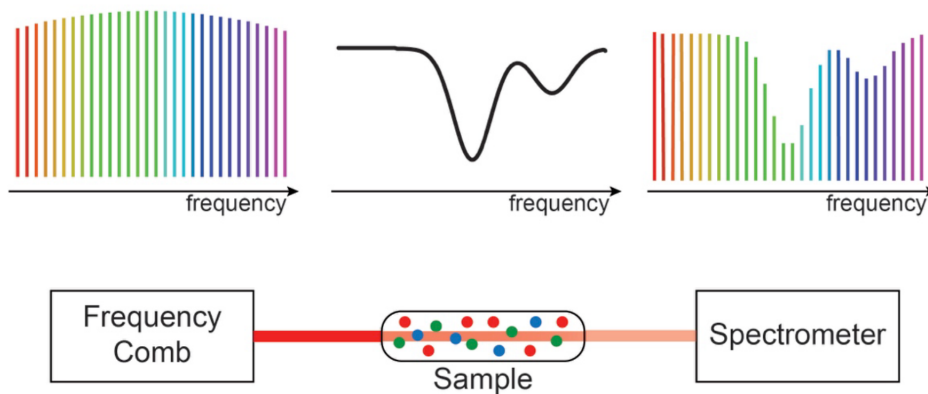


Fig. 1.3 *Simplest form of frequency comb spectroscopy. The frequency comb interrogates a sample. At the output, the light is sent to a spectrometer. The sample spectrum is reconstructed by analyzing the amplitude of the frequency comb teeth at the output. Extracted from [49].*

This heterodyne detection process translates the high-frequency optical spectrum down to the radio frequency (RF) or microwave range, making it easier to analyse with standard electronic equipment. The detected interferogram is then Fourier transformed to extract the spectral information. The resulting RF spectrum corresponds directly to the optical spectrum of the sample but is scaled down in frequency.

1.2.1 Two photon direct frequency comb spectroscopy

In the following, I will focus on methods that use a frequency comb to perform a two-photon transition. This will introduce the concept of Raman diffraction based on a frequency comb, which I have used to make a matter-wave coherent beamsplitter.

Several spectroscopy experiments use frequency comb lasers to excite two-photon transitions[32; 36; 53; 55]. These transitions can be carried out either in a ladder scheme or in a lambda scheme as shown on [Figure 1.4](#). In the first case, the atom absorbs two photons. In the latter, the atom first absorbs a photon and then emits a second photon by stimulated emission.

1.2.1.1 Ladder scheme

Ladder two-photon spectroscopy allows the measurement of high energy transitions, typically in the hundreds or thousands of terahertz range [40]. One of the most notable experiments is that of Grinnin et al [32], where they measured the 1S-3S transition of hydrogen at $2 \times 205\text{nm}$. The spectrum of the comb and the energy levels of the transition considered are shown on [Figure 1.5](#).

To excite the transition, the centre wavelength of the frequency comb is set to half the energy of the transition. In this way, the transition is excited by 2 photons, where the n tooth is coupled to the $n+q$ tooth to drive the transition. The resonance condition is then

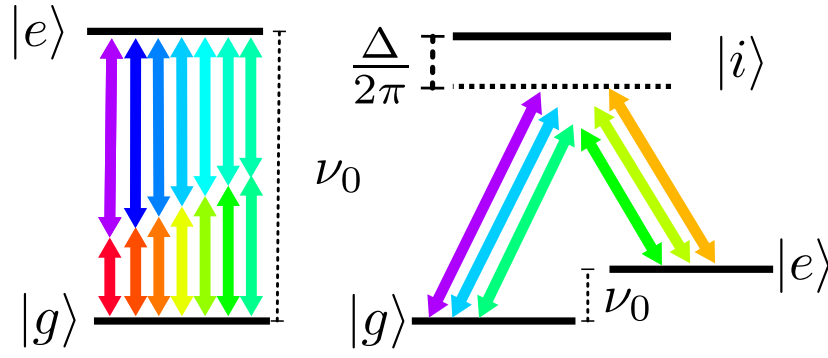


Fig. 1.4 Left: Two photon spectroscopy in the ladder scheme. Right: In the lambda scheme.

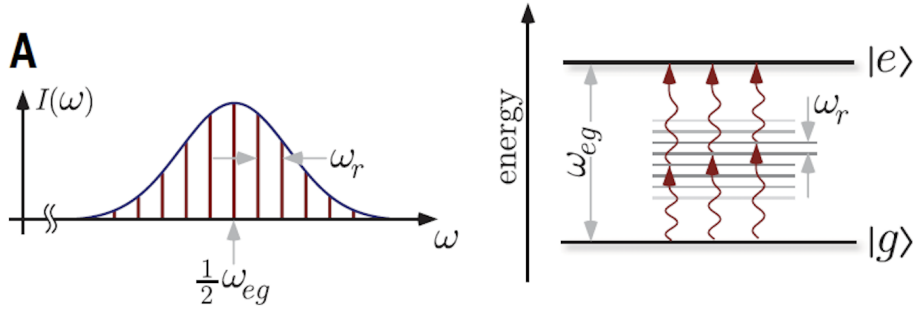


Fig. 1.5 Principle of two-photon excitation using a frequency comb spectrum. Extracted from [32].

given by

$$f_n + f_{n+q} = (2n + q)f_{\text{rep}} + 2f_{\text{ceo}} = f_{eg} \quad (1.1)$$

where n and q are integers and f_{rep} is the repetition rate of the frequency comb, f_{ceo} the carrier envelop frequency offset and f_{eg} is the frequency of the considered transition. The scheme of the experiment is shown on Figure 1.6. The authors quadrupled a picosecond frequency comb at 820 nm using two successive doubling cavities to generate up to 60 mW of laser power at 205 nm.

Two-photon spectroscopy of hydrogen was then performed in an optical resonator. The mode-locked Ti sapphire picosecond laser is referenced to a transfer laser, itself locked to an ultra-stable cavity, and referenced to a femtosecond frequency comb. Each doubling cavity length is also finely controlled to match a harmonic of the repetition rate. By driving the transitions in a counter-propagating geometry, the author suppresses the first-order Doppler effect. However, to drive these transitions in this configuration, the two pulses must overlap on the hydrogen atoms simultaneously. This overlapping region is referred to as the "pulse collision volume" in [32]. In the rest of this work we will refer to it as the "overlap zone".

Finally, by combining the 1S-2S and 1S-3S (the work presented here) measurements of

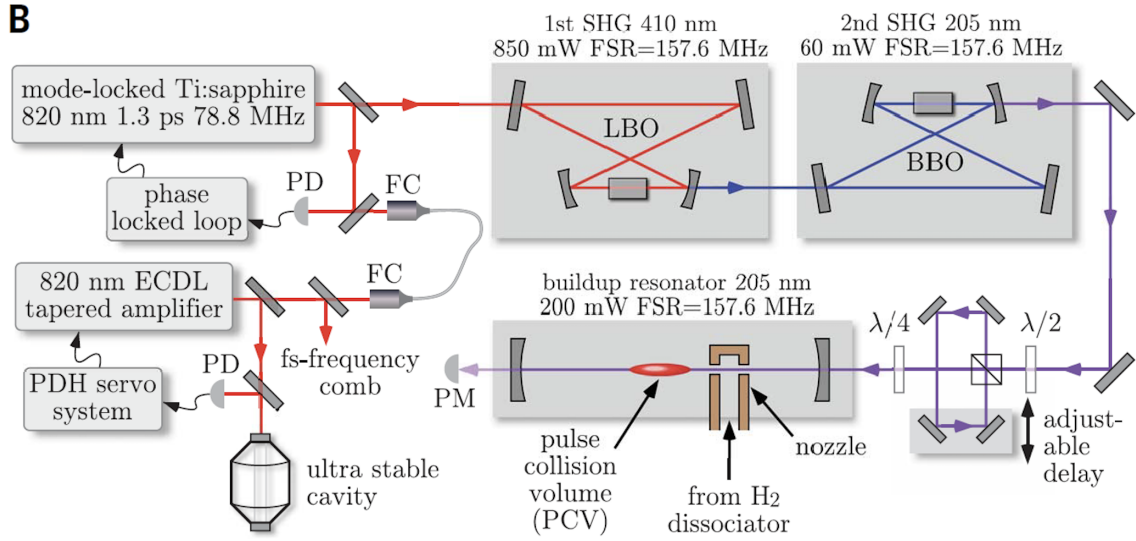


Fig. 1.6 Scheme of the experimental set-up. The red area in the resonator is the zone where the sample is interrogated. Extracted from [32].

the transition frequencies in the atomic transition, Grinnin et al. measure the proton charge radius of $r_p = 0.8482(38)$ femtometers, more than a fourfold improvement compared to the same measurement performed with continuous-wave lasers[30]. Notably, this result is in agreement with the value of the proton radius derived from muonic hydrogen spectroscopy.

1.2.1.2 Lambda scheme

It is also possible to perform lambda transitions, also known as stimulated Raman transitions. In this case, the atom, ion or molecule absorbs a photon from one comb tooth and then emits a photon by stimulated emission from another tooth. The resonance condition is given by

$$f_n - f_{n+q} = qf_{\text{rep}} = \nu_0 \quad (1.2)$$

With f_{rep} the repetition rate of the comb and ν_0 the frequency of the transition considered. The frequency range accessible by this method spans from f_{rep} to THz [52]. To carry out this type of transition, the laser emission spectrum must be wider than the frequency of the transition you wish to study. In other words, if you want to find two teeth separated by ν_0 , then $\Delta\nu > \nu_0$. In the literature, this condition is called the "impact condition" [31]. In the time domain, it implies that the duration of a laser pulse must be shorter than the characteristic period of the transition under consideration. Figure 1.7 illustrates the interpretation of this condition both in the time domain and in reciprocal space. In the temporal domain (on the right-hand part of the figure), we illustrate in dashed line the case when the impact condition is not respected, $\Delta\tau \sim T_0$, and in full line when the condition is met.

When the lambda transition is performed in a co-propagating configuration, the fre-

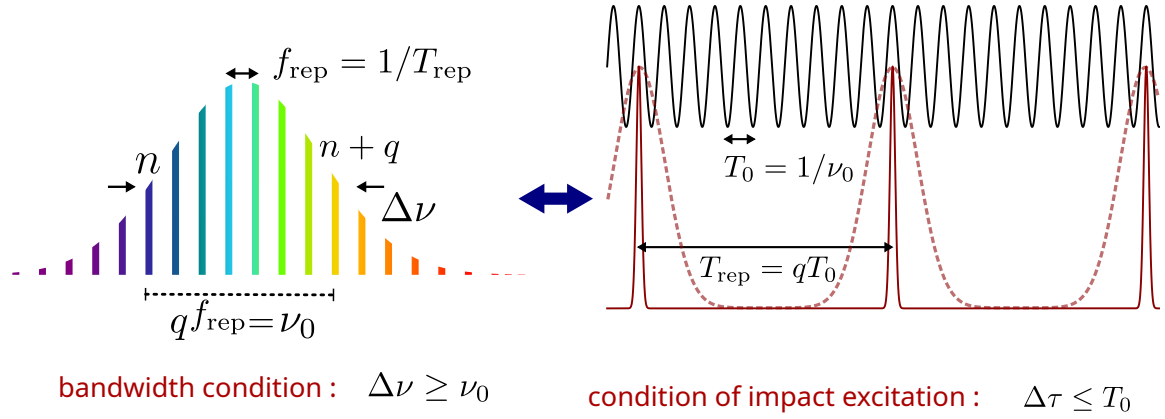


Fig. 1.7 Frequency and time domain representation of the impact condition. Left: if the spectrum of the emission of the laser is smaller than the frequency of the transition ν_0 , it is impossible to fulfill the resonance condition. In the temporal domain, the excitation by the picosecond laser must be shorter than the period $T_0 = 1/\nu_0$.

quencies leading to photon emission and absorption are present within the same pulse. In this case, it is not necessary to servo f_{ceo} . In a counter-propagating geometry, if the transition is performed by two different pulses, f_{ceo} must be locked.

This method is very versatile and allows transitions from the repetition rate frequency to the spectral width of the comb by considering another pair of teeth spaced by q . If a femtosecond comb is used, transitions up to 50 THz are possible. However, this frequency range requires a very stable repetition rate and careful compensation of the group velocity dispersion.

1.3 Context of this work

We have seen that the use of the frequency comb in spectroscopic measurements has shown great capacity and can even outperform conventional spectroscopic techniques using continuous wave lasers. In this context, we thought exploring the application of frequency combs in atom interferometers was worthwhile. The use of pulsed lasers, or more specifically frequency comb lasers, would allow the extension of light-pulse matter-wave interferometry to other wavelengths (e.g. deep UV to X-UV) and thus to new species. Indeed, one can take advantage of the high peak intensity of the ultrashort pulses, which makes frequency conversion in nonlinear media efficient. In particular, it could be used in the deep-UV on antihydrogen to measure the free-fall acceleration of antimatter and test the weak equivalence principle with antimatter [12; 47]. A major motivation for this project was to perform a proof-of-principle experiment by demonstrating the possibility of splitting, deflecting and recombining atomic wave packets using a frequency comb to drive the Raman transition in a counterpropagating geometry.

The experiment presented in this part was carried out on ^{87}Rb using stimulated Raman transition in a counter-propagating geometry. By using a counter-propagating geometry, we

can transfer a recoil velocity of ~ 11.8 mm/s, whereas the recoil velocity in a co-propagating geometry is of the order of hundreds of nm/s.

To interrogate the entire atomic sample, a single pulse must encompass it completely. Thus, we must satisfy $c\Delta\tau > \sigma_{\text{cloud}}$. Since we are using optical molasses, we have $\sigma_{\text{cloud}} \sim 0.5$ mm, and thus, it imposes $\tau > 1$ ps. We also need to obey the impact condition. With ^{87}Rb the hyperfine splitting between the two states that we will address through the Raman process is equal to $\nu_{\text{HFS}} = 6.8$ GHz, which means that we have to limit ourselves to pulse duration of less than 150 ps. In the experiment, we will use a picosecond frequency comb with a pulse duration from 1 to 2ps, meaning a spectral width from 150 to 300 GHz. The pulse duration and thus the spectral width will be tuned by changing the slit width in the laser cavity. This choice of picosecond pulse duration was limited by the available frequency comb laser source. Furthermore, the picosecond frequency comb laser used was already available in the Lab.

Furthermore, the use of a frequency comb to drive a counter-propagating Raman transition requires that the two pulses overlap on the atoms. This is the same constraint as in the experiment of Grinin et al. [32]. This condition is satisfied in the experiment by splitting a pulse into two and retro-reflecting one of the two pulses. The split picosecond pulse travels in a delay line whose length is finely tuned to fulfil this condition. We have developed a method based on co-propagating Raman transitions to adjust the length of this delay line. Also, it is not necessary to lock f_{ceo} because the transition is driven by the same pulse split in two. It might be important to point out that 2 consecutive pulses will not overlap near the atom sample. Indeed, we will use a laser with a repetition rate of around 76 MHz. Hence, the distance between two consecutive pulses escaping the laser cavity is on the order of 4 m. The repetition rate of the frequency comb can be tuned by more than 2 MHz by changing the laser cavity size.

In addition, because the atoms are free-falling, the Raman transition must be short compared to the time (denoted as T in [Figure 1.8](#)) it takes for the atoms to travel in the overlap zone. For picosecond pulses of the order of 1 ps, this time can be approximated as $T = 10$ ms.

It is also important to underline that, due to the broad spectrum of the frequency comb, the velocity recoil imparted to the atoms during the transition is not well defined, giving rise to a momentum dispersion called $\hbar\Delta k_{\text{eff}}$ in [Figure 1.8](#). In fact, the recoil velocity transferred to an atom during a Raman transition is $k_i - k_j$, where $k_{i,j}$ is the wave vector of the laser line i,j . In our case, there are a large number of tooth pairs driving the transition, resulting in a large number of effective wave vectors $k_n - k_m$. For two consecutive pairs of teeth, the difference in effective wave vectors will be on the order of the repetition rate frequency divided by c . The full-width half maximum of the total dispersion in wave vector (when we consider all the teeth of the comb) can be approximated as the full-width half maximum of the emission spectrum of the comb divided by c (on the order of a few hundred GHz). Furthermore, a spread in detuning noted as Δn , will be a source of coupling inhomogeneity causing dumping in the Rabi oscillation.

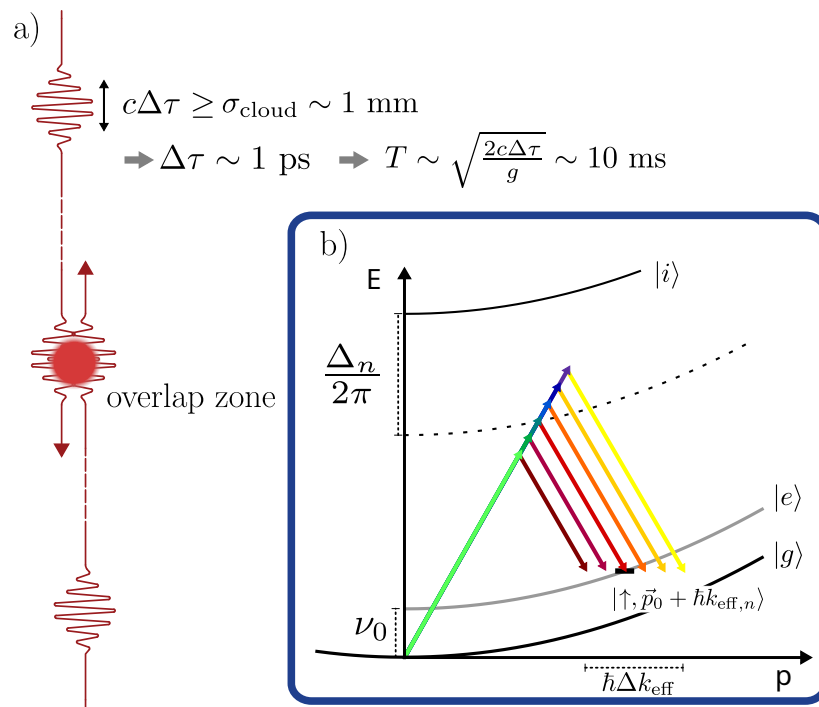


Fig. 1.8 Challenges arising from the use of a frequency comb. a) Overlap condition and restriction on the size of the laser pulse duration. The time T define the time taken by the atom to free fall through the overlap zone b) momentum energy diagram for a stimulated Raman transition using a frequency comb. We represent as Δn the spread in detuning that will affect the coupling inhomogeneity of the Raman transition. The spread in frequency of the different pair of teeth leads to a momentum dispersion after one transition.

Conclusion

Frequency comb-driven spectroscopy has shown great potential and can sometimes overcome the performance of continuous wave lasers in spectroscopy. By taking advantage of its high peak intensity, we believe it is possible to extend the light-pulse matter-wave interferometer to other wavelengths. In this introduction, we have described two spectroscopy experiments and highlighted two important features: the overlap condition and the impact condition.

In the case of a frequency comb-driven atomic interferometer, we have introduced two sensitivity limits: one related to the free fall of the atoms through the overlap zone and the other related to the momentum dispersion.

1.4 Outlook

This part of my thesis, dedicated to atom interferometry using a frequency comb, is divided into four chapters.

The second chapter is dedicated to the theory of atomic diffraction by a frequency comb and shows that this interaction can be perceived by the atoms as a simple interaction with a continuous laser. We will then theoretically demonstrate the versatility of frequency comb atom interferometry by considering the possibility of double diffraction and the interrogation of two different atomic species.

The third chapter describes the experimental setup used to drive the Raman transition and how we achieved total control of the experimental parameters of the frequency comb. A method for adjusting the length of the delay line, based on co-propagating Raman transition, is described in detail. Finally, the counter-propagating Raman transition is driven with a picosecond laser.

In the fourth chapter we will see the first realisation of an atom interferometer with a frequency comb laser. We will use a Monte Carlo simulation to study the effect of different parameters, such as the picosecond pulse duration and the total interrogation time, on the contrast of the interferometer. Then, we will demonstrate experimentally the versatility of this method by realising a double diffraction interferometer.

The final chapter of this part shows how we have increased the interrogation time of the interferometer by using a moving mirror. We will describe in detail the setup, consisting of a voice coil actuator, an acousto-optic modulator and heterodyne detection, used to achieve a longer interrogation time without increasing the phase noise of the interferometer. We will then explore a new interferometer configuration in which we were able to increase the contrast and investigate the fundamental limitations of this technique.

Chapter 2

Theory of atom-wave diffraction with a frequency comb

Usually, light pulse atom interferometers use diffraction of the matter wave by a CW laser to coherently split and recombine atomic wavepackets. Physical processes that induce atomic wave diffraction are either stimulated Raman transitions [37] or Bragg diffraction [45]. Similarly to the diffraction processes with CW lasers, the theoretical study of the Raman diffraction with a frequency comb has proven to be crucial for realising an efficient atomic splitter. Here we present a model to describe how a free-falling atom interacts with two trains of contra-propagating laser pulses. Light-matter effective coupling depends on the overlap between the pulses and the atomic wave packet.

First, we will perform a numerical simulation in the case of a co-propagating transition and show that the interaction of a pulsed laser with a three-level atom can drive the Raman transition if the repetition rate is well-tuned. This simulation will show that the intermediate state is only transiently populated.

Second, we will justify the adiabatic elimination of the excited state when using a picosecond laser.

Then, we will study Raman diffraction induced by counter-propagating picosecond pulses.

Finally, we will show that using a frequency comb can lead to features of interest such as a double diffraction scheme.

General consideration

Our goal is to understand and model the uses of a frequency comb to drive a Raman transition. To do so, we will consider a three-level system. Indeed, in the experiment studied in this part, the Raman process occurs between the $|F = 1, m_F = 0\rangle$ and $|F = 2, m_F = 0\rangle$ states of ^{87}Rb respectively noted $|g\rangle$ and $|e\rangle$. The difference in energy between these two states is the hyperfine splitting $\hbar\omega_{\text{HFS}}$. Furthermore, the one-photon detuning Δ is sufficiently large compared to the energy difference between each excited state to consider only one excited state denoted as $|i\rangle$. Also, in the experiment, the pulsation ω_{\downarrow} and ω_{\uparrow} will only differ by 160 MHz. Thus, for the sake of simplicity, we will consider that the two wave vectors k_{\downarrow}

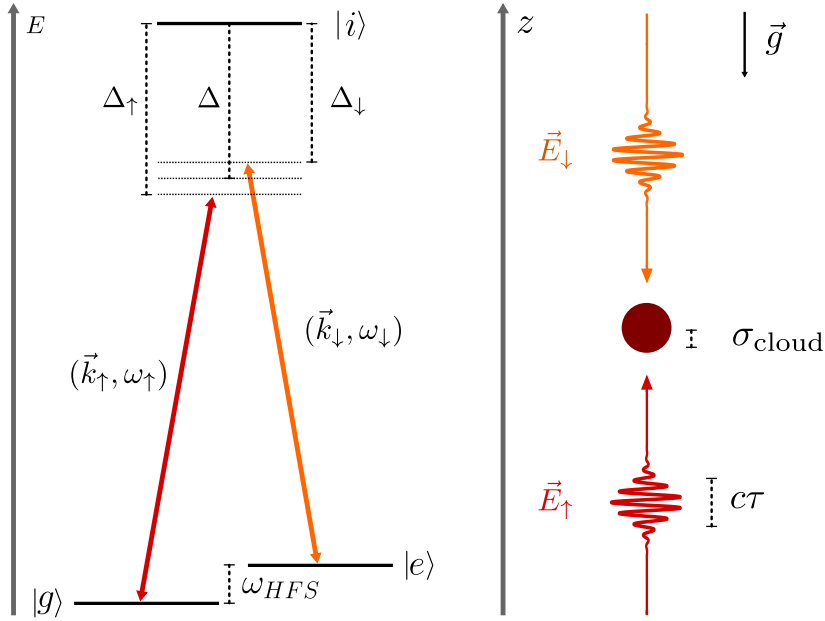


Fig. 2.1 a) Schematic of a three-level system interacting with two lasers. b) Geometry of the experiment.

and k_\uparrow are equals.

The laser used to drive the transition is a picosecond frequency comb with a typical duration of $\tau = 1$ ps. The repetition rate frequency of the laser is around 76 MHz and thus $T_r \sim 13$ ns. For the sake of simplicity, we consider a perfect laser source with no noise on the repetition rate and a carrier envelop frequency $f_{ceo} = 0$.

2.1 Three-level system and numerical simulation of a co-propagating transition

This section aims to show that the interaction between a three-level system and a train of picosecond pulses can lead to a coherent excitation process and that during that process the intermediate state $|i\rangle$ is only temporarily populated. For this section, we will only consider one train of picosecond pulses, the orange one on [Figure 2.1](#). We will show that this interaction can lead to a co-propagating Raman transition. Because we are studying co-propagating Raman transition, we neglect the dependency in position, consider an atom at rest at $z=0$ and are insensitive to the Doppler effect.

The electric field can be written as:

$$\vec{E}(t, z) = E_0 \vec{e} \cos(\omega_c t + kz + \phi) \sum_{n=1}^N f(t - nT_r + \frac{z}{c}) \quad (2.1)$$

where ω_c is the carrier frequency, k the wave vector and T_r the time between successive

pulses. The pulses' envelope is taken to be Gaussian:

$$f(t) = e^{-\frac{1}{2} \frac{t^2}{\tau^2}} \quad (2.2)$$

The field couples both the $|g\rangle$ and $|e\rangle$ states to the $|i\rangle$ state. The total Hamiltonian of the system is:

$$H = \sum_s \hbar\omega_s |s\rangle\langle s| + V(t, \hat{z}) \quad (2.3)$$

where $V(t, z)$ describes the coupling of the atoms with the light pulses:

$$V(t, z) = -\vec{d} \cdot \vec{E}(t, z) \quad (2.4)$$

with \vec{d} the electric dipole of the atom.

Let's first consider one pulse. In the $|g\rangle, |e\rangle, |i\rangle$ basis, the Hamiltonian of the system is :

$$H = \begin{pmatrix} \hbar\omega_g & 0 & \frac{\hbar\Omega_0 f(t)}{2} e^{i\omega_c t} \\ 0 & \hbar\omega_e & \frac{\hbar\Omega_0 f(t)}{2} e^{i\omega_c t} \\ \frac{\hbar\Omega_0 f(t)}{2} e^{-i\omega_c t} & \frac{\hbar\Omega_0 f(t)}{2} e^{-i\omega_c t} & \hbar\omega_i \end{pmatrix} \quad (2.5)$$

with $\Omega_0 = \frac{\mu E_0}{\hbar}$. Here, we suppose that $-e\langle i | \hat{r} \cdot \vec{\epsilon} | g \rangle$ and $-e\langle i | \hat{r} \cdot \vec{\epsilon} | e \rangle$ are equal to simplify the calculation and are written as μ .

The time dependence of the density matrix elements taking spontaneous emission into account can be calculated from Liouville's equation:

$$\frac{\partial \rho}{\partial t} = \frac{i}{\hbar} [\rho, H] + \Gamma(\rho) \quad (2.6)$$

where

$$\Gamma(\rho) = \begin{pmatrix} \Gamma_{ig}\rho_{ii} & 0 & \frac{\Gamma_{ig} + \Gamma_{ie}}{2} \rho_{gi} \\ 0 & \Gamma_{ie}\rho_{ii} & \frac{\Gamma_{ig} + \Gamma_{ie}}{2} \rho_{ei} \\ \frac{\Gamma_{ig} + \Gamma_{ie}}{2} \rho_{ig} & \frac{\Gamma_{ig} + \Gamma_{ie}}{2} \rho_{ie} & -(\Gamma_{ig} + \Gamma_{ie})\rho_{ii} \end{pmatrix} \quad (2.7)$$

Here, we have introduced the spontaneous emission rates $\Gamma_{i,m}$ with $m = \{g, e\}$

Using the rotating wave frame

$$\tilde{\rho}_{gi} = e^{-i\omega_c t} \rho_{gi} \quad (2.8)$$

$$\tilde{\rho}_{ei} = e^{-i\omega_c t} \rho_{ei} \quad (2.9)$$

$$\tilde{\rho}_{ge} = e^{-i\omega_c t} e^{i\omega_c t} \rho_{ge} = \rho_{ge} \quad (2.10)$$

$$(2.11)$$

which corresponds to $\tilde{\rho} = U^\dagger \rho U$ where U is the unitary matrix

$$U = \begin{pmatrix} 1 & 0 & 0 \\ 0 & 1 & 0 \\ 0 & 0 & e^{-i\omega_c t} \end{pmatrix} \quad (2.12)$$

We have

$$\frac{\partial \tilde{\rho}}{\partial t} = \frac{i}{\hbar} [\tilde{\rho}, \tilde{H}_{RWA}] + \Gamma(\tilde{\rho}) \quad (2.13)$$

with

$$H_{RWA} = \begin{pmatrix} 0 & 0 & \frac{\Omega_0}{2} f(t) \\ 0 & \omega_{HFS} & \frac{\Omega_0}{2} f(t) \\ \frac{\Omega_0}{2} f(t) & \frac{\Omega_0}{2} f(t) & \Delta \end{pmatrix} \quad (2.14)$$

and $\Delta = \omega_i - \omega_g - \omega_c$.

During free evolution, the system of equations becomes:

$$\dot{\rho}_{gg} = \Gamma_{ig} \rho_{ii} \quad (2.15)$$

$$\dot{\rho}_{ee} = \Gamma_{ie} \rho_{ii} \quad (2.16)$$

$$\dot{\rho}_{ii} = -(\Gamma_{ig} + \Gamma_{ie}) \rho_{ii} \quad (2.17)$$

$$\dot{\tilde{\rho}}_{ge} = i\omega_{HFS} \tilde{\rho}_{ge} \quad (2.18)$$

$$\dot{\tilde{\rho}}_{gi} = i\Delta \tilde{\rho}_{gi} - \frac{\Gamma_{ig} + \Gamma_{ie}}{2} \tilde{\rho}_{gi} \quad (2.19)$$

$$\dot{\tilde{\rho}}_{ei} = -i(-\Delta + \omega_{HFS}) \tilde{\rho}_{ei} - \frac{\Gamma_{ig} + \Gamma_{ie}}{2} \tilde{\rho}_{ei} \quad (2.20)$$

$$\dots \quad (2.21)$$

Now, we numerically solve the evolution of the system during a picosecond pulse, let the atom free evolve during a duration T_r and then apply a second pulse. The sets of differential equations are solved using the Python package `odeint`. We checked that the total population is conserved during the whole computed evolution. The results of the simulation are shown on **Figure 2.2**. For the simulation, we choose parameters consonant with the experiment: $\tau=2$ ps, a detuning $\Delta/2\pi=500$ GHz. However, we chose a peak one photon Rabi frequency $\Omega/2\pi=50$ GHz for the sake of visualization. In the experiment, we typically have $\Omega/2\pi=100$ MHz. In purple, we have plotted for visualization the Rabi frequency $\Omega(t) = \Omega_0 f(t)$. For the simulation, the population is initialized in the $|g\rangle$ state.

First of all, we see on the right-hand plot that after a picosecond pulse, the population is transferred to the $|e\rangle$ states. Furthermore, we see that the population in the $|i\rangle$ states is only transiently populated. One can notice that the evolution of the population in the intermediate state follows the same dynamics as the picosecond pulse.

Then, on the two remaining plots, we study the impact of the repetition rate on the population transfer. In the centre, we plot the evolution of the populations when we apply

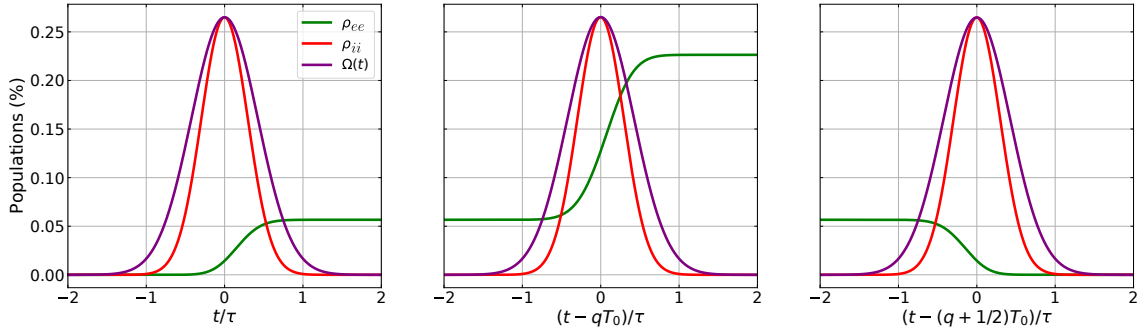


Fig. 2.2 Evolution of the intermediate state and the excited state. Here, $\Omega_0/2\pi = 50$ GHz, $\Delta/2\pi = 500$ GHz, $T_0 = 2\pi/\omega_{HFS}$, $\tau = 2$ ps. a) After one picosecond pulse. b) After two picosecond pulses separated by $T_r = qT_0$. c) After two picosecond pulses separated by $T_r = (q + 1/2)T_0$

a second picosecond pulse after a free evolution of duration $T_r = qT_0$ with q an integer and $T_0 = 2\pi/\omega_{HFS}$. The population transfer has increased compared to after only one pulse. This characteristic is typical of a coherent process. This phenomenon corresponds to a bright fringe of a Ramsey sequence.

Finally, we plot the population dynamic when the second pulse is applied after a free evolution duration of $(q + 1/2)T_0$. Here, we see that the population is transferred back into the ground state $|g\rangle$. This phenomenon corresponds to a dark fringe of a Ramsey sequence.

2.2 Raman diffraction induced by counter-propagating picosecond pulses

Here, I will present a theoretical model derived to obtain the analytical expression of an effective Hamiltonian related to the interaction between N pairs of picosecond pulses and a three-level system.

The main difference between the usual derivation with CW lasers and this derivation is related to the dependency in position. When driving Raman transition in a counter-propagating geometry with CW lasers, one usually writes that the coupling happens between states $|g\rangle = |g, \vec{P}\rangle$, $|e\rangle = |e, \vec{P} + \hbar\vec{k}_{\text{eff}}\rangle$ and $|i\rangle = |i, \vec{P} + \hbar\vec{k}_{\uparrow}\rangle$ where k_{eff} is the effective wave vector of the two lasers driving the transition. However, when using frequency combs, these states are not well defined and the laser pulses couple a continuum of momentum states.

The derivation presented here aims to show that we can overcome this difficulty by simply considering that the momentum dependency can be neglected during the evolution of one pair of counterpropagating pulses.

Here, we will first derive an effective Hamiltonian for one pair of pulses. We will retrieve the impact condition and show that there is a geometrical dependency in the Rabi coupling. Then, we will derive an effective Hamiltonian for N counter-propagating pulses

2.2.1 Description of the problem

We consider a three-level atom interacting with two counter-propagating trains of picosecond laser pulses. We write the electric field as:

$$\begin{cases} \vec{E}_\uparrow(t, z) = \vec{E}_{0\uparrow} \sum_{n=1}^N f(t - nT_r - \frac{z}{c}) \cos\left(\omega_\uparrow(t - \frac{z}{c})\right) \\ \vec{E}_\downarrow(t, z) = \vec{E}_{0\downarrow} \sum_{n=1}^N f(t - nT_r + \frac{z}{c}) \cos\left(\omega_\downarrow(t + \frac{z}{c})\right) \end{cases} \quad (2.22)$$

$$f(t) = e^{-\frac{1}{2} \frac{t^2}{\tau^2}} \quad (2.23)$$

The total Hamiltonian of the system is:

$$\hat{H} = \hat{H}_0 + V(t, \hat{z}) \quad (2.24)$$

where

$$\hat{H}_0 = \sum_s \hbar\omega_s |s\rangle\langle s| + \frac{\hat{p}^2}{2m} \quad (2.25)$$

and $V(t, \hat{z})$ is the coupling Hamiltonian:

$$V(t, \hat{z}) = -\vec{d} \cdot (\vec{E}_\uparrow(t, \hat{z}) + \vec{E}_\downarrow(t, \hat{z})) \quad (2.26)$$

For simplicity, we consider that the field $\vec{E}_\uparrow(t, \hat{z})$ couples the lowest eigenstate of H_0 , labeled $|g\rangle$, with the highest one $|i\rangle$ and that $\vec{E}_\downarrow(t, \hat{z})$ couples the second lowest one $|e\rangle$ with $|i\rangle$, as illustrated in [Figure 2.1](#). The opposite is true as well and, as discussed later, both processes can happen simultaneously under well-defined conditions.

The coupling can thus be written as :

$$V(t, \hat{z}) = V_{ig}(t, \hat{z}) |i\rangle\langle g| + V_{ie}(t, \hat{z}) |i\rangle\langle e| + h.c. \quad (2.27)$$

with

$$V_{ig}(t, \hat{z}) = \frac{\hbar\Omega_0}{2} \sum_{n=1}^N f(t - nT_r + \frac{\hat{z}}{c}) e^{-i\omega_\uparrow(t - \frac{\hat{z}}{c})} \quad (2.28)$$

and

$$V_{ie}(t, \hat{z}) = \frac{\hbar\Omega_0}{2} \sum_{n=1}^N f(t - nT_r - \frac{\hat{z}}{c}) e^{-i\omega_\downarrow(t + \frac{\hat{z}}{c})} \quad (2.29)$$

where $\Omega_0 = -\frac{\vec{d} \cdot \vec{E}_0}{\hbar}$. Again, we suppose that $-e\langle i | \hat{r} \cdot \vec{e} | g \rangle$ and $-e\langle i | \hat{r} \cdot \vec{e} | e \rangle$ are equals.

We write the laser detunings as $\Delta_{\uparrow} = \omega_{\uparrow} - (\omega_i - \omega_g)$ and $\Delta_{\downarrow} = \omega_{\downarrow} - (\omega_i - \omega_e)$ where $\hbar\omega_i$ is the energy of state $|i\rangle$, and define an average detuning $\Delta = (\Delta_{\uparrow} + \Delta_{\downarrow})/2$.

In [Appendix A](#), we show that the time-dependence comes from the pulses' envelop only and varies over a timescale τ which we assume to be smaller than $1/\Delta$. For small couplings ($V \ll \hbar\Delta$), the state $|i\rangle$ is only transitory populated during a pulse and an effective coupling between the states $|g\rangle$ and $|e\rangle$ can be derived using perturbation theory in the quasi-stationary approximation. Since $\delta \ll \Delta$, these states can be considered degenerate such that

$$V_{eg}^{\text{eff}}(\hat{z}, t) = \frac{V_{ie}(t, \hat{z})^{\dagger} V_{ig}(t, \hat{z})}{\hbar\Delta} \quad (2.30)$$

Using [Equation 2.28](#) and [Equation 2.29](#) we obtain :

$$V_{eg}^{\text{eff}}(z, t) = \hbar \frac{\Omega_0^2}{4\Delta} e^{-i(2kz - \omega_L t)} \sum_{n,m} f\left(t - nT_r + \frac{z}{c}\right) f\left(t - mT_r - \frac{z}{c}\right) \quad (2.31)$$

In the experiment, ω_L , the frequency difference between the two combs, is due to the AOM placed in the delay line. In order to simplify the calculation, we will first ignore this shift and set ω_L to zero. The sum over n and m is non-zero only when $n = m$. In the case of Gaussian pulse, we can separate the position and time. We then obtain:

$$V_{eg}^{\text{eff}}(z, t) = \hbar \frac{\Omega_0^2}{4\Delta} e^{-\frac{z^2}{(c\tau)^2}} \sum_n e^{-\frac{2(t-nT_r)^2}{\tau^2}} e^{-i2kz} \quad (2.32)$$

We have introduced $k = \frac{\omega_{\downarrow} + \omega_{\uparrow}}{2c}$

We have therefore the following Hamiltonian :

$$H = \frac{\hat{P}^2}{2m} + \hbar \begin{bmatrix} 0 & \frac{\Omega_i(t, \hat{z})^{\dagger}}{2} \\ \frac{\Omega_i(t, \hat{z})}{2} & \omega_{\text{HFS}} \end{bmatrix} \quad (2.33)$$

where

$$\Omega_i(t, z) = \frac{\Omega_0^2}{4\Delta} e^{-\frac{z^2}{(c\tau)^2}} \sum_n e^{-\frac{2(t-nT_r)^2}{\tau^2}} e^{2ikz} \quad (2.34)$$

2.2.2 Effective Hamiltonian

Because the Hamiltonian is periodic, one can write that at time $t = NT_r$, the evolution operator is given by

$$U(NT_r) = U(T_r)^N \quad (2.35)$$

Our goal it therefore to calculate the evolution $U(T_r)$ for one period. To perform this

calculation, we use the interaction frame defined by:

$$|\psi\rangle_{\text{int}} = Q_{\text{int}}(t) |\psi\rangle \quad (2.36)$$

with

$$Q_{\text{int}}(t) = \begin{bmatrix} 1 & 0 \\ 0 & e^{i\omega_{\text{HFS}}t+i\phi} \end{bmatrix} \quad (2.37)$$

where ϕ , which corresponds to a time at which we synchronize the two frames, will be fixed later. It has no physical meaning.

$|\psi\rangle_{\text{int}}$ is solution of the Schrödinger equation with the Hamiltonian H_{int} defined by:

$$H_{\text{int}}(t) = \frac{\hat{P}^2}{2m} + \hbar \begin{bmatrix} 0 & \frac{\Omega_i(t, \hat{z})^\dagger}{2} e^{-i\omega_{\text{HFS}}t-i\phi} \\ \frac{\Omega_i(t, \hat{z})}{2} e^{i\omega_{\text{HFS}}t+i\phi} & 0 \end{bmatrix} \quad (2.38)$$

In this frame, we can approximate the evolution operator by

$$U_{\text{int}}(T_r/2, -T_r/2) = 1 - \frac{i}{\hbar} \int_{-T_r/2}^{T_r/2} H_{\text{int}}(t) dt \quad (2.39)$$

We define $\Omega(z) = \frac{1}{T_r} \int_{-T_r/2}^{T_r/2} \Omega_i(t, z) e^{-i\omega_{\text{HFS}}t} dt$.

The approximation [Equation 2.39](#) is valid as long as $|\Omega(z)T_r|$ is small and that phase shift due to the kinetic energy is also negligible.

We obtain that :

$$\Omega(z) = \bar{\Omega} e^{-\left(\frac{\hat{z}}{c\tau}\right)^2} e^{2ikz} \quad (2.40)$$

where

$$\bar{\Omega} = \frac{\Omega_0^2}{4\Delta} \sqrt{\pi\tau} f_{\text{rep}} e^{-\frac{\omega_{\text{HFS}}^2 \tau^2}{4}} \quad (2.41)$$

This expression contains the impact condition $e^{-\frac{\omega_{\text{HFS}}^2 \tau^2}{4}}$. When this criterion ($\omega_{\text{HFS}}\tau \ll 1$) is fulfilled, $\bar{\Omega}$ is given by the average intensity of the laser.

We can now calculate the evolution operator over one period:

$$\hat{U}(T_r) = \begin{bmatrix} 1 - iT_r \frac{\hat{P}^2}{2m\hbar} & -\frac{iT_r \Omega(\hat{z})^\dagger}{2} e^{-\frac{iT_r \omega_{\text{HFS}}}{2} - i\phi} \\ \frac{iT_r \Omega(\hat{z})}{2} e^{\frac{iT_r \omega_{\text{HFS}}}{2} + i\phi} & \left(1 - iT_r \frac{\hat{P}^2}{2m\hbar}\right) e^{-iT_r \omega_{\text{HFS}}} \end{bmatrix} \quad (2.42)$$

As said above, for simplification, we choose $\phi = -\frac{T_r \omega_{\text{HFS}}}{2}$.

The key point of the demonstration is the term $e^{-iT_r \omega_{\text{HFS}}}$. When the hyperfine splitting is close to a multiple of the repetition rate, there is an integer q such that $\delta = \omega_{\text{HFS}} - q\omega_{\text{rep}}$ is small compared to ω_{rep} with $\omega_{\text{rep}} = 2\pi/T_r$, i.e. the phase shift $e^{-iT_r \omega_{\text{HFS}}} = e^{-iT_r \delta}$ is small. The number q corresponds to the number of oscillations of the transition during one period

of the frequency comb.

$$\hat{U}(T_r) = \begin{bmatrix} 1 - iT_r \frac{\hat{P}^2}{2m\hbar} & -\frac{iT_r \Omega(\hat{z})^\dagger}{2} \\ \frac{iT_r \Omega(\hat{z})}{2} & \left(1 - iT_r \frac{\hat{P}^2}{2m\hbar}\right) e^{-iT_r \delta} \end{bmatrix} \quad (2.43)$$

Assuming that $|\Omega(z)T_r| \ll 1$ and $\delta T_r \ll 1$, to the first order in those terms, we obtain that

$$\hat{U}(T_r) \simeq e^{-\frac{i}{\hbar} \hat{H}_{\text{eff}} T_r} \simeq \mathbb{1} - \frac{i}{\hbar} \hat{H}_{\text{eff}} T_r \quad (2.44)$$

with

$$\hat{H}_{\text{eff}} = \frac{\hat{P}^2}{2m} + \hbar\delta |e\rangle\langle e| + \frac{\hbar\bar{\Omega}}{2} e^{-\left(\frac{\hat{z}}{c\tau}\right)^2} \left(e^{2ik\hat{z}} |e\rangle\langle g| + e^{-2ik\hat{z}} |g\rangle\langle e| \right) \quad (2.45)$$

This effective Hamiltonian is time independent, and therefore using [Equation 2.35](#), we obtain:

$$U(NT_r) = e^{-\frac{i}{\hbar} \hat{H}_{\text{eff}} NT_r} \quad (2.46)$$

2.2.3 Discussion

First of all, one should remark that even though the two lasers driving the transition have the same frequency, we can drive the transition between the $|g\rangle$ state and $|e\rangle$ state. This is impossible in the case of CW lasers. It is made possible here because the coupling is performed by a short pulse.

The first key point of the demonstration is the use of the interaction frame. Indeed, this allows us to write [Equation 2.39](#). It is not possible to write this equation in the original frame because $\omega_{\text{HFS}} T_r \simeq q$ which is not negligible. By moving into the interaction frame, we rotate the coupling term phase at the speed ω_{HFS} and are now able to write [Equation 2.39](#). This approximation reveals the Fourier transform of the two-photon coupling term. Indeed, assuming that $T_r/2$ is much larger than τ , we can consider integrating over $]-\infty, \infty[$. This Fourier transform reveals a key term: $e^{-\frac{\omega_{\text{HFS}}^2 \tau^2}{4}}$. This term accounts for the impact condition and shows that two-photon transfer is only possible for short pulses, compared with ω_{HFS} . In addition, we found $\bar{\Omega}$, which is the Rabi frequency obtained for a CW laser with the same average power.

In the remainder of the demonstration, we return to the initial frame, going back at a periodical time T_r . Here, we show the expected resonance condition, taking into account the number of oscillations of the transition during a period T_r . This 'modulo' passage allows us to reduce the phase shift to a small one, and thus proceed to the approximation [Equation 2.44](#).

Finally, we obtain an effective Hamiltonian taking into account the atom's external states. Note that this calculation is only valid for times $t = NT_r$. It still allows us to estimate transition probabilities.

In order to take into account the frequency shift of the combs, it is sufficient to perform a first frame change, consisting of shifting the energy of the excited state vector $|e\rangle$ by the same frequency times $\hbar\omega_L$, the value of δ is then given by $\omega_{\text{HFS}} - \omega_L - q\omega_{\text{rep}}$

In the standard treatment of counterpropagating Raman transitions, momentum remains a good quantum number, in the sense that a state with a well-defined momentum will always retain a well-defined momentum. This property allows for straightforward calculations using the plane wave basis, enabling, for instance, the phase to be computed for any initial state, even if it is not a plane wave, as it can be easily written as a superposition of plane waves.

However, in the case of Raman transitions with a picosecond laser, the problem becomes significantly more complex: on the one hand, we know that the transition will be velocity-selective, but on the other hand, the transition will also be position-selective. This introduces a fundamental difficulty. Nevertheless, a quick calculation shows that there is no fundamental incompatibility.

One can estimate the velocity selectivity of the transition. As with the usual counter-propagating Raman transition, it is given by $2k\delta v = \Omega$, where k is the wavevector, δv the velocity spread, and Ω the Rabi frequency. Meanwhile, the position spread is given by $\delta x = c\tau$, where c is the speed of light and τ is the pulse duration. This yields the relation:

$$\frac{m\delta x\delta v}{\hbar} = \frac{c\tau\Omega}{2\hbar k/m} = \frac{c}{v_r}\Omega\tau$$

where v_r is the recoil velocity. Typically, $\frac{c}{v_r} \simeq 10^{10}$, and $\Omega\tau \simeq \frac{1}{N}$, where N is the number of pulses required to achieve a π -pulse. In our experiment, we typically have $N = 10^5$.

In conclusion, $\frac{m\delta x\delta v}{\hbar} \sim 10^5 \gg 1$. Therefore, the transition is not at all limited by the Heisenberg uncertainty principle. One can thus conceive of a wavepacket that has both a position spread $\ll c\tau$ and a velocity spread $\ll \Omega/2k$. In such a case, the position and velocity of the wavepacket can be treated as a classical variable. This allows the transition probability to be calculated by considering both the intensity at the wavepacket's position and its velocity to compute the Doppler shift. This approximation is at the core of the Monte Carlo simulation that we will perform for our experiment, where the initial atomic cloud is decomposed into a sum of Gaussian wavepackets.

When considering the velocity and the position as classical quantities, one can show that the resonance condition becomes

$$\omega_{\uparrow} - \omega_{\downarrow} - 2\pi q f_{\text{rep}} = \omega_{\text{HFS}} + \vec{k}_{\text{eff}} \cdot \vec{v} + \frac{\hbar|\vec{k}_{\text{eff}}|^2}{2m} \quad (2.47)$$

with $\vec{k}_{\text{eff}} = \vec{k}_{\uparrow} - \vec{k}_{\downarrow}$ and the Rabi Raman frequency is

$$\Omega_{\text{eff}} = \frac{\Gamma^2}{4\Delta} \frac{I}{2I_s} e^{-\frac{\omega_{\text{HFS}}^2 \tau^2}{4}} e^{-\left(\frac{z}{c\tau}\right)^2} \quad (2.48)$$

2.3 Excitation schemes

As shown previously, lambda-type two-photon transitions can be driven with a frequency-comb laser if both the resonance condition and the condition of impact excitation are met. Given a certain pulse duration τ , one can drive efficiently any transition in which frequency ω_0 lies in the range 0 to $1/\tau$. More specifically, the transition will be driven with an effective coupling strength scaled by $e^{-(\frac{\delta\tau}{2})^2}$ in comparison to the one obtained with two CW lasers having the same total average power as the frequency comb. One can thus drive Bragg transitions where the states $|g\rangle$ and $|e\rangle$ correspond to different momentum states of the same internal state as well as Raman transitions where states $|g\rangle$ and $|e\rangle$ correspond to different internal states. The resonance condition for a Bragg transition becomes:

$$\omega_{\uparrow} - \omega_{\downarrow} - 2\pi q f_{\text{rep}} = N \vec{k}_{\text{eff}} \cdot \vec{v} + N^2 \frac{\hbar |\vec{k}_{\text{eff}}|^2}{2m} \quad (2.49)$$

where $\vec{k}_{\text{eff}} \equiv \vec{k}_{\uparrow} - \vec{k}_{\downarrow}$ and N is an integer corresponding to diffraction order. The resonance condition for a Raman transition ($N = 1$):

$$\omega_{\uparrow} - \omega_{\downarrow} - 2\pi q f_{\text{rep}} = \omega_0 + \vec{k}_{\text{eff}} \cdot \vec{v} + \frac{\hbar |\vec{k}_{\text{eff}}|^2}{2m} \quad (2.50)$$

where $\hbar\omega_0$ is the energy difference between the two lowest internal states at rest.

Looking at the resonance conditions (2.49),(2.50) one can immediately infer the versatility of using a frequency-comb for driving lambda-type two-photon transitions. Three parameters can be set experimentally to verify the resonance condition: the repetition rate f_{rep} which can be controlled by tuning the comb resonator, the frequency difference $\omega = \omega_{\uparrow} - \omega_{\downarrow}$ which can be controlled by inserting, e.g., an acousto-optic modulator in the optical path of one of the two pulse trains [54], and the integer q , which can not be tuned strictly speaking but which adds flexibility for driving the transition. Notably, one can profit from this versatility to drive more than one transition simultaneously.

The first interesting case is two drive simultaneously two transitions with opposite wavevectors $\pm \vec{k}_{\text{eff}}$. This so-called double-diffraction technique was implemented at SYRTE and required three CW lasers [39]. In this case, the two resonance conditions

$$\begin{cases} \omega_{\uparrow} - \omega_{\downarrow} - 2\pi q f_{\text{rep}} &= \omega_0 + \vec{k}_{\text{eff}} \cdot \vec{v} + \omega_{\text{rec}} \\ \omega_{\downarrow} - \omega_{\uparrow} - 2\pi q' f_{\text{rep}} &= \omega_0 - \vec{k}_{\text{eff}} \cdot \vec{v} + \omega_{\text{rec}} \end{cases} \quad (2.51)$$

Adding this two equations member by member we obtain:

$$f_{\text{rep}} = -(\omega_0 + \omega_{\text{rec}})/\pi(q + q') \quad (2.52)$$

In our experiment, the Raman process is driven between the two hyperfine state of ^{87}Rb . The recoil frequency shift $\omega_{\text{rec}}/2\pi$ is around 15 kHz and the hyperfine splitting $\omega_0/2\pi = 6.834$ GHz and $q=q'=92$. Hence, to drive a double diffraction scheme, we have to detune the repetition rate from the co-propagating transition by only 16 Hz.

Another interesting application is two drive Raman transitions on two different atomic species simultaneously. The pair of resonance condition writes:

$$\begin{cases} \omega_{\uparrow} - \omega_{\downarrow} - 2\pi q f_{\text{rep}} &= \omega_{0,1} + \vec{k}_{\text{eff}} \cdot \vec{v} + \omega_{\text{rec},1} \\ \omega_{\uparrow} - \omega_{\downarrow} - 2\pi q' f_{\text{rep}} &= \omega_{0,2} + \vec{k}_{\text{eff}} \cdot \vec{v} + \omega_{\text{rec},2} \end{cases} \quad (2.53)$$

which gives using the same operation:

$$f_{\text{rep}} = -(\omega_{0,1} + \omega_{0,2} + \omega_{\text{rec},1} + \omega_{\text{rec},2}) / \pi(q + q') \quad (2.54)$$

This excitation scheme can be used for testing the universality of free-fall [2; 7; 10; 14]. In particular, this technique has the advantage of being spatially selective along z , due to the pulse overlap condition, and could thus mitigate position-dependent systematic effects.

Conclusion

In this chapter we have carried out a theoretical analysis of Raman diffraction induced by a frequency comb. The impact and overlap conditions have been obtained. Finally, we demonstrated the possibility of driving different excitation schemes with only one laser.

Chapter 3

Raman diffraction with a picosecond laser

This chapter describes the implementation of Raman diffraction with a frequency comb in a counterpropagating geometry. First, we present the picosecond laser and how we came to full control and knowledge of the central wavelength, the repetition rate, and the duration of the picosecond pulses. Then, briefly, we detail the cold atom sources before explaining the method used to make the picosecond pulses overlap on the cold atomic source. Finally, I will discuss some results of the Raman diffraction of cold atoms by a picosecond laser.

3.1 Pico-second frequency comb laser and characterization

The frequency comb used to drive the Raman transition is a picosecond mode-locked Ti:sapphire solid-state laser from Coherent Inc (model MIRA 900-P). We choose a picosecond laser to address the whole atomic sample (overlap condition). Also, this laser was already available in our laboratory and lent by Francois Nez.

The laser cavity is shown on [Figure 3.1](#). The pump laser is a Verdi V6 providing 6 W of light at 532 nm. This laser is focused on a Ti:Al₂O₃ crystal acting as a gain medium. The starter is used to start the pulse mode operation. The laser usually works in continuous wave (CW) mode. Yet, by changing the cavity's effective length at the proper speed with the starter, very high-power fluctuations can be induced. Once one of these fluctuations achieves a high enough power, a Kerr lens will be formed in the gain medium. The Kerr effect will lead to a smaller beam for the high-power perturbation. As shown on [Figure 3.2](#), if the slit is sufficiently closed, only this perturbation will pass through it and begin to resonate in the laser cavity. Once this soliton pulse is created, the starter stops moving, passive mode locking is achieved and the laser will now emit pulses.

The Gires-Tournois Interferometer is used to compensate for the group velocity dispersion induced by propagation in the cavity. The birefringent filter can be tuned to select the central wavelength of the laser. Changing the slit width enables to modify the pulse duration from 1 to 2 picoseconds.

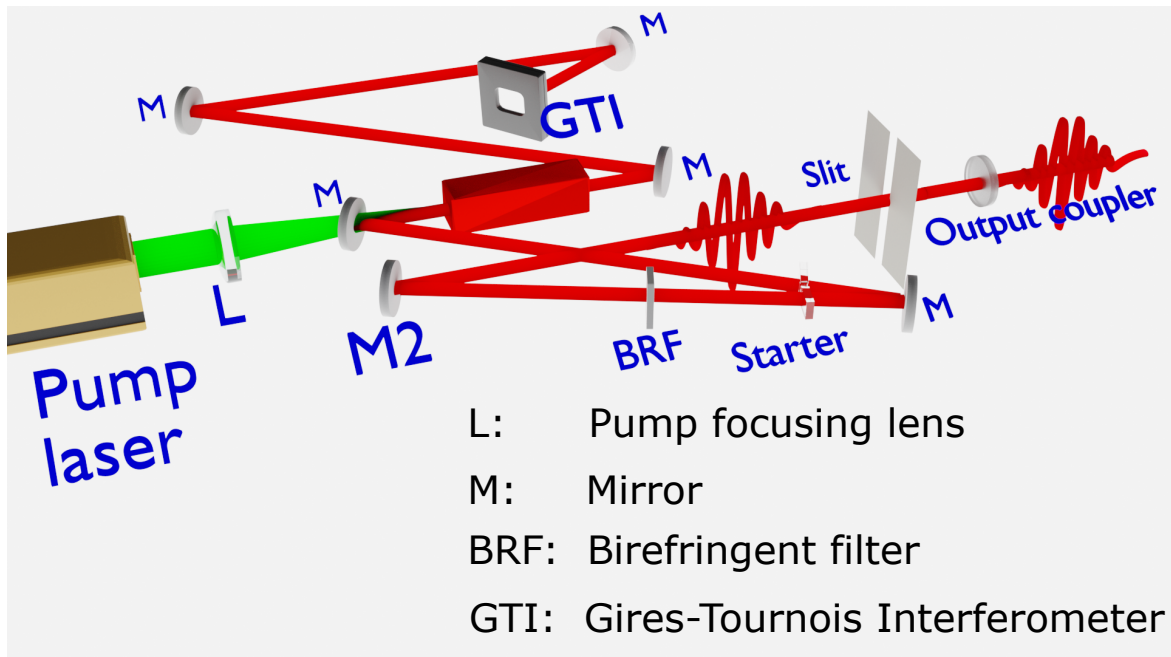


Fig. 3.1 *Optical Schematic of the Mira 900-P cavity. The pump laser is a 6W Verdi laser at 532nm. The gain medium of the laser is the red parallelepiped with Brewster angles.*

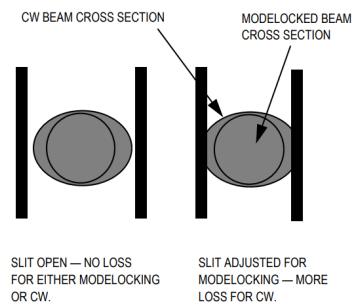


Fig. 3.2 *Beam cross-section in the laser cavity. When closing the slit, there is more loss for CW mode which achieves mode-locking.*

The time between pulses escaping the cavity is equal to the time it takes for light to make one round trip in the cavity. In our case, this time is approximately 13.2 ns, setting the repetition rate $f_{\text{rep}} = 1/T_r \sim 76$ MHz. The output mirror is mounted on a mechanical translating stage which enables to roughly change the size of the cavity. By changing the effective length of the cavity, we can control the repetition rate of the frequency comb and modify it by more than 2 MHz.

Changing the length of the cavity will be used to stabilize the repetition rate frequency. We will perform a feedback loop on the size of the cavity by retroacting on a mirror mounted on 2 piezo transducers (Mirror M2 on [Figure 3.2](#)). At the output of the cavity, we pick up a small amount of light that will be split in two. A part will go on a photodiode to obtain a measurement of the repetition rate and the other part to an optical spectrometer to measure the central wavelength and the duration of the picosecond pulses.

3.1.1 Repetition rate stabilization

We saw in the introduction ([Equation 1.2](#)) that the repetition rate f_{rep} needs to be controlled to drive Raman (also called Lambda) transition. By controlling the length of the laser's cavity, we can tune and lock the repetition rate of the laser. To do so, mirror M2 is mounted (on [Figure 3.1](#)) on two piezo-transducers as shown of [Figure 3.3](#). A slow, long-range piezo is used to compensate for long-term drift, and a fast, small-range one is used to follow high-frequency noise due to vibration. The long-range piezo is coupled to a translating stage to move the whole mirror mount. The fast piezo is meanwhile glued directly to the mirror.

The frequency chain of the repetition rate is displayed on [Figure 3.3](#). The synthesizer is referenced to a Cesium frequency standard delivered by the SYRTE. The error produced by mixing the photodiode signal f_{rep} and the synthesizer frequency ν_{synthe} is fed to an FPGA (RedPitaya). The FPGA will perform feedback on the two piezos. The long characteristic time fluctuation is sent to the slow, long-range piezo whereas the quick characteristic time constant is sent to the fast, short piezo. The PID parameters are carefully optimized to minimize the low-frequency phase noise. The repetition rate is controlled by changing the frequency of the synthesizer which is the command value of the PID.

To decrease the low-frequency noise on the repetition rate, the frequency of the synthesizer is set on a harmonic of the wanted repetition rate. By doing so, we increase by a factor p , where p the harmonic considered, the sensitivity to any error. To do so, before mixing f_{rep} with ν_{synthe} , the signal goes through a band pass filter centred on the harmonic wanted. In the experiment, we use the ninth harmonic. The signal-to-noise ratio on higher harmonic was too low to use them. Also, the repetition rate has a 50 Hz noise because of unknown sources. To reduce it, the experiment is synchronized on the 50 Hz of the sector meaning that the experimental sequence always begins at the same defined phase regarding the sector.

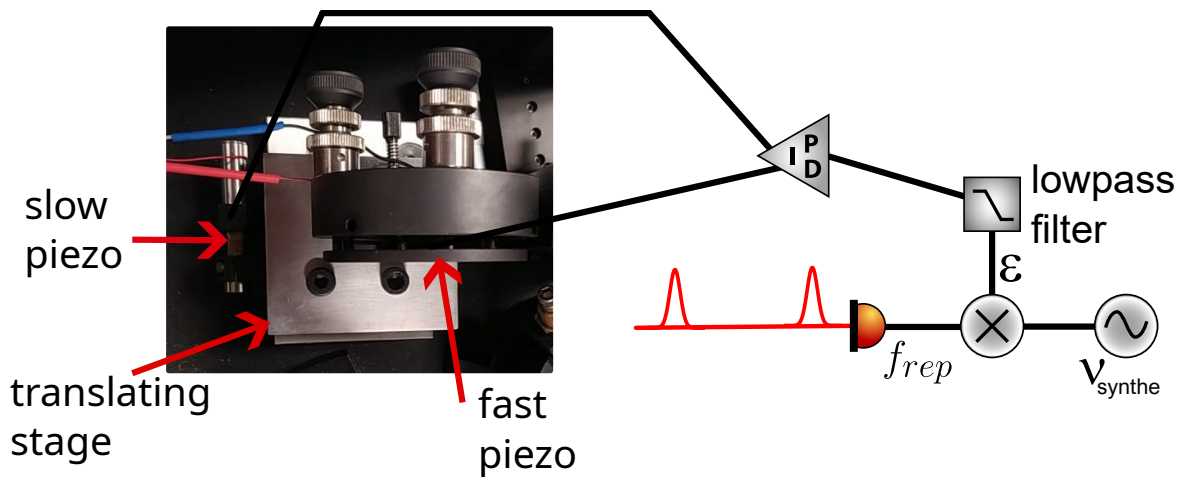


Fig. 3.3 *Repetition rate feedback loop.* The lock of the repetition rate is performed by changing the length cavity using two piezo transducers connected to mirror M2 (left). ν_r is the repetition rate frequency measured by the photodiode, ν_{synthe} the frequency of the synthesizer and ϵ is the residual error. The Proportional Integrator Derivator (PID) module will drive the two piezos.

3.1.2 Laser pulse characterization set-up

The laser's wavelength and the picosecond pulse duration must be measured to obtain full control of the laser. We performed two independent measurements of the picosecond pulse duration with a spectrometer (frequency domain) and an auto-correlation measurement (time domain). These two measurements showed that the pulses are close to being Fourier-limited.

3.1.2.1 Spectrometer measurement

To measure the pulse's spectral width, a part of the pulse picked at the output of the cavity is sent to an optical spectrometer, shown on [Figure 3.4](#). This spectrometer (Jarrell-Ash Model 82-410 Monochromator Spectrometer) was adapted and realigned to match its working point to the picosecond laser wavelength around 790 nm.

The laser is first sent on a curved mirror. The focal point of the mirror is on a grating. The light is then collimated by a second curved mirror. We collect the light on a CCD camera. Typical images are shown on [Figure 3.5](#).

Calibration

We need to calibrate the spectrometer to obtain a measurement of λ and of the spectral width of the frequency comb. We therefore need to calibrate the pixel to wavelength equivalence and the optical transfer function (OTF) of the spectrometer. The OTF of an optical system specifies how different optical frequencies are transmitted and reflected by the system. Mainly because of the grating in the spectrometer and because we want to accurately determine the spectral width of the frequency comb, the determination of the

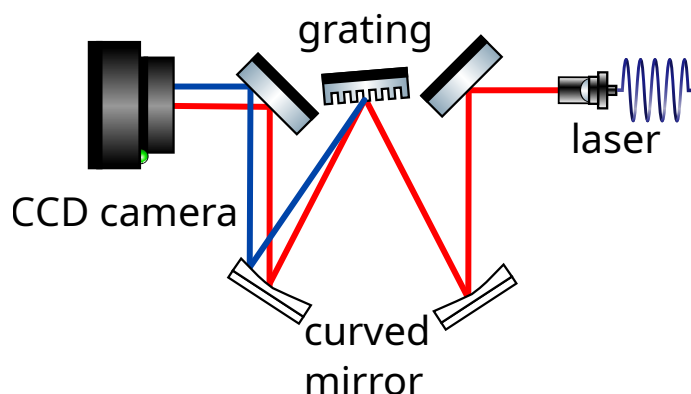


Fig. 3.4 Optical set-up of the spectrometer. The two colours represent the result for two different wavelengths. By rotating the grating, we adjust the wavelength imaged on the CCD camera.

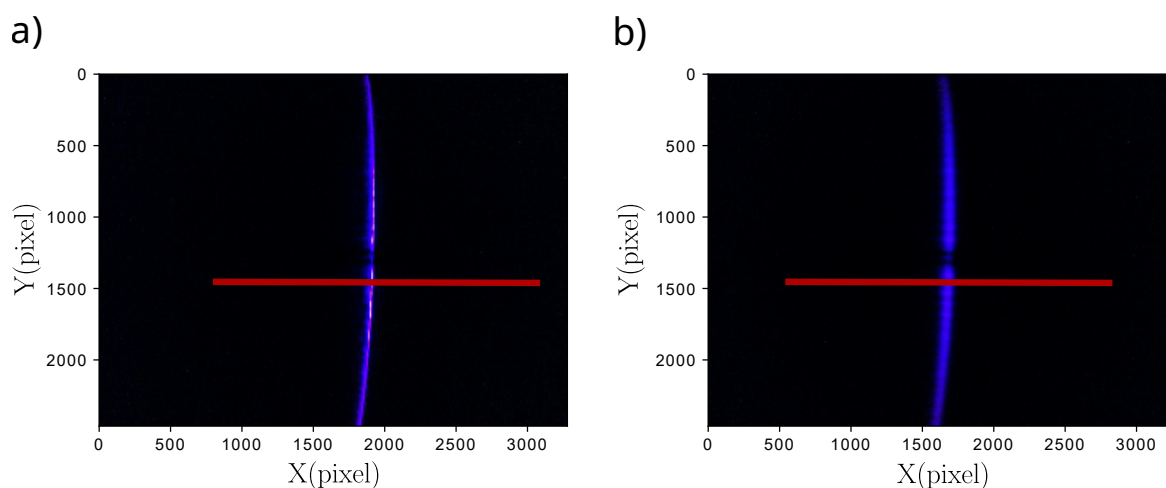


Fig. 3.5 a) Image recovered at the output of the optical spectrometer with a CW reference laser used to calibrate the spectrometer. b) Image at the output of the optical spectrometer with the frequency comb. The frequency comb line is larger because of its spectral width. The red line represents the slice taken for data analysis.

transfer function is critical. To perform the calibration, we use the Mira laser working in CW mode meanwhile its wavelength is measured with a wave meter.

First, we adjust the grating to centre the signal on the camera. Then, we take the image shown on **Figure 3.5a)** and take a slice of it along the red line. This gives us a measurement of the transfer function of the spectrometer. Indeed, we assume that the line-width of the Mira working in CW mode is infinitely narrow compared to the resolution of the spectrometer, estimated at around 20 GHz.

Then, we Fourier transform the fit function chosen to be a hyperbolic secant according to the data sheet of the Mira laser and multiply it with the Fourier transform of the transfer function of the spectrometer obtained previously. Finally, we apply the inverse Fourier transform to this function and obtain the fitting function.

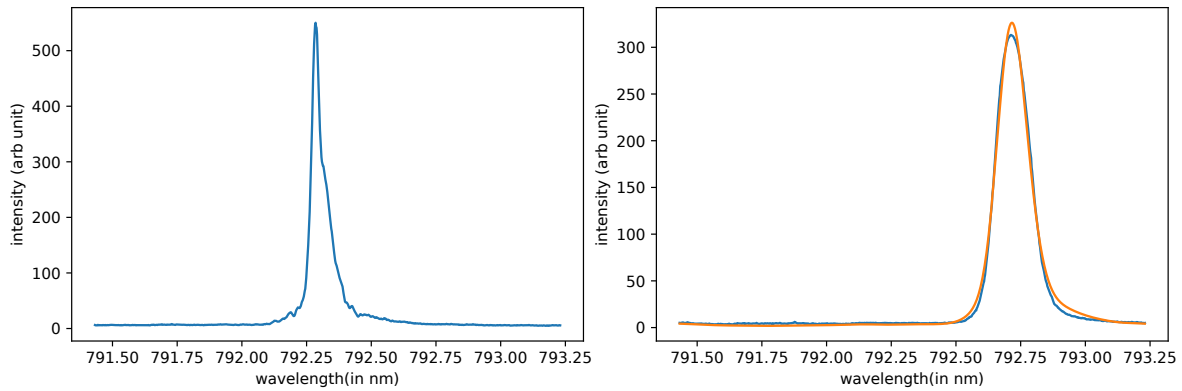


Fig. 3.6 Profile of the CCD image along the red line. Left: Experimental data acquired using a CW laser used to obtain the transfer function. Right: Signal with the Mira laser working in pulsed mode. Blue line: data for a picosecond pulse. The orange line is a fit by a hyperbolic secant convolve with the transfer function of the spectrometer. The fit gives $\Delta\nu = 260.6 \pm 1.2\text{GHz}$ and $\lambda_0 = 792.74(2)\text{nm}$.

Measurement

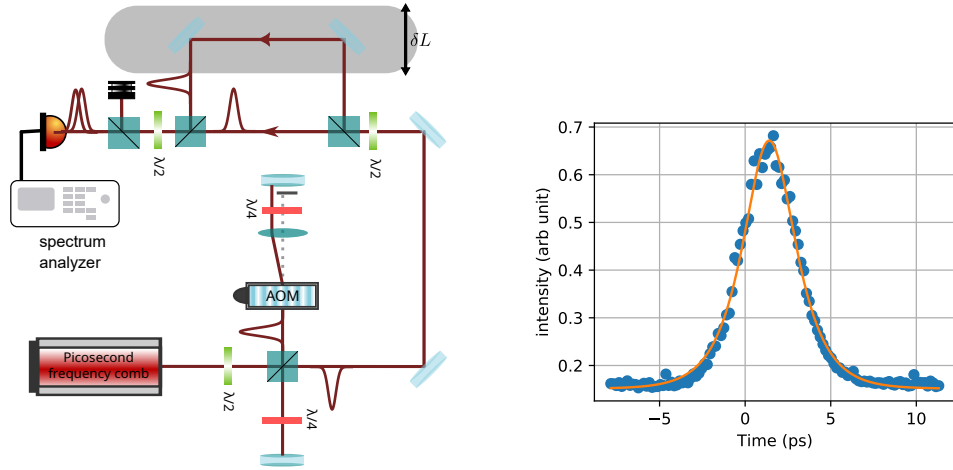
Next, we take an image while the laser is working in pulsed mode and obtain [Figure 3.5b](#)). The raw signal of the slice along the red axis is shown in blue on [Figure 3.6](#). By fitting the blue signal by the fit function defined here before, we obtain the orange curve.

Thanks to the calibration in CW mode and by measuring its wavelength with a wave meter, the central position of the ray on the CCD camera gives us the central wavelength. The FWHM of the power spectrum is given by the fit. The fit, shown on [Figure 3.6](#), gives $\Delta\nu = 260.6 \pm 1.2\text{GHz}$ and $\lambda_0 = 792.74(2)\text{nm}$

3.1.2.2 Intensity auto-correlation measurement

An auto-correlation measurement was performed to confirm the previous measurement of the picosecond laser power spectrum. This measurement was performed in parallel with the previous measurement. Indeed, the picosecond pulse duration can drift over time due to temperature variation for instance. Also, it is important to underline that the picosecond duration can be easily changed by a factor of two by simply opening or closing the slit. This is why these two measurements were performed in the same experimental configuration in a short time-lapse.

The set-up is shown on [Figure 3.7](#). A pulse is split in two by a beam splitters and the reflected beam enters a first delay line. Then, the transmitted pulse enters a second variable length delay line and the other one travels in a fixed length path of the second delay line. The two paths are then recombined on a PBS before being sent on a photodiode. If the two pulses arrive at the same time, or at least if they overlap a bit when arriving on the photodiode, a beating signal can be observed at twice the frequency of the AOM. The amplitude of the signal on the photodiode is given by



a) Auto correlation measurement set-up. The AOM is used to produce a signal at 80 MHz. By changing the size of the second delay line (grey shaded area), we obtain a measurement of the temporal duration of a picosecond pulse.

b) Auto-correlation measurement. The fit (orange line) gives $\tau_{ac} = 2.4$ ps

Fig. 3.7 Auto-correlation set-up and measurement.

$$I(t) = A \operatorname{sech}^2 \left(1.76 \frac{(t - t_{dl})}{\tau_{ac}} \right) \quad (3.1)$$

with t_{dl} the delay between the two pulses and τ_{ac} the FWHM of auto-correlation of the intensity envelope. The formula demonstrates that an increase in the degree of overlap between the pulses will result in a corresponding enhancement of the signal amplitude. Results are shown on **Figure 3.7**. t_{dl} is varied by changing the first delay line length. On the spectrum analyzer, we observe a signal at twice the frequency of the AOM (because of the double pass scheme). The fit, in orange, gives $\tau_{ac} = 2.4$ ps. To retrieve the duration τ_p , the FWHM of the intensity envelope in seconds, using τ_{ac} , we use the table below extracted from the Mira 900-P manual.

τ_p = FWHM of intensity envelope function in seconds.

τ_{AC} = FWHM of auto-correlation function of corresponding intensity envelope.

$\Delta\nu$ = FWHM of power spectrum in units of Hertz.

The coefficient for hyperbolic secant pulses to obtain τ_p from τ_{ac} is 0.648. Finally, we obtain $\tau_p = 1.55$ ps.

The Time-Bandwidth product is

$$\tau_p \times \Delta\nu = T \quad (3.2)$$

where T is the time-bandwidth product limit. For hyperbolic secant, this product is limited

FUNCTION	$I(t)$	τ_p/τ_{ac}	$\Delta\nu\tau_{ac}$	$\Delta\nu\tau_p$
Square	$I(t) = \begin{cases} 1; & t \leq \frac{\tau_p}{2} \\ 0; & t > \frac{\tau_p}{2} \end{cases}$	1	1	1
Gaussian	$I(t) = \exp\left[-\frac{4 \ln 2 t^2}{\tau_p^2}\right]$	0.707	0.624	0.441
Hyperbolic secant	$I(t) = \operatorname{sech}^2\left(\frac{1.76t}{\tau_p}\right)$	0.648	0.486	0.315
Lorentzian	$I(t) = \frac{1}{1 + \left(\frac{4t^2}{\tau_p^2}\right)}$	0.500	0.441	0.2206
Symmetric 2-sided exponential	$I(t) = \exp\left(-2\frac{ t \ln 2}{\tau_p}\right)$	0.413	0.344	0.142

Table 3.1: Comparison of different pulse shapes

by the Fourier limit and is equal to 0.315. The two measurements were performed in two distinct domains: the time domain, using the auto-correlation technique, and the spectral domain, employing a spectrometer. The same pulse was used for both measurements. We found $\Delta\nu = 260$ GHz and $\tau_p = 1.55$ ps which gives a time-bandwidth product of 0.403. The pulses are not Fourier limited but are close to.

3.2 Cold atom source

Now, we will present the experimental setup used to produce the cold atoms source that will be interrogated by the picosecond laser. This experiment was performed on the old h/m apparatus used for the fine structure constant measurement in 2011. Here, I will only briefly explain each building block. More details about the theory and techniques can be found in each thesis of the groups. Mainly, I would recommend the thesis of [5] as the experiment presented here-after is performed on the same vacuum chamber and optical set-up.

3.2.1 Ultra high vacuum chamber

We use an ultra-high vacuum chamber illustrated on [Figure 3.8](#). The vacuum chamber is composed of two distinct parts: the 2D MOT chamber and the 3D MOT chamber. The 2D MOT is used to cool down atoms using lasers and magnetic fields in two dimensions. The 3D MOT is fed by the 2D MOT using a push beam. With this apparatus, we can create a cloud of 10^8 atoms in less than 500 ms.

3.2.2 Trapping and cooling atoms

As it is routinely done, we use two lasers to trap and cool Rubidium atoms. Both lasers are generated through laser diodes in Extended Cavity Diode Laser configuration. They are delivering up to 20 mW. We then amplify their power, using a Tapered Amplifier, up to 1W.

The first one, the cooling, is red detuned from the $|5s^2S_{1/2}, F = 2\rangle \rightarrow |5s^2P_{3/2}, F' = 3\rangle$. This laser will cycle the transition and cool the atoms.

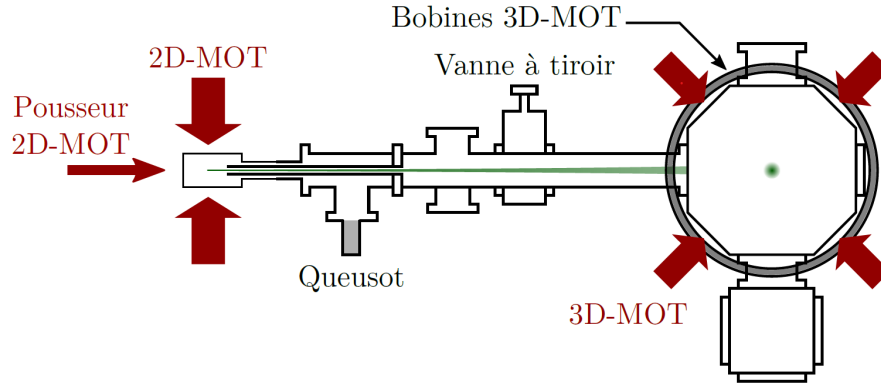


Fig. 3.8 Side view of the vacuum cell, including the 2D-MOT, the 3D-MOT, as well as the coils generating the magnetic field gradient necessary for the 3D-MOT. Extracted from [5].

The second laser, the repump laser, is at resonance with the $|5s^2S_{1/2}, F' = 1\rangle \rightarrow |5s^2P_{3/2}, F' = 2\rangle$ transition. Indeed, after the absorption of one photon from the cooling laser, the atoms might decay to the $|F = 1\rangle$. Thanks to the repump laser, we repump the atoms to the excited state and thus create a closed transition.

The atomic levels are represented on [Figure 3.9](#) as well as the frequency of the lasers presented here before. The repump's frequency is locked thanks to a saturated absorption of Rubidium atoms. The cooling laser is locked on the repump by performing an optical beating of the two lasers.

After the 3D-MOT sequence, we use optical molasses to achieve a cooling up to a few μK of around 10^8 atoms in a cloud of ~ 1 mm.

3.2.3 Time of flight detection

Below the 3D MOT chamber (also called the science chamber), we have a cubic vacuum chamber where we use time of flight technique to detect the atoms in each hyperfine level. This detection system, shown on [Figure 3.10](#), is composed of two laser light sheets at resonance with $|5s^2S_{1/2}, F = 2\rangle \rightarrow |5s^2P_{3/2}, F' = 3\rangle$ retro reflected to create a situation analogue to an optical molasses enhancing the fluorescence signal. The atoms, free-falling through these two circularly polarized light sheets, will first encounter the top light sheet. The atoms in the $|F = 2\rangle$ levels will emit photons collected on a first photodiode. A cache is positioned at the base of the upper light sheet to circumvent the 'molasses effect' and thus will allow atoms to be blown away thanks to radiation pressure. This allows for the removal of atoms in the $|F = 2\rangle$ level. We thus have a measurement of the number of atoms in one of the hyperfine levels. Then, the remaining atoms in the $|F = 1\rangle$ are repumped in the $|F = 2\rangle$ using a repump light sheet. The atoms are then detected in the last light sheet with a second photodiode, similar to the first sheet setup. This allows us to make a measurement of the population in the two hyperfine levels.

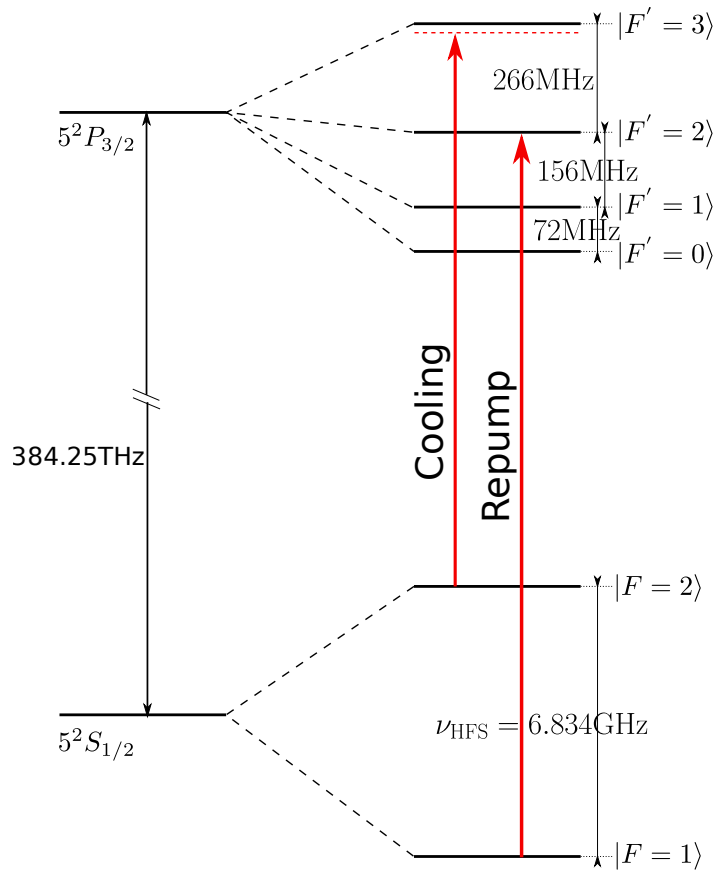


Fig. 3.9 Energy diagram of the D2 line of ^{87}Rb . The frequency of Repump and Cooling lasers are presented in red.

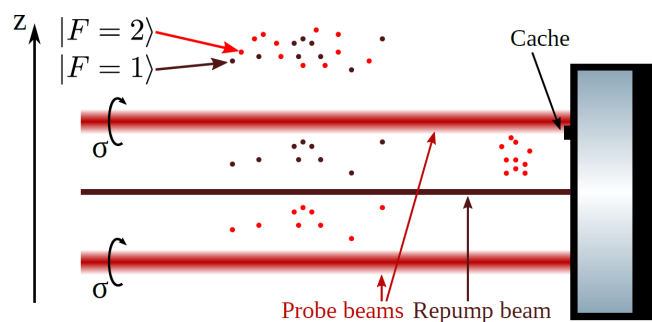


Fig. 3.10 Side view that shows the counterpropagating circularly polarized light sheets. The atoms in $|F = 2\rangle$ are detected in the first light sheet and blown away thanks to the cache placed on the retro-reflecting mirror in order to stop the molasses effect. The remaining atoms, in $|F = 1\rangle$, are then repumped and detected in the same way.

3.3 Fixed length delay line set-up

As mentioned before, if one wants to use stimulated Raman transition to diffract and deflect atoms, the transition must be driven by counterpropagating beams. Using a frequency comb, it imposes that the two counterpropagating pulses overlap at the position of the atoms.

3.3.1 Raman transition with a frequency comb: experimental realisation

To make the picosecond pulses overlap on the atoms, we used a delay line shown on [Figure 3.11](#) in the blue zone. A picosecond pulse is split in two by a PBS. The transmitted beam is coupled to a fiber and sent directly to the vacuum chamber. This pulse will be retro-reflected by the mirror placed at the bottom of the chamber before arriving at the atoms. During that, the reflected beam will enter a delay line with an accurately chosen length so that the distance the pulse travels in the delay line is equal to the distance between the atoms and the bottom mirror. An experimental protocol, presented hereafter, has been developed to ensure this condition. Once this condition is achieved, the pulses will overlap at the position of the MOT release. An acousto-optic modulator (AOM1) on [Figure 3.11](#) is placed in the delay line to compensate for the Doppler shift caused by the free fall of the atoms. AOM-2 is used as a switch to control the interrogation time between the atom and the laser.

The resonance condition for a counter-propagating Raman transition is

$$\omega_1 - \omega_2 = \omega_{HFS} + \vec{k}_{\text{eff}} \cdot \vec{v} + \omega_{\text{rec}} \quad (3.3)$$

Where ω_1 and ω_2 are the pulsations of the comb teeth that induce the Raman transition, ω_{rec} is the recoil shift acquired during the Raman transition, equal to $\sim 2\pi \cdot 15$ kHz for Rb^{87} , ω_{HFS} is the splitting between the two states we want to address, equal to $2\pi \cdot 6.834$ GHz and $\vec{k}_{\text{eff}} \cdot \vec{v}$ is the Doppler effect induced by the free fall of the atom. Because we split a picosecond pulse in two, the repetition rate and the carrier envelop frequency offset for the two pulsations (ω_1 and ω_2) are the same. Also, the pulses that traveled in the delay line (pulse 2) acquired twice the frequency of AOM1. All this gives

$$\begin{aligned} \omega_1 &= 2\pi((n+q)f_{\text{rep}} + f_{\text{fceo}}) \\ \omega_2 &= 2\pi(nf_{\text{rep}} + f_{\text{fceo}} + 2f_{\text{AOM}}) \end{aligned} \quad (3.4)$$

replacing ω_1 and ω_2 in equation 3.3, we obtain

$$2\pi(qf_{\text{rep}} - 2f_{\text{AOM}}) = \omega_{HFS} + \vec{k}_{\text{eff}} \cdot \vec{v} + \omega_{\text{rec}} \quad (3.5)$$

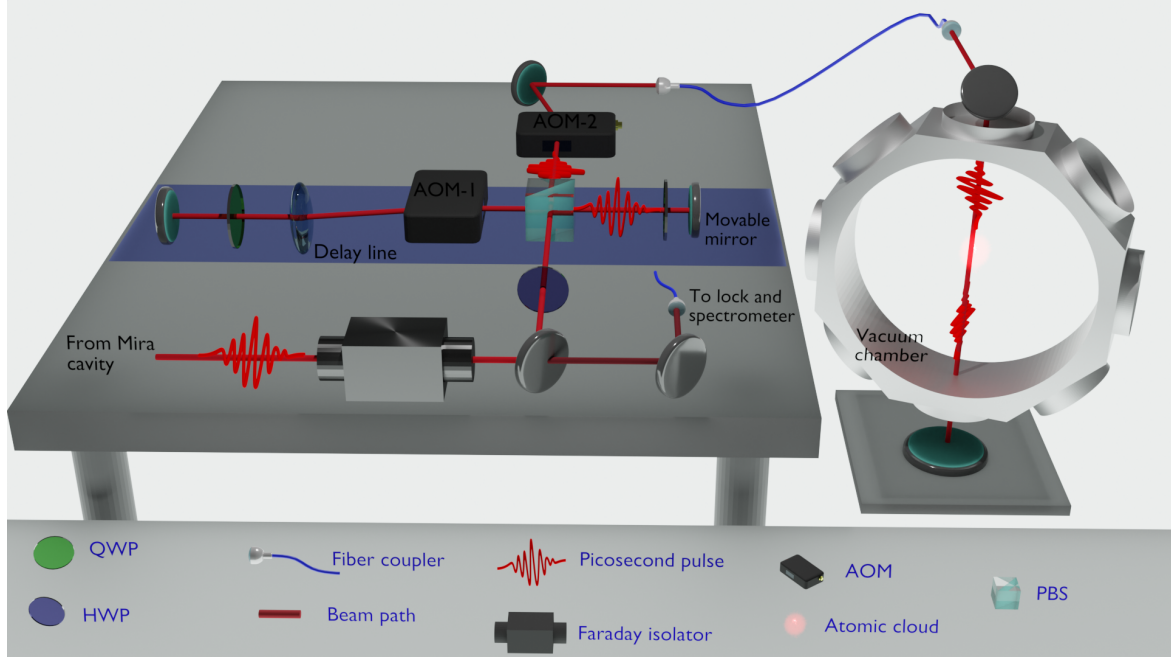


Fig. 3.11 *Experimental set-up. The blue area defines the delay line.*

By setting $4\pi f_{\text{AOM}}(t) = 4\pi f_{\text{rep}} - \vec{k}_{\text{eff}} \cdot \vec{v} - \omega_{\text{rec}}$, we obtain

$$(q - 2)f_{\text{rep}} = \nu_{\text{HFS}} \quad (3.6)$$

The picosecond laser has a repetition frequency of around 76 MHz and the hyperfine splitting of Rb^{87} is $\nu_{\text{HFS}} = 6.834$ GHz, it imposes $q = 92$. In the spectral domain, it means that the tooth labelled $n + 2$ (delayed pulse) will be coupled with the $n + 92$ (direct beam) tooth of the pulse to drive the transition (because of the AOM, all the teeth of the delayed pulse are shifted by $+2f_{\text{rep}}$). In the temporal domain, the atom oscillates 90 times at the hyperfine frequency between two picosecond pulses. The AOM acts, in the spectral domain, as an offset of frequency for the delayed pulse resulting in a shift of 2 teeth as shown on [Figure 3.12b](#).

3.3.2 Measurement of the delay line

To adjust the delay line's length and set it up equal to the distance between the initial position of the cloud and the bottom mirror, we developed a measurement technique based on co-propagating Raman transition. When driving co-propagating transition, the resonance condition becomes $\nu_1 - \nu_2 = \nu_{\text{HFS}}$. Thus, to be resonant, we set the repetition rate equal to $f_{\text{rep}} = \nu_{\text{HFS}}/q$ with $q = 90$.

Usually, to perform Raman transition with CW laser, we used perpendicular linear polarization between the two lasers or $\sigma^+ - \sigma^-$ polarization [21]. When using a frequency comb the teeth that induce Raman transitions will be part of the same pulse. This means that we can not have perpendicular linear polarization between the two frequencies. To perform co-propagating Raman transition we thus use σ polarization. However, later, when

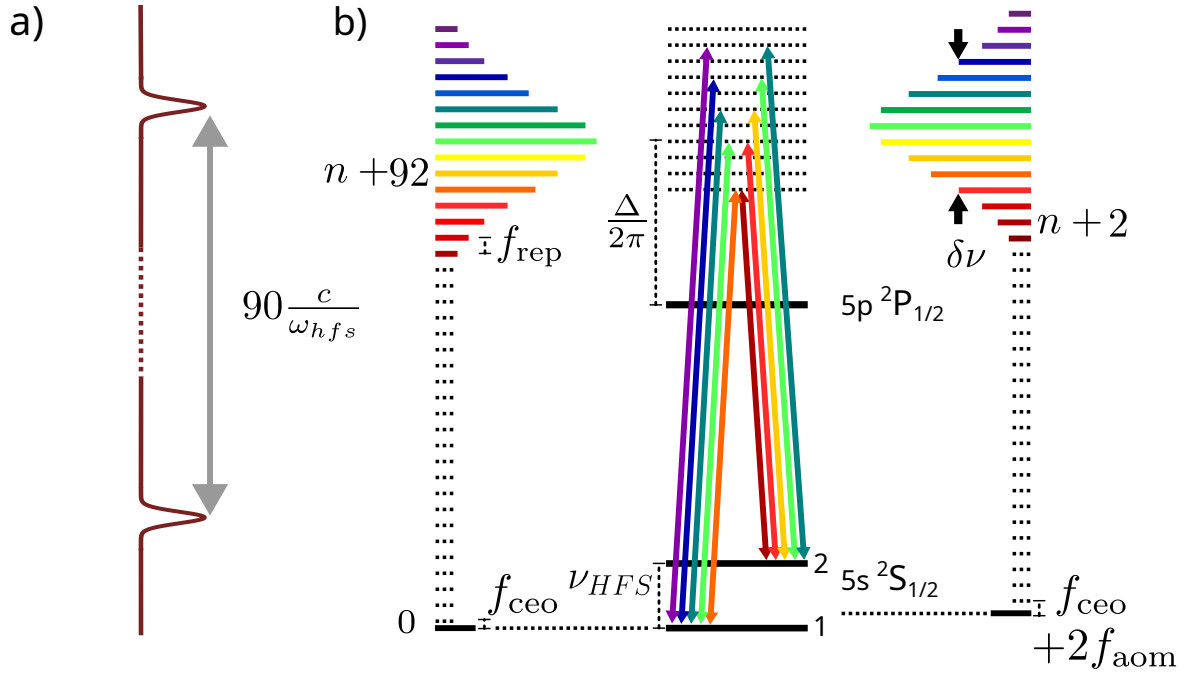


Fig. 3.12 Excitation scheme in the case $q=92$ a) in the temporal domain b) in the frequency domain.

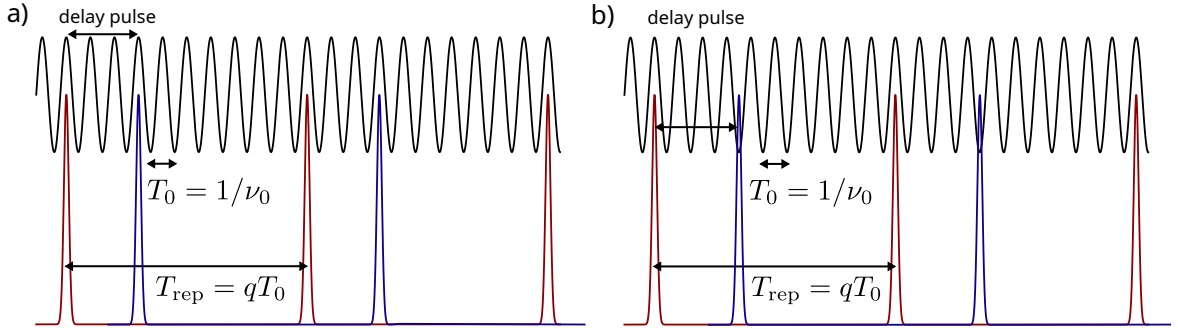


Fig. 3.13 a) The two pulses interfere constructively. b) The two pulses interfere destructively. The black sinusoid depicts the oscillation of the atom at ν_{HFS} . In red and blue, we display the trains of picosecond lasers delayed by a time delay pulse.

we drive counter-propagating transition we will use perpendicular linear polarization. This allows for higher Rabi frequency and also avoids spurious co-propagating transition. In practice, for this experiment, we place a quarter-wave plate (QWP) at the output of the collimator.

The method developed here to fix the delay line length uses two trains of picosecond pulses, with the delay between each pair of pulses being adjustable. In **Figure 3.13**, these two pulse trains are shown in red and blue. We adjust the repetition rates of these two trains so that they drive copropagating transitions. The principle of the method can be understood by considering two scenarios, illustrated in **Figure 3.13**:

- Case A: when the two picosecond pulses are in phase with the transition dipole, their

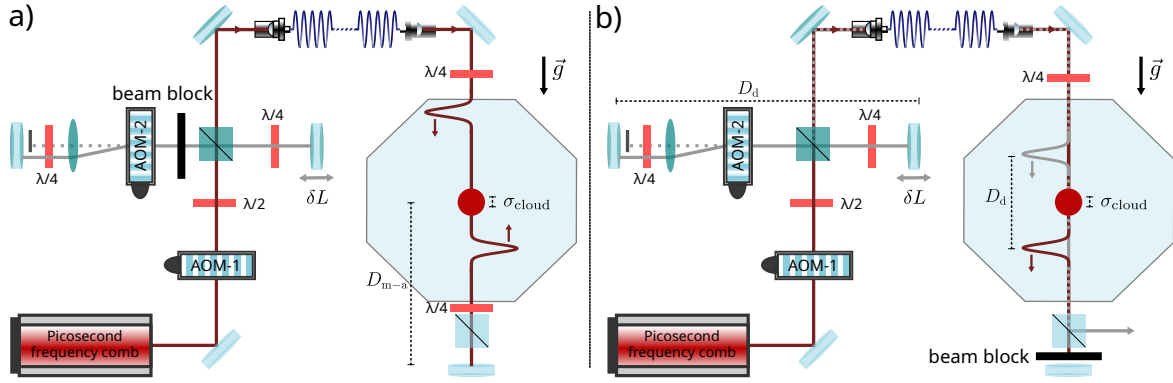


Fig. 3.14 a) *First experimental setup.* The two delayed pulse trains are here the direct train and the retro-reflected one. By changing the time at which we start the interaction between the cloud and the pulse train, we modify the distance D_{m-a} and thus the delay between the two trains. b) *Second experimental setup.* The two trains are coming from the delay line and the direct beam. By changing the size of the delay line, we change the delay between the two picosecond pulse trains D_d .

interaction with the atom interfere constructively. This means the combined effect of the pulses enhances the atomic transition.

- Case B: when the pulses are delayed such that the second pulse arrives out of phase with the transition dipole, the net transfer between the two hyperfine states is zero.

This experiment can also be viewed as a sequence of Ramsey fringes formed by the interaction of the red and blue pulses [60]. If the delay between pulses is a multiple of $1/\nu_{\text{HFS}}$, the pulses are in phase, leading to constructive interference. Conversely, if it is a half multiple of $1/\nu_{\text{HFS}}$, the pulses are out of phase, causing destructive interference. These scenarios were illustrated in [chapter 2](#).

Set-up and results

To fix the delay line length, we will perform two different experiments shown in [Figure 3.14](#).

In the first case, the transitions will be driven by pulses where the delay is due to the retro-reflection, and we will not use the delay line (beam block). By modifying the time from the beginning of the free fall at which we perform the transitions, we change the distance D_{m-a} (distance mirror-atoms) in [Figure 3.14](#). Thus, we modify the delay $T = 2D_{m-a}/c$ between the two pulses. By scanning the time at which we start the interaction between the atoms and the laser we obtain the measurement presented in [Figure 3.15a](#)). We observe interference fringes in the probability of finding the atom in the excited state as a function of the free fall distance. The oscillation period is approximately 2.2 cm, which agrees with the theory. Indeed, the bright fringes should be obtained when $T = 1/\nu_{\text{HFS}}$. In this configuration, $T = 2D_{m-a}/c$, thus giving

$$D_{m-a} = \frac{c}{2\nu_{\text{HFS}}} = 2.2 \text{ cm} \quad (3.7)$$

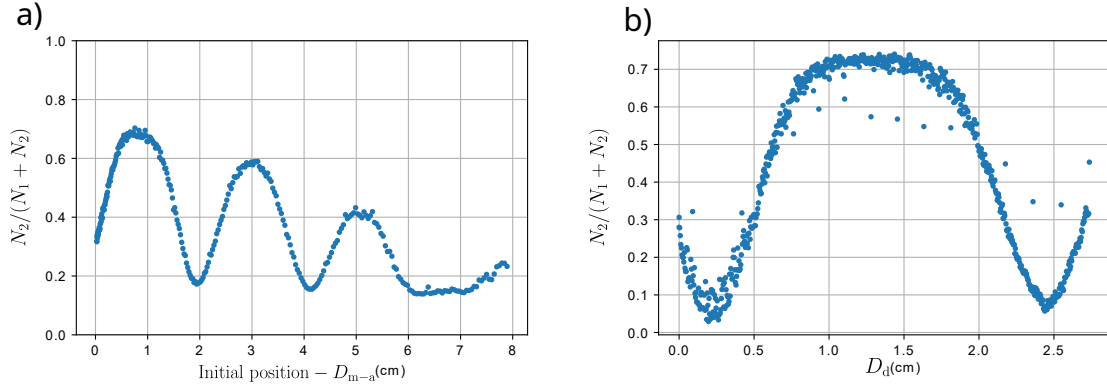


Fig. 3.15 a) Transition probability as a function of the free-fall distance. The loss of contrast can be attributed to the fact that for considerable free-fall distances, the cloud experiences disparate T_R during the transition, resulting in a loss of coherence. b) Transition probability as a function of mirror displacement.

Furthermore, we observe a drop in contrast as we increase the free fall distance. The longer the atoms fall, the faster they fall. Thus, during a co-propagating pulse with a duration of approximately 1 ms, the faster the atom moves, the more it will experience a different delay within the transition, resulting in a drop in contrast.

The second experiment we are going to perform is shown in Figure 3.14b). The delayed pulse, shown in grey, comes from the delay line. The time interval between the two pulses is therefore $T = 2D_d/c$. By varying the length of the delay line using a motorised mirror, we scan the delay between the pulses and obtain the results shown in Figure 3.15b). We observe the same periodicity as in the previous experiment.

We now need to reconcile the two curves. Experimentally, we look for the delay line lengths for which we get the same transition rate as at the initial position of the cloud on the curve in Figure 3.15a). In other words, it is when D_d is equal to the release position of the atomic cloud.

We identify two possible options: either around 0.5 cm or close to 2.7 cm. Note that these two distances are not physical distances as one should take into account the thickness and index of refraction of every optics on each beam path. Anyway, by attempting counter-propagating transitions around these two positions, we find the delay line length that allows the two counter-propagating pulses to overlap with the atomic cloud.

3.3.3 Counter-propagating Raman transition

The quarter-wave plates that were previously installed for the preceding experiment are now removed in order to achieve orthogonal linear polarisation for the two pulses (see Figure 3.11). Using the spectrometer to measure the wavelength of the picosecond laser, we set the central wavelength to be detuned by $\Delta/2\pi \sim 500$ GHz from the D1 line of rubidium. This detuning is chosen to minimise the π pulse duration while avoiding spontaneous emission. Due to the spectral width of the frequency comb, typically $\Delta\nu \sim 150$ GHz for picosecond pulses duration of 1ps, it is impossible to further reduce the detuning without

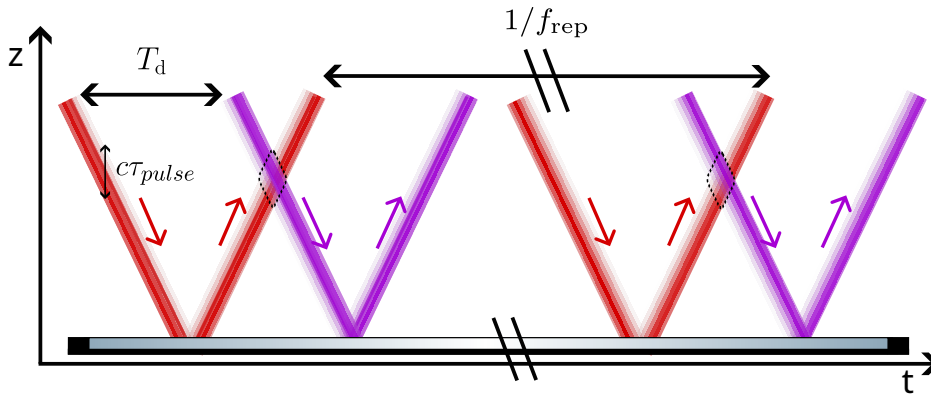


Fig. 3.16 Space time diagram of the overlap zone shown in the dashed diamond. The red beam is reflected by the retro-reflecting mirror. The purple beam comes from the delay line.

spontaneous emission.

On **Figure 3.16**, we show the space-time diagram of two overlapping picosecond pulses. The time D_d/c has been calibrated using the previous experiments so that the dashed diamond is at the initial position of the MOT. It may also be important to note that thousands of pairs of picosecond pulses will drive a transition. For example, for π pulse duration of 0.6 ns, or in other words, for Rabi frequency of $\Omega = 5.2$ kHz, we need 22000 pairs of picosecond pulses overlapping on the cloud to transfer the atoms from one hyperfine level to the other.

Figure 3.17 a) shows a dumped Rabi oscillation. After a π pulse of counterpropagating Raman transition which acts as a velocity selector, we apply a second Raman pulse and scan its duration. We observe dumped Rabi flopping. The damping of the oscillation is identified as a result of coupling inhomogeneity, mainly due to the picosecond pulse duration. Imagine an atom at the centre of the overlap zone when AOM1 is switched on. An increase in the duration of the interaction will result in the atom falling and undergoing different Rabi couplings due to the Gaussian spatial shape of the Rabi coupling, which will dampen the oscillation.

Figure 3.17b) shows a Rabi spectrum. We apply a π Raman pulse and scan the detuning regarding the two photons' resonance by changing the repetition rate of the Mira laser. Thus, we address different velocity classes of the atomic cloud. This experiment measures the velocity distribution of the cloud. The fit gives a temperature of 4.9 μ K.

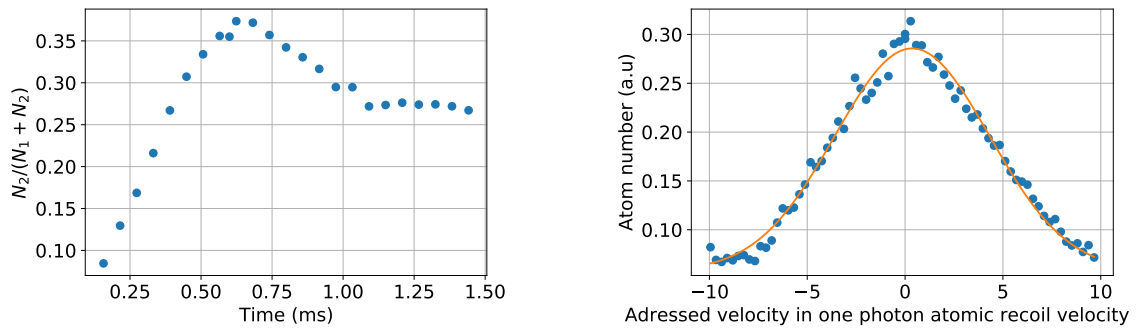


Fig. 3.17 a) Transition probability as a function of the duration of the second pulse. The π pulse duration is around 0.65ms. b) Measurement of the velocity distribution: Temperature $4.91 \pm 0.18 \mu\text{K}$.

Conclusion

In this chapter, we have detailed the experimental setup used to cool rubidium atoms and shown how to fully control each characteristic of the frequency comb laser saying; the repetition rate, the central wavelength and the duration of the picosecond pulses. We then performed two complementary experiments to set the delay line length so that the picosecond pulses overlap at the initial position of the atomic cloud. Finally, we drove a counter-propagating Raman transition with the frequency comb laser. We are now able to create a spatially separated coherent superposition of an atom using a frequency comb driven Raman transition in a counterpropagating geometry.

Chapter 4

First atom interferometer driven by a frequency comb

This chapter is devoted to the development and first demonstration of an atom interferometer based on stimulated Raman transitions driven by a picosecond laser. We will briefly present the theory of atomic interferometers using a $\pi/2 - \pi/2 - \pi/2 - \pi/2$ pulse sequence. Using a Monte Carlo simulation, we will discuss some subtleties related to frequency comb atom interferometry.

4.1 Theory of atom interferometry

The key parameter in light pulse atom interferometry is the difference in phase of the two atomic waves that interfere at the output of the interferometer. Usually, the Feynman path integral approach is used to derive the phase acquired by an atom along a classical trajectory [57]. Here, we will use a formalism presented by Professor W.P. Schleich at the FOMO summer school and detailed in [51]. This formalism uses the manipulation of evolution operators. We consider a Ramsey-Bordé atom interferometer produced by a sequence of 4 $\pi/2$ pulses.

General consideration

We consider a two-level atom with level $|g\rangle, |e\rangle$ interacting with a laser, at resonance, of wavevector k . The energy of the $|g\rangle$ state is chosen to be zero and the one of $|e\rangle$ to be $\hbar\omega_e$. The momentum kick acquired when performing the transition is $\hbar k$. The interaction between the lasers and the atoms is considered infinitely short (delta pulses). This approximation will not impact the phase sensitivity results and will allow for simpler calculations. In the experiment, the $|g\rangle$ and $|e\rangle$ states are the hyperfine levels addressed through Raman transition. The system considered here consists then of two quantum degrees: 1) two internal states $|g\rangle, |e\rangle$ introduced earlier. 2) centre-of-mass motion in state $|j\rangle$ labelled $|\Psi_j\rangle$. To obtain the signal at the output of the atom interferometer, we focus on the evolution of the $|\Psi\rangle$ state defined by

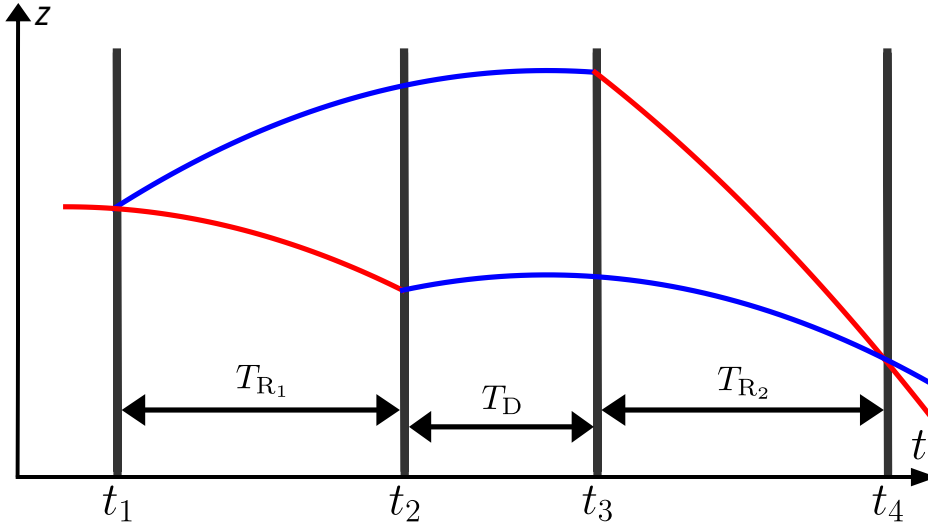


Fig. 4.1 Ramsey Bordé interferometer in the lab-frame. In red and blue we represent respectively the trajectory of the $|g\rangle$ and $|e\rangle$ levels. In black, we represent the Raman pulses considered as infinitely short.

$$|\Psi(t)\rangle = |g\rangle |\Psi_g\rangle + |e\rangle |\Psi_e\rangle \quad (4.1)$$

We consider the Ramsey-Bordé interferometer shown on **Figure 4.1**. It is performed using a sequence of four $\pi/2$ pulses, each one inducing a Raman transition between the two internal levels $|g\rangle$ and $|e\rangle$. The interrogated atoms fall freely in the field of gravity. The corresponding Hamiltonian is

$$\hat{H} = \hat{H}_0 + \hat{H}_1 \quad (4.2)$$

With:

1. $\hat{H}_0 = \left(\frac{\hat{p}^2}{2m} + mg\hat{z} \right) + \hbar\omega_e |e\rangle \langle e|$
2. \hat{H}_1 the Hamiltonian of interaction with the laser

The Schrödinger equation is

$$i\hbar \frac{d}{dt} |\Psi(t)\rangle = \hat{H} |\Psi(t)\rangle \quad (4.3)$$

As long as \hat{H} is time independent $|\Psi(t)\rangle = U(t,0) |\Psi(0)\rangle = e^{-\frac{i\hat{H}t}{\hbar}} |\Psi(0)\rangle$. Here, however, the Hamiltonians are explicitly time-dependent due to the interaction with the laser. Yet, we can decompose the evolution operator as follow:

1. when not interacting with the laser: $U_e(t',t) = e^{-\frac{i}{\hbar} \left(\frac{\hat{p}^2}{2m} + mg\hat{z} + \hbar\omega_e \right) (t'-t)}$ if in the $|e\rangle$ state.

2. when not interacting with the laser: $U_g(t', t) = e^{-\frac{i}{\hbar} \left(\frac{\hat{p}^2}{2m} + mg\hat{z} \right) (t' - t)}$ if in the $|g\rangle$ state.
3. when interacting with the laser, assuming δ like pulses $U_{l\pm}(t) = e^{\pm i(k\hat{z} - \omega t \pm \phi(t))}$ (see [51] appendix A.4). The sign depends if the photon is absorbed or emitted by the atom. We will consider a plus sign when the atom absorbs a photon.

We denote $|\Psi^{up}\rangle$ (resp $|\Psi^{down}\rangle$) the wave function at the exit port of the interferometer coming from the upper (resp. lower) arm of the interferometer.

$$|\Psi^{up}\rangle = U^{up} |\Psi(0)\rangle \quad (4.4)$$

with

$$U^{up} = U_g(t_4, t_3) U_{l-}(t_3) U_e(t_3, t_1) U_{l+}(t_1) \quad (4.5)$$

and

$$|\Psi^{down}\rangle = U^{down} |\Psi(0)\rangle \quad (4.6)$$

with

$$U^{down} = U_{l-}(t_4) U_g(t_4, t_2) U_{l+}(t_2) U_g(t_2, t_1) \quad (4.7)$$

For now, we will focus on the upper path.

Looking at **Figure 4.3**, the atom first interacts with the laser, evolves freely in the $|e\rangle$ state during a time $T_{R_1} + T_D = T_{D_1}$ before interacting again with the laser, and to evolve freely in the $|g\rangle$ state during T_{R_2} . The wave function can be written as:

$$|\Psi^{up}\rangle = N_1 e^{-\frac{i}{\hbar} \left(\frac{\hat{p}^2}{2m} + mg\hat{z} \right) T_{R_2}} e^{-i(k\hat{z} - \omega t_3 - \phi_3)} e^{-\frac{i}{\hbar} \left(\frac{\hat{p}^2}{2m} + mg\hat{z} + \hbar\omega_e \right) T_{D_1}} e^{+i(k\hat{z} - \omega t_1 + \phi_1)} |\Psi(0)\rangle \quad (4.8)$$

with t_i the times at which we apply the i -th pulse, ω the frequency of the laser, ϕ_i the phase of the laser at the time t_i and N_1 a pre-factor linked to the transition probability of each pulse. This factor only matters when taking care of the contrast which is not the case right now. For the sake of simplicity, we will not consider these factors in the following part.

We get from the previous equation

$$|\Psi^{up}\rangle = e^{-i\omega_e T_{D_1}} e^{-i(\omega t_1 - \omega t_3 + \phi_1 - \phi_3)} e^{-ik\hat{z}} e^{-\frac{i}{\hbar} \left(\frac{\hat{p}^2}{2m} + mg\hat{z} \right) T_{D_1}} e^{+ik\hat{z}} |\Psi(0)\rangle \quad (4.9)$$

We now want to simplify this expression. First, lets focuses on $e^{-ik\hat{z}} e^{-\frac{i}{\hbar} \left(\frac{\hat{p}^2}{2m} + mg\hat{z} \right) T} e^{+ik\hat{z}}$.

We have:

$$\begin{aligned} e^{-ik\hat{z}} e^{-\frac{i}{\hbar} \left(\frac{\hat{P}^2}{2m} + mg\hat{z} \right) T} e^{+ik\hat{z}} &= e^{-ik\hat{z}} \sum_{n=0}^{+\infty} \frac{1}{n!} \left(\frac{-i}{\hbar} \left(\frac{\hat{P}^2}{2m} + mg\hat{z} \right) T \right)^n e^{+ik\hat{z}} \\ &= \sum_{n=0}^{+\infty} \frac{1}{n!} \left(\frac{-i}{\hbar} T \right)^n e^{-ik\hat{z}} \left(\frac{\hat{P}^2}{2m} + mg\hat{z} \right)^n e^{+ik\hat{z}} \end{aligned} \quad (4.10)$$

We recall the identity

$$e^{-ik\hat{z}} \left(\frac{\hat{P}^2}{2m} + mg\hat{z} \right) e^{+ik\hat{z}} = \left(\frac{(\hat{P} + \hbar k)^2}{2m} + mg\hat{z} \right) \quad (4.11)$$

which together with [Equation 4.10](#) leads to

$$\begin{aligned} &= \sum_{n=0}^{+\infty} \frac{1}{n!} \left(\frac{-i}{\hbar} T \right)^n \left(\frac{(\hat{P} + \hbar k)^2}{2m} + mg\hat{z} \right)^n \\ &= e^{-\frac{i}{\hbar} \left(\frac{(\hat{P} + \hbar k)^2}{2m} + mg\hat{z} \right) T} \end{aligned} \quad (4.12)$$

To simplify, we introduce $\hat{H}_g = \frac{\hat{P}^2}{2m} + mg\hat{z}$ and $\hat{H}_e = \frac{(\hat{P} + \hbar k)^2}{2m} + mg\hat{z}$. One can remark that

$$\hat{H}_e = \hat{H}_g + \frac{\hbar k}{m} \hat{P} + \frac{(\hbar k)^2}{2m} \quad (4.13)$$

We obtain

$$|\Psi^{up}\rangle = e^{-i\omega_e T_{D1}} e^{-i(\omega t_1 - \omega t_3 + \phi_1 - \phi_3)} e^{\frac{-i\hat{H}_g T_{R2}}{\hbar}} e^{\frac{-i\hat{H}_e T_{D1}}{\hbar}} |\Psi(0)\rangle \quad (4.14)$$

Simplifying the calculation by assuming that $\omega = \omega_e$, we have

$$|\Psi^{up}\rangle = e^{i(\phi_1 - \phi_3)} e^{\frac{-i\hat{H}_g T_{R2}}{\hbar}} e^{\frac{-i\hat{H}_e T_{D1}}{\hbar}} |\Psi(0)\rangle \quad (4.15)$$

If one consider that the laser is detuned from resonance, a phase shift will appear in the final phase sensitivity of the interferometer. Yet, our goal for now is to study the phase sensitivity in the simplest case.

The goal is now to merge the two last exponential terms. The issue is that the two Hamilto-

nians do not commute. However, their commutator is a c-number. Indeed :

$$\begin{aligned}
[\hat{H}_e, \hat{H}_g] &= [\hat{H}_g + \frac{\hbar k}{m} \hat{P} + \frac{(\hbar k)^2}{2m}, \hat{H}_g] \\
&= \frac{\hbar k}{m} [\hat{P}, \hat{H}_g] \\
&= \hbar k g [\hat{P}, \hat{z}] \\
&= -i\hbar^2 k g
\end{aligned} \tag{4.16}$$

Thus, using the Baker-Campbell-Hausdorff formula and we obtain

$$|\Psi^{up}\rangle = e^{-i(\phi_1 - \phi_3)} e^{\frac{-i(\hat{H}_g T_{R_2} + \hat{H}_e T_{D_1})}{\hbar}} e^{-\frac{i}{2\hbar} [\hat{H}_g, \hat{H}_e] T_{R_2} T_{D_1}} |\Psi(0)\rangle \tag{4.17}$$

giving finally

$$|\Psi^{up}\rangle = e^{-i(\phi_1 - \phi_3)} e^{\frac{-i(\hat{H}_g T_{R_2} + \hat{H}_e T_{D_1})}{\hbar}} e^{-\frac{i}{2} k g T_{R_2} T_{D_1}} |\Psi(0)\rangle \tag{4.18}$$

For the lower path, one can show, using the same derivation that

$$|\Psi_i^{down}\rangle = e^{-i(\phi_2 - \phi_4)} e^{\frac{-i(\hat{H}_g T_{R_1} + \hat{H}_e T_{D_2})}{\hbar}} e^{+\frac{i}{2} k g T_{D_2} T_{R_1}} |\Psi(0)\rangle \tag{4.19}$$

We can define the phase operator as :

$$|\Psi^{up/down}\rangle = e^{i\hat{\Phi}_{up/down}} |\Psi(0)\rangle \tag{4.20}$$

The quantum state at the exit port of the interferometer is $|\Psi\rangle \propto (U^{up} + U^{down}) |\Psi(0)\rangle$. Here, we only have a proportionality because we neglect the pre-factor N_1 and N_2 . The phase of the interferometer will be obtain computing $e = \langle \Psi^{up} | \Psi^{down} \rangle$ with

$$e = \langle \Psi(0) | U^{up\dagger} U^{down} | \Psi(0) \rangle \tag{4.21}$$

$$= \langle \Psi(0) | e^{-i\hat{\Phi}_{up}} e^{+i\hat{\Phi}_{down}} | \Psi(0) \rangle \tag{4.22}$$

Again, the two operators do not commute. However, the commutator is a c-number and can be evaluated as:

$$[-\hat{\Phi}_{up}, \hat{\Phi}_{down}] = -k g (T_{R_2} (T_{R_2} + T_D) - (T_{R_1} (T_{R_1} + T_D))) \tag{4.23}$$

Using the BCS formula, we obtain

$$e^{-i\hat{\Phi}_{up}} e^{+i\hat{\Phi}_{down}} = e^{i(-\hat{\Phi}_{up} + \hat{\Phi}_{down} + \frac{1}{2\hbar} [-\hat{\Phi}_{up}, \hat{\Phi}_{down}])} = e^{i\Delta\hat{\Phi}} \tag{4.24}$$

Finally, it leads us to:

$$\Delta\hat{\Phi} = \phi_1 - \phi_2 - \phi_3 + \phi_4 + \frac{kg}{2}(T_{D_2}T_{R_1} + T_{R_2}T_{D_1}) - \frac{\hat{H}_g}{\hbar}(T_{R_1} - T_{R_2}) + \frac{\hat{H}_c}{\hbar}(T_{R_1} - T_{R_2}) - \frac{kg}{2}(T_{R_2}(T_{R_2} + T_D) - T_{R_1}(T_{R_1} + T_D))$$

$$\Delta\hat{\Phi} = \phi_1 - \phi_2 - \phi_3 + \phi_4 + \frac{kg}{2}(2T_{R_2}T_{R_1} + T_D(T_{R_1} + T_{R_2}) - T_{R_2}(T_{R_2} + T_D) + T_{R_1}(T_{R_1} + T_D)) + \left(\frac{k}{m}\hat{P} - \frac{\hbar k^2}{2m}\right)(T_{R_1} - T_{R_2})$$

We identify different term in the previous equation:

1. $\frac{kg}{2}(2T_{R_2}T_{R_1} + T_D(T_{R_1} + T_{R_2}) - T_{R_2}(T_{R_2} + T_D) + T_{R_1}(T_{R_1} + T_D))$ arises from the non commutation of the position and momentum operator. This is the phase shift induced by the earth's gravitational field in a Ramsey-Bordé interferometer.
2. $\phi_1 - \phi_2 - \phi_3 + \phi_4$ is linked to the phase of the laser at the atom position. This term is often written as $k\beta t^2$. This is as writing that in order to stay resonant with the free-falling atoms, we chirp the frequency of the laser at a rate $k\beta$. If $\beta = g$, for the free falling atom, the phase of the laser is constant.
3. $\frac{\hbar k^2}{2m}(T_{R_1} - T_{R_2})$ is the nonzero recoil shift linked to the asymmetry in the pulse timing.
4. $\frac{k}{m}\hat{P}(T_{R_1} - T_{R_2})$ is also linked to the asymmetry in the pulse timing. It is related to the non-closure of the interferometer.

Experimentally, we consider a symmetric interferometer, meaning when $T_{R_1} = T_{R_2} = T_R$. In that case, we obtain the usual phase sensitivity of a Ramsey-Bordé interferometer[15]

$$\Delta\Phi = \phi_1 - \phi_2 - \phi_3 + \phi_4 + kgT_R(T_R + T_D) \quad (4.25)$$

In the case of a symmetric interferometer, the phase difference is a scalar. Thus, this phase is independent of the state at the input of the interferometer. From this equation, we see that if we chirp the frequency of the laser at a rate $-\beta$ the output phase becomes

$$\Delta\Phi = k(g - \beta)T_R(T_R + T_D) \quad (4.26)$$

First, if one scans β , it is possible to determine the value at which g and β cancels out, meaning it is possible to determine the Earth gravitational acceleration with a Ramsey-Bordé interferometer. Second, the sensitivity scales as the square of the interrogation. As usual, the longer you measure, the more sensitive you are.

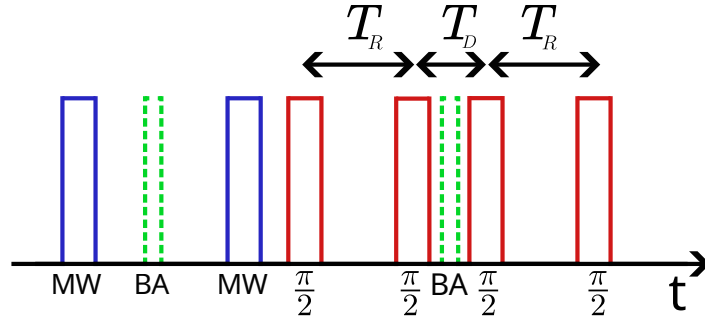


Fig. 4.2 Temporal sequence used first to prepare the atoms and then to perform the Ramsey-Bordé interferometer. MW: microwave pulse BA: blow away. In red, we display the Raman pulses used to split and recombine the atomic wavepacket

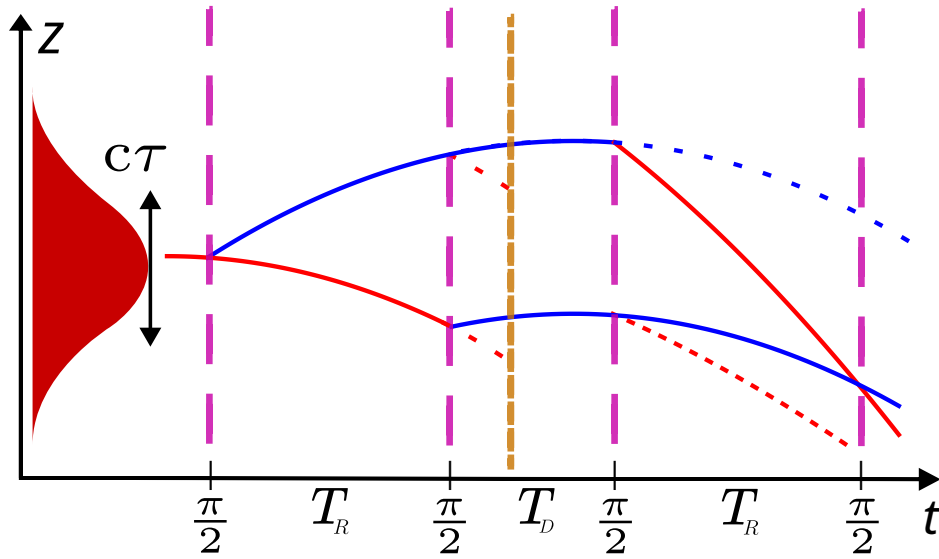


Fig. 4.3 Space-time diagram of a Ramsey-Bordé interferometer in the lab frame. The red Gaussian represents the calculated Rabi frequency from Equation 2.48. The trajectories of the atomic wave packet are in full line. The purple dashed lines represent the Raman light pulses used to split and deflect the wave packets. In yellow, I represent the blow away pulse applied during the sequence to remove the parasitic atomic path (in dashed lines). In the end, two spurious trajectories remain (red and blue dashed lines). These trajectories limit the contrast of a Ramsey Bordé.

4.2 Experimental results

The time sequence of the experiments is shown on Figure 4.2. After the MOT and the molasses sequence, we have about 10^8 atoms in the $|F = 2\rangle$ states. Then, we prepare atoms in the $|F = 2, m_F = 0\rangle$ states with two microwave pulses. In between, we apply a light pulse to blow away the remaining atoms in $|F = 2\rangle$. The blow away pulse is made using the cooling laser set at resonance with the $|5s^2S_{1/2}, F = 2\rangle \rightarrow |5s^2P_{3/2}, F' = 3\rangle$ transition. The radiation pressure will blow the atoms in the $|F = 2\rangle$ away. The pre-selection allows for the following to start the interferometer with a pure cloud of $m_F = 0$ atoms. Thus, the

atoms in the interferometer are insensitive to the first-order Zeeman.

After 5 ms of this cloud preparation, we implement a Ramsey-Bordé interferometer as shown on [Figure 4.3](#). On the left, we have shown the overlap zone of size $c\tau$. It is clear from this drawing that the interferometer must take place within this overlap zone. The red and blue lines represent respectively the ground and excited state trajectory. The purple dashed line represents the Raman $\frac{\pi}{2}$ pulse. Each $\frac{\pi}{2}$ pulse is realised by two counter-propagating trains of about $N \sim \tau \frac{\pi}{2} f_{\text{rep}}$ picosecond pulses. In the experiment, with a Rabi frequency on the order of 3.5 kHz, a beamsplitter is composed of $N \sim 15000$ picosecond pulses that overlap. Between each pair of $\frac{\pi}{2}$ pulses, the atoms are allowed to freely evolve during T_D . During this time we also apply blow-away pulses to remove the atoms in the $|F = 2\rangle$ state represented by the red dashed line before the blow away pulse. This will increase the contrast of the interferometer. Indeed, without the blow away pulse, these atoms would have reach the end of the interferometer, creating a background of atoms not interfering in the detection. Finally, we record the population in the two hyperfine states using a time-of-flight setup. By changing the chirp rate β of AOM1, which is used to compensate for the Doppler effect, we retrieve atomic fringes.

A typical data set obtained at the output of the interferometer is shown in [Figure 4.4](#). Each data point corresponds to an average of three repetitions of the experimental cycle. The inset in [Figure 4.4](#) shows a fit of the central fringe from which we derive the contrast of the interferometer. The contrast is defined, as it is commonly done in the community, by the difference between the maximum and the minimum of the fringes. The uncertainty in the position of the central fringe allows the gravitational acceleration g to be determined with a relative uncertainty of the order of 10^{-5} in 5 min. The sensitivity reached by the setup is far from being competitive with usual gravimeters working with CW lasers. For instance, the gravimeters at Syrte using CW lasers can reach a sensitivity of 5.7×10^{-9} in a second. Yet, the interrogation times are clearly not comparable (4.2ms in the experiment and around typically 60ms for the Syrte gravimeter) and we will see later how we can increase the interrogation time in the case of frequency comb atom interferometry. The orange line represents the result of a Monte Carlo simulation.

4.2.1 Monte Carlo Simulation

I have conducted a Monte Carlo simulation to model the interferometer. The initial position and velocity of N atoms are chosen randomly according to a normal distribution of position (the experimentally measured size of the cloud) and velocity (the temperature of the cloud, see [Figure 3.17](#)). Then we calculate the classical trajectories during the free fall and evaluate, using the matrix density formalism, the number of atoms in each internal state after each $\frac{\pi}{2}$ pulse using [Equation 2.48](#), where the effective Rabi frequency is

$$\Omega_{\text{eff}} = \frac{\Gamma^2}{4\Delta} \frac{I}{2I_s} e^{-\left(\frac{z}{c\tau}\right)^2} e^{-2\left(\frac{r}{\omega}\right)^2} \quad (4.27)$$

with r the position of the atom in the x,y plan (the free fall direction is along z), ω is the waist of the laser, z the position of the atom along the free fall, and τ the picosecond pulse

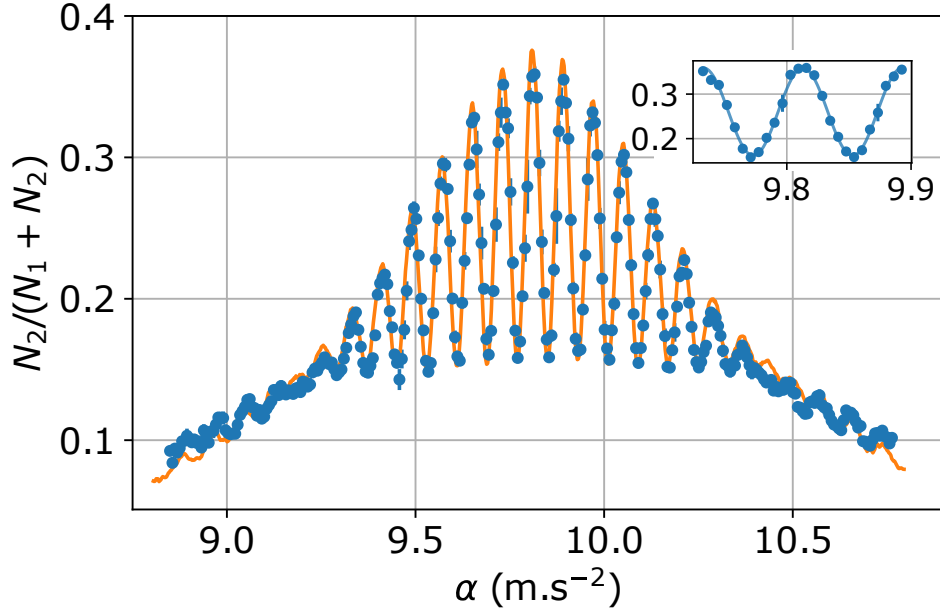


Fig. 4.4 Atomic fringes at the output of the interferometer: Fraction of atoms in $|5s^2 S_{1/2}, F = 2\rangle$ state as a function of the frequency chirp used to compensate for the Doppler effect due to free fall. Experimental data are shown as blue points. The simulated fringes, obtained from the Monte Carlo simulation, without any adjusted parameters except the central position are shown as a solid orange line. Here $\Delta/2\pi = 0.41(5)$ THz, $T_R = 1.5$ ms, $T_D = 1.2$ ms, $\tau = 2.00$ ps and $\sigma_{\text{cloud}} = 0.67$ mm. Inset zoom: A fit (solid line) to the central fringe is used to determine the fringe contrast and the Earth's gravitational acceleration with a relative statistical uncertainty $\sim 10^{-5}$.

duration. The impact condition was neglected as we have $\omega_{\text{HFS}} \ll 1/\tau$.

Note that for a CW laser, the Rabi frequency is the same removing the pulse envelop $e^{-(\frac{z}{c\tau})^2}$. Here we assume that the interaction of an atom with a pulsed laser is the same as the interaction with a CW laser (the atom sees only the average power of the comb and not the peak power of each pulse) times a term due to spatial coupling. Finally, we calculate the fraction of atoms in each arm of the interferometer. By changing the frequency chirp rate in the simulation, we obtain the orange curve on [Figure 4.4](#). To obtain this curve, we used all the experimental parameters measured: τ_π duration, Rabi frequency, Ramsey time, free evolution time, cloud size, laser waist and picosecond pulse duration, with no adjustment except for the central fringe position.

This simulation is in very good agreement with the experimental results. It also allows us to estimate the fraction of atoms involved in the interferometer. This fraction, $\sim 15\%$ of the initial number of atoms, which was also estimated in the experiment using absorption imaging of the initial and final atomic cloud, is limited by the initial velocity distribution of the atomic cloud, but also by the duration of the picosecond pulses. Indeed, the pulse overlap size is of the order of $c\tau \sim 0.5$ mm and the cloud size is of the order of $\sigma_{\text{cloud}} \sim 1$ mm. This leads to coupling inhomogeneity (loss of contrast) but also to a lower number of atoms at the ends of the interferometer.

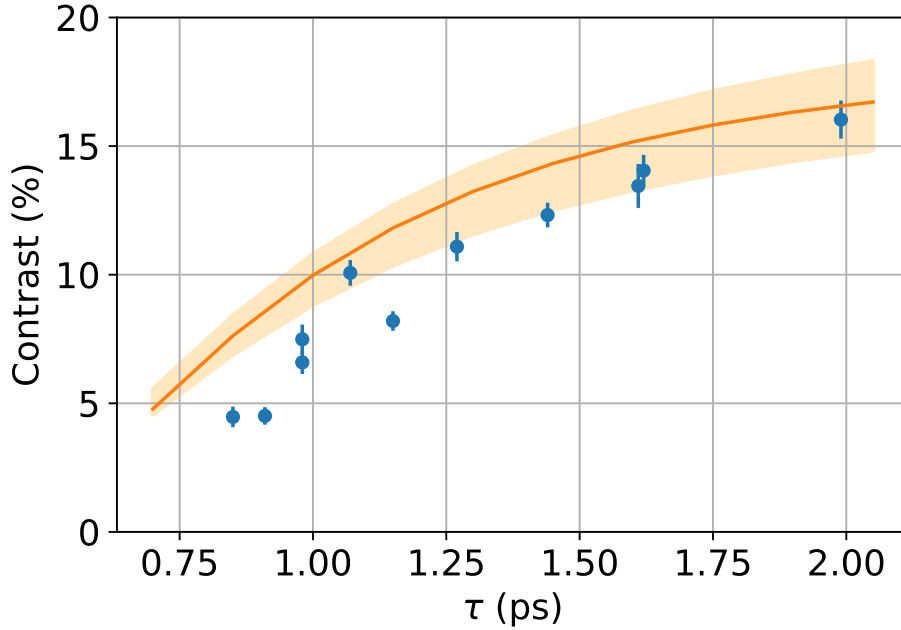


Fig. 4.5 Contrast of the central fringe as a function of the picosecond pulse duration, for $\sigma_{\text{cloud}} = 0.97(1)$ mm, $\Delta/2\pi = 0.87(5)$ THz, $T_R = 1$ ms and $T_D = 1.2$ ms. Experimental data are shown as blue points. The simulation without adjusting parameters is shown as a solid line, while the shaded area corresponds to the simulated 1σ uncertainty due to the uncertainties on the experimental parameters showing worst and best case scenarios. For short pulse duration, the discrepancy is explained by the increase of spontaneous emission due to a larger comb bandwidth

4.2.2 Study of the contrast

Figure 4.5 shows the evolution of the contrast, define as the amplitude of the central fringe (maximum minus minimum), as a function of the pulse duration. The blue dots are experimental data. The contrast was estimated by fitting the central fringe of the interferometer. The orange line corresponds to the Monte Carlo simulation performed with the measured experimental data. The shaded area corresponds to the simulated 1σ uncertainty due to the uncertainties in the experimental parameters, showing the worst and best-case scenarios. The uncertainty on σ_{cloud} of 0.01mm was obtained by fitting to an absorption image of the cloud. The uncertainty on λ , estimated at 0.15nm, is related to the drift of the central wavelength during data acquisition. The Rabi frequency uncertainty was obtained by fitting a Rabi spectrum after a first pulse of velocity selection and was estimated to be 0.44 kHz.

As expected, increasing the pulse duration increases the contrast of the interferometer because the size of the overlap zone increases, allowing less coupling inhomogeneity and more atoms to participate in the interferometer. Note that every experimental parameter was kept constant during the data acquisition even the Rabi frequency (adjusting the power of the frequency comb). We also observe a discrepancy between the experiment and the simulation at a small pulse duration. As we decrease the pulse duration, we increase the

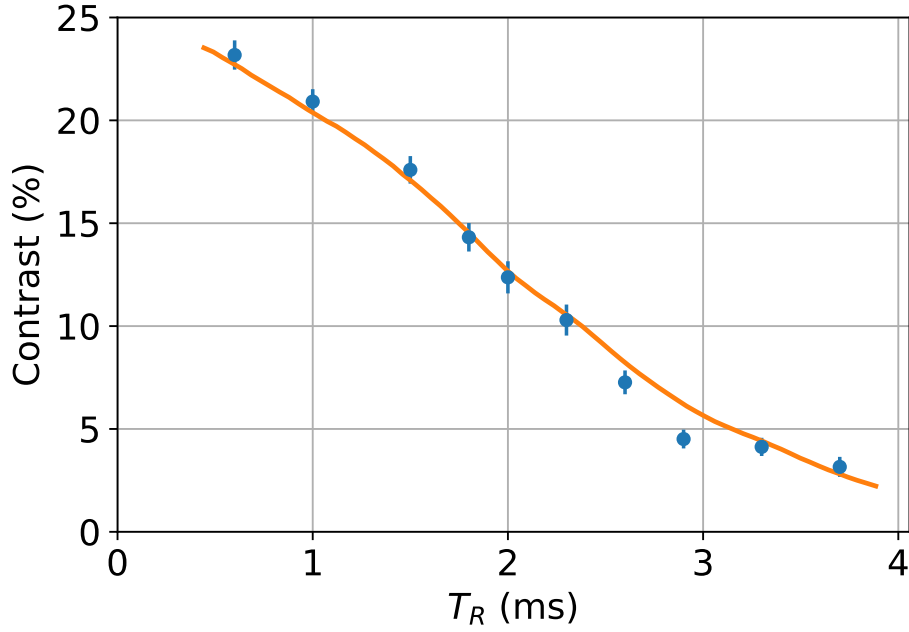


Fig. 4.6 Contrast of the central fringe as a function of T_R with $T_D = 1.2$ ms. Here, $\tau = 2.00$ ps, $\sigma_{cloud} = 0.67$ mm and $\Delta/2\pi = 0.51(5)$ THz

spectral bandwidth of the comb, which leads to an increase in spontaneous emission and a decrease in the contrast of the interference.

The evolution of the contrast as a function of the interrogation time was also studied. Figure 4.6 shows the evolution of the contrast as a function of T_R . We observe a drastic decrease in contrast as we increase the interrogation time. In fact, the atoms are free-falling through the overlap zone. Therefore, the interferometer cannot be closed if the total interrogation time is longer than the time taken for the atom to free-fall through the overlap zone. The total interrogation time is $T = T_D + 2T_R \sim 10$ ms for $T_R = 4$ ms. This is the time it takes for the atom to fall out of the overlap zone.

This limitation of the interrogation time due to the finite size of the overlap zone can also be understood in reciprocal k-space. In fact, only the average phase $k_{comb}z(t)$ is compensated by the AOM. There remains a dispersion $\Delta_k z(t)$, where $\Delta_k \simeq \frac{1}{c\tau}$ is the dispersion in the wave vector of the pulsed laser. Due to this dispersion, the contrast drops to zero when $\Delta_k z(t) \gtrsim 1$, i.e. $z(t) \gtrsim c\tau$. This also gives a fundamental limit to the precision of the measurement, since k_{comb} is not a well-defined quantity. It is not possible to extend the duration of the interrogation at this time, due to the limitations of the current setup. The potential for overcoming this limitation will be discussed subsequently. In the experiment it limits T_R to ~ 4 ms with $T_D = 2$ ms and $\tau \sim 2$ ps. The orange line is the Monte Carlo simulation performed with the experimental parameters. Again, it reproduces the experimental data well.

4.3 Double diffraction

The output phase of a light pulse interferometer is proportional to the embraced spatio-temporal region defined by the trajectory of each arm of the interferometer [Equation 4.26](#). The sensitivity of these interferometers can therefore be improved by increasing the interrogation time or by using more than one recoil velocity to increase the spatial separation between the two arms. We have seen in the previous section that the total interrogation time is limited to 10 ms. To increase the sensitivity of the interferometer, we will drive a double diffraction transition.

This technique was first developed at the SYRTE laboratory in 2009 [39]. It has the advantage of making the interferometer perfectly symmetrical. The internal states of the two arms are always the same. Systematic effects related to light shift or second order Zeeman shift are therefore mitigated.

In this experiment, instead of three CW lasers or two modulated lasers, we will use only one laser, the frequency comb, to perform double diffraction. We recall that the resonance condition for a counterpropagating Raman transition is

$$\omega_1 - \omega_2 = \omega_{\text{HFS}} + \vec{k}_{\text{eff}} \cdot \vec{v} + \omega_{\text{rec}} \quad (4.28)$$

where we consider ω_1 is the pulsation of the beam coming from the top of the atoms and ω_2 being the one of the retro-reflected beam. In this case, the atom performing the transition will acquire a recoil velocity along the free fall. In order to transfer a velocity in the opposite direction, the following condition must be met:

$$\omega_2 - \omega_1 = \omega_{\text{HFS}} - \vec{k}_{\text{eff}} \cdot \vec{v} + \omega_{\text{rec}} \quad (4.29)$$

In the experiment, ω_2 is the pulsation of the delayed beam, shifted by the frequency of the AOM and ω_1 is the pulsation of the direct beam.

To perform a double diffraction, the two conditions must be fulfilled at the same time. The set of equations is

$$\begin{cases} \omega_1 - \omega_2 = \omega_{\text{HFS}} + \vec{k}_{\text{eff}} \cdot \vec{v} + \omega_{\text{rec}} \\ \omega_2 - \omega_1 = \omega_{\text{HFS}} - \vec{k}_{\text{eff}} \cdot \vec{v} + \omega_{\text{rec}} \end{cases} \quad (4.30)$$

looking at the teeth of the comb it gives

$$\begin{cases} (n + q)\omega_{\text{rep}} - n\omega_{\text{rep}} - 2\omega_{\text{AOM}} = \omega_{\text{HFS}} + \vec{k}_{\text{eff}} \cdot \vec{v} + \omega_{\text{rec}} \\ n\omega_{\text{rep}} + 2\omega_{\text{AOM}} - (n + q')\omega_{\text{rep}} = \omega_{\text{HFS}} - \vec{k}_{\text{eff}} \cdot \vec{v} + \omega_{\text{rec}} \end{cases} \quad (4.31)$$

again the AOM frequency is close to the repetition rate and used to compensate for the Doppler shift, one can write ω_{AOM} as $\omega_{\text{rep}} + \delta\omega_{\text{AOM}} - \frac{1}{2}\vec{k}_{\text{eff}} \cdot \vec{v}$, where $\delta\omega_{\text{AOM}}$ correspond to a frequency shift applied to the pulsation of the AOM.

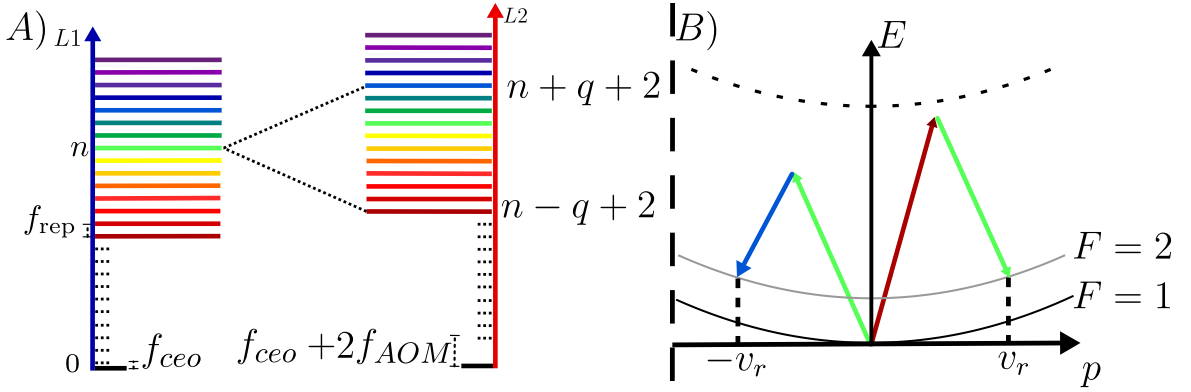


Fig. 4.7 A) The spectral domain of the retroreflected comb (L1) and the delayed comb (L2). The red comb is shifted by twice the AOM frequency. The dashed line shows the coupled teeth to drive the two Raman transitions. B) Energy momentum diagram of the double diffraction scheme.

$$\begin{cases} (q-2)\omega_{\text{rep}} - 2\delta\omega_{\text{AOM}} = \omega_{\text{HFS}} + \omega_{\text{rec}} \\ -(q'-2)\omega_{\text{rep}} + 2\delta\omega_{\text{AOM}} = \omega_{\text{HFS}} + \omega_{\text{rec}} \end{cases} \quad (4.32)$$

It all boils down to

$$(q-2)\omega_{\text{rep}} - (q'-2)\omega_{\text{rep}} = 2\omega_{\text{HFS}} + 2\omega_{\text{rec}} \quad (4.33)$$

choosing $q = -q'$, we obtain

$$\omega_{\text{rep}} = (\omega_{\text{HFS}} + \omega_{\text{rec}})/q \quad (4.34)$$

By detuning the repetition rate by ω_{rec}/q , so by only 150Hz as $q=90$ and $\omega_{\text{rec}} \sim 15\text{kHz}$, and by setting the AOM's frequency at $\omega_{\text{rep}} - \frac{1}{2}k_{\text{eff}} \cdot \vec{v}$, we are able to conduct a double diffraction. The visualization of this resonance condition can be seen on [Figure 4.7](#). A) shows the frequency domain of the two lasers L1 and L2 with L2 being shifted by $2f_{\text{AOM}}$. The dashed lines show the 3 frequencies that will perform the transition. On B) we plotted the energy momentum diagram of a double diffraction transition. The blue, green, and red arrows are related to the teeth connected by the dashed line in A)

We are now resonant with the two transitions. It is however important to underline that for double diffraction the duration of the pulses acting as an atomic splitter should have a duration τ_s of [39]

$$\tau_s = \frac{1}{\sqrt{2}} \frac{\pi}{\Omega_{\text{eff}}} \quad (4.35)$$

The timing of the interferometer and the trajectories of the atoms are shown on [Figure 4.8](#). After the first and third Raman pulses, we apply push beams resonant with the $F=2$ state.

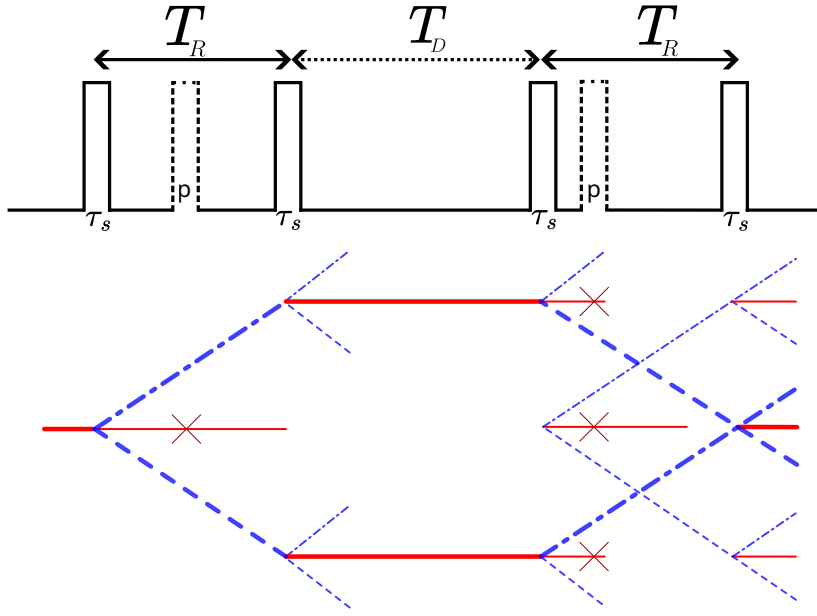


Fig. 4.8 Temporal sequence and trajectories of the atoms in the Ramsey-Bordé type interferometer with double diffraction. The blue and red lines define the hyperfine. The red cross shows the impact of the pusher beam applied during the Ramsey sequence to maximize the contrast.

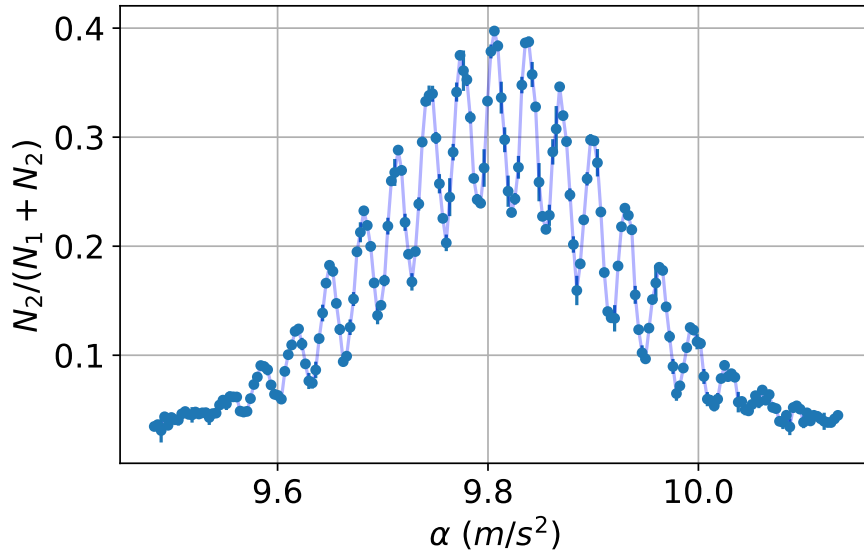


Fig. 4.9 Atomic fringes for double diffraction at the output of the interferometer: transfer probability to the $|5s^2S_{1/2}, F = 2\rangle$ state as a function of the frequency chirp used to compensate for the Doppler effect due to free fall in a double diffraction scheme. Experimental data are shown as blue points. Here $\Delta/2\pi = 0.39(5)$ THz, $T_R = 2.5$ ms, $T_D = 1.2$ ms, $\tau = 1.25$ ps and $\sigma_{\text{cloud}} = 0.8$ mm.

These push beams are critical as they allow the rejection of other trajectories that would reduce the contrast of the interferometer fringes.

Typical data are shown on [Figure 4.9](#). Compared to normal diffraction, the inter-fringes are divided by a factor of 2 for the same interrogation time, which means that the sensitivity is increased by a factor of 2. An analysis of the phase noise, performed by computing the standard deviation of the transfer probability at mid fringe with the double diffraction scheme and with the usual scheme, shows a drastic reduction of it compared to a simple diffraction scheme as in [Figure 4.4](#). Indeed, the phase noise of the laser is imprinted on both arms due to the use of a single laser source. Consequently, the same noise is imprinted on both arms, resulting in an overall lack of sensitivity to laser phase noise in this configuration.

It can be observed that the availability of two degrees of freedom, namely the repetition rate and the frequency of the AOM, allows for the implementation of a multitude of double transition schemes, in addition to double diffraction schemes. For example, it is possible to address two atoms with relatively close hyperfine transitions (e.g. isotopes). It is also possible to drive both Raman and Bragg transitions. This feature has been developed in [chapter 2](#).

Conclusion

In this chapter we have shown that it is possible to drive an atom interferometer using a frequency comb. We have highlighted the limit of the interrogation time, which in the time domain is related to the time it takes for the atoms to free-fall through the overlap zone. A Monte Carlo simulation was performed to understand the effect of the picosecond pulse duration and the interrogation time on the contrast. Finally, we have experimentally shown that FCAI is a versatile tool capable of performing a double diffraction scheme with only one laser source.

Chapter 5

Moving delay line frequency comb atom interferometer

In the prior chapter, we demonstrated the feasibility of performing atom interferometry using a frequency comb. However, the sensitivity of such frequency comb-driven atom interferometers is constrained by the time it takes for atoms to traverse the overlap zone of the laser pulses driving the Raman transition. To address this limitation, we have devised a method involving a moving mirror, enabling the overlap zone to track the free fall of the atomic cloud, as illustrated by [Figure 5.1](#).

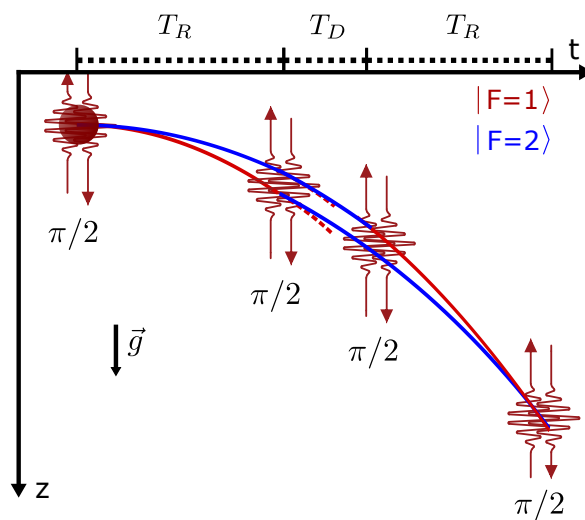


Fig. 5.1 *Ramsey-Bordé interferometer with the new apparatus. The two red pulses represent the picosecond pulses following the free fall of the atomic cloud*

The aim of this chapter is to show how we increase the interrogation time by using moving mechanical parts without increasing the phase noise. We also present a new interferometer configuration that allows independent interrogation of each arm of the interferometer. A Monte Carlo simulation was performed to analyze the effect of experimental parameters on the interferometer contrast. In conclusion, we examine a fundamental

constraint on the sensitivity of frequency comb atom interferometry, which is associated with a dispersion in the momentum of the wave packet.

5.1 Moving delay line apparatus

The new apparatus is shown on [Figure 5.2](#). The M2 mirror, placed in the delay line, is mounted on a translation stage that allows the mirror to slide along a rail with a maximum travel of about 2 cm. The mirror is also mounted on a voice coil actuator (VC250/M Thorlabs). By applying a current to the voice coil, the mirror M2 is moved. The voice coil consists of a magnet surrounded by a coil. The Lorentz force is applied to the mirror by driving a current into the coil. By changing the polarity of the current, we change the direction of the displacement.

A CW laser (purple beam in [Figure 5.2](#)) of known frequency is added to the setup. The laser is the cooling laser, phase-locked to a repump laser whose frequency is referenced to a saturated absorption. It is taken from an unused zero order of an AOM. This laser is used to measure the displacement of the mirror M2. Using a beam splitter (BS), the laser will travel in the opposite direction to the picosecond laser and follow the same path into the delay line. Photodiode-1 (PD1) measures the phase shift on the CW laser induced by the displacement of M2. To eliminate parasitic beams on the photodiode, an interferometric filter (IF) is positioned to filter out any spurious picosecond laser beam that might hit the photodiode and produce a signal at the repetition rate.

The phase shift measured by PD1 is then mixed with a demodulation signal and fed to a Redpytia FPGA. We now need to detail the phase shift imprinted on the different lasers.

5.1.1 Phase shift calculation

The phase measured by the photodiode noted as $\Phi_{beatnote1}$ is the phase accumulated by the cw laser (violet in [Figure 5.2](#)) by going through the AOM-2 and by propagating in the delay line.

This phase shift is composed of two terms: A phase shift coming from the AOM placed in the delay line and another caused by the displacement of M2.

$$\Phi_{beat1}(t) = 2\Phi_{AOM}(t) + k_{CW}x_{mirror}(t) \quad (5.1)$$

The factor 2 comes from the double pass AOM and $x_{mirror} = 2x_{M2}$

As mentioned before, we demodulate this signal with a phase Φ_{Demo} giving

$$\Phi_{error} = \Phi_{beat1} - 2\Phi_{Demo} \quad (5.2)$$

The factor 2 comes from a multiplier added to match the factor 2 of the AOM.

We can write the phase of the demodulation as a sum of two phases. One that we compute $\Phi_{DemoSeq}$ and one coming from the open feedback-loop called "phase modulation"

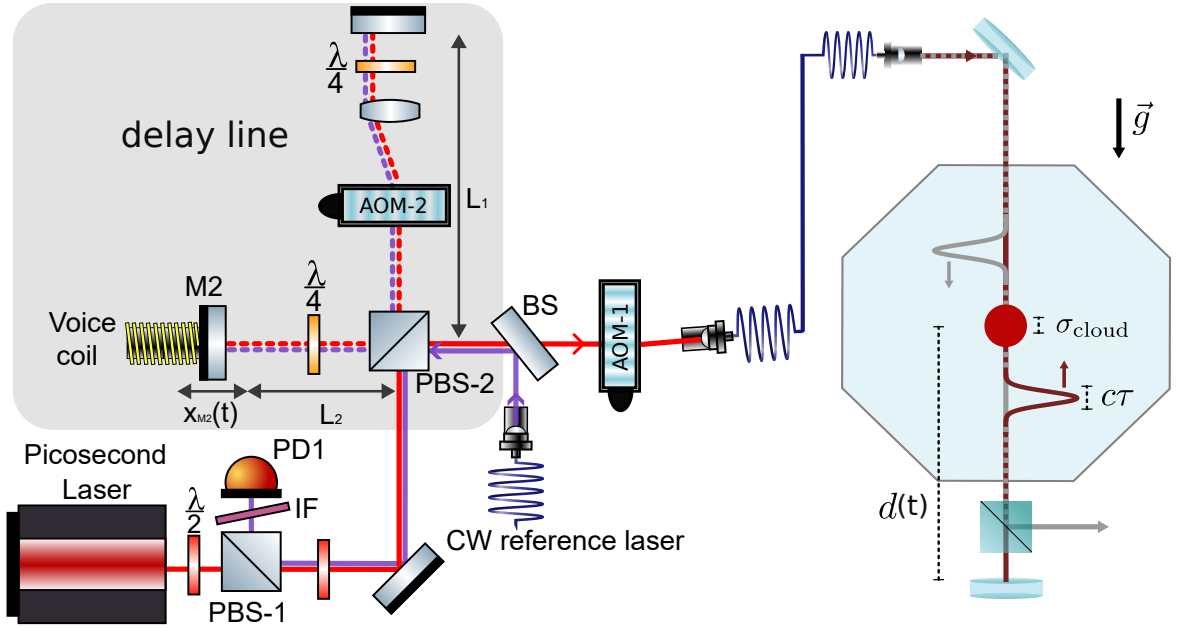


Fig. 5.2 Overview of the experimental setup. The picosecond laser (red line) is split in two on the polarizing beam splitter PBS-2. One part is sent directly to the atoms and will be retro-reflected from the bottom mirror. The other part passes through two delay lines. The mirror M2 of the second delay line is moved using a voice coil (Thorlabs VC500/M) with a controllable acceleration, displacing the overlap position and chirping the frequency of the delayed beam. A CW reference laser, with a known wavelength (in purple), is used to measure the position of M2 using a heterodyne detection scheme. An interferometric filter (IF) is placed in front of the photodiode (PD1) to filter any spurious reflection.

written here as Φ_{ModFB}

$$\Phi_{\text{Demo}} = \Phi_{\text{DemoSeq}} + \Phi_{\text{ModFB}} \quad (5.3)$$

Similarly, we can write the phase of the AOM as:

$$\Phi_{\text{AOM}} = \Phi_{\text{AOMSeq}} + \Phi_{\text{ModFB}} \quad (5.4)$$

We now look at the phase of red lasers on [Figure 5.2](#), the frequency comb laser. We compute the phase just before the fiber goes to the experiment chamber. The red laser in full line is the laser not passing by the delay line, we denote its phase Φ_{L1}

The laser in dashed line is the one passing by the delay line, his phase is $\Phi_{L2} + 2\Phi_{\text{AOM}} + k_{\text{comb}}x_{\text{mirror}}(t)$

The phase difference between the two beams, which I will call Φ_{atom} , is the phase difference printed on the atoms. This phase is the one we want to control to interrogate as we wish to the atoms.

$$\Phi_{\text{atom}} = 2\Phi_{\text{AOM}} + k_{\text{comb}}x_{\text{mirror}}(t) + \Delta\Phi \quad (5.5)$$

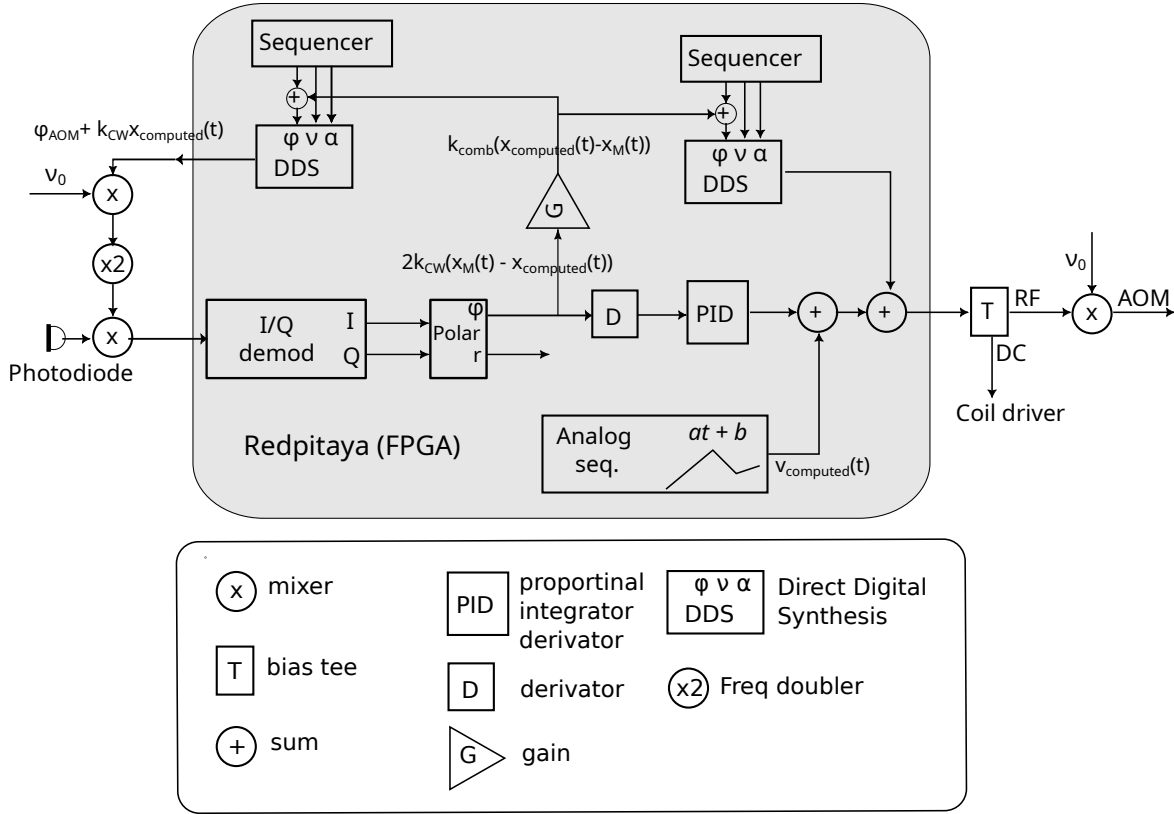


Fig. 5.3 Control system implemented using a Redpitaya board. To accommodate for the relatively low bandwidth of the board (50 MHz), we use frequency mixers to shift the frequencies from the digital to analog converter to the AOM and from the photodiodes to the analog to digital converter. The command of the coil driver is digitally added to the radio frequency in the FPGA and then extracted using a bias T, to accommodate the limited number of outputs of the board. x_M stands for x_{mirror}

with $\Delta\Phi = \Phi_{L2} - \Phi_{L1}$

The error signal measured after mixing the signal of the photodiode with the demodulation signal is

$$\begin{aligned}
 \Phi_{error} &= \Phi_{beat1} - 2\Phi_{Demo} \\
 &= 2\Phi_{AOM} + k_{CW}x_{mirror}(t) - 2\Phi_{Demo} \\
 &= 2\Phi_{AOMSeq} + 2\Phi_{ModFB} + k_{CW}x_{mirror}(t) - (2\Phi_{DemoSeq} + 2\Phi_{ModFB}) \\
 &= 2\Phi_{AOMSeq} - 2\Phi_{DemoSeq} + k_{CW}x_{mirror}(t)
 \end{aligned} \tag{5.6}$$

and on the atoms we have

$$\begin{aligned}
 \Phi_{atom} &= 2\Phi_{AOM} + k_{comb}x_{mirror}(t) + \Delta\Phi \\
 &= 2\Phi_{AOMSeq} + 2\Phi_{ModFB} + k_{comb}x_{mirror}(t) + \Delta\Phi
 \end{aligned} \tag{5.7}$$

We now need to treat Φ_{ModFB} :

$$\Phi_{\text{ModFB}} = G\Phi_{\text{error}} \quad (5.8)$$

where G is a gain factor that we will define hereafter. The phase printed on the atoms becomes

$$\Phi_{\text{atom}} = 2\Phi_{\text{AOMSeq}} + 2G\Phi_{\text{error}} + k_{\text{comb}}x_{\text{mirror}}(t) + \Delta\Phi \quad (5.9)$$

replacing Φ_{error} by its expression given by the equation 5.6 we obtain

$$\Phi_{\text{atom}} = 2\Phi_{\text{AOMSeq}} + 4G\Phi_{\text{AOMSeq}} - 4G\Phi_{\text{DemoSeq}} \quad (5.10)$$

$$+ 2Gk_{\text{CW}}x_{\text{mirror}}(t) + k_{\text{comb}}x_{\text{mirror}}(t) + \Delta\Phi \quad (5.11)$$

But we want Φ_{atom} independent of $x_{\text{mirror}}(t)$ to have total control of the phase on the atoms without any influence coming from the position of the mirror. This imposes that $2Gk_{\text{CW}} + k_{\text{comb}} = 0$, giving us $G = -\frac{k_{\text{comb}}}{2k_{\text{CW}}}$

Also, when we perfectly control the whole setup, we calculate the displacement of the mirror x_{computed} so that $\Phi_{\text{error}} = 0$.

$$\begin{cases} \Phi_{\text{atom}} & = 2\Phi_{\text{AOMSeq}} - 2Gk_{\text{CW}}x_{\text{computed}}(t) + \Delta\Phi \\ k_{\text{CW}}x_{\text{computed}}(t) & = 2\Phi_{\text{DemoSeq}} - 2\Phi_{\text{AOMSeq}} \end{cases} \quad (5.12)$$

Finally, to perfectly control the setup, we need to compute :

$$\boxed{\begin{cases} 2\Phi_{\text{AOMSeq}} & = \Phi_{\text{atom}} - \Delta\Phi + 2Gk_{\text{CW}}x_{\text{computed}}(t) \\ 2\Phi_{\text{DemoSeq}} & = 2\Phi_{\text{AOMSeq}} + k_{\text{CW}}x_{\text{computed}}(t) \end{cases}}$$

with

$$\boxed{G = -\frac{k_{\text{comb}}}{2k_{\text{CW}}}}$$

These two formulas will be used to compute the phase plugged in the demodulation and in the AOM DDS to stay resonant with the atoms. In the case where the lock is perfect (no error on the position of the mirror), the frequency of the AOM will not be changed over time and the demodulation will simply make a frequency chirp at gravity acceleration g .

5.1.2 FPGA programming

To control both the acceleration of the mirror and the AOM, we use an FPGA (redpitaya board). The [Figure 5.3](#) describes the logic implemented. Two direct digital synthesis (DDS) cores are implemented in the FPGA. The first DDS is used to control the AOM and the

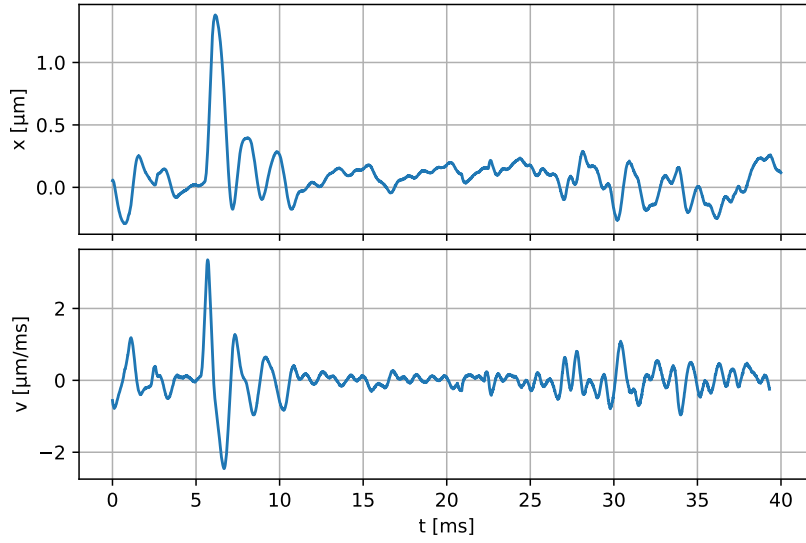


Fig. 5.4 Performance of the lock on M2 position and velocity. Top: Residual error on the position of M2 regarding the atoms' position. The position of M2 can be controlled with an accuracy of up to a few hundred nm. Bottom: residual error on the velocity of M2 regarding the velocity of the atoms. The origin of time corresponds to the release time of the cloud. We observe at $t = 5$ ms an oscillation that corresponds to the change of velocity of the mirror after the first Raman pulse.

second to control the demodulation signal. Because the output frequency of the board is limited to 50 MHz, the signal is mixed with a constant frequency ($\nu_0 \sim 30\text{MHz}$) to shift the output to the 80 MHz range. The output of each DDS is defined by the phase ϕ (position), frequency ν (velocity), and linear frequency sweep rate α (acceleration) and controlled using a digital sequencer.

Assuming that the AOM frequency is constant (and set equal to the repetition rate of the comb), the beat note of the photodiode will be around 160 MHz. Again, the board is not fast enough to handle such a signal. The demodulation is performed in two steps: first using an analog mixer with a demodulation signal at a frequency close to 160 MHz and the second consists of using an internal I/Q demodulator. All the time-dependent frequency demodulation is performed in the analogue mixer and the I/Q demodulator works at a fixed frequency (set at 5 MHz). The output of the I/Q demodulator is fed to a Cartesian to polar converted based on the CORDIC algorithm. The remaining phase, which can be unwrapped around many revolutions, is the measure Φ_{error} .

The current in the coil is controlled with a voltage, therefore we have to compensate for the electromotive force. This is performed using an analogue sequencer that produces linear ramps. On top of this voltage, we apply feedback to control the mirror. Because we control the force, proportional feedback will be unstable (the error signal is proportional to a phase). A derivator is used to convert the phase to a signal proportional to the velocity error, which is then fed to a PID and added to the analogue sequencer, forming a closed loop.

On [Figure 5.4](#) we show the accuracy of the position and the velocity of the translating

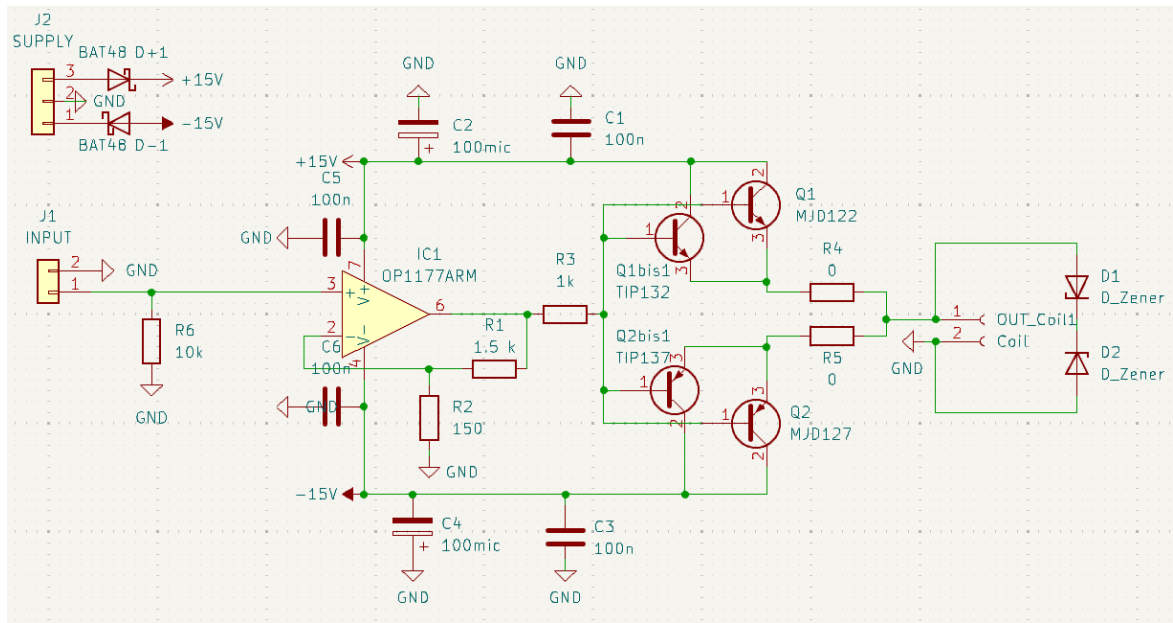


Fig. 5.5 PCB board used to drive the voice coil actuator.

stage with respect to the command. The mirror M2 can move up to 60 ms with an acceleration close to g . The gain and the integration constant are chosen to minimize the position error. With this apparatus, we can make the overlap zone follow the free fall of the atoms for more than 60 ms and thus reach typical interrogation time used in atom interferometry with CW lasers. Also, on [Figure 5.4](#), note that at 5 ms, there is a surge in the error on the position. This surge arises from a change in the wanted velocity and will be discussed later.

Yet, as for interferometers driven by cw lasers, controlling the phase difference between the two counterpropagating beams is critical. Because the phase Φ_{atom} on the atomic cloud depends on $k_{\text{comb}}x_{\text{mirror}}(t)$ and due to residual error in position, shown on [Figure 5.4](#), the phase noise on the atom is of the order of 0.5 rad. To compensate for this phase noise caused by moving mechanical parts, we retro-act on the phase of AOM2. We feedback on the error in the position shown on [Figure 5.4](#) into the phase of the AOM. By doing so, $\Phi_{\text{atom}} \propto kx_{\text{mirror}}(t) + 2\Phi_{\text{AOM}}(t)$ and the set-up is nearly insensitive to mechanical phase noise caused by the displacement of the mirror. With the scheme presented on [Figure 5.3](#), we are also able to control independently both the position of the mirror and the phase of the laser on the atoms, a feature of importance that will be used in the following.

5.1.3 Electronic driver of the voice coil

To drive the voice coil actuator, we design a PCB board shown on [Figure 5.5](#). Because we control the voltage at the output of the RedPitaya, we want to convert this voltage into current with both polarities so we can accelerate and decelerate the coil.

With a gain $\times 10$, we first amplify the input signal using an OP276 (footprint OP1177 on [Figure 5.5](#)). Then, the analog signal is split, depending on its polarity, using a diode and sent to an NPN or PNP junction (BD743C/BD744C) (footprint TIP132 and TIP137) delivering up

to 15 A. The output current of these junctions depends on the input voltage. Because the force applied on the mirror is proportional to the current into the voice coil, by adjusting the input voltage we can thus finely tune the applied force. Then, the two outputs are merged and sent to the voice coil. The head-to-tail Zener diodes are here to avoid high voltage at the terminals of the coil when rapid cuts of the current are applied.

5.2 Following the mid-point of the interferometer

Instead of moving simply the mirror with a constant acceleration close to g , we decide to follow the mid-point of the interferometer. The trajectory, that we will call the midpoint, and that the overlap zone will follow for this experiment, is shown in purple on [Figure 5.6b](#)). If not following this trajectory, the coupling inhomogeneity linked to the finite size of the overlap zone would cause a drop in contrast at the interferometer output. The Rabi coupling on the arm that received a recoil would decrease by $\exp(-V_r t/c\tau)$, where V_r is the recoil velocity transmitted to the atom and τ is the duration of the picosecond pulse. This back of envelop estimation is obtained by simply taking the Rabi coupling [Equation 2.48](#) with an atom shifted from the centre of the overlap by $V_r t$.

The schematic of the interferometer is shown on [Figure 5.6b](#)). After the first pulse, the control of the translation stage is changed, i.e. Φ_{Demo} is modified. In this experiment, in the free-fall frame, the mirror is asked to move at a speed of $V_r/2$ after the first pulse, then at V_r after the second pulse, and then at $V_r/2$ after the 3rd pulse. Looking at [Figure 5.6](#), it is easy to see that the trajectory shown in a) is sub-optimal and would lead to a decrease in contrast.

The computed frequencies of the AOM and Demodulator are shown on [Figure 5.7](#) in the case of a Ramsey-Bordé interferometer with a total interrogation time of 20ms with $T_r = 5ms$. This figure shows the perfect case, meaning that there is no error in the position of M2 and thus no feedback. The demodulator frequency, which controls the velocity of the mirror, is shifted after every Raman pulse (vertical lines). This shift, proportional to the recoil velocity, is made to follow the midpoint of the interferometer. The AOM frequency is also shifted by the same quantities but with opposite signs. Indeed, the goal is to stay resonant with the atoms regardless of the velocity given to the mirror. By shifting the frequency of the AOM, we cancel out the shift imprinted on the lasers by the displacement of M2. After the interferometer, the demodulator frequency is swept back and the lock is turned off to place M2 at its initial position.

5.2.1 Monte-Carlo simulation

I conducted a Monte Carlo simulation to estimate the contrast in both scenarios (a) and b) of [Figure 5.6](#)). The simulation determines the number of atoms in each state at one exit port of the considered interferometer. To do so, we randomly chose the initial velocity and position of an atom. We then simulate the interaction of this atom with each picosecond pulse along

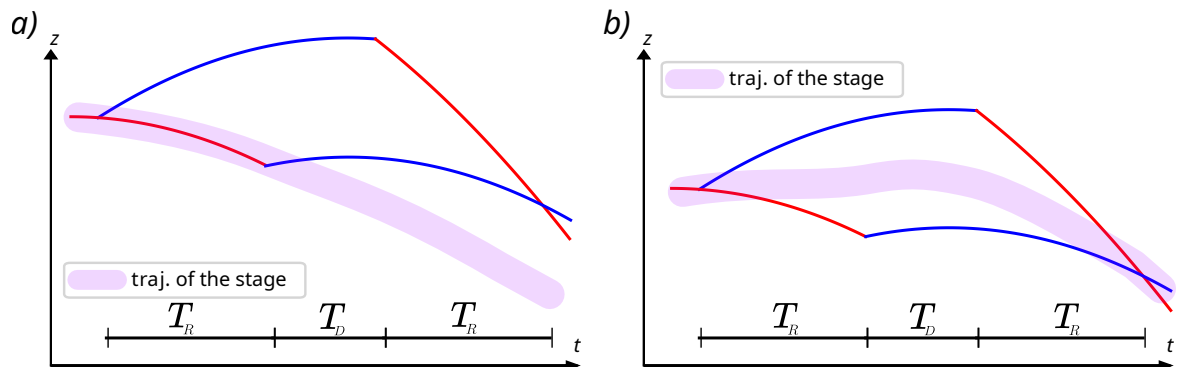


Fig. 5.6 Schematic of the Ramsey-Bordé interferometer. The trajectory of the overlap zone in the shaded area for the interferometer in the case of following with the overlap zone a) the free-fall of the atoms and b) the mid-point trajectory. The two internal state trajectories are represented in blue and red full lines.

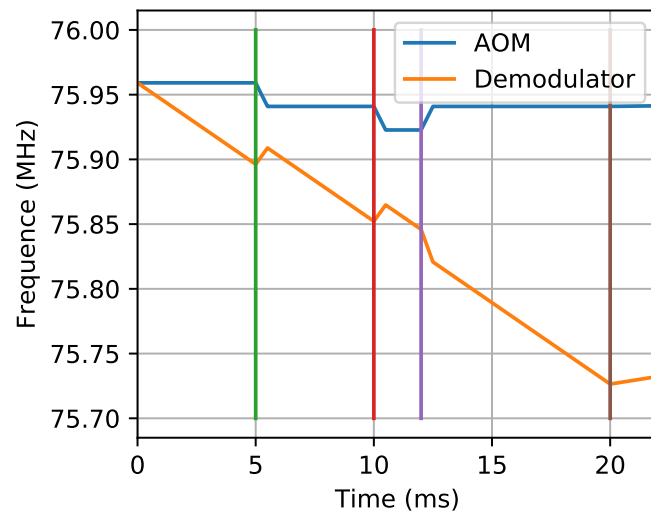


Fig. 5.7 Computed frequency for the AOM and the demodulator in the case where we follow the midpoint of the interferometer. Both frequencies are shifted to follow the midpoint of the interferometer while staying resonant with the atoms. Each vertical line represents a Raman pulse of the interferometer.

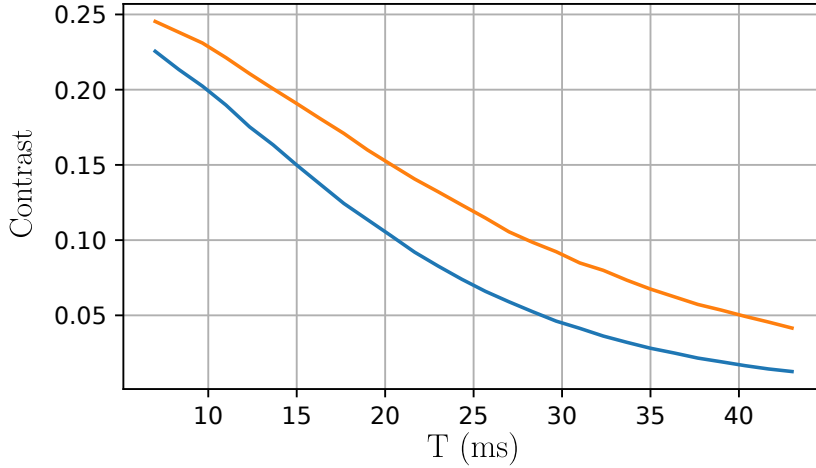


Fig. 5.8 Monte Carlo simulation of the contrast of the interferometer. The blue and orange curves are obtained when we follow respectively the free fall of the cloud and the midpoint of the interferometer.

the two trajectories of the interferometer. The Rabi coupling is calculated according to

$$\Omega(r, z) = \frac{\Omega_0^2}{2\Delta} \operatorname{sech} \left(1.78 \frac{z}{c\tau} \right) \exp \left(-\frac{2r^2}{w^2} \right) \quad (5.13)$$

where Ω_0 and Δ are respectively the Rabi frequency and detuning with respect to one-photon transition, c is the speed of light, τ the duration of a picosecond pulse, z is the position of the atom with respect to the centre of the overlap zone and r its transverse position. The pulse shape is chosen to be a hyperbolic secant function according to the data sheet of the Coherent manual of the picosecond laser (in the previous chapters we considered Gaussian pulses for calculation convenience). With the simulation, we can also select the trajectory of the overlap zone and thus simulate the contrast when the mirror moves with the free fall and when we decide to follow the mid-point of the interferometer. We then extract the number of atoms a_1 and a_2 in each internal state at one output port of the interferometer. The contrast is given by $\mathcal{C} = 4 \langle a_1 a_2 \rangle / \langle a_1^2 + a_2^2 \rangle$.

Figure 5.8 shows the evolution of the contrast as a function of T_R in the two configurations discussed above. The blue line is the evolution of the contrast when the mirror is accelerated at g . In orange, we display the contrast's evolution when we follow the midpoint of the interferometer. We see a small improvement in the contrast when following the mid-point of the interferometer, which justifies the use of the midpoint configuration. For this simulation, we took $\tau = 1$ ps, a π pulse duration equal to 0.6 ms, $T_D = 3$ ms, an initial cloud size of 1 mm. Here T_R is the Ramsey time and T_D is the spacing time between the two pairs of $\pi/2$ pulses.

5.2.2 Results

The experimental results when following the mid-point trajectory are shown on Figure 5.9. We plot the variation of contrast as a function of interrogation time defined as $T = 2T_R + T_D$.

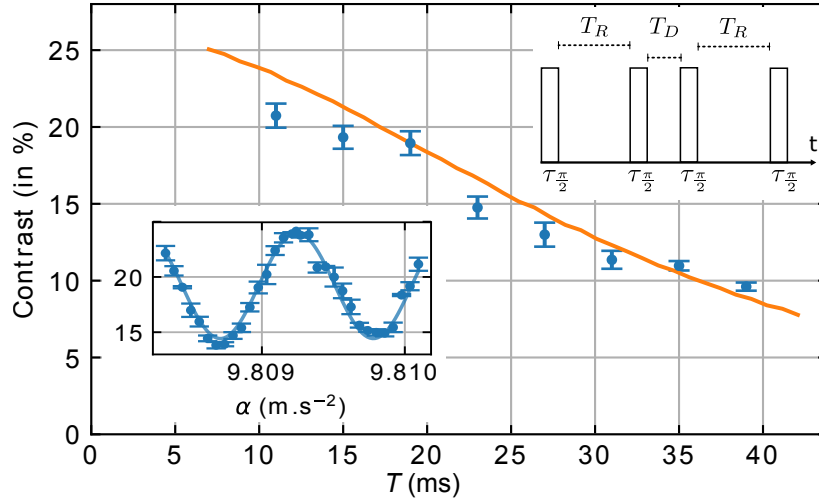


Fig. 5.9 Contrast of the central fringe as a function of the total interrogation time with $\tau = 1.47$ ps, a π -pulse duration of 0.6 ms and T_D of 3 ms. Experimental data are shown in blue. The Monte-Carlo simulation is shown in the orange full line. Typical fringes are shown in the bottom inset for $T = 39$ ms. The contrast is deduced from a fit of the fringes (blue line). The upper insert shows the interferometer sequence

The blue point is extracted by fitting the atomic fringe pattern by the cosine's function. The orange line is extracted from the Monte Carlo simulation presented above. The contrast drops by 50% after a total interrogation time of 25 ms, this is a 5-fold improvement compared to the previous chapter where the delay line was fixed, where a 50% drop in contrast was observed for a total duration of 5 ms ($T_R = 2$ ms).

We performed an interferometer with two CW phase-locked lasers as Raman lasers (instead of the frequency comb) to test the phase noise induced by the translating stage. On [Figure 5.10](#), we show the output fringe with the CW lasers and the translating stage. Each point is only one repetition rate of the experiment. The comparison of two fringes in the same experimental condition except for the laser sources (CW or frequency comb) shows a drastic difference in phase noise. The phase noise with the CW lasers appears to be lower than when using the frequency comb.

Firstly, we can say that the translation stage does not produce phase noise at the level of sensitivity of the experiment on the fringes but also that we are neither limited by vibration noise nor by the detection. Secondly, we can identify the noise arising from the lock on the repetition rate of the frequency comb. To reduce the phase noise when using the frequency comb, one could think of feed-backing the error signal in the repetition rate into the AOM of the delay line, as we already do with the velocity error of the translating stage.

The fall of the contrast in [Figure 5.9](#) is due to the finite size of the overlap zone as shown on [Figure 5.11](#). If the two arms of the interferometer are separated by a distance larger than the size of the overlap zone, the Rabi coupling decreases during the second pulse of the interferometer, and the $\pi/2$ criterion is not fulfilled.

In the reciprocal k -space, the momentum dispersion ($\Delta k = \frac{2\pi\Delta\nu}{c}$ where Δk is the FWHM of the momentum distribution of the comb) induces recoil dispersion and therefore

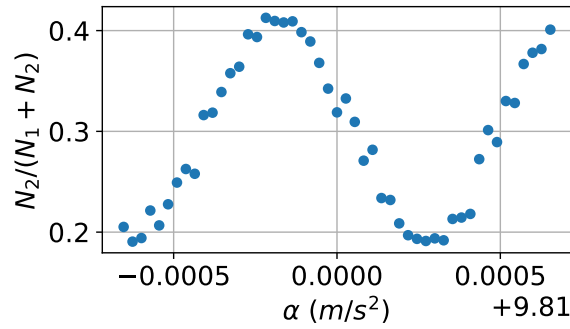


Fig. 5.10 Fringes obtained with two CW lasers and the moving delay line. Each point is one repetition of the experiment. Here $T_D = 2$ ms, $T_R = 20$ ms a π -pulse duration of 0.6 ms and $\Delta = 40$ GHz

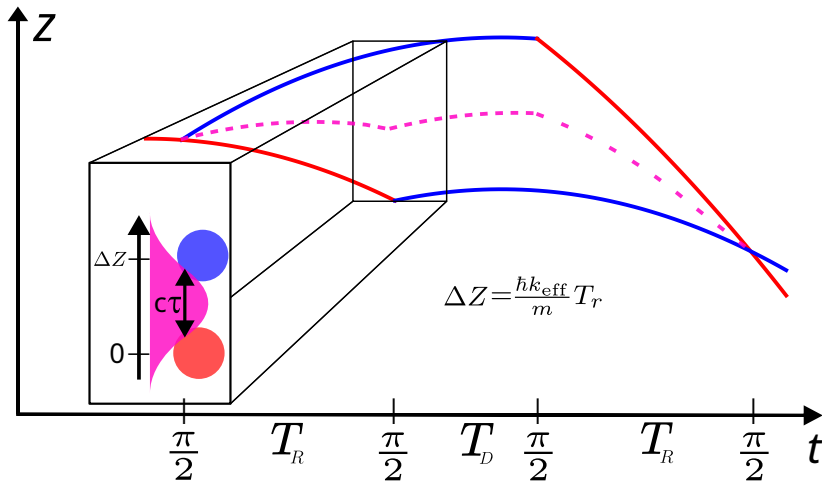


Fig. 5.11 Ramsey-Bordé interferometer when we follow the midpoint of the interferometer. The zoom shows that if the two clouds (red and blue) are spaced by more than $c\tau$ we can not perform perfect $\frac{\pi}{2}$ pulses resulting in a drop of contrast.

a loss of interferometer contrast. After a time T , the phase difference due to recoil for a pair of blue teeth and a pair of red teeth can be written as:

$$\Delta\phi = \frac{\hbar k_{\text{eff}}}{m} T \Delta k_{\text{eff}}$$

5.3 Atom interferometer using spatially-localized beam splitters

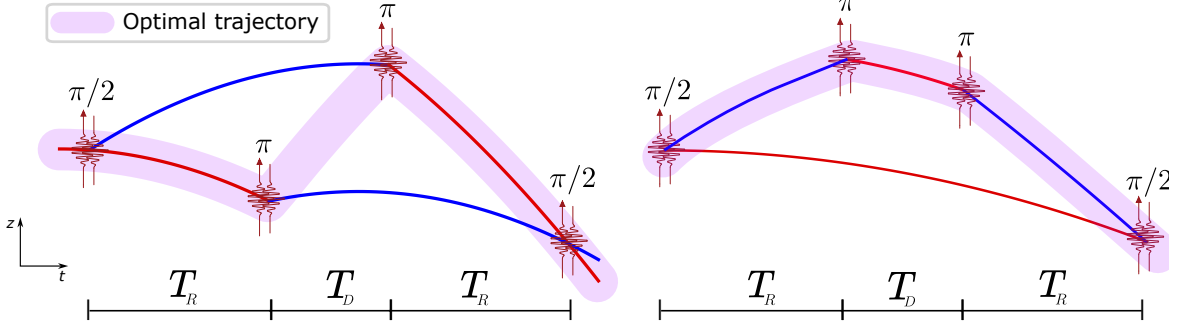


Fig. 5.12 *Space-time diagram of the Ramsey-Bordé interferometer. The trajectory of the overlap zone is displayed in a shaded area (optimal trajectory). The two internal state trajectories are represented in blue and red full lines.*

For a Ramsey-Bordé interferometer based on the CW laser, the fact that the two $\pi/2$ middle pulses interact with both arms limits the contrast to 50 per cent and leads to a loss of atoms number. With this technique of moving the mirror, because the interaction is localized, it is possible to interact with only one part of the coherent superposition of the atom. By doing so, we eliminate the limitation in contrast and increase the total number of atoms participating in the interferometer. Indeed, the two middle pulses can now be π pulses, so nearly all atoms resonant with the first pulse will participate in the interference.

On [Figure 5.12](#), we display two possible interferometer configurations using localized atomic beam splitters. The figure shows two possible configurations using the pulse sequence $\{\pi/2 - \pi - \pi - \pi/2\}$, depending on whether the first π -pulse catches one or the other wave packet. In the first configuration, the phase difference at the output of the atom interferometer is only sensitive to the external degrees of freedom. In contrast, in the second configuration, it is sensitive to both external and internal degrees of freedom [15].

From now on, we will only consider the left configuration.

To perform this interferometer, we program the moving mirror as shown on [Figure 5.13](#). First, we want the mirror to move at g up to the second $\frac{\pi}{2}$ pulse, then to accelerate up to a velocity equal to $2V_r(T_R + T_D)/T_D$ during $T_D/2$ after the second pulse and finally to decelerate to g during $T_D/2$. The stage accelerates at g after the 3rd pulse for the rest of the interferometer. Yet, because we can not apply an infinitely high force on the voice coil, we can not let T_D to a few milliseconds when we work at high T_R . The balance between T_D and T_R is chosen by looking at the error signal in the position of the translating stage. If we decide on a short T_D , meaning that we do not give the time to the translating stage to catch up with the upper path, we would see a dropout in the error signal. Note that this feature is not present in the right configuration of [Figure 5.12](#) where any T_D can be chosen.

On [Figure 5.14](#) top, we display the error in position regarding the command in position. The red lines highlight the times at which we ask the stage to change its velocity. We see two surges. One when we accelerate to reach a velocity equal to $2V_r(T_R + T_D)/T_D$ and the

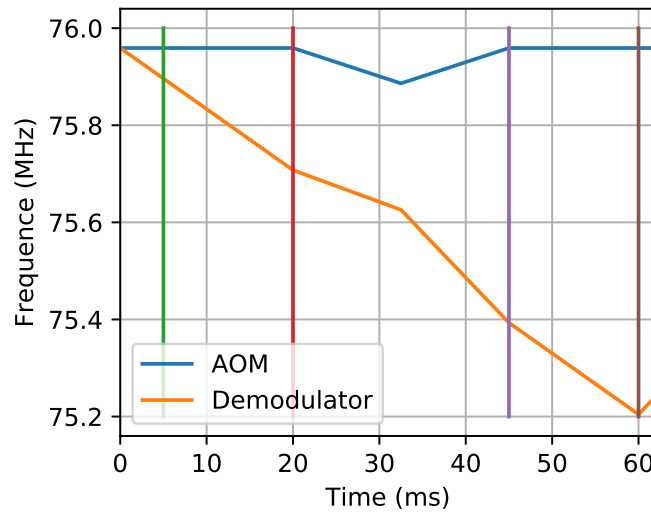


Fig. 5.13 Computed frequency for the AOM and the demodulator in the case where we perform the new type of the interferometer. Both frequencies are shifted to follow the trajectory shown in purple on [Figure 5.12](#) left while staying resonant with the atoms. Each vertical line represents a Raman pulse of the interferometer.

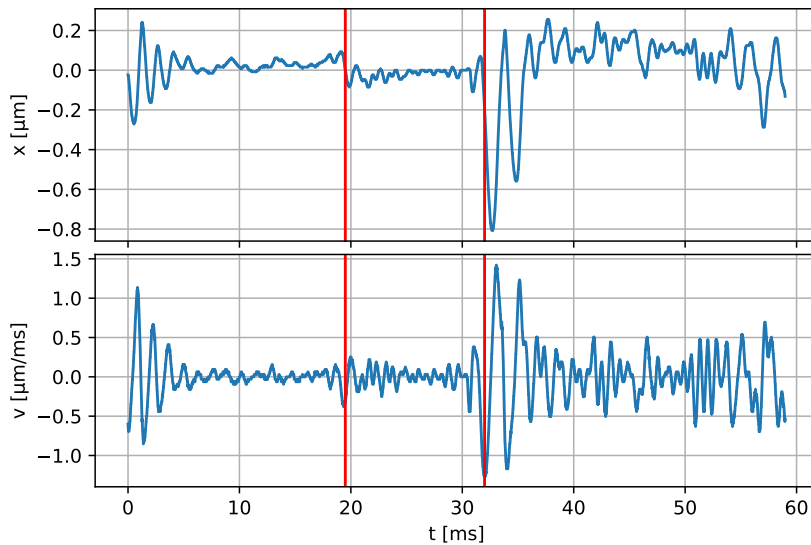


Fig. 5.14 Performance of the lock on M2 position and velocity when performing the interferometer shown on [Figure 5.12](#) left. Top: Residual error on the position of M2 regarding the atoms' position. Bottom: residual error on the velocity of M2 regarding the velocity of the atoms. The red lines correspond to the change in velocity detailed previously

second one when we ask to decelerate up to an acceleration of g .

We have plotted in [Figure 5.15](#) the typical fringes at the interferometer output with the new interferometer configuration. Each point is an average of over 5 repetitions of the experiment. The error bars are calculated using the standard deviation of these points. Even

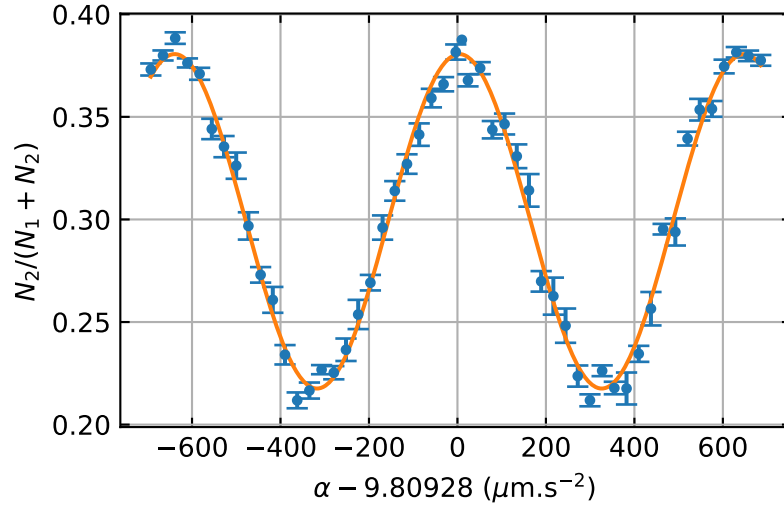


Fig. 5.15 *Atomic fringes at the output of the interferometer: fraction of atoms in $F = 2$, the excited state, as a function of the acceleration of the mirror M2. Experimental data are shown as blue points. Each point is an average of over 5 points, with an error bar given by the dispersion of those points. Here $\Delta = 1.1$ THz, $\tau = 1.23$ ps, $T_R = 15$ ms, $T_D = 25$ ms.*

with a total interrogation time of 55 ms ($T_R = 15$ ms and $T_D = 25$ ms), we achieve to get up to 16 per cent of contrast. This is nearly a 5-fold improvement compared with the previous experiment where we followed the mid-point of the interferometer. The interrogation time is limited only by the travel range of the voice coil actuator. A fit (continuous orange line) by a cosine function allows us to determine the frequency of the central fringe with a relative uncertainty of 10^{-7} in 5 min of integration, corresponding to a sensitivity of about 1 mrad. Note that this configuration is efficient only if, during the 2nd pulse, the wave packets are split by a distance larger than the size of the overlap. If we take the example of the interferometer shown on [Figure 5.12](#), when the condition is not fulfilled, the second pulse, which is now a π pulse, will address the upper path, resulting in a loss of atoms and thus to a loss of contrast.

We can perform the Monte-Carlo simulation discussed in [subsection 5.2.1](#) with the overlap zone position moving as the purple shaded area on [Figure 5.12](#) and applying the sequence $\{\pi/2 - \pi - \pi - \pi/2\}$. The simulation results, with the same parameters as in the experiment, are shown in [Figure 5.16](#). The orange point is extracted from [Figure 5.15](#). Only one experimental data was taken with these parameters experimental parameters and mainly with the same T_D . The simulation was performed by changing T_R . If one wants to do so in the experiment, then the issue of having a too short time for T_D would appear. First, the contrast drops slightly because we do not respect the condition discussed here before. Then, as the arms separate further, the contrast rises before falling again. This second drop in contrast has been studied using the simulation. It is mainly related to the initial velocity dispersion of the cloud, as the cloud might expand to a size larger than the overlap zone.

Now, if we plug an infinitely cold cloud of atoms into the simulation, we obtain that

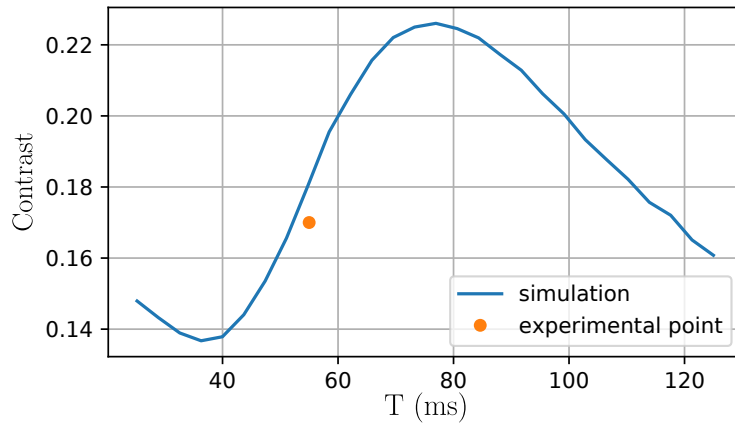


Fig. 5.16 In blue: Monte Carlo simulation of the contrast of the interferometer as a function of the total interrogation time. Orange dot: Contrast of the fringe extracted from Figure 5.15

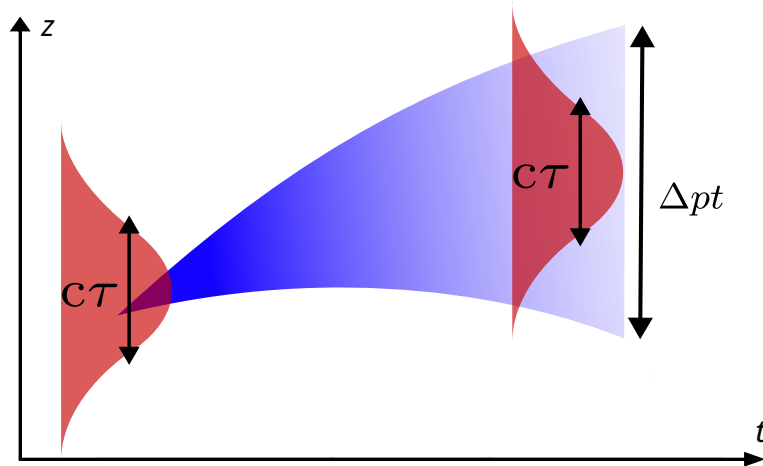


Fig. 5.17 Evolution of the atomic wave function (in blue) after a Raman transition driven by a frequency comb in a counter-propagating geometry. Because of the finite size of the overlap zone (in red), the wave function will be diffracted with a dispersion in momentum $\Delta p = \hbar/(c\tau)$.

the contrast stays still after the increases. However, for very long interrogation times, the fact that the Raman coupling is spatially localized will eventually limit the contrast of such an interferometer. Indeed, by diffracting a wave packet with a picosecond laser, we will measure the position of the atoms. Because of the Heisenberg principle, the wave packet will spread with uncertainty in momentum given by $\Delta p = \hbar/\Delta z$ with Δz being the size of the overlap zone.

Figure 5.17 illustrate this effect on the interferometer. A back-of-the-envelope calculation shows that the contrast will be zero if the spread in position relative to the spread in momentum is greater than the size of the overlap zone. This is when $\Delta p T_R > c\tau$. For a picosecond laser, this gives a maximum interrogation time of ten seconds, which is

much longer than the usual interrogation time used in any atom interferometry experiment. However, if one wants to use femtosecond lasers to drive Raman transition, the limit of the interrogation time is only tens of milliseconds.

Also, the confinement of the initial wave packet increases the energy of the selected wave packet by $(\Delta p^2/2m)$. This change in energy induces a phase shift $\hbar T_R/2m(c\tau)^2$. This phase shift is the analogue of the Gouy phase for a Gaussian optical beam. It cancels out in usual calculations where it is assumed that the two interfering wave packets have the same size and therefore undergo the same phase shift [57]. Considering the current experimental parameters, this phase shift is estimated to be $80 \mu\text{rad}$, too small to be observed considering the current sensitivity of the interferometer.

Conclusion

In this chapter, we presented a method to extend the interrogation time of frequency comb atom interferometry using a mirror mounted on a translating stage. We have presented an atom interferometer with beam splitters that are spatially localized and whose position can be dynamically and precisely controlled during the interferometer sequence. A Monte-Carlo simulation was carried out to model the effect of the wave packet separation and showed good agreement with the experimental results. We have implemented an interferometer configuration where the atomic beam splitters interact selectively with the wave packets propagating in either arm of the interferometer and have investigated the fundamental limitations of this interferometer.

Conclusion and outlooks

This part of my thesis presents the development and implementation of a novel method for atom interferometry using a frequency comb.

Summary of Contributions

- **Implementation of an Atom Interferometer with a Frequency Comb:** We demonstrated the use of a frequency comb to realize an atom interferometer with ^{87}Rb atoms in the visible spectrum.
- **Simulation and Experimental Validation:** A Monte Carlo simulation was created and conducted to model the effect of the separation of the interferometer arms, showing excellent agreement with experimental results. This validation reinforced the understanding of the underlying mechanisms which enabled the optimization of experimental parameters to maximize sensitivity.
- **Extension of the Interrogation Time:** By developing a new method to adjust the length of the delay line during the interferometry sequence, we were able to track the free fall of the atoms by moving a mirror with controlled acceleration. This enabled us to increase the interrogation time of the interferometer up to 50 ms, a five-fold improvement over previous work.
- **New Interferometer Scheme:** We demonstrated a new type of interferometer capable of independently interrogating each arm of the interferometer. This configuration highlighted a new fundamental sensitivity limit due to the atomic wavefront curvature acquired by the atoms during diffraction.
- **Measurement of gravity acceleration :** With the new apparatus, we measured the Earth's gravitational acceleration with a relative statistical uncertainty of $\sim 10^{-7}$. This precision, not competitive with usual gravimeters using CW laser, can still open doors for new tests in physics by, for instance, allowing to address atomic species in the far UV.

Future Work and Developments

The results obtained in this thesis demonstrate the potential of frequency combs atom interferometry. Several avenues for further development can be envisaged:

- **Increasing the mirror travel distance:** By increasing the travel distance of the mirror, it would be possible to further extend the interrogation time and improve sensitivity.
- **Exploring other atomic species:** The spectral flexibility of frequency combs enables experiments with other atomic species, paving the way for new applications in metrology and fundamental tests.
- **Applications in fundamental physics:** Frequency-comb-driven atomic interferometers could be used for a test of the universality of free fall on anti-hydrogen. Unfortunately, the properties of the anti-hydrogen sources produced to date mean that this experiment is not yet feasible.

Our team is currently building a new experiment on Ytterbium atoms. We already frequency-doubled the picosecond laser with a bismuth triborate (BIBO) crystal and are working on producing a MOT of Ytterbium. We plan on using the frequency comb to drive Bragg transition between the $1S_0 \rightarrow 1P_1$ transition of ^{174}Yb . Performing an interferometer with the frequency comb on this transition at 399 nm brings us closer to the UV-XUV region. It would also prove that after frequency doubling, it is possible to perform atom interferometry with a frequency comb.

Part II

Progress on atomic recoil measurement

Chapter 6

Introduction

The fine-structure constant was introduced in 1916 by Arnold Sommerfeld [56] to explain the splitting of atomic lines in hydrogen. This constant, α , is a fundamental dimensionless constant in quantum electrodynamics (QED), defined as:

$$\alpha = \frac{e^2}{4\pi\epsilon_0\hbar c} \quad (6.1)$$

where e is the elementary electric charge, ϵ_0 is the permittivity of free space, \hbar is the reduced Planck constant, and c is the speed of light in vacuum. The modern understanding of α is that it sets the scale of the electromagnetic interaction. Consequently, many experiments involving the interaction of charged particles with electromagnetic fields can be used to determine α . In 1998, the experiments considered by the CODATA task group on fundamental constants to provide the best estimate of the fine structure constant ranged from solid-state physics and atomic physics to quantum electrodynamics [59].

Currently, the most accurate determinations of the fine structure constant come mainly from two methods. The first method involves combining the measurement of the electron's gyromagnetic anomaly, a_e , with QED calculations. This allows for the extraction of the value of α from the following relationship:

$$a_e = A_1 \left(\frac{\alpha}{\pi}\right) + A_2 \left(\frac{\alpha}{\pi}\right)^2 + A_3 \left(\frac{\alpha}{\pi}\right)^3 + \dots + a_e \left(\frac{m_e}{m_\mu}, \alpha\right) + a_e \left(\frac{m_e}{m_\tau}, \alpha\right) + a_e(\text{weak}) + a_e(\text{had})$$

The coefficients A_i are dimensionless numbers calculated using Feynman diagrams. The first few coefficients, A_1 , A_2 , and A_3 , are known analytically. The coefficients A_4 and A_5 are calculated numerically, with the latter involving more than 12,000 diagrams. The terms $a_e \left(\frac{m_e}{m_\mu}, \alpha\right)$ and $a_e \left(\frac{m_e}{m_\tau}, \alpha\right)$ account for the effects due to the electron to muon and electron to tau mass ratios, respectively. Additionally, $a_e(\text{weak})$ and $a_e(\text{had})$ include contributions from weak and hadronic interactions.

Alternatively, the constant α can be expressed in terms of the Rydberg constant R_∞ , the mass ratio between a rubidium atom and an electron, and the ratio h/m_{Rb} between the Planck constant and the mass of a rubidium atom:

$$\alpha^2 = \frac{2R_\infty}{c} \frac{m_{\text{Rb}}}{m_e} \frac{h}{m_{\text{Rb}}} \quad (6.2)$$

In this equation, we have

- R_∞ , the Rydberg constant, known to 1.9 ppt (parts per trillion) by spectroscopy of the $1S \rightarrow 2S$ transition of the hydrogen atom [59].
- m_{Rb}/m_e , a mass ratio. The precision for the rubidium 87 mass is 69 ppt [33]. The mass of the electron is obtained with a precision of 29 ppt by measuring the magnetic moment of a single electron bound to a carbon nucleus [58].
- h/m_{Rb} , which is obtained by measuring the recoil velocity of an atom absorbing a photon. This is currently the limiting factor in the precision of α in this equation. The most precise measurement of h/m_{at} was obtained by the group in 2020 at 142 ppt [42].

Our team determines α by measuring the ratio h/m_{Rb} , which is related to the recoil velocity of rubidium atoms. Note that now \hbar is a constant; thus, our experiment measured the mass of a Rubidium atom. However, for the historical question (our group is named h/m), I will always consider that we measure the ratio between \hbar and the mass of a Rubidium atom.

Our atom interferometer acts as a velocity sensor, providing precise velocity measurements. This capability is combined with the technique of Bloch oscillations in an optical lattice to transfer a large number, N , of recoils to the atoms, reducing the uncertainty in the measurement of h/m by $1/N$.

Comparing the two methods, saying the direct measurement of a_e [29] and α [41; 48], allows one to perform a test of the standard model. The experiments are so precise that they enable us to test QED at the tenth order and observe corrections due to muons in laboratory-sized experiments[16].

6.1 Measurement of the ratio h/m

In the group, the ratio h/m is determined using atom interferometry. To do so, we implement a Ramsey-Bordé interferometer coupled to Bloch oscillation. To grasp the following, we will first introduce the tool used to split and recombine the atom's wave packet before discussing briefly the concept of Bloch oscillation used to enhance the sensitivity of the measurement.

6.1.1 Stimulated Raman transition

One could think about using one photon transition to create a coherent spatial separation of an atom. However, the first excited state of the alkaline atom has a lifetime too short to be used in an atom interferometer.

Therefore, one can use the long lifetime of the hyperfine levels of these atoms. We use two-photon transitions, and more specifically stimulated Raman transitions, in a counterpropagating geometry to split, deflect, and recombine atomic wave packets. The atom first absorbs a photon and then emits through stimulated emission a second photon. This transition allows us to create coherent spatial superposition between these states. The advantage of this transition is that the final internal state is different from the initial internal state, making it easier to detect the population of these states.

Some experiments use two-photon Bragg transition, where the final internal state of the transition is the same as the initial internal state but the external degree of freedom is shifted by $2\hbar k$. These transitions have the benefit that it is possible to transfer more than $2\hbar k$ in one transition.

6.1.1.1 General considerations

We consider a three-level atom with two hyperfine states $|g\rangle = |F = 1, m_F = 0\rangle$, $|e\rangle = |F = 2, m_F = 0\rangle$ and an excited state $|i\rangle$. Two laser fields (ω_1, \vec{k}_1) and (ω_2, \vec{k}_2) couple the excited state to the ground states in a Λ scheme. To avoid spontaneous emission from the excited state ($\Gamma \sim 6$ MHz) the one-photon laser coupling is far detuned from this transition ($\Delta \sim 60$ GHz). Furthermore, because the typical Raman transition coupling is ~ 5 kHz and because the Zeeman sub-levels are spaced by more than 50 kHz (due to a magnetic field of 30 mG in the experiment) we can consider only two Zeeman sub-levels and restrict ourselves to the $m_F = 0$ hyperfine states. In the experiment, we choose the $m_F = 0$ states to be insensitive to the first-order Zeeman effect.

6.1.1.2 Resonance condition

Stimulated Raman transition is a process in which an atom absorbs a photon from a laser field 1 with (ω_1, \vec{k}_1) and emits through stimulated emission a photon in a laser field 2 with (ω_2, \vec{k}_2) . In the lab frame, the resonance condition for an atom in the fundamental state of energy E_g with initial velocity \vec{v}_i can be found by writing energy and momentum

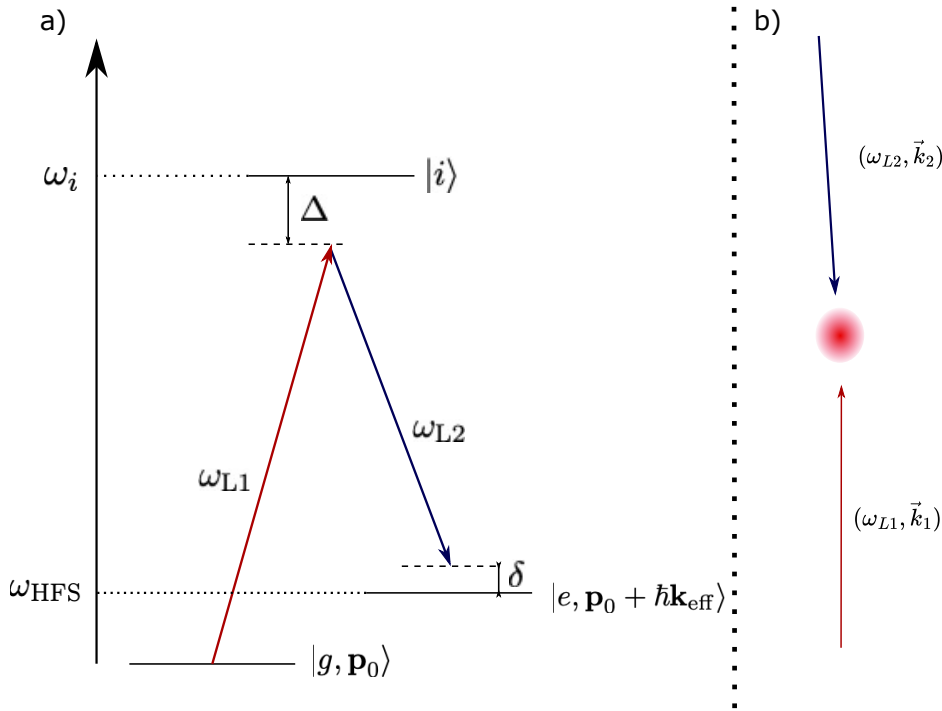


Fig. 6.1 (a): Three level system for the description of Raman transitions. The excited state is coupled to the two ground states through two beams that are detuned by Δ from the one-photon transition. The mismatch between the two-photon frequency $\omega_1 - \omega_2$ and the atomic internal energy ω_{HFS} is written δ . The scaling with respect to the experimental conditions is not respected since $\Delta \sim 60$ GHz, $\omega_{HFS} \sim 6.8$ GHz and $\delta \sim 0 - 20$ MHz. (b): Example of a geometric configuration where an atom is subjected to two beams. Extracted from [41].

conservation:

$$\begin{aligned} E_g + \frac{1}{2}mv_i^2 + \hbar\omega_1 &= E_e + \frac{1}{2}mv_f^2 + \hbar\omega_2 \\ m\vec{v}_i + \hbar\vec{k}_1 &= m\vec{v}_f + \hbar\vec{k}_2 \end{aligned} \quad (6.3)$$

where E_e is the energy of the excited state and v_f the final velocity. By merging these two equations, we have

$$\delta = \omega_1 - \omega_2 - \omega_{HFS} = \frac{\vec{p}_i \cdot \vec{k}_{\text{eff}}}{m} + \frac{\hbar\vec{k}_{\text{eff}}^2}{2m} \quad (6.4)$$

where $\hbar\omega_{HFS} = E_e - E_g$ is the hyperfine energy splitting, $\vec{k}_{\text{eff}} = \vec{k}_1 - \vec{k}_2$ is the Raman transition effective wavevector and δ the two photon detuning. The first term on the right part of the equation can be identified as the Doppler effect, and the second one is the recoil frequency shift. We can see that by controlling the frequency difference of the lasers δ we can select a class of initial velocity that will perform the transition. We also need to highlight that the internal degree of freedom is associated with the external degree of

freedom, an important feature of the Raman transition. By scanning δ and looking at the transition probability, we can also measure the initial velocity distribution of an atomic sample.

6.1.1.3 Raman coupling

In this section, we aim at modeling the coupling of the two laser fields with a three-level atom. The field (1) couples the states $|g\rangle$ with the excited state $|i\rangle$, the field (2) couples $|e\rangle$ with $|i\rangle$. Here, it is important that a more realistic model would take into account the action of field (1) on $|e\rangle$ and the action of (2) on $|g\rangle$. This treatment can be found in [6; 11; 21]. For the sake of simplicity, we will not consider these coupling. Yet, they will be taken into account in the final equation.

We use the dressed atom picture. We consider the following set of states:

$$\begin{aligned} |g\rangle &= |g, \vec{P}, n_1, n_2\rangle \\ |e\rangle &= |e, \vec{P} + \hbar\vec{k}_{\text{eff}}, n_1 - 1, n_2 + 1\rangle \\ |i\rangle &= |i, \vec{P} + \hbar\vec{k}_1, n_1 - 1, n_2\rangle \end{aligned} \quad (6.5)$$

with n_1 and n_2 being respectively the number of photon in laser 1 and 2. The left part is a simplified notation used for the rest of the section.

The free Hamiltonian of the subset states consider above is:

$$H_0 = \begin{pmatrix} \delta + \frac{\vec{p}^2}{2m} & 0 & 0 \\ 0 & \frac{(\vec{p} + \hbar\vec{k}_{\text{eff}})^2}{2m} & 0 \\ 0 & 0 & \Delta + \frac{(\vec{p} + \hbar\vec{k}_1)^2}{2m} \end{pmatrix} \quad (6.6)$$

The two first diagonal terms differ by less than few MHz whereas $\Delta \sim 60$ GHz as mention before. As a result, the excited state $|i\rangle$ stays nearly unpopulated. We can consider $|g\rangle$ and $|e\rangle$ as being nearly degenerated regarding the laser coupling. The coupling can be written as

$$\hat{V}_i = -\hat{\mathbf{d}} \cdot \hat{\mathbf{E}}_i \quad (6.7)$$

where $\hat{\mathbf{d}}$ is the dipole operator of the atom and $\hat{\mathbf{E}}_i$ is the electric field operator associated with the field.

$$\hat{\mathbf{E}}_i = \xi_i \left(e^{ik_i\hat{z}} a_i - e^{-ik_i\hat{z}} a_i^\dagger \right) \quad (6.8)$$

where a_i are the annihilation operators of laser mode i .

We define the Rabi frequencies which describe the coupling strength between the states:

$$\Omega_1/2 = \frac{1}{\hbar} \langle i | \hat{V}_1 | g \rangle \quad (6.9)$$

$$\Omega_2/2 = \frac{1}{\hbar} \langle i | \hat{V}_2 | e \rangle \quad (6.10)$$

This leads to a total Hamiltonian:

$$H = \hbar \begin{bmatrix} \delta + \frac{\vec{p}^2}{2m} & 0 & \frac{\Omega_1}{2} \\ 0 & \frac{(\vec{p} + \hbar \vec{k}_{\text{eff}})^2}{2m} & \frac{\Omega_2}{2} \\ \frac{\Omega_1^*}{2} & \frac{\Omega_2^*}{2} & \Delta + \frac{(\vec{p} + \hbar \vec{k}_1)^2}{2m} \end{bmatrix} \quad (6.11)$$

As in [chapter 2](#), we can apply perturbation theory and constrain ourselves to only two states with a direct effective coupling between $|g\rangle$ and $|e\rangle$. The formal procedure to reduce a three-level system to a two-level system is given in [24].

In the $|g\rangle, |e\rangle$ frame, the total Hamiltonian (free Hamiltonian and light atom coupling) becomes:

$$H_e = \hbar \begin{pmatrix} \delta + \Omega_f^{\text{LS}} & \frac{\Omega}{2} \\ \frac{\Omega^*}{2} & \delta_{\text{Doppler}} + \Omega_e^{\text{LS}} \end{pmatrix} \quad (6.12)$$

where

$$\Omega_f^{\text{LS}} = -\frac{|\Omega_1|^2}{4\Delta} \quad (6.13)$$

$$\Omega_e^{\text{LS}} = -\frac{|\Omega_2|^2}{4\Delta} \quad (6.14)$$

are the lights shift induced by off resonant coupling and

$$\Omega = -\frac{\Omega_1 \Omega_2^*}{2\Delta}$$

is the complex two-photon Raman Rabi frequency. Also,

$$\delta_{\text{Doppler}}(\vec{v}) = \vec{k}_e \cdot \vec{v} + \frac{\hbar \vec{k}_{\text{eff}}^2}{2m} \quad (6.15)$$

highlights the sensitivity of the transition to the Doppler effect. We split the Rabi frequency in phase and modulus

$$\Omega = \Omega e^{-i\Phi} \quad (6.16)$$

with $\Phi = \Phi_2 - \Phi_1$. Φ_i describes the intrinsic phase of the laser. Using Pauli matrices and by

choosing an appropriate energy origin, the Hamiltonian goes to

$$\begin{aligned} \frac{H}{\hbar} &= \begin{pmatrix} \frac{\delta^R(\vec{v})}{2} & \Omega/2 \\ \Omega/2 & -\frac{\delta^R(\vec{v})}{2} \end{pmatrix} \\ &= \frac{\delta^R(\vec{v})}{2} \sigma_z + \frac{\Omega}{2} (\cos(\Phi) \sigma_x + \sin(\Phi) \sigma_y) \end{aligned} \quad (6.17)$$

with

$$\delta^R(\vec{v}) = \delta - (\Omega_e^{\text{LS}} - \Omega_f^{\text{LS}}) + \delta_{\text{Doppler}}(\vec{v}) \quad (6.18)$$

being the extended detuning. From equation 6.17, we can compute the transition probability for an atom starting from the $|g\rangle$ state:

$$P_{a \rightarrow b}(\tau, \delta^R(\vec{v})) = \frac{\Omega^2}{\Omega^2 + \delta^R(\vec{v})^2} \sin^2\left(\sqrt{\Omega^2 + \delta^R(\vec{v})^2} \frac{\tau}{2}\right) \quad (6.19)$$

The effective Raman Rabi frequency is

$$\Omega_{\text{eff}} = \sqrt{\Omega^2 + \delta^R(\vec{v})^2} \quad (6.20)$$

One should notice that when the duration verifies $\Omega\tau = \frac{\pi}{2}$ the atom is in a coherent superposition of the initial and final state with a probability of 50 per cent to be in each of the states. This is what we will call a $\frac{\pi}{2}$ pulse or a beam splitter pulse.

Likewise, when the duration τ of the Raman pulse verifies $\Omega_{\text{eff}}\tau = \pi$ the probability for an atom, at resonance, to be in the excited state after the pulse is equal to one, this is what we will call a π pulse, or a mirror pulse.

In the experiment, for typical detuning of 60 GHz and intensity of 100 mW cm⁻² the Raman π pulse duration is on the order of 50 μ s.

Also, we need to point out that the detuning of the transition depends on the atom's initial velocity. The width of the transition probability scale as

$$\Delta v \sim \frac{\Omega}{k_{\text{eff}}} \quad (6.21)$$

where k_{eff} is the norm of the effective wavevector which depends on the geometry of the lasers beams presented thereafter.

6.1.1.4 Co and counter-propagating geometry

We can identify two geometrical configurations of interest when using Raman transition. The co-propagating is where the two laser fields propagate along the same direction and the counterpropagating is where they travel in opposite directions.

Respectively, their effective wavevector are given by :

$$\begin{aligned} k_{\text{eff,copro}} &= k_1 - k_2 \\ k_{\text{eff,counter}} &= k_1 + k_2 \end{aligned} \quad (6.22)$$

using the resonance condition, we obtain

$$\begin{aligned} k_{\text{eff,copro}} &\sim 0 \\ k_{\text{eff,counter}} &\sim \frac{2\omega_1}{c} \end{aligned} \quad (6.23)$$

where c is the speed of light.

In the experiment, on ^{87}Rb , $\omega_{\text{HFS}} \sim 2\pi \times 6.8 \text{ GHz}$ and $\omega_1 \sim 2\pi \times 384 \text{ THz}$. From this, we can estimate the recoil velocity given to an atom during the Raman process. The recoil velocity is $\hbar k_{\text{eff}}/m$. With the previous number, we find that the counterpropagating recoil velocity is $\sim 12 \text{ mm/s}$.

Therefore, using counterpropagating Raman transition, an atomic wave-function can be put in a coherent spatial separation. These transitions are excellent tools for atom interferometry. Indeed, the sensitivity of the interferometer scale with the enclosed area. A higher recoil velocity will increase the enclosed area and therefore the sensitivity of the interferometer.

6.1.2 Representation free approach

Here, we will use the same derivation as in [section 4.1](#) to derive the sensitivity of the h/m interferometer. This derivation will differ by the implementation of Bloch oscillation between the two Ramsey sequences of the interferometer. We will show how this interferometric configuration can be used to measure the ration h/m .

General consideration

We consider a two-level atom with level $|g\rangle, |e\rangle$ interacting with a laser, at resonance, of wavevector k . The energy of the $|g\rangle$ state is chosen to be zero and the one of $|e\rangle$ to be $\hbar\omega_e$. The momentum kick acquired when performing the transition is $\hbar k$. The interaction between the lasers and the atoms is considered infinitely short (delta pulses). In the experiment, the $|g\rangle$ and $|e\rangle$ states are the hyperfine levels addressed through Raman transition. The system considered here consists then of two quantum degrees: 1) two internal states $|g\rangle, |e\rangle$ introduced earlier. 2) centre-of-mass motion in state $|j\rangle$ labelled $|\Psi_j\rangle$. To obtain the signal at the output of the atom interferometer, we focus on the evolution of the $|\Psi\rangle$ state defined by

$$|\Psi(t)\rangle = |g\rangle |\Psi_g\rangle + |e\rangle |\Psi_e\rangle \quad (6.24)$$

We consider the \hbar/m interferometer shown on [Figure 6.2](#). It is performed using a sequence of four $\pi/2$ pulses, each one inducing a Raman transition between the two internal levels $|g\rangle$ and $|e\rangle$. The interrogated atoms fall freely in the field of gravity. The corresponding Hamiltonian is

$$\hat{H} = \hat{H}_0 + \hat{H}_{\text{laser}} \quad (6.25)$$

1. $\hat{H}_0 = \left(\frac{\hat{p}^2}{2m} + mg\hat{z} \right) + \hbar\omega_e |e\rangle \langle e|$
2. \hat{H}_1 the Hamiltonian of interaction with the laser

The Schrödinger equation is

$$i\hbar \frac{d}{dt} |\Psi(t)\rangle = \hat{H} |\Psi(t)\rangle \quad (6.26)$$

As long as \hat{H} is time independent $|\Psi(t)\rangle = U(t,0) |\Psi(0)\rangle = e^{-\frac{i\hat{H}t}{\hbar}} |\Psi(0)\rangle$. Here, however, the Hamiltonians are explicitly time-dependent due to the interaction with the laser. Yet, we can decompose the evolution operator as follows:

1. when not interacting with the laser: $U_e(t',t) = e^{-\frac{i}{\hbar} \left(\frac{\hat{p}^2}{2m} + mg\hat{z} + \hbar\omega_e \right) (t'-t)}$ if in the $|e\rangle$ state.
2. when not interacting with the laser: $U_f(t',t) = e^{-\frac{i}{\hbar} \left(\frac{\hat{p}^2}{2m} + mg\hat{z} \right) (t'-t)}$ if in the $|g\rangle$ state.
3. when interacting with the laser, assuming δ like pulses $U_{l\pm}(t) = e^{\pm i(k\hat{z} - \omega t \pm \Phi(t))}$ (see [\[51\]](#) appendix A.4). The sign depends if the photon is absorbed or emitted by the atom. We will consider a plus sign when the atom absorbs a photon.
4. when performing Bloch oscillation, that we will also consider infinitely short $U_b(t) = e^{+i(Nk\hat{z})}$

We denote $|\Psi^{up}\rangle$ (resp $|\Psi^{down}\rangle$) the wave function in the upper (resp. lower) arm of the interferometer at the lower exit port of the interferometer.

We are considering a symmetrical interferometer. Otherwise, doing so would make the calculations much more cumbersome, especially as we always use a symmetrical interferometer in the experiment.

$$|\Psi^{up}\rangle = U_e(T_R)U_{l-}(t_3)U_e(T_B)U_b(t_b)U_e(T_R + T_B)U_{l+}(t_1) |\Psi(0)\rangle \quad (6.27)$$

$$|\Psi^{down}\rangle = U_{l-}(t_4)U_e(T_R)U_e(T_B)U_b(t_b)U_e(T_B)U_{l+}(t_2)U_e(T_R) |\Psi(0)\rangle \quad (6.28)$$

For the upper path, with the same derivation as in [section 4.1](#), one can show that

$$|\Psi^{up}\rangle = e^{-i(\phi_1 - \phi_3)} e^{iNk\hat{z}} e^{-\frac{i}{\hbar} \hat{H}_N T_R} e^{-\frac{i}{\hbar} \hat{H}_{N+1} T_B} e^{-\frac{i}{\hbar} \hat{H}_1 (T_B + T_R)} |\Psi(0)\rangle \quad (6.29)$$

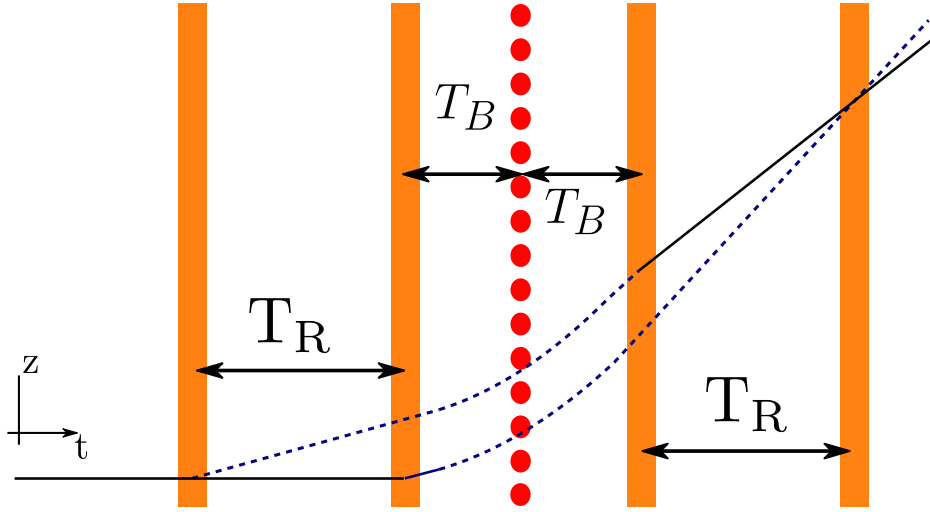


Fig. 6.2 h/m interferometer. Full line: Atom in the ground state. Dashed line: Atom in the excited state. In yellow we represent the Raman pulses. The red dashed line represents the Bloch oscillation applied in-between the two Ramsey sequences.

with

$$\hat{H}_j = \frac{(\hat{P} + j\hbar k)^2}{2m} + mg\hat{z} \quad (6.30)$$

As previously, we want to merge the exponential. Because the commutators are c-number, we obtain using the Baker-Campbell-Hausdorff formula

$$|\Psi^{up}\rangle = e^{-i(\phi_1 - \phi_3)} e^{iNk\hat{z}} e^{-\frac{i}{\hbar}(\hat{H}_N T_R + \hat{H}_{N+1} T_B)} e^{-[\hat{H}_N; \hat{H}_{N+1}] \frac{T_B T_R}{2\hbar^2}} e^{-\frac{i}{\hbar} \hat{H}_1 (T_B + T_R)} |\Psi(0)\rangle \quad (6.31)$$

By calculating $e^{[\hat{H}_N; \hat{H}_{N+1}] \frac{T_B T_R}{2\hbar^2}}$, one gets

$$|\Psi^{up}\rangle = e^{-i(\phi_1 - \phi_3)} e^{iNk\hat{z}} e^{-\frac{i}{\hbar} \hat{H}_N T_R + \hat{H}_{N+1} T_B} e^{-\frac{i}{\hbar} \hat{H}_1 (T_B + T_R)} e^{-\frac{i}{2} kg T_B T_R} |\Psi(0)\rangle \quad (6.32)$$

Repeating the same calculation, we finally have

$$\begin{aligned} |\Psi^{up}\rangle &= e^{-i(\phi_1 - \phi_3)} e^{iNk\hat{z}} e^{-\frac{i}{\hbar}(\hat{H}_N T_R + \hat{H}_{N+1} T_B + \hat{H}_1 (T_B + T_R))} \\ &e^{-\frac{i}{2}(-(N-1)kg T_R (T_R + T_B) - Nkg T_B (T_R + T_B) + kg T_B T_R)} |\Psi(0)\rangle \end{aligned} \quad (6.33)$$

If one performs the same calculation on the lower path

$$\begin{aligned} |\Psi^{down}\rangle &= e^{-i(\phi_2 - \phi_4)} e^{iNk\hat{z}} e^{-\frac{i}{\hbar}(\hat{H}_{N+1} T_R + \hat{H}_{N+1} T_B + \hat{H}_1 T_B + \hat{H}_0 T_R)} \\ &e^{-\frac{i}{2}(-(N+1)kg T_R (T_R + T_B) - Nkg T_B (T_R + T_B) - kg T_B T_R)} |\Psi(0)\rangle \end{aligned} \quad (6.34)$$

We define the operator phase as

$$|\Psi^{\text{up/down}}\rangle = e^{i\hat{\Phi}_{\text{up/down}}} |\Psi(0)\rangle \quad (6.35)$$

The phase of the interferometer will be obtain computing $e = \langle \Psi^{\text{up}} | \Psi^{\text{down}} \rangle$ with

$$e = \langle \Psi(0) | U^{\text{up}\dagger} U^{\text{down}} | \Psi(0) \rangle \quad (6.36)$$

$$= \langle \Psi(0) | e^{-i\hat{\Phi}_{\text{up}}} e^{+i\hat{\Phi}_{\text{down}}} | \Psi(0) \rangle \quad (6.37)$$

Again, we need to evaluate $[-\hat{\Phi}_{\text{up}}, \hat{\Phi}_{\text{down}}]$. One can verify that

$$[-\hat{\Phi}_{\text{up}}, \hat{\Phi}_{\text{down}}] = 0 \quad (6.38)$$

Thus $e^{-i\hat{\Phi}_{\text{up}}} e^{+i\hat{\Phi}_{\text{down}}} = e^{-i\hat{\Phi}_{\text{up}} + i\hat{\Phi}_{\text{down}}} = e^{-i\Delta\hat{\Phi}}$ and it all boils down to :

$$\begin{aligned} \Delta\hat{\Phi} = & \phi_1 - \phi_2 - \phi_3 + \phi_4 + \frac{kg}{2} (-(N-1)T_R(T_R + T_B) - NT_B(T_R + T_B) + T_B T_R \\ & + (N+1)T_R(T_R + T_B) + NT_B(T_R + T_B) + T_B T_R) \\ & + \frac{1}{\hbar} (\hat{H}_N T_R + \hat{H}_{N+1} T_B + \hat{H}_1 (T_B + T_R) - \hat{H}_{N+1} T_R - \hat{H}_{N+1} T_B - \hat{H}_1 T_B + \hat{H}_0 T_R) \end{aligned} \quad (6.39)$$

Which, after some simplification gives

$$\Delta\Phi = \phi_1 - \phi_2 - \phi_3 + \phi_4 + kgT_r T_{\text{delay}} - k\Delta v T_r \quad (6.40)$$

With $T_{\text{delay}} = T_r + 2T_B$ and $\Delta v = N \frac{\hbar k}{m}$.

By scanning $\phi_1 - \phi_2 - \phi_3 + \phi_4$ and determining the value for which the phase shift is zero, one measures the velocity difference between the first and second Ramsey sequences (as long as you know the value of g). Because we can control the number of recoil N given during Bloch oscillation and by measuring k precisely, a measurement of $\Delta\Phi$ allows one to measure h/m . This behavior justifies the denomination of differential velocity sensor configuration.

6.1.3 Bloch oscillation

We have seen that when transferring a large number of recoil velocities in a Ramsey-Bordé interferometer, the sensitivity to h/m scales proportionally to the number of recoils transferred. We use the technique of Bloch oscillations for this purpose. This technique allows for controlled and precise transfer of a large number of recoil velocities. A more detailed treatment of the theory of Bloch oscillations can be found in [21].

At first glance, Bloch oscillations can be interpreted as a succession of counter-propagating Raman transitions in the same internal state. With each transition, the atom acquires a recoil velocity. By chirping the frequency of one of the two lasers, we transfer recoil velocities one by one.

Another way to view Bloch oscillations is to imagine a lattice generated by two counter-propagating lasers. When scanning the frequency of one of the lasers, the atom trapped in this lattice will move with it, acquiring a velocity equal to the chirping of the laser frequency.

From a more calculative perspective, consider two counter-propagating lasers described as:

$$E_{\pm}(t, z) = E_0 \exp \left[i \left(\pm kz - \omega t \pm \int \delta\omega(t) dt + \phi_{\pm} \right) \right] \quad (6.41)$$

where $\delta\omega(t)$ is the chirping rate of the lasers' frequencies. The sign depends on the propagation direction of the laser. Considering a common phase for both lasers, the potential (related to the light shift) experienced by the atom can be written as [21]:

$$V = V_0 \cos^2 \left(kz - \int \delta\omega(t) dt \right) \quad (6.42)$$

with:

$$V_0 = \frac{3\pi c^2}{2\omega_{\text{atom}}^3} \frac{\Gamma}{\Delta} 4I_0 \quad (6.43)$$

where the frequency ω_{atom} is the frequency of the optical transition used to create the potential and Δ is the detuning from this transition. Experimentally, we choose a positive detuning, meaning we are blue-detuned. Thus, the atoms are trapped in the minima of the intensity or nodes of the optical lattice. This choice of detuning minimizes spontaneous emission and, consequently, limits the number of scattered atoms during the Bloch oscillations.

When we scan the frequency of the lasers, we generate a lattice with an acceleration:

$$a = \frac{\lambda}{2\pi} \frac{d\delta\omega}{dt} \quad (6.44)$$

where λ is the wavelength of the Bloch laser. Once the acceleration is known, the Bloch oscillation period τ_B can be deduced as ([41] equation 2.30.20):

$$\tau_B = \frac{2\hbar k_B}{ma} \quad (6.45)$$

Typically, in the experiment, $\tau_B \sim 12 \mu\text{s}$ and $N_B = 500$, which means that we can now transfer 1000 recoil velocities to the atom in around 6 ms. Each Bloch oscillation has a very high efficiency of 0.9993. This atom accelerator provides an easy and precise way to control the atoms.

6.2 2020 measurement

In 2020, the group performed the most precise measurement of the fine-structure constant to date [42]. This measurement has allowed us to obtain a new determination of the fine-structure constant with an unprecedented relative precision of 81 parts per trillion (ppt):

$$\frac{h}{m_{\text{Rb}}} = 4.591\,359\,258\,90(65) \times 10^{-9} \quad (6.46)$$

$$\alpha^{-1} = 137.035\,999\,206(11) \quad (6.47)$$

This corresponds to a 2.5-fold improvement in precision compared to the measurement by the Berkeley team using cesium. However, a 5.5σ discrepancy is observed between the measurement we performed and the one at Berkeley[48]. The work described in this section is part of the effort to understand the discrepancy between the values obtained by determining h/m .

On [Figure 6.3](#), we show the error budget of the 2020 measurement. We see that the global systematic effects uncertainty of 6.8×10^{-11} limits the measurement. To mitigate some of the systematic effects, the group decided to use a colder atomic source: a Bose-Einstein Condensate (BEC). The first motivation for using a BEC is to reduce the effect related to the transverse expansion of the cloud during the interferometer (residual light shift and beam profile) [43]. Other systematic effects, such as the Gouy phase, will however be enhanced using a BEC. Indeed, what we denote as the Gouy Phase is related to the transverse Laplacian of the intensity profile. In the case of a BEC situated at the centre of a Gaussian beam, this effect will be more pronounced than in the case of molasses, due to the smaller distance over which averaging can be performed. The use of a BEC would assist in the mitigation of these effects, thereby facilitating a more comprehensive understanding of them.

Source	Correction [10^{-11}]	Relative uncertainty [10^{-11}]
Gravity gradient	-0.6	0.1
Alignment of the beams	0.5	0.5
Coriolis acceleration		1.2
Frequencies of the lasers		0.3
Wave front curvature	0.6	0.3
Wave front distortion	3.9	1.9
Gouy phase	108.2	5.4
Residual Raman phase shift	2.3	2.3
Index of refraction	0	< 0.1
Internal interaction	0	< 0.1
Light shift (two-photon transition)	-11.0	2.3
Second order Zeeman effect		0.1
Phase shifts in Raman phase lock loop	-39.8	0.6
Global systematic effects	64.2	6.8
Statistical uncertainty		2.4
Relative mass of ^{87}Rb : 86.909 180 531 0(60)		3.5
Relative mass of the electron : $5.485 799 090 65(16) \cdot 10^{-4}$		1.5
Rydberg constant : $10 973 731.568 160(21)\text{m}^{-1}$		0.1
Total: $\alpha^{-1} = 137.035 999 206(11)$		8.1

Fig. 6.3 Error budget of the measurement conducted in 2020. We have highlighted the major sources on which we worked during my work (green for [chapter 8](#), red for [section 8.2](#)

)

6.3 Outlook

A part of my work on the h/m experiment is a direct following of the thesis of C. Carrez [20]. Together with C. Carrez, we found that the wavefront distortion systematic effect is exalted when using a BEC. In the next, we will detail how we investigated and managed the effect due to wavefront distortions using BEC. Also, we will discuss new setups used to study the phase shifts in the Raman phase lock loop (highlighted in green on [Figure 6.3](#)).

This part is organized into 3 chapters:

Chapter 8 details the experimental setup, how we produce the BEC, and the experimental protocol to measure h/m .

Chapter 9 is dedicated to the study of the phase shift in the Raman phase lock loop. We present two distinct setups put in place to reduce the phase shift. An in-parallel study, using a scope, is implemented to measure the impact of our new setups.

In Chapter 10, we begin by explaining the problem related to the uses of a BEC for our

experiment. Then, new homemade collimators are studied. They show an improved intensity wavefront quality with no optical aberration. Even though the improved collimators, we show that the value of h/m still shifts with the initial velocity given to the BEC. We conclude that spurious beams are responsible for this shift.

Chapter 7

Experimental set-up and measurement of h/m

The current experimental setup has been developed over the past ten years. It is mainly described in the theses of R. Jannin [35] and C. Courvoisier [25]. Improvements and modifications made during my PhD will be presented in the next chapters.

7.1 Vacuum cell

The schematic presentation of the vacuum cell is shown in [Figure 7.1](#). Our vacuum cell is L-shaped. The horizontal part contains a 2D MOT which precools the atoms before they enter the main chamber. The center of the 'L' is the main chamber where the 3D optical molasses is prepared. The vertical part is the interferometry area where we conduct the atom interferometry measurements.

The vacuum cell must maintain a pressure below 10^{-9} mbar to ensure that the trapped atoms have a lifetime of more than 10 seconds. To achieve this, we use NEX Torr pumps and an ion pump. This setup has allowed us to maintain a vacuum of 2×10^{-10} mbar continuously for almost 4 years. However, in late 2023, the Rubidium cell broke "spontaneously". We had to wait for the new glassblower, Tom Chevy, of the LKB to make a new one for us. During this time, we also took advantage of the vacuum break to clean the 2D MOT windows. In fact, over time, a reaction took place between the windows and the rubidium, and a thin, opaque film appeared on the windows. We managed to clean them by simply whipping them carefully with ethanol. After receiving the new rubidium cell and reassembling the now clean 2D MOT chamber, we were able to achieve the same vacuum as before. Having clean windows resulted in faster MOT loading and an increase in the overall signal in the detection.

The vertical part is a tube surrounded by a solenoid that generates a bias field along the vertical axis. Since the atom interferometer operates in this vertical part, we need a highly controlled magnetic field that is well isolated from external magnetic disturbances. A two-layer cylindrical μ -metal magnetic shield is used to reduce the residual rms magnetic field measured value is $\simeq 50$ nT. Between the atom interferometer tube and the main

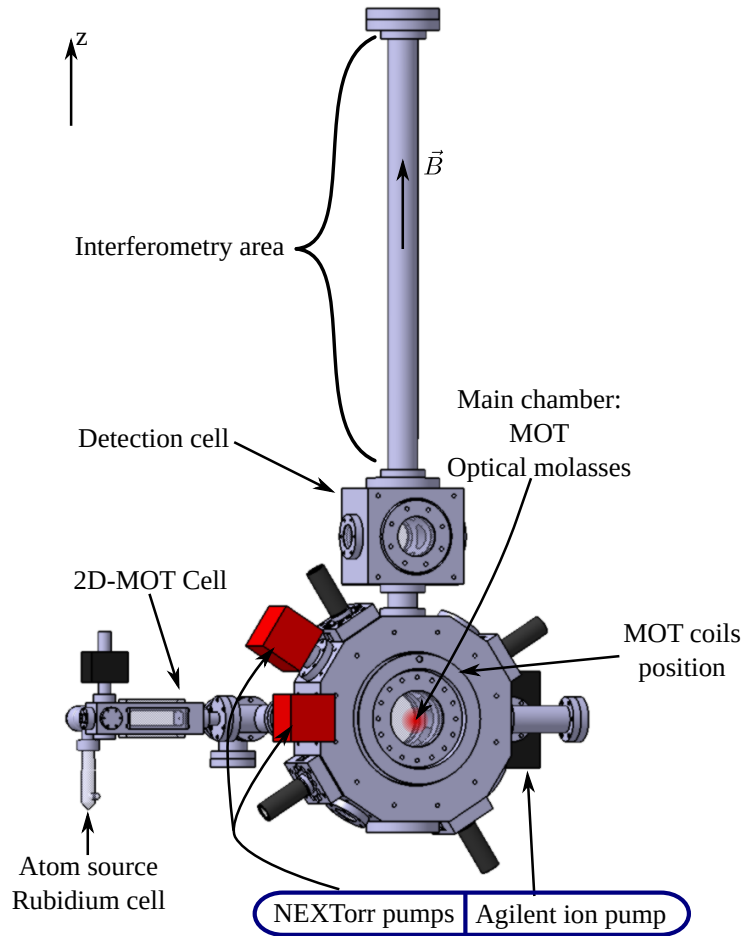


Fig. 7.1 Schematic of the vacuum cell and main experimental part of the atom interferometer. The vertical bias field is generated by a solenoid wrapped around the tube of the interferometry area. It is isolated from the surrounding magnetic field by a magnetic shield, which is not shown in this picture. Extracted from [41]

chamber, a square chamber is used to detect the atoms.

Finally, the vacuum cell is enclosed in an aluminium profile system. In 2023, together with the former PhD student, we built a tiny house around the experiment to protect it from airflow induced by the air conditioning.

7.2 Cold atom production: from molasses to a BEC

To prepare and cool the atoms, we use analog lasers as in Part I. Here I will only present the optical setup. At the output of the two lasers, let us say the repump laser and the cooling laser, we have about 20 mW of optical power.

The repump laser is divided into 4 parts: about 500 μW is sent to the saturated absorption, 3.5 mW to the auxiliary repump, 1 mW to the optical beat between the cooling and the

repump, and the rest to the tapered amplifier. The auxiliary repump is used when a mechanical shutter cuts off the repump before amplification.

The cooling laser is split into 2. We send 1 mW for the optical beating with the repump laser and the rest to the tapered amplifier.

The frequency lock of the repump is performed using a saturated absorption and a heterodyne detection using an EOM operating at 10 MHz.

The two combined beams are sent to the optical table shown on [Figure 7.2](#). The two beams are amplified by a tapered amplifier. At the output, we get a total of 1.3 W optical power with 300 mW repump and 1 W cooling. The amplified beams are then split as shown [Figure 7.2](#). We use AOMs as fast shutters and optical power controllers. As the extinction of an AOM is not perfect, we use mechanical shutters as beam blockers. For more details see [\[42\]](#).

7.2.1 Magneto optic trap

A vacuum element (2D MOT chamber) connected to a rubidium cell is placed horizontally with respect to the main chamber. The 2D MOT chamber is filled with rubidium, creating a 2D MOT. Atoms are then pushed with a push beam into the main chamber. The 3D-MOT is loaded by an atomic beam produced by a two-dimensional magneto-optical trap (2D-MOT).

After a 6-beam splitter, the 3D MOT laser beams are collimated by a 4-lens system followed by a quarter waveplate to produce circularly polarised beams. This collimator produces a large beam (waist around 5 mm) which increases the trapping efficiency of the MOT. Each beam typically has a power of 20 mW.

The magnetic field is generated by a pair of coils in an anti-Helmholtz configuration, powered by a fast response power supply. The current through the coils is controlled by an analogue signal, allowing switching from MOT to optical molasses.

The MOT loading is followed by an optical molasses phase presented hereafter.

7.2.2 Optical molasses

The conversion from a MOT to an efficient optical molasses sequence is performed by several manipulation steps, as shown [Figure 7.3](#). The MOT loading takes about 800 ms. The trapping laser is then detuned to about -1.9Γ with a magnetic field gradient of about $9 \text{ G}\cdot\text{cm}^{-1}$. For 5 ms, the magnetic field is ramped up to about $15 \text{ G}\cdot\text{cm}^{-1}$ while the laser is detuned to -3.3Γ . This compression phase lasts for 25 ms and maximises the atomic cloud density.

Next, the magnetic field is reduced to zero over 20 ms while the laser is detuned to -6Γ . The molasses phase lasts 20 ms, during which the laser is further detuned to -22Γ over 5 ms. Finally, the laser power is ramped down to 15% of its maximum value over 10 ms before an abrupt shutdown. The total duration of this phase is approximately 80 ms, resulting in an optical molasses phase that is completed in approximately 700 ms.

In the end, we obtain a gas at a temperature of about $4\mu\text{K}$ containing 10^8 atoms with a $1/e$ radius of $600\mu\text{m}$

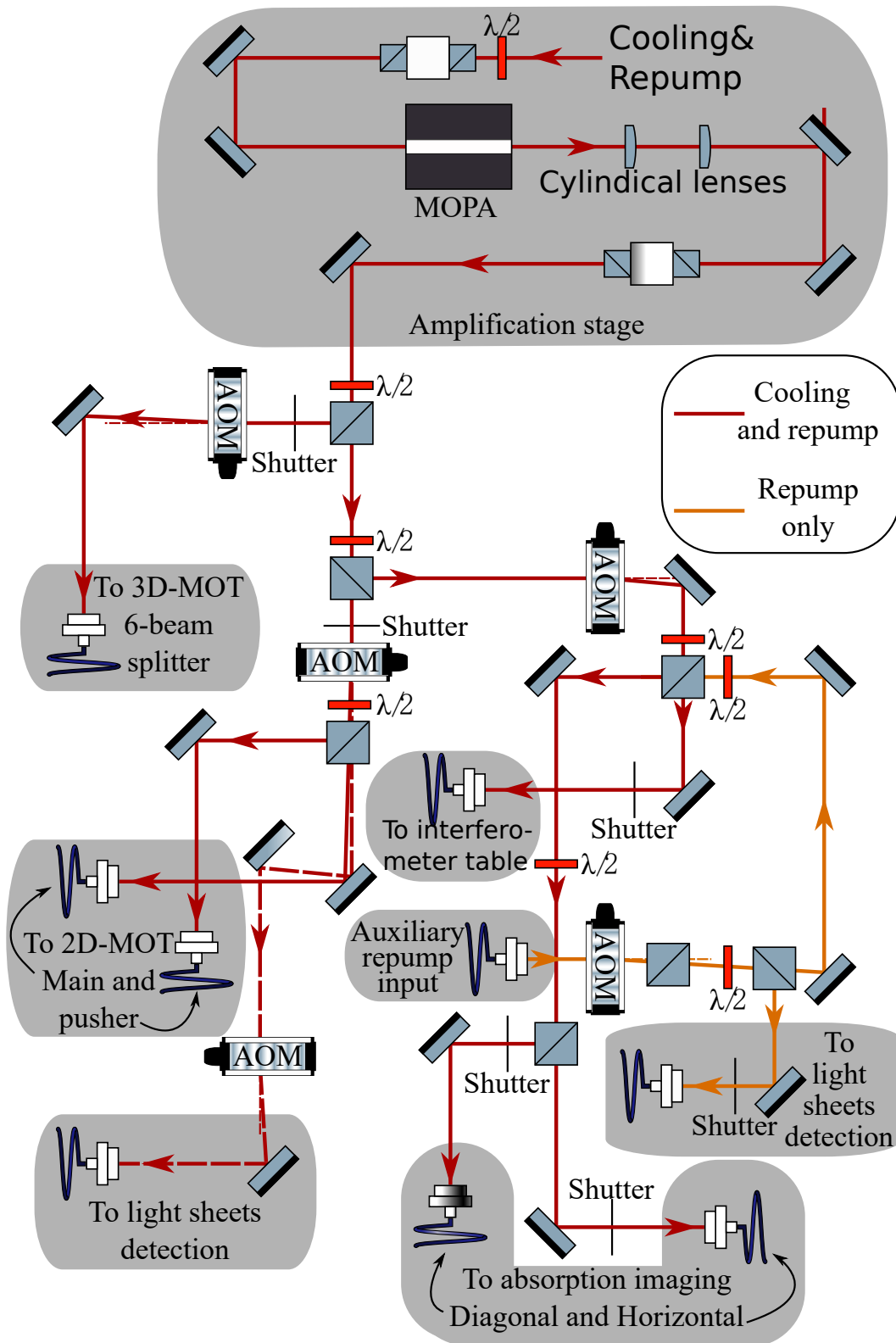


Fig. 7.2 Schematic representation of the MOT tables. This table contains the lasers used for the MOT preparation but also the lasers for the detection and for BEC preparation. Extracted from [41].

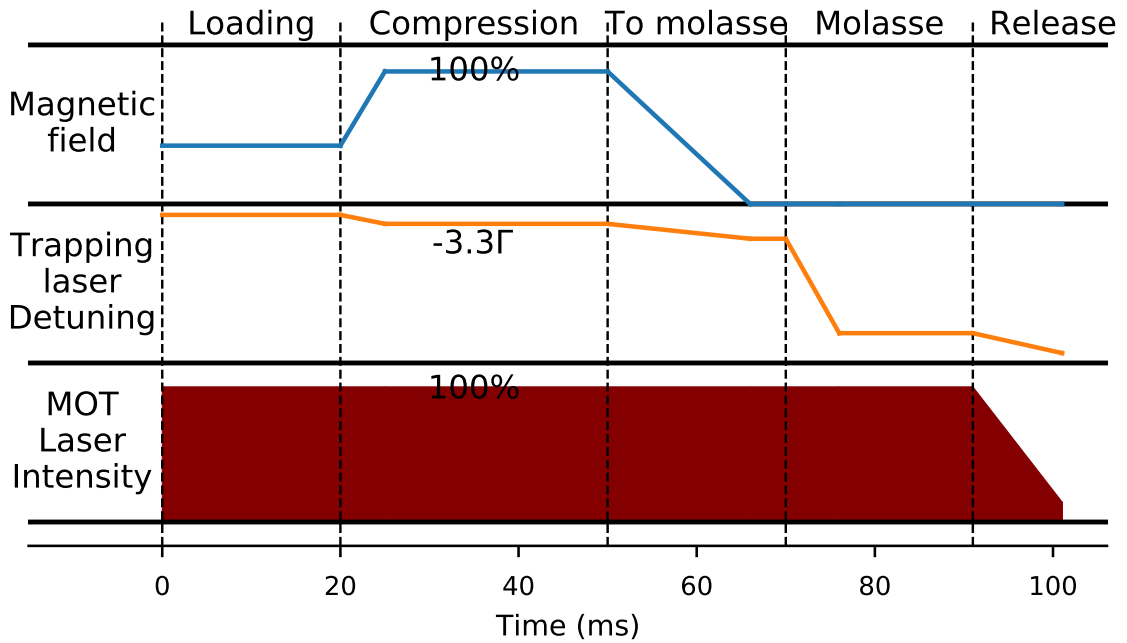


Fig. 7.3 Steps sequence for the optical molasses. Extracted from [41].

7.3 BEC production

To reduce the transverse velocity of the cloud during the interferometry sequence, the group decided to use colder, smaller atomic sources. The process of evaporative cooling in an optical dipole trap and the experimental setup have been extensively discussed in [25]. Here, we will only present the main features.

7.3.1 Evaporation optical setup

The dipole laser operates at a wavelength of 1070 nm and has an optical power of 50 W. After exiting the collimator, the beam has a linear polarization, which is refined using a polarizing beam splitter cube. The beam is then divided into two unequal parts using a half-wave plate and another polarizing beam splitter cube. The larger part is used to create the reservoir beam, while the smaller part is used to create the dimple beam.

The power of the reservoir beam is computer-controlled by adjusting the optical power directed into its first-order beam using an acousto-optic modulator (AOM) (control of the diffraction efficiency of the AOM). The zero-order beam is removed from the optical system with a beam blocker that dissipates its power. The beam is then split into two beams spatially close with equal power. These two beams do not interfere with each other because their polarizations are crossed. The beam pair is then focused onto the atomic cloud using a single lens mounted on a translation stage. Thus, the reservoir beam is composed of two beams with a waist of 100 μm and a maximum power of 12 W.

The dimple beam also passes through an AOM, which controls the power in the -1 order.

The order used is different from that of the reservoir beam to prevent interference between the two beams. Consequently, the two beams are separated by approximately 160 MHz. The dimple beam then passes through a telescope to enlarge its size before being focused on the atoms by a lens mounted on a translation stage. The dimple beam consists of a single beam with a waist of 30 μm and a maximum power of 4 W.

7.3.2 Evaporation sequence

The step sequence for evaporation is shown in [Figure 7.5](#). Starting with molasses in the $|F = 2\rangle$ state, we increase the magnetic field to compress the cloud (compressed MOT phase). The repumping light is mechanically shut down, and the dipole beam is switched on at full power in the reservoir beams without the dimple to avoid high initial density and three-body losses.

The repump amplitude, controlled through auxiliary channels, is shut down at the end of the dipole loading stage, causing atoms to fall into the $|F = 1\rangle$ state and become insensitive to the cooling laser. Without photon diffusion, the cloud becomes colder and denser, termed 'Dark molasses'. The atoms are then trapped by the dipole beams, with negligible spontaneous emissions due to far-red detuning.

We slowly sweep down the power in the reservoir and dimple beams to load atoms into the dimple beam for effective evaporation, as shown in [Figure 7.5](#). In the middle of the evaporation, we switch on the magnetic field to implement spin distillation.

After around 1.7 s of evaporation, we obtain a BEC containing 200,000 atoms at 80nK in a magnetically insensitive state.

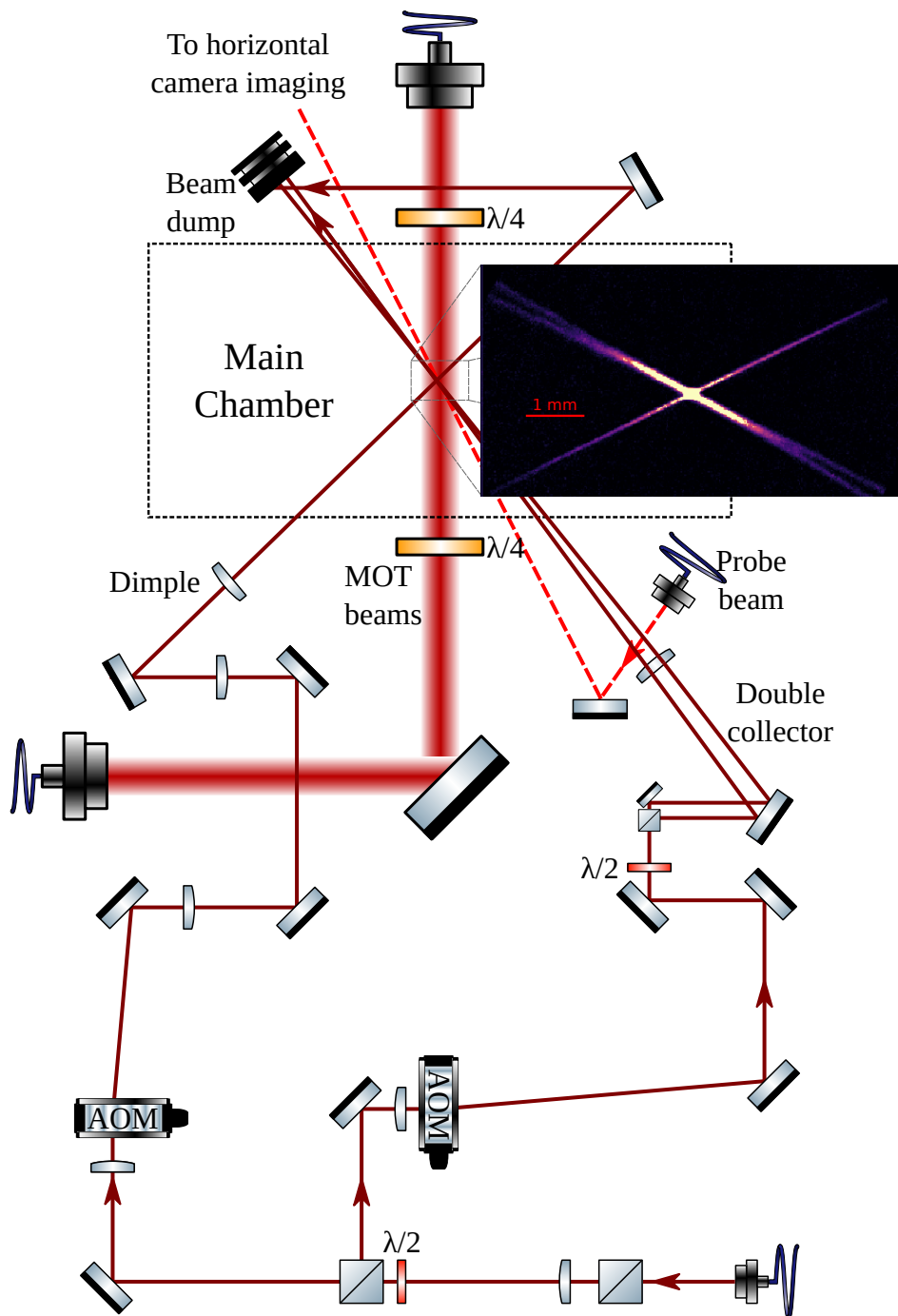


Fig. 7.4 *Evaporation optical setup. Extracted from [41].*

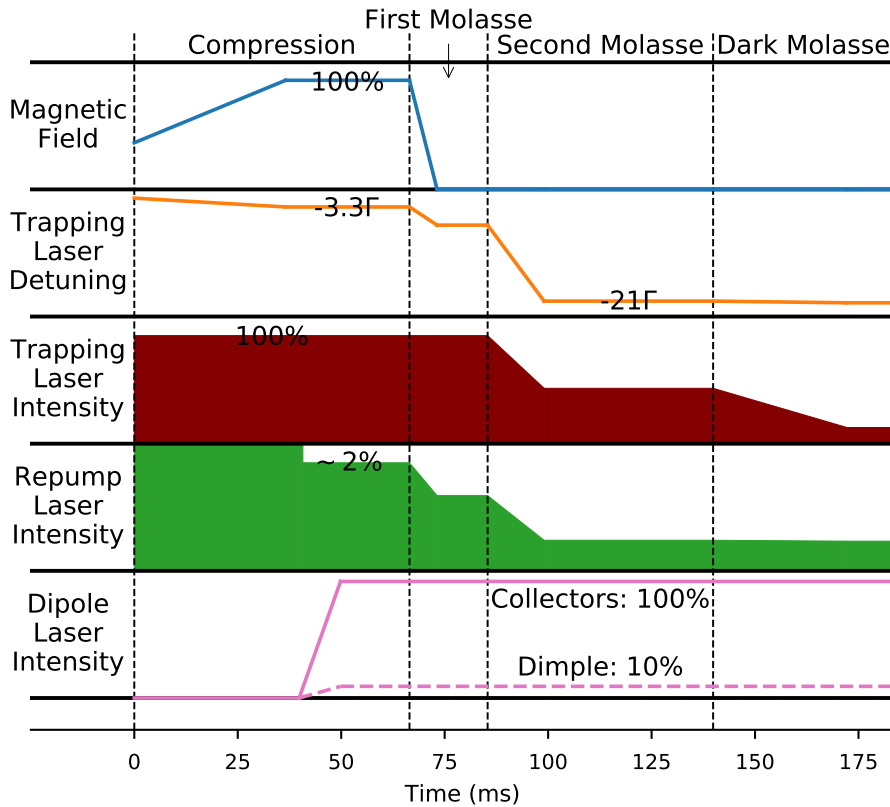


Fig. 7.5 Steps sequence for the efficient loading of the dipole trap. At the end of the sequence, the trapping and repump lasers are abruptly shut off while the dipole laser powers are ramped up for the evaporation sequence. Extracted from [42].

7.4 Raman and Bloch lasers

To manipulate the atoms, we use four different laser beams. The two Raman lasers will split and recombine the atom wave packet. The two Bloch lasers are used to accelerate (or decelerate) the atoms.

7.4.1 Amplifier and SHG generation

To obtain a high-power laser at 780 nm for Raman and Bloch lasers, we use Muquans modules composed of amplifier and doubling module that we seed with narrow bandwidth lasers at 1560 nm. First, the seed laser is sent to the Erbium-Doped Fiber Amplifier (EDFA). Then this amplified laser is sent to a Periodically Poled Lithium Niobate (PPLN) crystal to achieve Second Harmonic Generation, which produces a laser at 780 nm. The whole process is presented on [Figure 7.6](#)

However, under a high pump, the ions of the EDFA also have non-negligible spontaneous emissions probability during the amplification. Although this process is supposed to be random, there are many random photons coupled into the fiber and subsequently amplified. This process will produce a significant background which we call amplified spontaneous

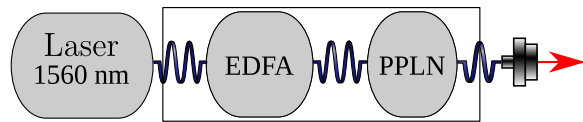


Fig. 7.6 The amplifier double frequency module based on a seed laser at 1560nm

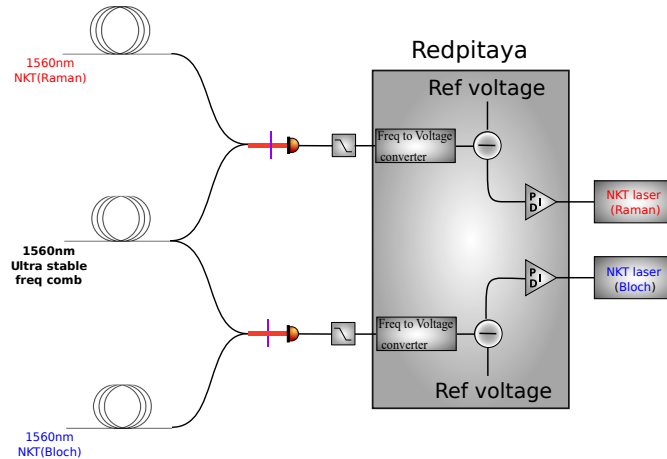


Fig. 7.7 Frequency stabilization system. In purple, we represent optical filter used to select only few teeth of the comb.

emission (ASE) background. By using a heated Rubidium cell, we can filter out the ASE.

In the end, we obtain around 800 mW output power at 780 nm for each Bloch and Raman laser. This power allows us to use a larger beam size to reduce the systematic effects in the experiment.

Absolute frequency lock

The seed lasers at 1560 nm of Raman and Bloch are separated into two parts before the Muquans module. Most of the optical power is sent to the Muquans module, the rest (around 10%) is sent to a phase lock with a 1560 nm frequency comb. The whole system is presented on **Figure 7.7**. The ultra-stable frequency comb with repetition rate locked at 200 MHz is delivered by the group of L. Hilico. The 1560 nm frequency comb laser is split half and half and mixed with the Bloch and Raman laser to obtain a beat note signal. We then remove the DC component and filter using a low-pass filter to retain only frequencies below 98 MHz. This cutoff frequency was chosen because the beat note between a comb tooth and the Raman laser is less than 100 MHz. This signal is then amplified and sent to a RedPitaya to digitally generate an error signal. This error signal is zero when the beat note is at 15 MHz. It is then sent to a PID (proportional, integrative, derivative) controller performing a feedback on the piezoelectric actuator of the NKT to correct frequency drifts.

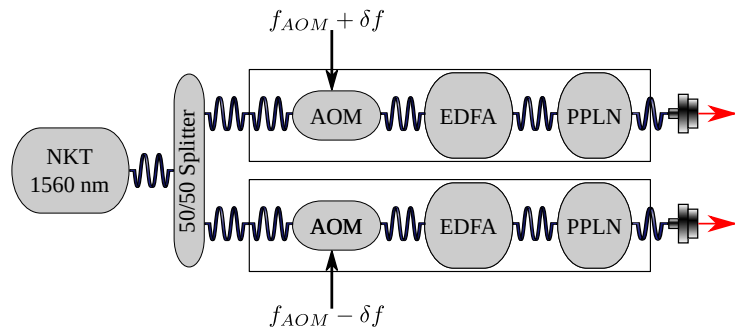


Fig. 7.8 Bloch laser setup.

7.4.2 Bloch Lasers

To generate a stable and moving lattice and implement Bloch oscillations we use the same laser source: another narrow linewidth NKT laser. We require an extensive frequency scanning range to implement more Bloch oscillations in the experiment. Instead of using double-pass AOMs at 780 nm, where power is lost, we perform frequency tuning before the laser is amplified and doubled in frequency, as shown in Figure 7.8. This approach allows for increased power.

With this, we can give up to 1000 photons momenta with an efficiency of around 99.93% per Bloch oscillation

7.4.3 Raman lasers

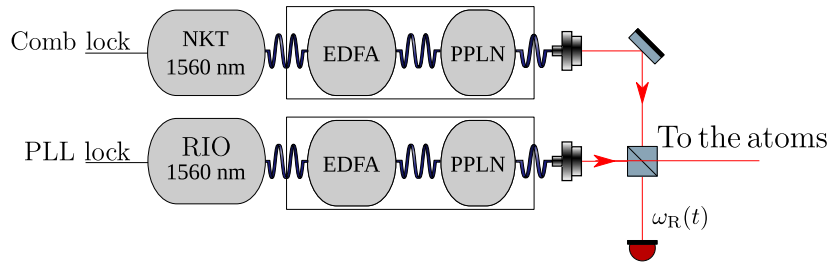


Fig. 7.9 Raman laser setup.

The Raman laser setup is presented on Figure 7.9. The NKT laser is referenced using the comb lock presented there-before. For the second Raman laser, we use a RIO diode. The use of this RIO diode allows us to achieve fast feedback on the frequency. We will implement feedback on this diode using a Phase Lock Loop (PLL). The schematic of the PLL is presented in Figure 7.10.

We combine the beams of Raman 1 and Raman 2 and direct a small portion of their overlap to a fast photodiode to generate a beat note signal at around 6.834 GHz. After amplifying this signal by 35 dB, a portion is used for monitoring, while the main part is mixed with a signal at approximately 6.514 GHz and passed through a low-pass filter,

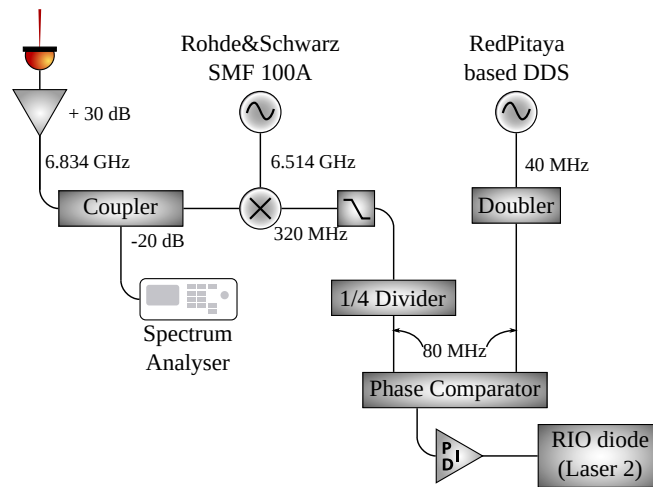


Fig. 7.10 Phase Lock Loop (PLL) used for fast frequency feedback on the RIO diode. Extracted from [41].

resulting in a signal at around 320 MHz. This signal is then divided by 4 and sent to the Phase Comparator device. The synchronization input of the phase comparator receives an output from a RedPitaya operating in direct digital synthesizer (DDS) mode, producing a 40 MHz signal that is frequency-doubled to obtain two 80 MHz signals for phase locking. The phase-locked loop (PLL) is completed with a PID controller to provide feedback to the RIO diode laser, locking its phase to the first Raman laser. The frequency and phase of the Raman laser are precisely controlled by the DDS in the RedPitaya. The RedPitaya is referenced using a synthesizer at 125 MHz, which itself is referenced to the 10 MHz from the SYRTE.

7.4.4 Beam path of the science lasers

The two Raman beams are combined using a polarization beam splitter. A small portion of the combined beam is directed to a photodiode to perform the phase lock loop. The remaining part is sent to the AOM acting as a shutter. Before reaching the AOM, a movable $\lambda/2$ wave plate is placed to allow switching the direction of the Raman beams (Raman 1 from the top and Raman 2 retro-reflected or vice versa). A blow-away beam and a repump beam are overlapped with the Raman lasers using the 0-order "path" of the AOM.

The Bloch lasers are first sent through a Rubidium cell to filter out amplified spontaneous emission (ASE). After this, they pass through acousto-optic modulators (AOMs) acting as shutters. One Bloch laser is directed to the bottom collimator, while the other is coupled into the same fiber as the two Raman lasers, the repump laser, and the blow-away laser. For the Bloch lasers, we employ two fast shutters to prevent any spurious light that could cause a loss of coherence or induce light shifts during the interferometry sequence.

The lasers are then sent onto the experimental chamber as shown on [Figure 7.12](#).

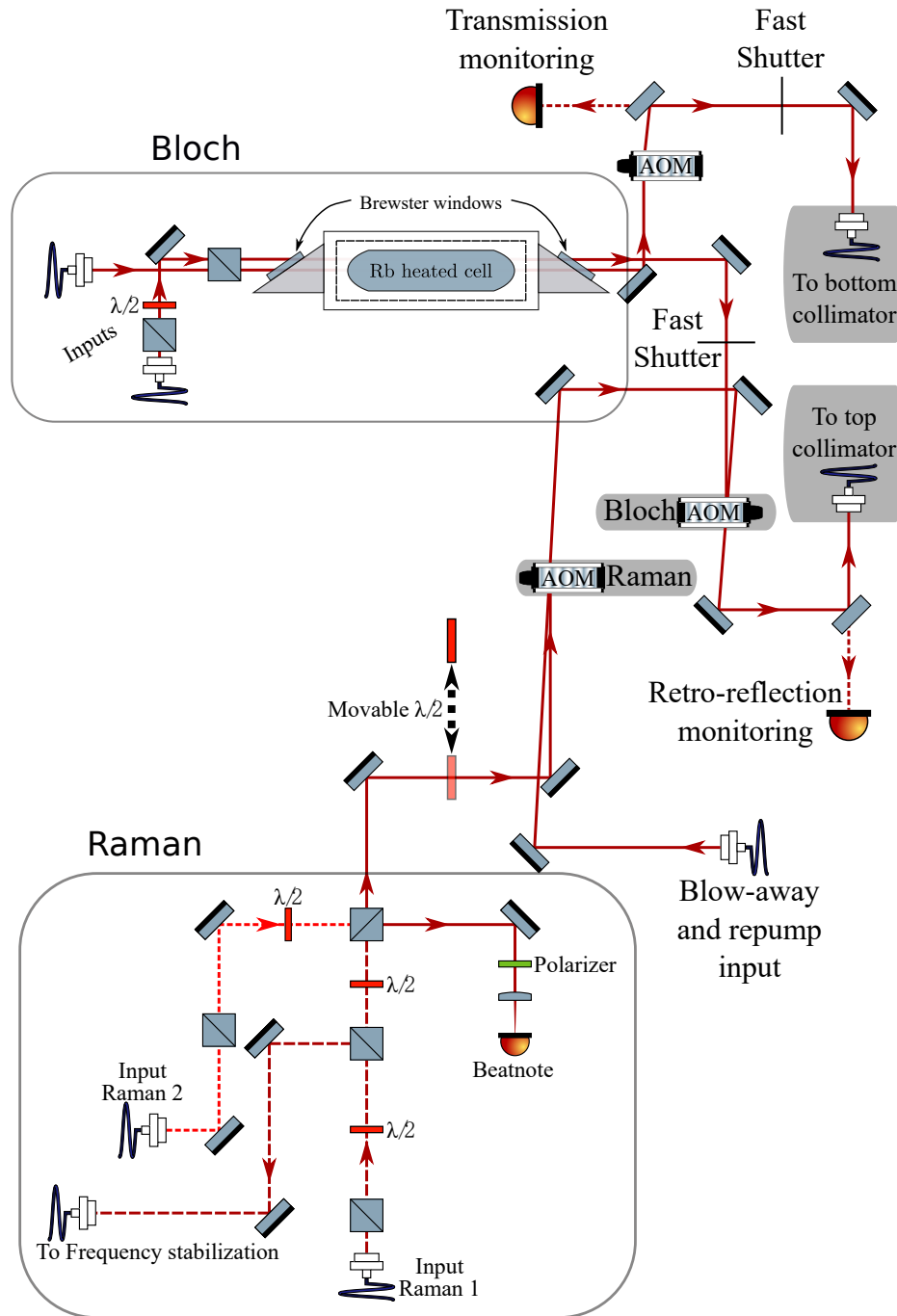


Fig. 7.11 Schematic representation of the interferometry table.

The choice of a vertical configuration for the interferometry lasers is guided by the fact that the atoms are subjected to gravitational acceleration. Any horizontal configuration would be limited by this acceleration. With vertical acceleration, we ensure that gravity does not move the atoms out of the laser beams.

Moreover, because Bloch oscillations are implemented during the interferometer, we should ensure that the Bloch beams induce as little decoherence as possible. Besides the blue detuning that traps the atoms at the minima of intensity within the lattice, we should use a configuration that limits residual lattices, as they would translate to a non-zero mean intensity perceived by the atoms.

Consequently, we use a configuration where each Bloch beam travels only once through the vacuum cell. The downward-going beam is deflected by a PBS at the output of the vacuum cell and sent to the upward-going beam collimator to ensure proper alignment. The beams at the output of the collimators have a Gaussian shape. To approximate a plane wave, we need to use large beams. We use a commercial collimator that produces a beam with a 6.25 mm waist.

For the measurement of the recoil velocity, the beam alignments (counter-propagating condition) need to be controlled within a few μrad . Alignment drifts prevent us from reaching such precision over an extended period. We use PZT transducers on mirror mounts and observe the transmitted (or reflected) power through the input fiber. We set the PZTs at the maximum observed power to ensure the best alignment possible between the different beams. This procedure is run approximately every 45 minutes, so that the alignment is continuously optimized.

During the interferometers, Bloch acceleration is applied on both arms of the interferometer. Because we accelerate both arms of the interferometer, the phase is also imprinted on both arms. As a result, the phase difference between the upper path and lower path is insensitive to this phase. Thus, we do not need phase coherence of the two beams. This is not the case for the Raman beams, as their phase coherence is necessary to run the interferometer.

If the Raman beams were sent through different fibers, each fiber would induce a differential phase shift. This phase shift would not be constant over time, as it would depend on environmental fluctuations such as temperature. In the early stages of the experiments, a compensation for this phase noise was attempted, but it did not achieve sufficient stability.

Therefore, the two Raman beams should be sent to the vacuum cell through the same fiber. For the counter-propagating configuration, we need the beams to be retro-reflected. Due to the selection rules of the Rubidium atom, the polarization of the Raman beams should be orthogonal. Since we use linear polarization, we split the beams with a PBS. Above the retro-reflecting mirror, we place a PBS to reflect only one of the Raman beams. This PBS is also used to send the upward-going Bloch beam and discard the downward-going one, so the polarization of the Bloch beams should be linear and dictated by the PBS.

The retro-reflecting mirror is placed on an anti-vibration table (Minus-K table). This retro-reflecting mirror is considered as the phase reference of the two Raman lasers. Any displacement of this mirror along the z -axis would lead to phase noise directly imprinted on the atoms during the Raman transition. During my thesis, we re-optimized this table and observed a reduction in the phase noise at the output of the interferometer. This, coupled

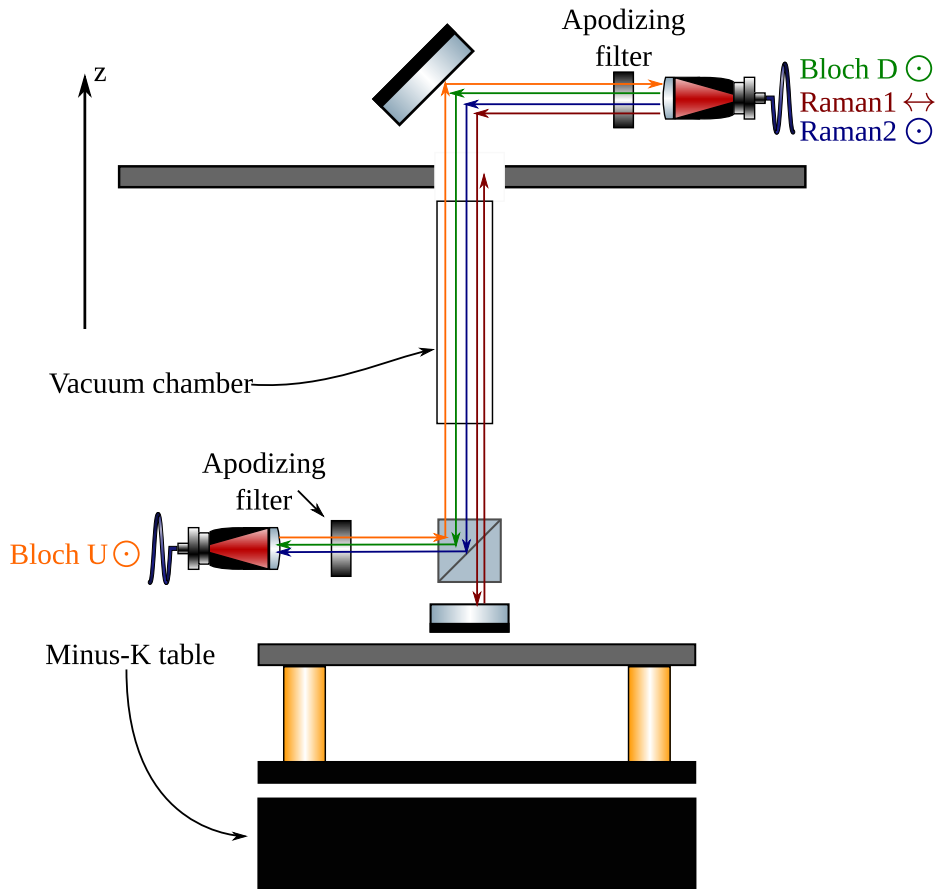


Fig. 7.12 Scheme of the interferometry lasers' path. The two Bloch beams are distinguished by their direction of propagation (Downwards (D) or Upwards (U)). Each interferometry beam is indicated next to its input fiber with its corresponding axis of linear polarization. Extracted from [41].

with a new Raman lock scheme (presented in the next chapter) allowed us to increase the sensitivity of the interferometer by 30%.

7.5 Measurement of h/m

To measure the change in velocity induced by Bloch oscillations we use a Ramsey Bordé atom interferometer consisting of two pairs of $\pi/2$ Raman pulses. The phase difference $\Delta\phi$ at the output of the interferometer depends on the velocity change between the two pairs of $\pi/2$. Bloch oscillations allow us to impart N_B recoil velocities v_r to the atoms (typically $N_B = 500$), but in the experiment, the atoms are also affected by gravity. The expression of

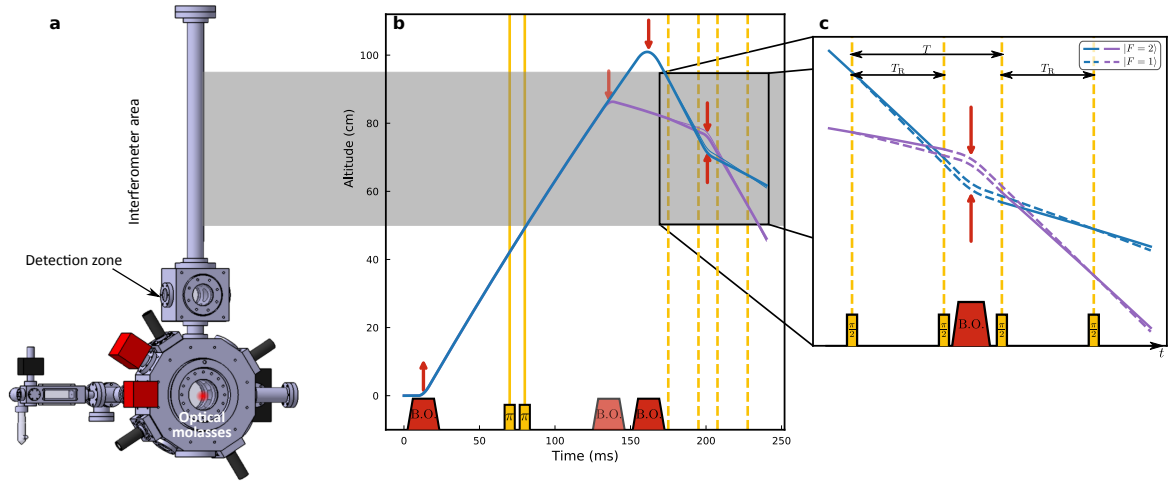


Fig. 7.13 *Experimental setup. a) Design of the vacuum chamber, featuring a 70-cm-long magnetically shielded tube housing the atom interferometer in the upper section. b) Sequence of Bloch oscillations (B.O., red) and Raman pulses (yellow) used to control the atomic trajectories before initiating the atom interferometer. c) Atom interferometer light pulse sequence, with atomic trajectories for upward (blue) and downward (purple) accelerations calculated in advance to mitigate the gravity gradient effect. The separation between the two paths of each interferometer is exaggerated for clarity. Extracted from [42].*

the phase difference $\Delta\phi$ is:

$$\Delta\phi = T_R \left(\epsilon_R k_R \left(\epsilon_B 2N_B k_B \frac{\hbar}{m} - gT_D \right) - \delta\omega \right) + \Phi_{LS} \quad (7.1)$$

where $\delta\omega$ is the frequency detuning shift between the two Ramsey sequences, $\epsilon_R = \pm 1$ describes the direction of the Raman beam, $\epsilon_B = \pm 1$ describes the direction of the acceleration induced by the Bloch lasers, and Φ_{LS} is the phase shift induced by the light shifts of the interferometric pulses. Note that depending on ϵ_R , this phase shift differs as the two Raman beams might not have exactly the same optical power. Thus, we need to determine two phase shifts Φ_{LS} .

This formula differs from [Equation 6.40](#). Indeed, during the derivation, we assumed delta-like pulses. As a result, the AC stark shift induced by the laser during the transition was neglected.

The exchange of direction of the Raman beams (ϵ_R) and Bloch acceleration (ϵ_B) enables four determinations of $\Delta\Phi$. As we have four unknowns, saying g , the two Φ_{LS} and h/m , we are able to determine precisely h/m with minimal systematic effects.

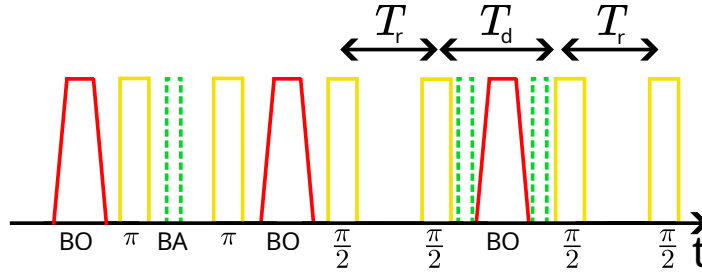


Fig. 7.14 Sequence of Bloch oscillations (B.O), Raman pulses (yellow) and blow away (BA, green) for one h/m . The 5 first pulses are part of the elevator. The atoms are placed in the interferometry area. The Raman pulses coupled with the blow away allow the selection of only the coldest atom of the cloud.

7.5.1 Temporal sequence

Our experiment begins with molasses at a temperature of $4 \mu\text{K}$ or a BEC. To transfer atoms into the interferometer area, we use an atomic elevator that consists of two Bloch oscillation pulses. One pulse accelerates the atoms, and the other decelerates them. By adjusting the parameters of the elevator (number of Bloch oscillations and delay), we can precisely control the position z_0 and velocity v_0 of the cloud inside the interferometer area. The trajectory of the atoms during one measurement of h/m is shown on [Figure 7.13](#).

The pulse sequence used for one measurement is shown in [Figure 7.14](#). Between the two Bloch oscillation pulses of the elevator, we apply a pair of Raman π pulses coupled to a blow-away pulse. A blow-away pulse is made using the cooling laser set at resonance with the $|5s^2S_{1/2}, F=2\rangle \rightarrow |5s^2P_{3/2}, F'=3\rangle$ transition, allowing to blow the atoms in the $|5s^2S_{1/2}, F=2\rangle$ state. With this sequence, atoms are prepared in the magnetically insensitive state $m_F=0$. By controlling the intensity and duration of the first Raman π pulse, we set the width of the vertical velocity distribution of the atomic cloud. These steps are the preparation sequence before the atom interferometer. After the preparation sequence, 500,000 atoms remain in the cloud. The time delay between two $\pi/2$ Raman pulses is T_R and the total duration of the interferometer is T . The entire interferometer sequence occurs in the interferometer area where the magnetic field is well-controlled. After the end of the interferometer, we let the atoms free-fall into the time-of-flight detection region and measure the ratio $N_2/(N_1 + N_2)$. Then, we repeat this sequence multiple times. Each time, we randomly change the $\delta\omega$ between the two Ramsey sequences to obtain the spectras.

7.5.2 Four configurations

As we discussed before, we can cancel gravity and light shifts by inverting the Raman and Bloch direction. Looking at [Equation 7.1](#), we can choose $\epsilon_R = \pm 1$ and $\epsilon_B = \pm 1$. Thus, we have to measure four different spectra by inverting the direction of the Raman lasers and Bloch acceleration. These points, totalling 204 for one determination of h/m , are sampled randomly to avoid systematic effects due to potential drifts during data collection. We use a sinusoidal function to fit the fringes and extract the estimations of frequency $\delta\omega$ at which

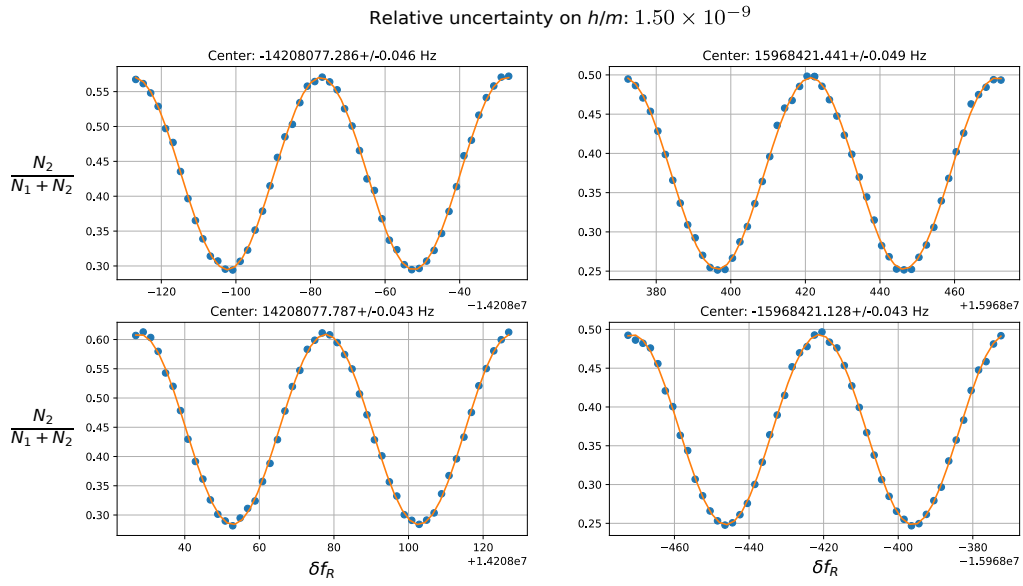


Fig. 7.15 Typical set of four spectra recorded by inverting the directions of the Raman and Bloch beams for $T_R = 20$ ms and $N_B = 500$. Each spectrum displays the variation of the relative atomic population with respect to the parameter δf_R . The lines are least-squares fits used to determine the position of the central fringe displayed at the top of each spectrum.

we are at the center of the fringe. A total acquisition lasts around 5 minutes when using molasses. For a BEC, because the atom preparation is longer, it lasts around 15 minutes. A typical data set obtained during the 2020 measurement is presented on [Figure 7.15](#).

Chapter 8

Phase shift in Raman phase lock loop

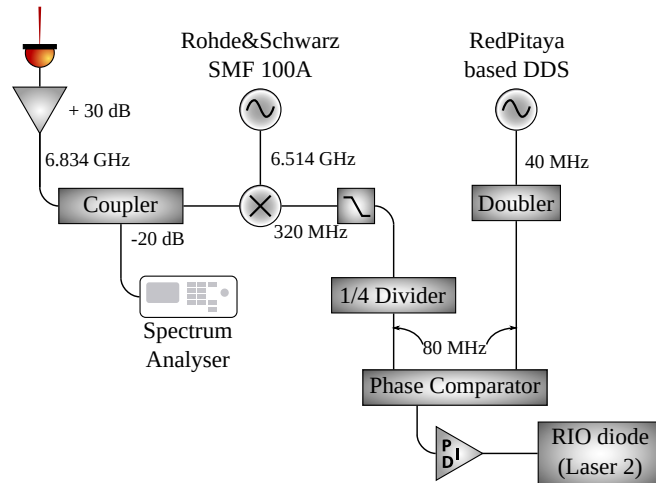


Fig. 8.1 Raman Phase Lock Loop (PLL) frequency chain. Extracted from [41]

During the 2020 measurement, the group found that the Raman phase-lock loop induced a phase shift on the Raman phase during the interferometry sequence and thus caused a systematic effect on the value of h/m . The setup used to control the frequency difference $\omega_R(t)$ between the two Raman lasers is presented in Figure 8.1. It is based on a phase-lock loop (PLL) that controls precisely the phase of the beat note signal between the two lasers. To compensate for the Doppler shift induced by gravity, we implement a frequency ramp of rate $\beta \approx \pm 25 \text{ MHz s}^{-1}$ during the Ramsey sequences of the interferometer, where the sign of the ramp is dictated by the direction of Raman beams, ϵ_R . Any delay δt in the PLL system induces a shift $\beta \delta t$ in the frequency seen by atoms. A constant delay cancels over the interferometer sequence. However, because the frequency shift between the two Ramsey sequences depends on the direction of Bloch acceleration, this delay varies between related spectra and a phase error appears. An independent measurement of the beat note signal was performed to measure this phase shift. The correction on α is highlighted in green on Figure 6.3. In this Chapter, we will present how we tried to reduce this effect.

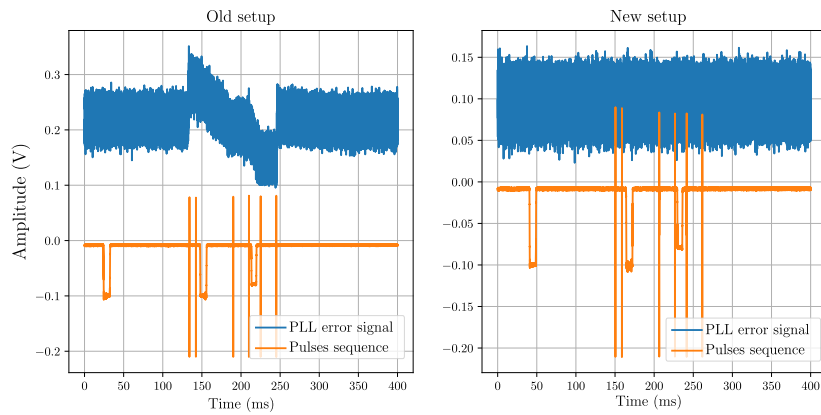


Fig. 8.2 In blue, the error signal sent by the PID to correct the current of the photodiode; in orange, the signal from a photodiode observing the light pulse in the interferometer's time sequence. Data was collected using an oscilloscope.

8.1 AOM set-up

Our initial proposal was to integrate two AOMs into the Raman configuration to execute the frequency chirps required to correct for the Doppler shift caused by the free-fall and the velocity boost transmitted via Bloch oscillation. In fact, the system implemented is analogue to the Bloch lasers one. The AOMs are implemented at $1.5 \mu\text{m}$ before the frequency doubling. The key principle of using an AOM to perform the frequency chirp for the Raman lasers is that it causes the phase-lock loop to not "work" meaning that the error signal is always around zero. The PLL will only compensate for the noises. The implementation of this setup is shown on [Figure 8.4](#) Top left

Each AOM's frequency, with a central frequency of around 80 MHz, is driven by a RedPitaya. Because the output frequency of the RedPitaya is limited to 50 MHz, the signal is mixed with a constant frequency to shift the output frequency to the 80 MHz range. On [Figure 8.2](#), we show the error signal of the PLL during an interferometric sequence. The orange curve shows the interferometric pulses acquired thanks to a photodiode. The data were acquired using an oscilloscope.

On the left, we plot the response of the PLL when the PLL performs the frequency chirps. On the right, when we use the new setup. When the frequency chirp is performed with the AOM, we observe that the PID response is flat without any chirp, confirming that the setup works.

We performed h/m measurements, shown on [Figure 8.3](#), while alternating between the old and new setup (without and with the AOMs). The measurement shows no discrepancy up to 2×10^{-10} on h/m . In 2020, the group measured a systematic effect of $(-8.2 \pm 0.12) \times 10^{-10}$ to h/m . The system appears ineffective at canceling the phase shift in the Raman phase lock loop.

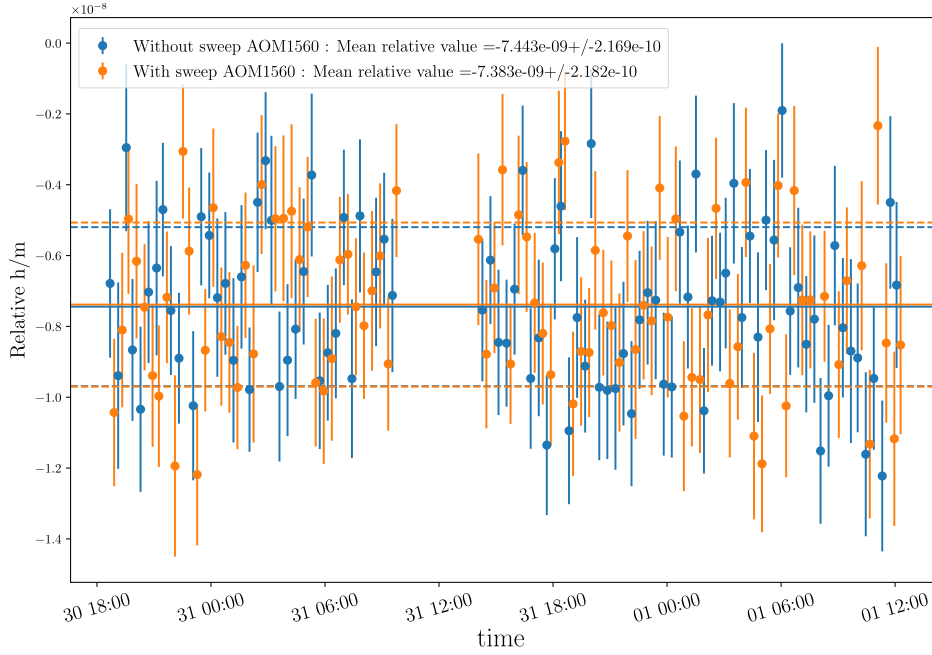


Fig. 8.3 h/m measurement. We alternate between the setup where the chirp is performed through the PLL in blue and in orange when the AOM are used. We stopped the experiment for around 4 hours explaining the gap in the dataset

Independent phase measurement of the beat note signal

To further investigate the impact of the AOM in the frequency chain, an independent measurement was conducted. This measurement was performed as shown on Figure 8.4. The beat note signal of the two Raman lasers (at 6.8 GHz) is mixed with a microwave synthesizer to lower its frequency up to tens MHz. We then record this signal on a 1 GHz bandwidth oscilloscope. The signal is then demodulated numerically with the signal computed to chirp the Raman frequencies. The time base of the oscilloscope is obtained by recording the 10 MHz reference frequency distributed by the Syrte.

The analysis is divided into two parts detailed below

Time scale calibration:

- The 10-MHz reference signal is sent to one channel of the oscilloscope, described by $S = A \cos(\omega_r t_r + \phi_0)$, where $t_r = j dt_r$ with j and index and dt_r the sample rate that we want to measure.
- To retrieve t_r , we mix S with a digital signal of the same frequency ω_r and time $t_d = j dt_d$ with j being the index and dt_d the known digital time step, which is the acquisition time divided by the number of points.

$$s_1 = S \times \cos(\omega_r t_d) = \frac{A}{2} [\cos(\omega_r(t_r + t_d) + \phi_0) + \cos(\omega_r(t_r - t_d) + \phi_0)]$$

$$s_2 = S \times \sin(\omega_r t_d) = \frac{A}{2} [\sin(\omega_r(t_r + t_d) + \phi_0) + \sin(\omega_r(-t_r + t_d) - \phi_0)]$$

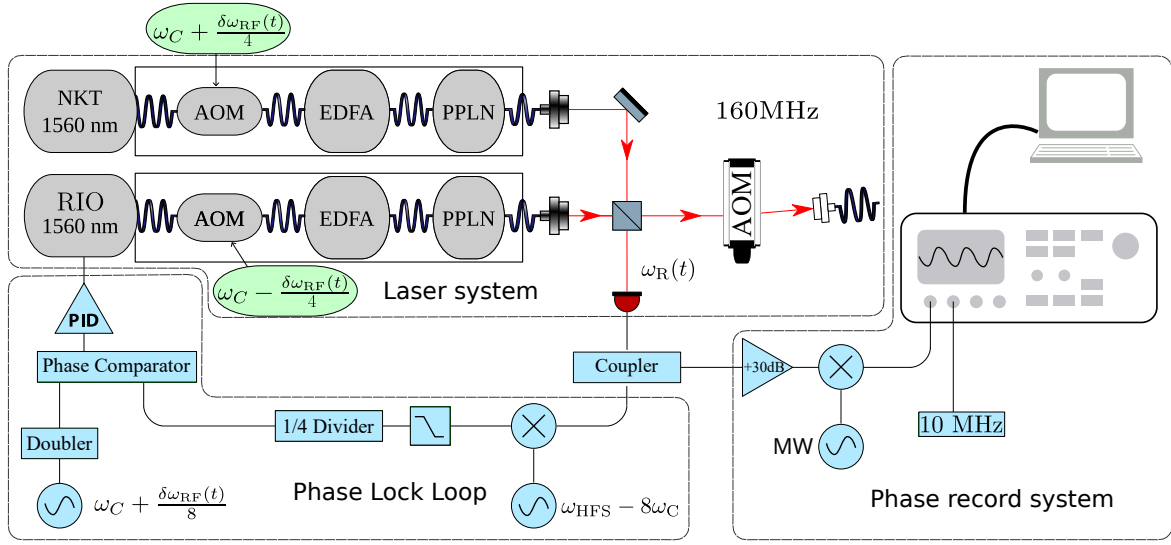


Fig. 8.4 Top left: laser arrangement used to extract a beat note between the two lasers. Bottom left: radio-frequency chain for the phase lock. Right: setup used for the measurement of the phase between the two lasers.

$$= \frac{A}{2} [\sin(\omega_r(t_r + t_d) + \phi_0) - \sin(\omega_r(t_r - t_d) + \phi_0)]$$

We can write $\omega_+ = \omega_r \left(\frac{t_r}{t_d} + 1 \right)$ and $\omega_- = \omega_r \left(\frac{t_r}{t_d} - 1 \right)$. As t_r and t_d are very close, $\frac{t_r}{t_d} \sim 1$ which implies that $\omega_+ \gg \omega_-$.

$$s_1 = \frac{A}{2} [\cos(\omega_+ t_d + \phi_0) + \cos(\omega_- t_d + \phi_0)]$$

$$s_2 = \frac{A}{2} [\sin(\omega_+ t_d + \phi_0) - \sin(\omega_- t_d + \phi_0)]$$

- We then remove the high-frequency components by averaging the signals, resulting in

$$\langle s_1 \rangle = \frac{A}{2} \cos(\omega_- t_d + \phi_0)$$

$$\langle s_2 \rangle = -\frac{A}{2} \sin(\omega_- t_d + \phi_0)$$

Giving

$$\begin{aligned}
 \arctan\left(-\frac{\langle s_2 \rangle}{\langle s_1 \rangle}\right) &= \omega_- t_d + \phi_0 = \omega_r(t_r - t_d) + \phi_0 \\
 &= \omega_r j(dt_r - dt_d) + \phi_0 \\
 &= \omega_r \underbrace{\left(\frac{dt_r}{dt_d} - 1\right)}_{\omega_{data}} j dt_d + \phi_0
 \end{aligned} \tag{8.1}$$

- Now, we measure the pulsation ω_{data} of the reference signal (which is supposed to be equal to 10 MHz if the sample rate of the oscilloscope is perfect) with the least square method. As we have

$$\omega_{data} dt_d = \omega_r j(dt_r - dt_d) \tag{8.2}$$

It all boils down to

$$dt_r = \left(\frac{\omega_{data}}{\omega_r} - 1\right) dt_d \tag{8.3}$$

Note that this time step dt_r is constantly changing along the data acquisition. To compensate for these shifts, we calibrate every time step $j dt_r$ for every index j .

Extraction of the phase Φ_{PLL}

- Now that we have calibrated the oscilloscope's time scale, we acquire the signal obtained by mixing the beating between the two Raman lasers and the microwave detuned from 6.834 GHz by few ten's of MHz noted as S_{BN} .
- Then, we digitally mixed this signal S_{BN} with two signals in quadrature. The frequency of these digital signals is the frequency ramp computed during the interferometry sequence.

$$S_1 = S_{BN} \cdot \cos\left(\omega_i(t - t_i) + \beta \frac{(t - t_i)^2}{2}\right) \tag{8.4}$$

$$S_2 = S_{BN} \cdot \sin\left(\omega_i(t - t_i) + \beta \frac{(t - t_i)^2}{2}\right) \tag{8.5}$$

- As before, we remove the high-frequency part by averaging S_1 and S_2 and use the arctan function to retrieve the phase difference between the computed frequencies and the signal from the Phase Lock Loop
- Finally, we average the computed phase on each Raman pulse of the interferometer and obtain the phase shift imprinted by the lasers

$$\Phi_{PLL} = \Phi_1 - \Phi_2 - \Phi_3 + \Phi_4 \tag{8.6}$$

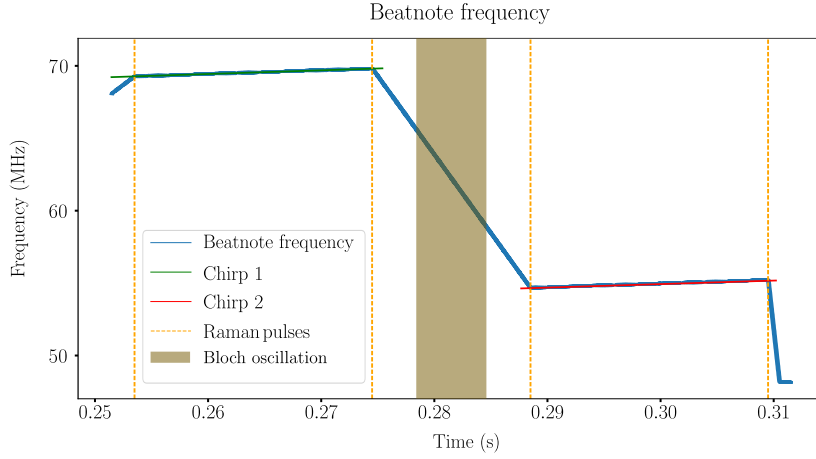


Fig. 8.5 *Beatnote frequency in blue during the interferometry sequence. In green and red we plot the computed frequency sent to the Redpitaya of the PLL or the AOM. The orange dashed line and full line are the Raman and Bloch pulses composing the interferometer*

On **Figure 8.5**, we plot the evolution of the beatnote signal during the interferometer. The orange dashed line depicts the Raman pulses. Finally, we extract the phase error for each spectra ($\epsilon_B = \pm 1$ and $\epsilon_R = \pm 1$).

At the end, we can compute the relative correction to h/m with ([41] eq.6.1.7)

$$\frac{\Delta h/m}{h/m} = -\frac{\sum_{\epsilon_B, \epsilon_R} \epsilon_B \epsilon_R \Delta \phi_{\epsilon_B, \epsilon_R}}{T_R \sum_{\epsilon_B, \epsilon_R} \epsilon_B \epsilon_R \delta \omega_{\epsilon_B, \epsilon_R}} \quad (8.7)$$

where $\Delta \phi_i$ are the phase shift measured for the spectrum i , $\delta \omega$ the frequency difference between the two ramps and T_R the Ramsey time of the interferometer.

Results

For each chirp configuration, meaning when we are using or not the AOM, we performed the independent measurement presented here-before on measurements of h/m . We measure a systematic shift of $\frac{\Delta h/m}{h/m} = -2.38 \pm 0.3 \times 10^{-9}$ and no discrepancy between the two configurations, in agreement with what we measure with the atoms **Figure 8.3**. However, one must highlight that the phase shift measured is nearly 3 times higher than the one measured in 2020.

8.2 Double lock scheme

It appears that using AOM to perform the frequency chirp instead of the PLL was ineffective at reducing the phase shift in the Raman phase lock loop. To reduce this phase shift, we implemented a new lock scheme. It consists of a double-stage lock at both 1.5 μm and 780nm. The idea is to obtain a beat note before the AOM at 1.5 μm to obtain a Phase lock

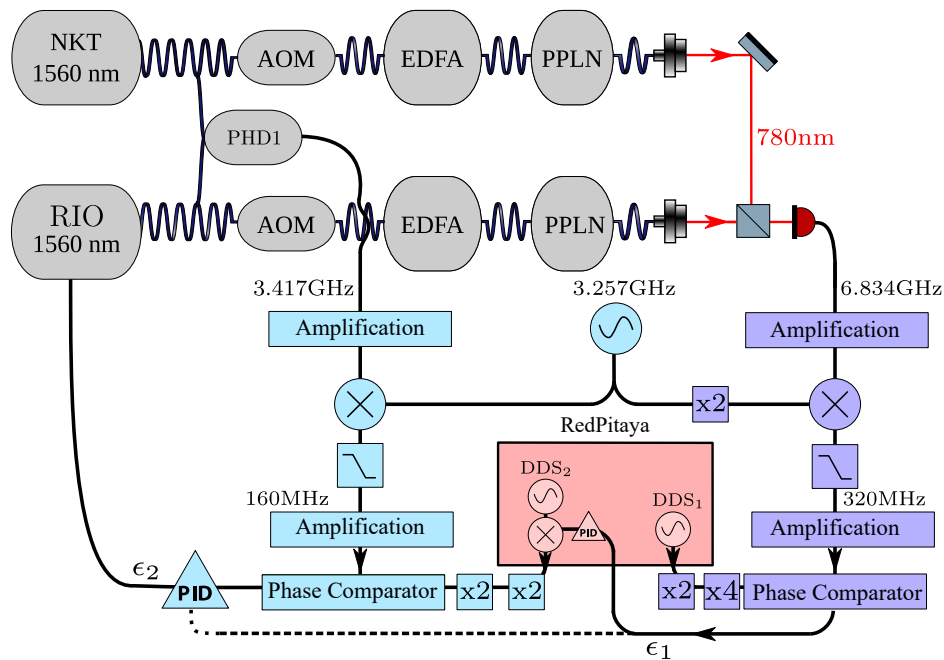


Fig. 8.6 Double electronic feedback schematic for the stabilization of the Raman beams. The feedback system derived from the beat note signal of the 780 nm beams influences the feedback system derived from the beat note signal of the 1560 nm lasers, to regulate the phase noise $\delta\phi$ linked to the propagation in the EDFA fibers. The old lock scheme is represented in purple. The blue boxes depict the added parts. The RedPitaya which generates the two DDS is represented in red. The dashed line is a part of the old lock.

loop at a fixed frequency. The lock at 780 nm is used to compensate for phase noise at low frequency induced by the propagation in the EDFA. This scheme has two advantages. First, it increases the bandwidth of the Raman feedback loop. Indeed, with the simple lock at 780 nm, the bandwidth was limited to 0.4 MHz by the 20 meters of fibers of the EDFA device which limits the retro-action time leading to a lower bandwidth in the feedback. Second, because the beat note is picked before the two AOMs, the PLL will work at a fixed frequency and we hope it will reduce the phase shift induced by the feedback loop. The electronic scheme of the double lock scheme is presented on [Figure 8.6](#).

The first beat note at 1.5 μm is obtained via fiber splitters 90/10. The 10% are sent into a fiber combiner before being connected to a fibered photodiode. On [Figure 8.6](#), the purple boxes represent the old lock scheme. The combination of the blue and purple parts represents the new lock system. The error of the purple phase comparator, ϵ_1 , which is directly proportional to the phase noise induced by the EDFA fibers after the AOM, is fed into the RedPitaya. This signal is added to the DDS_2 signal to compensate for the phase noise. At the end, we obtain the following beat note of the two Raman lasers [Figure 8.7](#).

We see an increase in the feedback loop bandwidth when we use the new setup. The bandwidth is now around 0.7 MHz, an increase by a factor two compared with the old lock scheme. By carefully optimizing the PID parameters in the RedPitaya to minimize the

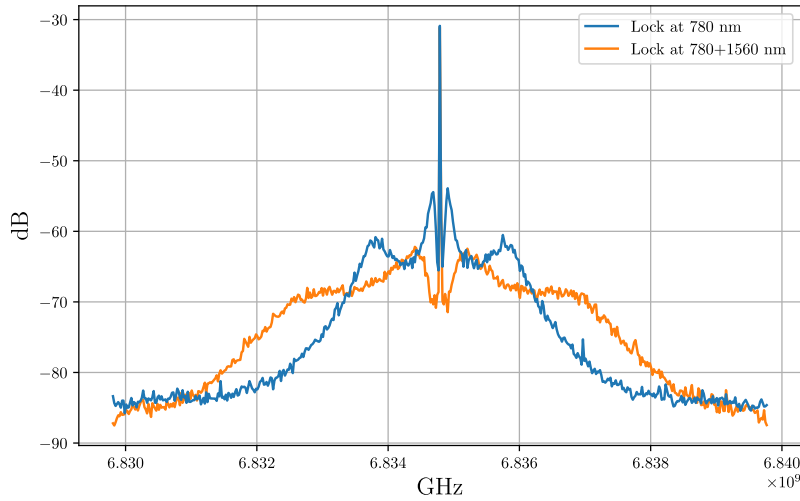


Fig. 8.7 Spectra of the signal observed at the photodiode for the beat signals of the 780 nm beams. The stabilization using the beat signal from the 1560 nm sources allows for a wider bandwidth than the simple stabilization based on the beat signal of the 780 nm beams (spectral resolution of 3 kHz).

low-frequency noise, we obtained the following measurement of h/m shown on [Figure 8.8](#). The relative uncertainty on one measurement of h/m is now of 1.12×10^{-9} in 5 min. During the 2020 measurement campaign, the mean uncertainty was 1.52×10^{-9} with the same acquisition time. With the new lock scheme and careful optimization of each experimental parameter (vibration table, detection...), we managed to decrease by a factor of 30% the statistical uncertainty on h/m shot to shot.

We plot on [Figure 8.9](#), the Allan deviation on $\sigma_{h/m}$ as a function of the integration time τ . These data were obtained in one night of measurement. The orange line correspond to $\sigma_{h/m} = 4.5 \times 10^{-10} / \sqrt{\tau}$. For the previous measurement[42], the coefficient $\beta = 6 \times 10^{-10}$, confirming that we reduce the uncertainty by a factor of 30%.

To verify the effectiveness of the double lock scheme in reducing the phase shift in the Raman phase lock loop, we measured h/m with the new (double lock scheme) and old (only 780 locks) apparatus. The result is shown on [Figure 8.10](#). The two sets of measurements are acquired one after the other. Indeed, to switch from one configuration to the other, we need to modify the cable connection of the phase lock loop. However, we were careful not to change any other parameters of the experiment between the two data sets. Between the orange and blue points, we observe a discrepancy on $\frac{\Delta h/m}{h/m}$ of $\frac{\Delta h/m}{h/m}_{1560+780} - \frac{\Delta h/m}{h/m}_{780} = 2.92 \pm 0.28 \times 10^{-9}$.

Independent measurement with the scope

To confirm or infirm what we measured with the atoms, we performed the same independent measurement using the scope. We measure a systematic shift of $\frac{\Delta h/m}{h/m}_{1560} = 5.16 \pm 0.34 \times$

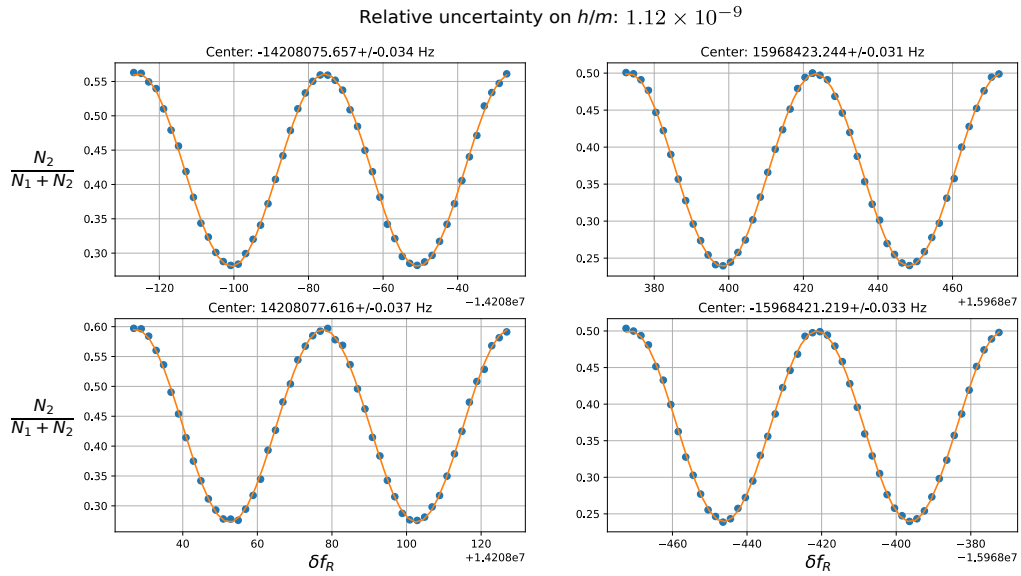


Fig. 8.8 Typical set of four spectra obtained with the new lock scheme recorded by inverting the directions of the Raman and Bloch beams for $T_R = 20$ ms and $N_B = 500$. The relative uncertainty on h/m is 1.12×10^{-9} , a 30% decrease compared with the results obtained with the old lock.

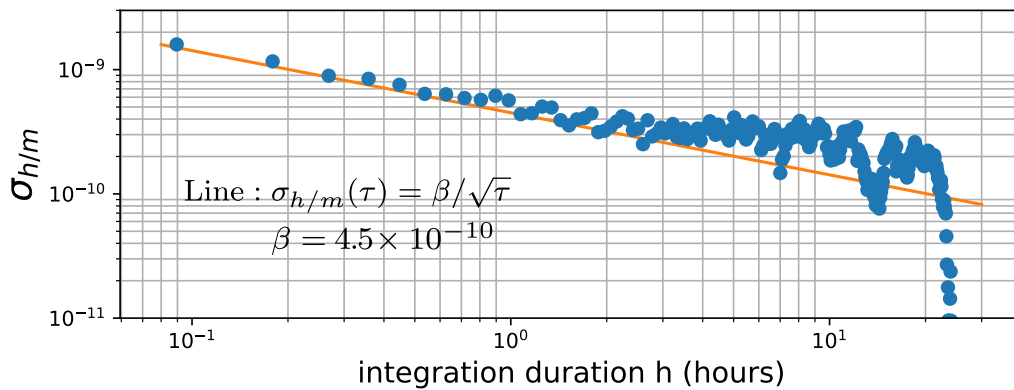


Fig. 8.9 b) Allan deviation $\sigma_{h/m}$ of the measurement of the ratio h/m at maximum sensitivity ($T_R = 20$ ms, $N_B = 500$) as a function of the integration time τ . The line corresponds to $\sigma_{\alpha}(\tau) = \frac{4.5 \times 10^{-10}}{\sqrt{\tau}}$, with τ expressed in hours.

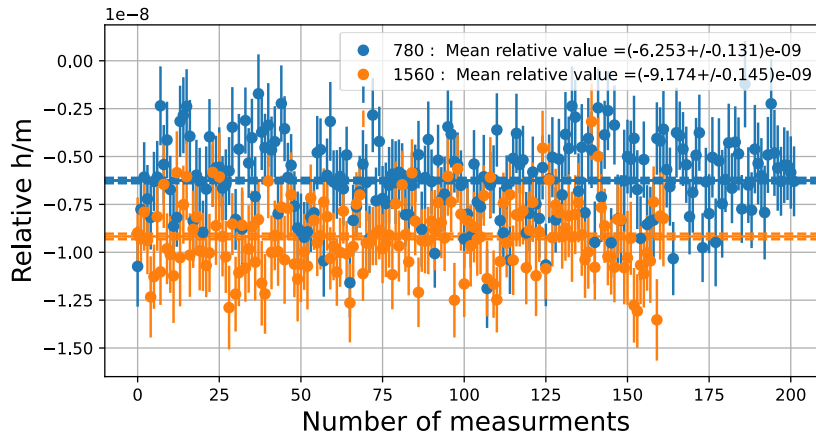


Fig. 8.10 h/m measurement. In blue we plot the results for the old lock. In orange for the new lock system

10^{-9} . Between the two configurations, saying the simple and double lock. The difference is thus of $\frac{\Delta h/m}{h/m}_{1560+780} - \frac{\Delta h/m}{h/m}_{780} = 2.78 \pm 0.65 \times 10^{-9}$. In agreement with what was measured on the atoms.

Conclusion

In this chapter, we addressed the phase shift in the Raman phase-locked loop. Acousto-optic modulators (AOMs) were implemented to perform the frequency chirp. Running the experiment with and without these AOMs, we observed no discrepancy in the measurement of h/m . As this result was unsatisfactory, we implemented a two-stage locking scheme. Measurements with the atoms revealed an increase in the phase shift in the Raman PLL. An independent measurement using an oscilloscope was conducted to analyze the effect of our new setups on the phase shift. This measurement confirmed the observation with atoms. Although we were unable to reduce this systematic effect, we are now able to precisely quantify this phase shift. Further understanding of the causes of this effect is still required. Additionally, we have carefully optimized each of the experimental parameters, and using our new locking scheme, we have been able to reduce the shot-to-shot uncertainty by almost 30%.

Chapter 9

The BEC problem

In 2023, while measuring h/m with a BEC, Corentin Carrez, the previous PhD student on the experiment, observed that the measured value of h/m drifted with time. With him, we found that the value of h/m varies with the initial transverse position of the BEC with respect to the Raman and Bloch beams. The [Figure 9.1](#) shows the evolution of the relative value of h/m during a weekend. In orange, the value does not move with the molasses. In blue, with a BEC, we see that the value drifts. Note that these measurements were made alternatively and randomly.

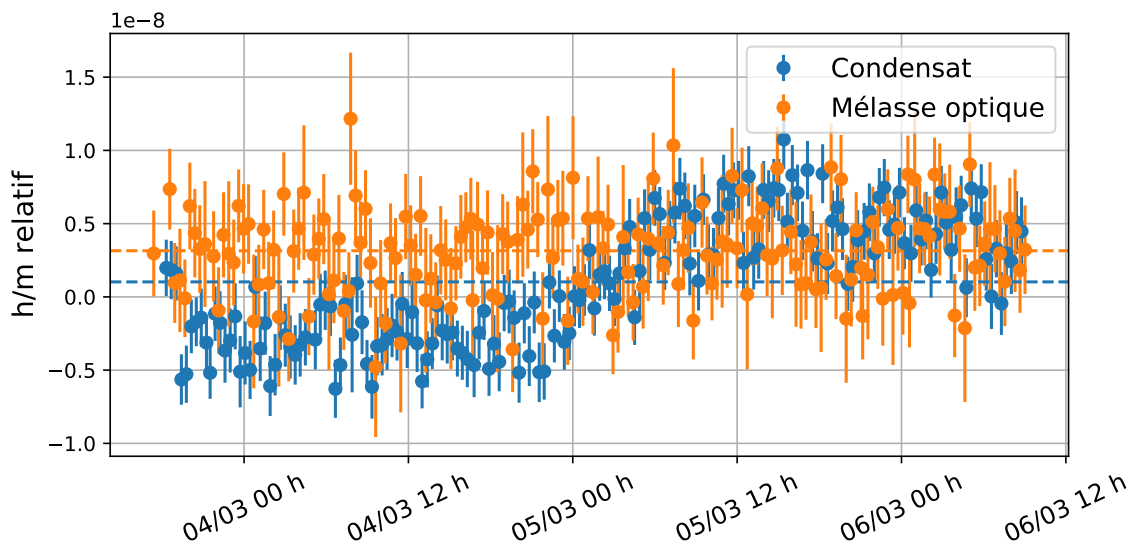


Fig. 9.1 The alternating measurement of the $\frac{h}{m}$ ratio relative to a reference with the condensate and the optical molasses is illustrated. The weighted average of the measurement series is shown as a dashed line. We have $x_{\text{mean}}^{\text{condensate}} = 1.02 \times 10^{-9}$ and $x_{\text{mean}}^{\text{molasses}} = 3.15 \times 10^{-9}$. Extracted from [20]

We hypothesized that this variation was linked to the spatial fluctuations of the beam's intensity profile.

9.1 The BEC to scan the wavefront

The determination of the \hbar/m ratio relies on the exchange of momentum between lasers and atoms. However, calculating the momentum of a photon is not a straightforward task. In the experiment, because the beams are aligned along the z -direction, we will consider only the component along z of the photon momentum:

$$p_z = \hbar k_z = \hbar \frac{\partial \phi}{\partial z}. \quad (9.1)$$

Let us consider a laser beam propagating along the z axis, of which we know the amplitude $A(x, y, z_0)$ and phase $\phi(x, y, z_0)$ in the plane $z = z_0$. Knowledge of these two quantities is enough to calculate the complex amplitude of the beam at each position z using the Helmholtz equation and therefore to calculate k_z . Using the paraxial approximation, we obtain $k_z = k(1 + \delta k_{\text{rel}})$ with

$$\delta k_{\text{rel}} = -\frac{1}{2k_{\text{plan}}} \|\vec{\nabla}_{\perp} \phi(\vec{r})\|^2 + \frac{1}{k_{\text{plan}}} \frac{\Delta_{\perp} I(\vec{r})}{I(\vec{r})} \quad (9.2)$$

where k_{plan} is the transverse wavevector, $\vec{\nabla}_{\perp} \phi(\vec{r})$ is the transverse phases gradient, $I(\vec{r})$ is the intensity of the beam at a given position and δk_{rel} is the correction to the effective wavevector of the beams. However, in the experiment, the following proportionality relations hold, where l_c is a characteristic length:

$$\|\nabla_{\perp} \phi\|^2 \sim \frac{\delta \phi^2}{l_c^2} \quad (9.3)$$

$$\Delta_{\perp} I \sim \frac{\delta I}{l_c^2} \quad (9.4)$$

During propagation, the contribution of spatial amplitude fluctuations dominates over phase fluctuations, with δI being of the first order and $\delta \phi^2$ being of the second order [9]. Therefore, the correction due to phase fluctuations in [Equation 9.2](#) is negligible compared to that due to spatial intensity fluctuations of the beam. The intensity profile of the beams was analyzed using a CCD camera and found that the characteristic length is of the order of $l_c = 100 \mu\text{m}$ with an amplitude of less than 5%.

Now, let us consider a BEC, with a size of $\sim 0.4 \text{ mm}$ during the interferometer and intensity fluctuation with a correlation length of the order of the BEC size. If the BEC moves with time, relatively to the beams, then it will experience different effective wave-vector k_{eff} . This would lead to a variation of the expected value of \hbar/m .

So, now we have two hypotheses: whether it is the BEC that moves or it is the beams. To invalidate the first hypothesis, we look at the central position of the BEC, using absorption imaging and a CCD camera, during a whole night and saw that the initial position of the BEC moves by less than $10 \mu\text{m}$ or that the initial velocity of the BEC changes by less than

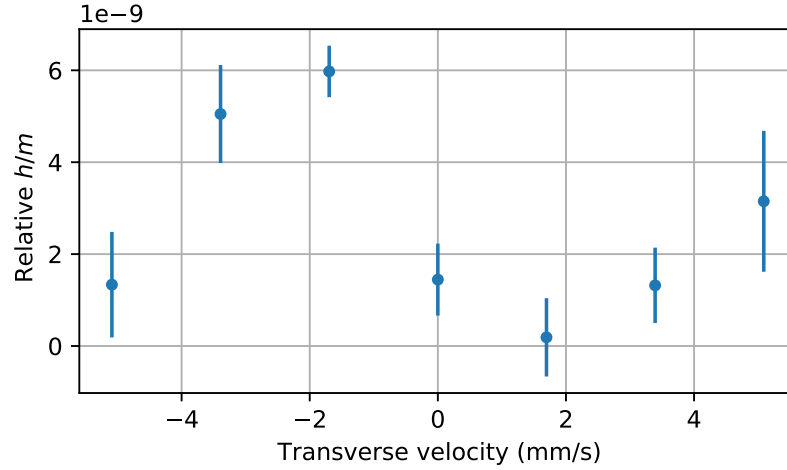


Fig. 9.2 Effect on the $\frac{h}{m}$ measurement of an initial transverse velocity when using a BEC. Each point is an average of 7 measurements

0.1 mm/s. If the first hypothesis was true, then the value of h/m would not vary since the characteristic length of the intensity fluctuation is of 100 μm .

We then decided to measure h/m at different initial transverse positions of the BEC. In the experiment, it is hard to move the relative position of the BEC by hundreds of micrometres. We decide to increase the initial velocity of the BEC. We did so by changing the frequency of the reservoir's AOM at the end of the evaporation (more detail in [20]). We calibrated the transverse velocity given using absorption imaging and got the following curve. The data acquisition lasted only one night. By doing so, we minimize the effect of the temporal drift. **Figure 9.2** shows the evolution of h/m regarding the initial velocity given to the BEC. We observe a systematic effect of the order of 6×10^{-9}

9.1.1 Monte Carlo simulation

To analyze the experimental results, a Monte Carlo simulation was conducted by P. Cladé to understand the effect of wavefront fluctuations on the condensate. The simulation calculates the phase acquired by an atom's wave function with initial transverse position, velocity, phase, and amplitude, considering contributions from Raman transitions, Bloch oscillations, interferometer path, and free evolution, detailed in [41]. The simulation is repeated for N wave packets from the initial cloud distribution for the two interferometer paths. Atoms are initially at (0,0) with Gaussian velocity distributions \vec{v}_x and \vec{v}_y with $\sigma_v = \sqrt{\frac{k_B T}{m}}$ ($\sigma_v \approx 3\text{mm/s}$ for the condensate and $\sigma_v \approx 20\text{mm/s}$ for the molasses). We then convolve the h/m ratio with the velocity distribution and beam fluctuation survival probability and extract the average. The additional transverse velocity is taken along \vec{v}_x . **Figure 9.3** shows these curves for different σ_v values. The effect is more significant for the condensate ($\sim 1 \times 10^{-9}$) than for the molasses ($< 1 \times 10^{-10}$). The observed fluctuation sizes match the experimental measurement in **Figure 9.3**. However, the wavefront fluctuation coherence length was increased to $l_c = 600\mu\text{m}$ to match magnitudes, indicating a discrepancy with

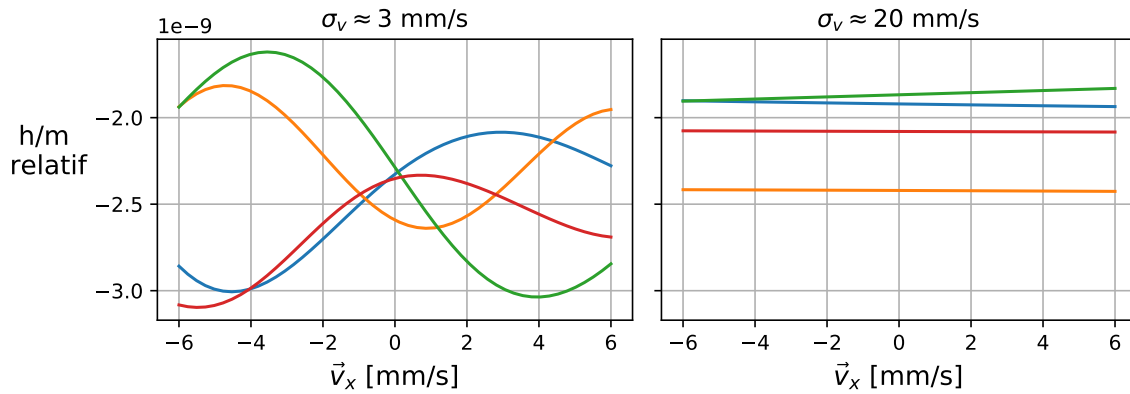


Fig. 9.3 Relative value of the ratio $\frac{h}{m}$ as a function of the final velocity of the atoms, obtained by Monte-Carlo simulation. The fluctuations are due to fluctuations in the beam whose parameters are $l_c = 600\mu\text{m}$ and $\sigma_I = 2\%$.

assumed parameters.

Conclusion

At the current stage of the experiment, it is not possible to determine the value of h/m using a BEC. In our experiment, we found that the intensity profile of the beam was not smooth enough and needed to be improved. However, the BEC could be used to probe the transverse intensity profile of the laser beams.

9.2 New collimators

We built new collimators to improve the intensity profile of the beams. These new collimators are shown on [Figure 9.4](#). First, the beam free propagates for 50 cm with a waist of $500\mu\text{m}$ before a x10 telescope. Then the beam propagate for about 3 metres before reaching the atoms.

The idea of free propagating a small beam instead of a larger one is based on the fact that the smaller beam becomes cleaner faster than a larger beam. Also, the correlation length of the smoothed fluctuation is different.

9.2.1 Propagation of a Noisy Gaussian Beam

To understand how our collimators works, let's consider a Gaussian beam with waist w_0 . Let $a(x, y; z)$ be its amplitude and $\tilde{a}(k_x, k_y; z)$ the Fourier transform of this amplitude at position z . At $z = 0$, we have

$$a(x, y; 0) = \exp\left(-\frac{x^2 + y^2}{w_0^2}\right) \quad (9.5)$$

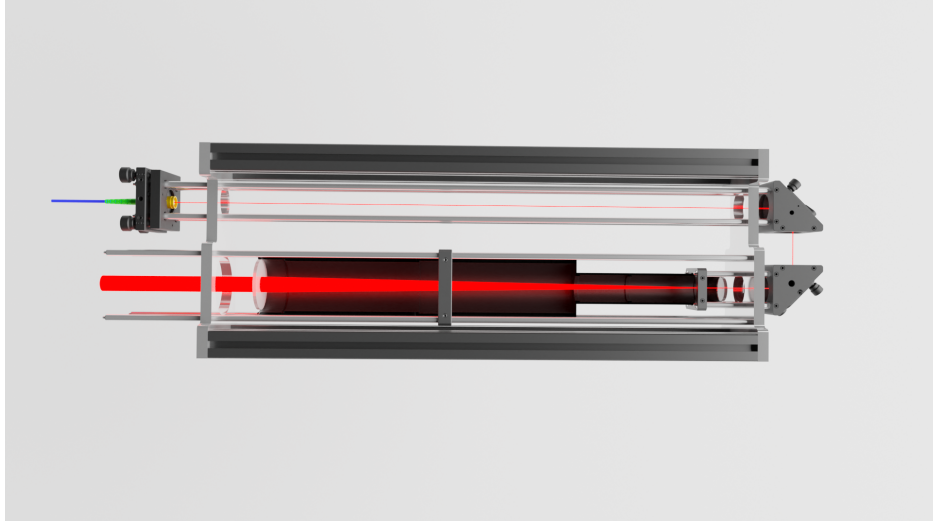


Fig. 9.4 3D scheme of the new collimators. The laser is expanded in the black tube by the two lenses.

and

$$\tilde{a}(k_x, k_y; 0) = \frac{w_0^2}{4\pi} \exp\left(-\frac{w_0^2(k_x^2 + k_y^2)}{4}\right) \quad (9.6)$$

The norm is chosen so that there is no factor when performing the inverse Fourier transform. Suppose there is initially noise $b(x, y)$. This noise is characterized by an amplitude (which we take as 1) and a characteristic correlation length λ_c . More precisely, we assume that the auto-correlation function is given by

$$\Gamma_b(x, y) = \exp\left(-\frac{x^2 + y^2}{2\lambda_c^2}\right) \quad (9.7)$$

The noise density is given by

$$S_b(k_x, k_y) = \frac{\lambda_c^2}{2\pi} \exp\left(-\frac{\lambda_c^2(k_x^2 + k_y^2)}{2}\right) \quad (9.8)$$

The norm is chosen so that $\iint S_b(k_x, k_y) dk_x dk_y = 1$. Let $e(x, y; z)$ denote the amplitude of the noisy signal: $e(x, y; 0) = a(x, y; 0)b(x, y)$. We can then transform into Fourier space:

$$e(k_x, k_y; 0) = \iint \tilde{a}(k_x - \kappa_x, k_y - \kappa_y; 0) \tilde{b}(\kappa_x, \kappa_y) d\kappa_x d\kappa_y \quad (9.9)$$

We let the beam propagate over a distance z in the paraxial approximation:

$$\tilde{e}(k_x, k_y; z) = \tilde{e}(k_x, k_y; 0) \exp\left(-i\frac{k_x^2 + k_y^2}{2k}z\right) \quad (9.10)$$

Thus,

$$e(0, 0; z) = \iint \tilde{a}(k_x - \kappa_x, k_y - \kappa_y; 0) \tilde{b}(\kappa_x, \kappa_y) e^{-i \frac{k_x^2 + k_y^2}{2k} z} dk_x dk_y d\kappa_x d\kappa_y \quad (9.11)$$

The integral over k_x and k_y is a Gaussian integral, and we obtain:

$$e(0, 0; z) = \iint \exp\left(-\frac{zw_0^2}{4} \frac{(\kappa_x^2 + \kappa_y^2)}{z - iz_R}\right) \tilde{b}(\kappa_x, \kappa_y) d\kappa_x d\kappa_y \quad (9.12)$$

where we have introduced $z_R = \frac{kw_0^2}{2}$. We have thus expressed the amplitude of the field as an integral of the noise in k -space. Its fluctuation is then given by

$$\sigma_e^2(z) = \int \left| \exp\left(-\frac{zw_0^2}{4} \frac{(\kappa_x^2 + \kappa_y^2)}{z - iz_R}\right) \right| S_b(\kappa_x, \kappa_y) d\kappa_x d\kappa_y \quad (9.13)$$

which can be calculated from the real part of the exponential argument:

$$\sigma_e^2(z) = \int \exp\left(-\frac{z^2 w_0^2}{2} \frac{\kappa_x^2 + \kappa_y^2}{z^2 + z_R^2}\right) S_b(\kappa_x, \kappa_y) d\kappa_x d\kappa_y \quad (9.14)$$

By substituting S_b from [Equation 9.8](#), we get:

$$\sigma_e^2(z) = \frac{1}{1 + \left(\frac{zw_0}{z_R \lambda_c}\right)^2} = \frac{1}{1 + \left(\frac{2z}{kw_0 \lambda_c}\right)^2} \quad (9.15)$$

This is the intuitive result: a spot of size λ_c will diffract with an angle of $\frac{1}{k\lambda_c}$. We will have an attenuation of the fluctuations when the diffraction spot size is larger than w_0 , i.e., $\frac{z}{k\lambda_c} > w_0$. By propagating a smaller beam, the large size fluctuation (with a size larger than the waist) will be flattened out of the beam. However, this method only works if the intensity fluctuation is linked to the fiber exit and not to the optics. In fact, if the intensity fluctuation is linked to the optics, then the collimator lenses will induce noise, destroying any smoothing of the propagation as a small beam. To confirm the hypothesis of noises linked to the fiber, we analyze the intensity profile at the output of the new collimator

9.2.2 Study of the intensity profile

We tested the performance of the collimators on an optical bench. For the test, we used a CCD camera and a laser diode below the laser threshold to avoid interference from the glass in front of the detector. We examined two different configurations. In the first, the collimator is adjusted so that there is no free propagation of the small beam. This situation is analogous to that of the old collimators. In the second, the beam is expended after 0.5 metres of free propagation and imaged as a large beam after 1.5 metres of free propagation. Typical images are shown on [Figure 9.5](#). It is immediately apparent that the new configuration, where the small beam propagates over a longer distance, allows the laser beam to be smoothed.

To obtain a formal characterization of the laser beams, we computed the standard

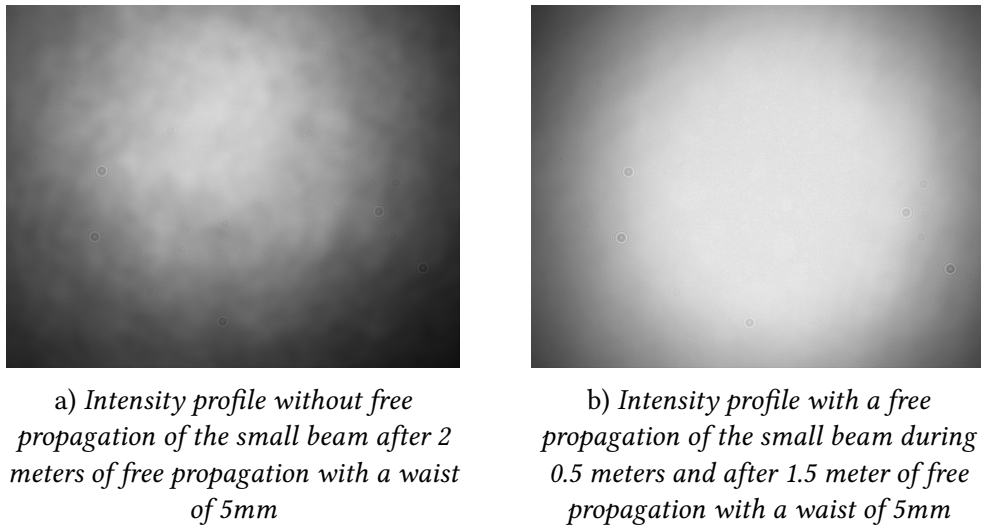


Fig. 9.5 CCD images at the output of the new collimator in two distinct configurations

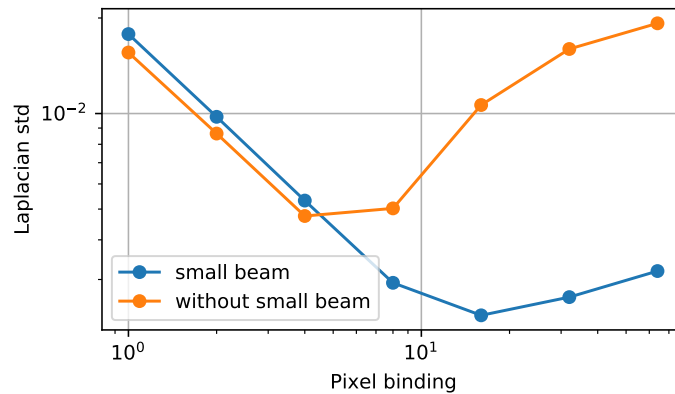


Fig. 9.6 Standard deviation of the laplacian as a function of the pixel binding

deviation of the 2D Laplacian of the intensity as a function of the pixel binding. By calculating the Laplacian, we obtain the intensity variation from pixel to pixel. The results are shown on [Figure 9.6](#). The orange line is obtained for the situation analogue to the old collimators. The blue curve is obtained for free propagation of the 500 μm beam at 50 cm. For small pixel bindings, i.e. at a small distance, there is not much difference between the two setups. However, for pixel bindings above 4 (with a pixel size of $\sim 5 \mu\text{m}$), the new configuration performs better. This means that the intensity fluctuations with a characteristic length above 20 μm have been smoothed out, confirming that the new collimators produce a flatter intensity wavefront. We also found that the intensity fluctuations associated with the shift of h/m with a BEC had a correlation length of around 100 μm . With the new collimator, we had high hopes of reducing this effect.



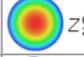
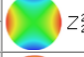

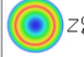
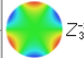
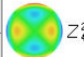

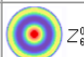
1 #	2 ZERNIKE TERM (often erroneously referred to as coefficient)	3 ZERNIKE ORTHOGONAL CIRCLE POLYNOMIAL	4 RMS ERROR (Zernike coefficient's absolute value)	5 ABERRATION			6 WF Map ^[2] w/ANST sign PEAK VALLEY
				Name	Standard aberration function ^[1]		
					Paraxial focus	Best focus *deviation from zero mean	
0	Z ₀	1	Z ₀	PISTON	-	-	 Z ₀ ⁰
1	Z ₁	ρcosθ	Z ₁ /2	DISTORTION/TILT	ρcosθ	ρcosθ	 Z ₁ ⁻¹
2	Z ₂	ρsinθ	Z ₂ /2		-	-	
3	Z ₃	2ρ ² -1	Z ₃ /√3	DEFOCUS/FIELD CURVATURE	ρ ²	ρ ² ρ ² -0.5*	 Z ₃ ⁰
4	Z ₄	ρ ² cos2θ	Z ₄ /√6	PRIMARY ASTIGMATISM	ρ ² cos ² θ	ρ ² (cos ² θ-0.5) *	 Z ₄ ²
5	Z ₅	ρ ² sin2θ	Z ₅ /√6		-	-	
6	Z ₆	(3ρ ³ -2ρ)cosθ	Z ₆ /√8	PRIMARY COMA	ρ ³ cosθ *	(ρ ³ -2ρ/3)cosθ *	 Z ₆ ⁻¹
7	Z ₇	(3ρ ³ -2ρ)sinθ	Z ₇ /√8		-	-	
8	Z ₈	6ρ ⁴ -6ρ ² +1	Z ₈ /√5	BALANCED PRIMARY SPHERICAL ABERRATION	ρ ⁴	ρ ⁴ -ρ ² ρ ⁴ -ρ ² +1/6 *	 Z ₈ ⁰
9	Z ₉	ρ ³ cos3θ	Z ₉ /√8	ELLIPTICAL COMA (ARROWS, TREFOIL)	ρ ³ cos ³ θ *	ρ ³ cos ³ θ *	 Z ₉ ⁻³
10	Z ₁₀	ρ ³ sin3θ	Z ₁₀ /√8		-	-	
11	Z ₁₁	(4ρ ⁴ -3ρ ²)cos2θ	Z ₁₁ /√10	SECONDARY ASTIGMATISM	ρ ⁴ cos ² θ	(ρ ⁴ -0.75ρ ²)cos ² θ *	 Z ₁₁ ²
12	Z ₁₂	(4ρ ⁴ -3ρ ²)sin2θ	Z ₁₂ /√10		-	-	
13	Z ₁₃	(10ρ ⁵ -12ρ ³ +3ρ)cosθ	Z ₁₃ /√12	SECONDARY COMA	ρ ⁵ cosθ	(ρ ⁵ -1.2ρ ³ +0.3ρ)cosθ *	 Z ₁₃ ⁻¹
14	Z ₁₄	(10ρ ⁵ -12ρ ³ +3ρ)sinθ	Z ₁₄ /√12		-	-	
15	Z ₁₅	20ρ ⁶ -30ρ ⁴ +12ρ ² -1	Z ₁₅ /√7	SECONDARY SPHERICAL ABERRATION	ρ ⁶	ρ ⁶ -1.5ρ ⁴ +0.6ρ ² ρ ⁶ -1.5ρ ⁴ +0.6ρ ² -0.05 *	 Z ₁₅ ⁰

Fig. 9.7 Zernik term and decomposition of the optical aberration. The representation of the wavefront distortion is presented on the far right. The colour map represents the peak-to-valley amplitude.

9.2.3 Simulation of the collimators

An Oslo simulation was performed to study the optical aberration induced by the homemade collimator.

The simulation allows us to obtain the Zernike coefficient of the wavefront. The decomposition into Zernike polynomials allows the extraction of useful information for the analysis of the used wavefront. This involves transforming the wavefront surface into a sum of elementary surfaces, each corresponding to a specific degree and type of optical aberration. The Zernike decomposition is given in Figure 9.7. The Zernike terms of interest in this case are Z₈ and Z₁₅, which are responsible for spherical aberration. Since we are working on the optical axis, other aberrations, such as primary coma, are not taken into account. Also, the Zernike terms Z₀ and Z₃ are not really 'optical aberrations' as they do not lead to wavefront distortion. The Oslo simulation gives the following coefficient for the Zernike polynomial:

considered polynom	Expression of the Zernike polynom	Zernike coefficient
[8]	$6R^4 - 6R^2 + 1$	0.000787
[15]	$20R^6 - 30R^4 + 12R^2 - 1$	-9.2426e-6

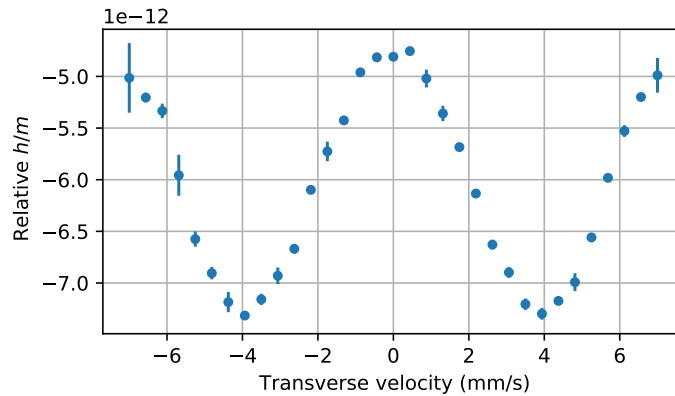


Fig. 9.8 Measured value of h/m with a BEC as a function of the initial transverse velocity with the considered optical aberration induced by the collimators. For a molasses, because this effect averages out, the correction on h/m is on the order of 10^{-15}

9.2.4 Numerical simulation

The next step is to see how these aberrations affect the measurement. A Monte Carlo simulation was performed by a PhD student of the group Rayan Si-ahmed. This simulation calculates the phase acquired by the atoms, taking into account Raman transitions, Bloch oscillations, the path in the interferometer and free evolution. By repeating the process for many wave packets with centred Gaussian initial velocities, the simulation determines the relative value of the h/m ratio for different spectra. The simulation, shown on [Figure 9.8](#), showed a systematic effect up to 5×10^{-12} related to the wavefront distortion induced by the optical aberration when using a BEC.

9.3 Implementation and new measurement with the BEC

These collimators, now fully characterised, were implemented in the experiment. We decided to implement them as shown in [Figure 9.9](#).

This design was chosen to maximise the free propagation of the beam while minimising the number of mirrors. In this configuration, each beam travels a minimum of 3 meters. The beam paths are now tubed to avoid dust on the mirrors and optics. The collimators were carefully aligned and collimated with a waist of 5.003 and 5.000 mm respectively using a shear plate. Alignment to centre the beams on the BEC was performed using a co-propagating Raman transition with a clipped beam to increase the accuracy of the alignment.

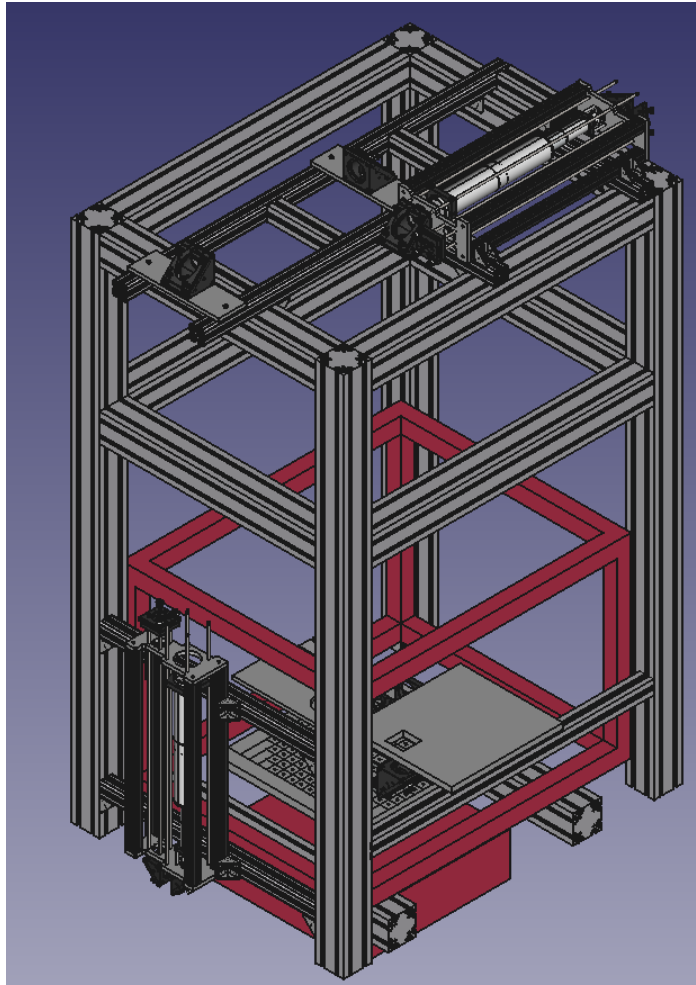


Fig. 9.9 CAD of the implementation of the collimators.

9.3.1 New BEC measurement

We now have clean beams and want to see the effect on the measurement of h/m using a BEC. We prepare a BEC of 200 K atoms at 80 nK. By switching the frequency of the reservoir AOM at the end of the evaporation process, we give a transverse velocity to the BEC. We ran the experiment for 3 days. The results are shown on [Figure 9.10](#)

Each image was taken in about 10 hours. Firstly, we can see that we still have the variation of h/m with the initial position. Secondly, it looks like there is a fringe pattern that moves with time. So it seems that the variation of h/m when using a BEC is not related to the quality of our collimators. To obtain variations in h/m of this order of magnitude, variations in the intensity profile of around 5% would be required (according to simulations carried out in the thesis of C. Carrez [20]). However, the analysis of our collimators with the CCD camera gives us variations of about 0.2% of the intensity when using the homemade collimators. Moreover, the pattern in the variation of h/m leads us to consider parasitic interference fringes. We can estimate the interfringe by calibrating the velocity kick given to the BEC. We found that $i \sim 800\mu m$. In the simulation ran by P. Cladé described above,

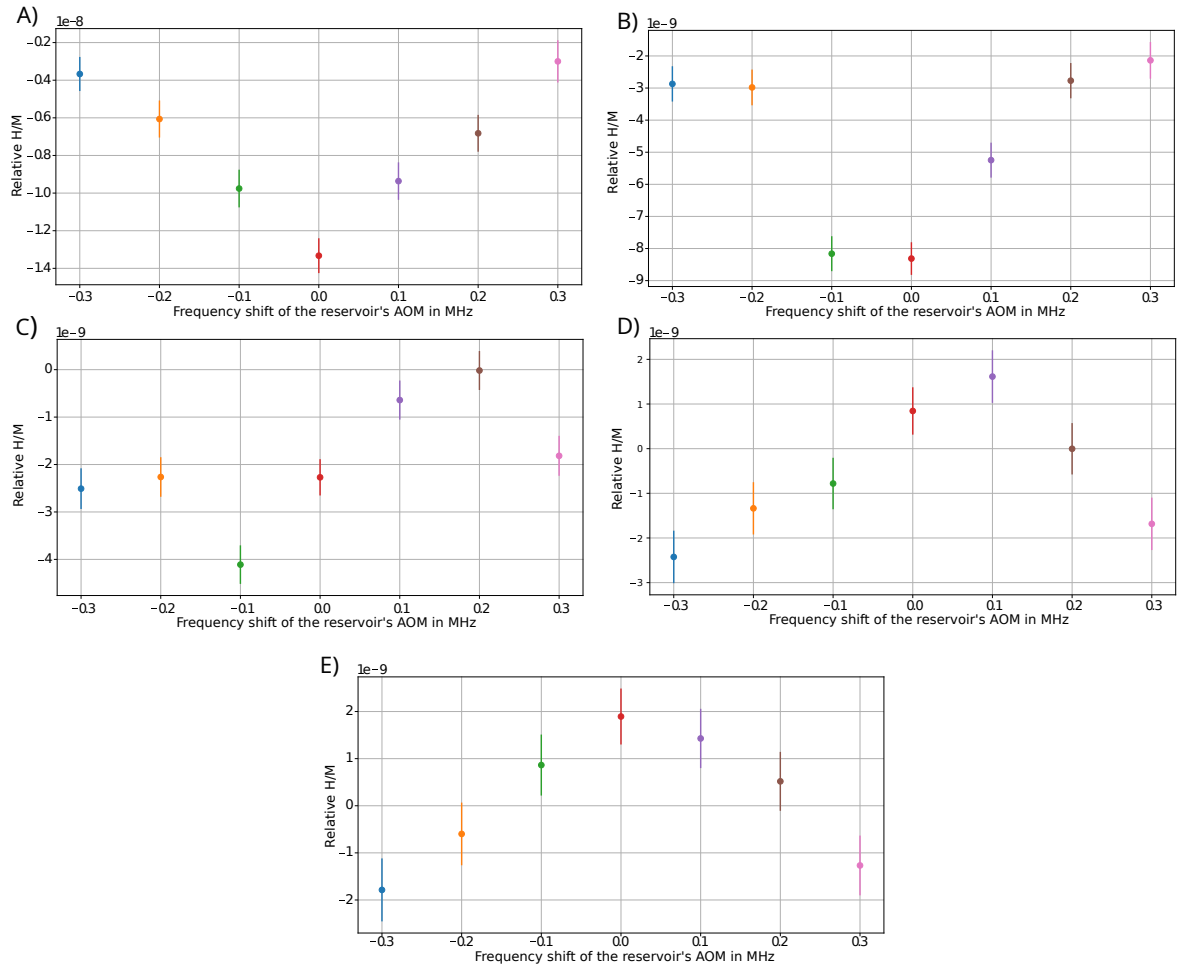


Fig. 9.10 Effect on the $\frac{h}{m}$ measurement of an initial transverse velocity. Each curve is an average of over 10 Hours. The first measurement is shown on A).

the correlation length of the intensity fluctuation was increased to $600 \mu\text{m}$ in order to match the fluctuation pattern. The problem was not the collimators and the noisy intensity profile, but a fringes pattern.

Fringes in the beam can be observed when beams with the same polarisation and "close frequency" travel with different wave vectors. Such a situation can be caused, for example, by parasitic reflections on the vacuum windows. We have therefore studied the different parasitic reflections from the different optics that could produce an interference fringe pattern with the main beam.

9.3.2 Parasitic reflection

After some investigation, we discovered that the main source of parasitic beams comes from the new polarisation beam splitter (PBS) located at the bottom of the vacuum chamber. Note that this PBS is twice the size of the one we used for the 2020 measurement and appears to be of poorer quality.

This PBS recombines the two Bloch beams above the reflecting mirror. Each time one

of the beams passes one of the interfaces of the PBS, a reflection can occur. Because the cube cannot be perfectly perpendicular to the incoming beam, or because each face of the cube is not parallel, part of the beam may be reflected at an angle that causes fringes in the incoming beam.

If one wants to remove the PBS, you have two options. The first option is to send the two Raman beams in two different fibers. However, due to phase noise during propagation in different fibers, our two Raman lasers would acquire a phase difference which would directly affect the phase noise at the output of our interferometer. The second option is to use a single collimator. The lower Bloch laser can be coupled into the same fiber as the two Raman lasers and the upper Bloch laser. However, because the two Bloch lasers have the same polarization, this would create spurious grating, which would lead to atom losses, new systematic effects, and so on.

With this in mind, we did not want to remove the PBS. However, we have changed the PBS for a thin film polarizing beam splitter.

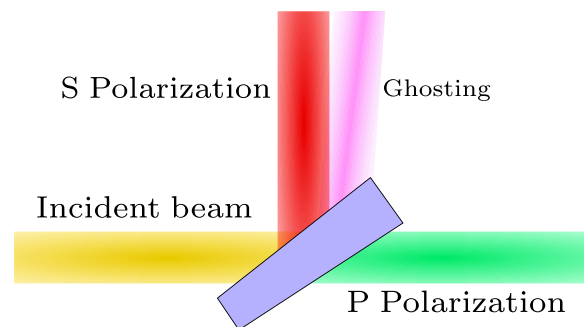


Fig. 9.11 *Thin film polarization optical scheme. The ghosting is a back reflection of the transmitted beam on the second surface.*

On [Figure 9.11](#) we show the working principle of a thin film polarising beamsplitter. The first face of the incident beam is coated with a polarising beamsplitter coating, which reflects only the S-type polarisation (from the German "senkrecht", meaning perpendicular). There is a wedge between the two surfaces, typically 30 arcmin, which explains why the ghost beam is tilted with respect to the red beam. By using this type of polarising beam splitter, we minimise the number of interfaces encountered by the incident beam for both S and P polarisation, and thus the number of potential parasitic reflections.

As I write, we have just received the thin film polarisation beamsplitter. Samuel Gaudout is currently implementing it on the experiment. The first characterization on the experiment looks promising as no spurious reflection has been observed.

Conclusion

This chapter presents the progress towards solving the problem related to the measurement of h/m with a condensate. Initially, we thought that intensity fluctuations caused by the collimator were the source of the drift in the value of h/m when using a condensate. To address this, we implemented and characterized new homemade collimators. These collimators showed improved intensity profiles. However, new measurements of h/m showed the same pattern as when using the old collimators. Additionally, a fringe pattern appeared in our measurements over time. We hypothesized that these fringes in the value of h/m were due to parasitic reflections. We concluded that these reflections originated from the polarization beam splitter. A new type of polarizer is currently being installed in the experiment. At first glance, we do not observe any spurious beams. We hope that future measurements with atoms will corroborate this.

Conclusion

In this part, we present our work on the experimental setup dedicated to the measurement of the ratio h/m . We have investigated two independent systematic effects.

Firstly, we addressed the phase shift in the Raman phase-locked loop. Acousto-optic modulators (AOM) were implemented to perform the frequency chirp. When running the experiment with and without these AOMs, we observed no discrepancy in the measurement of h/m . An independent measurement using an oscilloscope was conducted to analyze the effect of our new setup on the phase shift, revealing no improvement. As this result was unsatisfactory, we implemented a two-stage locking scheme. The Raman lasers are locked at a fixed frequency before frequency doubling, and a second beat note at 780 nm is used to reduce the phase noise due to propagation in the amplifier. Measurements with the atoms and with the scope revealed an increase in the phase shift in the Raman PLL. Although we were unable to reduce this systematic effect, we are now able to precisely quantify this phase shift. Further understanding of the causes of this effect is still required. Additionally, we have carefully optimized each of the experimental parameters, and using our new locking scheme, we have been able to reduce the shot-to-shot uncertainty by almost 30%.

Secondly, we continued our work on utilizing a colder atomic source to measure h/m . In the thesis of C. Carrez [20], it was concluded that local intensity fluctuations affect the measurement and lead to variations in the measured value of h/m . To improve our intensity profile, we built new collimators. The characteristics of these collimators have been extensively studied. The homemade collimators show an improved intensity profile in amplitude by a factor of 10 compared to the previous ones. We carried out simulations to quantify the effect of optical aberrations and concluded that the shift in h/m was only -5×10^{-12} . Using our collimators, we measured h/m with a BEC while varying the initial position in the beam. We observed no improvement over the old collimators. However, we noticed a fringe pattern and concluded that parasitic reflections could lead to intensity fringes in the main beam. A new polarization beam splitter has now been implemented and is currently being characterized. We hope that this new device will allow (h/m) to be measured with the BEC without any variation associated with the intensity profile.

General conclusion

In this thesis, we have implemented the first atomic beam splitter based on a stimulated Raman transition using a frequency comb. I used this beam splitter to realise an atomic gravimeter with a relative sensitivity of 10^{-7} . In particular, I have developed a system for controlling a delay line length, which enables two picosecond pulses to be superimposed on the atomic cloud so that both pulses follow the cloud for 60 ms. As Raman diffraction is localised in the pace where the two laser pulses overlap, I studied a configuration based on a $\pi/2 - \pi - \pi - \pi/2$ sequence where it is possible to talk to each arm of the interferometer, which is not feasible using a CW laser. I also carried out a detailed theoretical study to understand Raman transitions stimulated using a pulsed laser and performed numerical simulations that agreed with the experimental results.

The second part of my thesis was focused on investigating and mitigating the two systematic effects that limited the accuracy of the previous measurement of the ratio h/m carried by the team in 2020: the phase shift observed in the phase-lock loop of the Raman lasers and the effect due to distortions of the laser beams. I first perform measurements with BEC. This study shows that measurements with BEC are sensitive to local fluctuations of laser intensity. These fluctuations average when using optical molasses. This means that by measuring with BEC at different transverse positions one can probe the transverse profile of the laser beam inside the vacuum chamber.

Because of spurious reflections induced by the new polarization splitter cube (PBS), I was unable to evaluate the benefits of the two collimators I built and characterized in detail. The team has recently set up a new type of polarization splitter and studies are in progress.

Secondly, we investigated the phase shifts in the Raman phase-locked loop. We implemented two setups, the first using AOMs to chirp the frequencies and the second using a double lock scheme. However, both setups appeared to be ineffective in cancelling this effect, and the double lock scheme actually increased the phase shift. An independent measurement with a scope confirmed our measurements with atoms. Although we were unable to cancel out the phase shift, we were able to fully characterise the effect and further investigations are planned. Furthermore, with the double-lock scheme and careful optimisation of each experimental parameter, I reduced the shot-to-shot uncertainty by almost 30%.

All the necessary components are now in place, and we hope to make a new measurement of α soon, using several atomic sources (from molasses to condensates) with different transverse velocity distributions. We expect that this study will lead to a better understanding of the systematic effects associated with the wavefront.

Appendices

Appendix A

Effective Hamiltonian, Raman Transition with a Picosecond Laser

Three-Level System

We consider a three-level system denoted as $|1\rangle$, $|2\rangle$, and $|3\rangle$. In [chapter 2](#), these states correspond to $|1\rangle = |g\rangle$, $|2\rangle = |e\rangle$, and $|3\rangle = |i\rangle$

Let \hat{H}_0 be the Hamiltonian without coupling, represented by the following matrix:

$$\hat{H}_0 = \begin{bmatrix} 0 & 0 & 0 \\ 0 & \delta & 0 \\ 0 & 0 & \Delta \end{bmatrix} \quad (\text{A.1})$$

The two levels $|1\rangle$ and $|2\rangle$ are nearly degenerate, meaning that $\Delta \gg \delta$. In what follows, we will also denote E_i as the energy of state $|i\rangle$ (i.e., $E_i = \langle i | \hat{H}_0 | i \rangle$).

We introduce the coupling between the states. Formally, let \hat{V} be the coupling operator, represented by the matrix:

$$\hat{V} = \begin{bmatrix} 0 & 0 & \frac{\overline{\Omega_1(t)}}{2} \\ 0 & 0 & \frac{\overline{\Omega_2(t)}}{2} \\ \frac{\overline{\Omega_1(t)}}{2} & \frac{\overline{\Omega_2(t)}}{2} & 0 \end{bmatrix} \quad (\text{A.2})$$

When the perturbation \hat{V} is introduced, the eigenstates of the Hamiltonian will be perturbed. We can evaluate these states to the first order. Let $|\psi_i^{(0+1)}\rangle$ denote the state $|i\rangle$ to the first order. For $i \in \{1, 2\}$, this state is written as:

$$|\psi_i^{(0+1)}\rangle = |i\rangle + \frac{V_{3i}}{E_i - E_3} |3\rangle \quad (\text{A.3})$$

and

$$|\psi_3^{(0+1)}\rangle = |3\rangle + \sum_{i \in \{1,2\}} \frac{V_{i3}}{E_3 - E_i} |i\rangle \quad (\text{A.4})$$

We have introduced the notation $V_{ij} = \langle i | \hat{V} | j \rangle$. It is important to note that the term V_{12} is zero, which is why there is only one term in $|\psi_i^{(0+1)}\rangle$ for $i \in \{1, 2\}$.

We can now solve the Schrödinger equation for the Hamiltonian $\hat{H} = \hat{H}_0 + \hat{V}$. For this, we will use the basis of the first-order eigenstates. We denote:

$$|\psi(t)\rangle = \sum_i c_i(t) |\psi_i^{(0+1)}\rangle \quad (\text{A.5})$$

We obtain the following equation for c_i :

$$i\hbar \dot{c}_i = \sum_j \langle \psi_i^{(0+1)} | \hat{H} | \psi_j^{(0+1)} \rangle c_j - i\hbar \sum_j \langle \psi_i^{(0+1)} | \frac{d}{dt} | \psi_j^{(0+1)} \rangle c_j \quad (\text{A.6})$$

When the intensity evolves slowly, the right-hand term is negligible. The adiabatic condition is written as:

$$\sum_j \langle \psi_i^{(0+1)} | \frac{d}{dt} | \psi_j^{(0+1)} \rangle \ll |E_i - E_j| \quad (\text{A.7})$$

For the case $i \in \{1, 2\}$ and $j = 3$, we obtain a condition of the type $\frac{\dot{\Omega}}{\Delta} \ll \Delta$, which in order of magnitude is $\frac{\Omega_0}{\Delta} \ll \Delta \times \tau$. In our experiment, we use pulses of duration on the order of the picosecond, detuning of 500 GHz and the peak Rabi frequency is around 100 MHz. We can thus proceed to the adiabatic elimination.

The terms for $i = 1$ and $j = 2$ are in $\frac{\Omega_0^2}{\Delta^2} \ll \Delta\tau$, and the adiabatic condition is also satisfied if the first condition is met.

We thus obtain an equation of the type:

$$i\hbar \dot{c}_i = \sum_j H_{ij}^{(0+2)} c_j \quad (\text{A.8})$$

where $H_{ij}^{(0+2)} = H_{ij}^{(0)} + H_{ij}^{(2)}$ is the Hamiltonian corrected to the second order (there is no first order because $V_{ii} = 0$).

We can calculate, for example, the term $H_{i1}^{(0+2)}$. We then use:

$$\hat{H} |\psi_1^{(0+1)}\rangle = E_1 |1\rangle + \frac{V_{31}}{E_1 - E_3} E_3 |3\rangle + V_{31} |3\rangle + \sum_{i \in \{1,2\}} \frac{V_{i3} V_{31}}{E_1 - E_3} |i\rangle \quad (\text{A.9})$$

$$= E_1 |\psi_1^{(0+1)}\rangle + \sum_{i \in \{1,2\}} \frac{V_{i3} V_{31}}{E_1 - E_3} |i\rangle \quad (\text{A.10})$$

We thus find in this example that $H_{11}^{(0)} = E_1$, $H_{21}^{(0)} = 0$, and that

$$H_{i1}^{(2)} = \frac{V_{i3}V_{31}}{E_1 - E_3} \quad (\text{A.11})$$

We have neglected a term due to the fact that in the last term of [Equation A.10](#) we have $|i\rangle$ and not $|\psi_i^{(0+1)}\rangle$.

In general, we have the following formula for $i \in \{1, 2\}$:

$$H_{ij}^{(0)} = E_i \delta_{ij} \quad (\text{A.12})$$

and

$$H_{ij}^{(2)} = \frac{V_{i3}V_{3j}}{E_j - E_3} \quad (\text{A.13})$$

A.1 System with More Than Three Levels

In the calculation above, we separated the lower states (1 and 2) from the upper states (state 3). This separation arises because the coupling \hat{V} occurs only between the lower and upper states. Thus, at the first order, we couple only with opposite states.

We can generalize this formula: consider multiple states $|i\rangle$ with energy E_i . In what follows, we will separate the lower states and the upper states. We denote α as the index of the latter and i or j for the former.

By generalization, we have:

$$|\psi_i^{(0+1)}\rangle = |i\rangle + \sum_{\alpha} \frac{V_{\alpha i}}{E_i - E_{\alpha}} |\alpha\rangle \quad (\text{A.14})$$

and a Hamiltonian given by

$$H_{ij}^{(0)} = E_i \delta_{ij} \quad (\text{A.15})$$

and

$$H_{ij}^{(2)} = \sum_{\alpha} \frac{V_{i\alpha}V_{\alpha j}}{E_j - E_{\alpha}} \quad (\text{A.16})$$

A.2 System with Three Internal Levels and an External Variable

We now consider the position/momentum of the atoms. The Hamiltonian is thus written as

$$\hat{H}_0 = \frac{\hat{p}^2}{2m} + \begin{bmatrix} 0 & 0 & 0 \\ 0 & \delta & 0 \\ 0 & 0 & \Delta \end{bmatrix} \quad (\text{A.17})$$

where it is understood that the term in \hat{p} leaves the internal state invariant, just as the matrix leaves the external state invariant.

The coupling will also change the internal state:

$$\hat{V} = \begin{bmatrix} 0 & 0 & \frac{\overline{\Omega}_1(\hat{z}, t)}{2} \\ 0 & 0 & \frac{\overline{\Omega}_2(\hat{z}, t)}{2} \\ \frac{\Omega_1(\hat{z}, t)}{2} & \frac{\Omega_2(\hat{z}, t)}{2} & 0 \end{bmatrix} \quad (\text{A.18})$$

The zero-order eigenstates are given by the internal state and plane waves of momentum p , denoted as $|i, p\rangle$.

Thus, we have:

$$H_{(i,p)(j,p')}^{(0)} = E_i \delta_{ij} + \frac{p^2}{2m} \delta(p - p') \quad (\text{A.19})$$

and

$$H_{(i,p)(j,p')}^{(2)} = \int \frac{\langle p | \hat{V}_{i3} | p'' \rangle \langle p'' | \hat{V}_{3j} | p' \rangle}{E_j - E_3 + \frac{p'^2 - p''^2}{2m}} dp'' \quad (\text{A.20})$$

In this expression, we have kept the $\hat{\cdot}$ on \hat{V}_{i3} to indicate that it is an operator on the external variables. This expression is the generalization of [Equation A.16](#) to the case where there is a continuum of excited states. In the case where V corresponds to plane waves (continuous laser situation), we find the condition that $p'' = p + \hbar k$, which allows us to simplify the integral. We cannot do this directly here.

However, in the denominator, the kinetic energy is negligible compared to $|E_j - E_3|$, so we can eliminate it. We thus obtain:

$$H_{(i,p)(j,p')}^{(2)} \simeq \int \frac{\langle p | \hat{V}_{i3} | p'' \rangle \langle p'' | \hat{V}_{3j} | p' \rangle}{E_j - E_3} dp'' = \langle p | \frac{\hat{V}_{i3} \hat{V}_{3j}}{E_j - E_3} | p' \rangle \quad (\text{A.21})$$

where we have used the closure relation $\int |p''\rangle \langle p''| dp'' = \mathbb{I}$. This allows us to define an operator $\hat{H}_{ij}^{(2)}$ that acts on the external variables and is given by:

$$\hat{H}_{ij}^{(2)} = \frac{\hat{V}_{i3} \hat{V}_{3j}}{E_j - E_3} = \frac{\overline{\Omega}_i(\hat{z}, t) \Omega_j(\hat{z}, t)}{4\Delta} \quad (\text{A.22})$$

To obtain this expression, we made the approximation that $|\psi_{(i,p)}^{(0+1)}\rangle \simeq |i,p\rangle$, which is valid for calculating the second-order term.

This second-order term is thus diagonal in the position representation. We can also write it as:

$$V_{ij}^{\text{eff}}(z, t) = \frac{V_i(t, \hat{z})^\dagger V_j(t, \hat{z})}{\hbar\Delta} \quad (\text{A.23})$$

Bibliography

- [1] X. ALAUZE, A. BONNIN, C. SOLARO & F. Pereira Dos SANTOS 2018. “A Trapped Ultracold Atom Force Sensor with a Mm-Scale Spatial Resolution”. *New Journal of Physics* **20(8)**, p. 083 014. Publisher: IOP Publishing. Cited page 5
- [2] Henning ALBERS, Alexander HERBST, Logan L. RICHARDSON, Hendrik HEINE, Dipankar NATH, Jonas HARTWIG, Christian SCHUBERT, Christian VOGT, Marian WOLTMANN, Claus LÄMMERZAHN *et al.* 2020. “Quantum Test of the Universality of Free Fall Using Rubidium and Potassium”. *The European Physical Journal D* **74(7)**. Publisher: Springer Science and Business Media LLC. Cited page 30
- [3] R. K. ALTMANN, L. S. DREISSEN, E. J. SALUMBIDES, W. UBACHS & K. S. E. EIKEMA 2018. “Deep-Ultraviolet Frequency Metrology of H 2 for Tests of Molecular Quantum Theory”. *Physical Review Letters* **120(4)**, p. 043 204. Cited page 9
- [4] R. K. ALTMANN, S. GALTIER, L. S. DREISSEN & K. S. E. EIKEMA 2016. “High-Precision Ramsey-Comb Spectroscopy at Deep Ultraviolet Wavelengths”. *Physical Review Letters* **117(17)**, p. 173 201. Cited page 9
- [5] Manuel ANDIA 2015. *Bloch Oscillations of Ultra-Cold Atoms : Application to High-Precision Measurements*. Theses Université Pierre et Marie Curie - Paris VI. Issue: 2015PA066241. Cited pages 38 and 39
- [6] Manuel ANDIA, Étienne WODEY, François BIRABEN, Pierre CLADÉ & Saïda GUELLATI-KHÉLIFA 2015. “Bloch Oscillations in an Optical Lattice Generated by a Laser Source Based on a Fiber Amplifier: Decoherence Effects Due to Amplified Spontaneous Emission”. *Journal of the Optical Society of America B: Optical Physics* **32(6)**, p. 1038–1042. Publisher: OSA. Cited page 91
- [7] Peter ASENBAUM, Chris OVERSTREET, Minjeong KIM, Joseph CURTI & Mark A. KASEVICH 2020. “Atom-Interferometric Test of the Equivalence Principle at the 10^{-12} Level”. *Physical Review Letters* **125(19)**, p. 191 101. Cited page 30
- [8] Peter ASENBAUM, Chris OVERSTREET, Tim KOVACHY, Daniel D. BROWN, Jason M. HOGAN & Mark A. KASEVICH 2017. “Phase Shift in an Atom Interferometer Due to Spacetime Curvature across Its Wave Function”. *Physical Review Letters* **118(18)**, p. 183 602. Cited page 5
- [9] Satyanarayana BADE, Lionel DJADAOJEE, Manuel ANDIA, Pierre CLADÉ & Saïda GUELLATI-KHÉLIFA 2018. “Observation of Extra Photon Recoil in a Distorted Optical Field”. *Physical Review Letters* **121(7)**, p. 073 603. Publisher: American Physical

- Society. Cited page 132
- [10] B. BARRETT, G. CONDON, L. CHICHET, L. ANTONI-MICOLLIER, R. ARGUEL, M. RABAUULT, C. PELLUET, V. JARLAUD, A. LANDRAGIN, P. BOUYER *et al.* 2022. “Testing the Universality of Free Fall Using Correlated 39K–87Rb Atom Interferometers”. *AVS Quantum Science* **4**(1), p. 014 401. Publisher: American Vacuum Society. Cited pages 5 and 30
- [11] R. BATTESTI, P. CLADÉ, S. GUELLATI-KHÉLIFA, C. SCHWOB, B. GRÉMAUD, F. NEZ, L. JULIEN & F. BIRABEN 2003. “Acceleration of Ultracold Atoms: Towards a Measurement of $h/M\lambda$ ”. *J. Opt. B.: Quantum Semiclassical* **5**, p. S178–S182. Cited page 91
- [12] W. A. BERTSCHE 2018. “Prospects for Comparison of Matter and Antimatter Gravitation with ALPHA-g”. *Philosophical Transactions of the Royal Society A: Mathematical, Physical and Engineering Sciences* **376**(2) Cited page 15
- [13] Y. BIDEL, N. ZAHZAM, C. BLANCHARD, A. BONNIN, M. CADORET, A. BRESSON, D. ROUXEL & M. F. LEQUENTREC-LALANCETTE 2018. “Absolute Marine Gravimetry with Matter-Wave Interferometry”. *Nature Communications* **9**(1). Publisher: Springer Science and Business Media LLC. Cited page 5
- [14] A. BONNIN, N. ZAHZAM, Y. BIDEL & A. BRESSON 2013. “Simultaneous Dual-Species Matter-Wave Accelerometer”. *Physical Review A* **88**(4), p. 043 615. Publisher: American Physical Society (APS). Cited page 30
- [15] J. BORDÉ 1989. “Atomic Interferometry with Internal State Labelling”. *Physics Letters A* **140**(1-2), p. 10–12. Cited pages 54 and 77
- [16] Rym BOUCHENDIRA, Pierre CLADÉ, Saïda GUELLATI-KHÉLIFA, Francois NEZ & Francois BIRABEN 2011. “New Determination of the Fine Structure Constant and Test of the Quantum Electrodynamics”. *Physical Review Letters* **106**(8), p. 080 801. Publisher: American Physical Society. Cited page 88
- [17] A. BÉGUIN, T. RODZINKA, J. VIGUÉ, B. ALLARD & A. GAUGUET 2022. “Characterization of an Atom Interferometer in the Quasi-Bragg Regime”. *Physical Review A* **105**(3), p. 033 302. Cited page 5
- [18] B CANUEL, S ABEND, P AMARO-SEOANE, F BADARACCO, Q BEAUFILS, A BERTOLDI, K BONGS, P BOUYER, C BRAXMAIER, W CHAIBI *et al.* 2020. “ELGAR— a European Laboratory for Gravitation and Atom-interferometric Research”. *Classical and Quantum Gravity* **37**(22), p. 225 017. Cited page 5
- [19] O. CARNAL & J. MLYNEK 1991. “Young’s Double-Slit Experiment with Atoms: A Simple Atom Interferometer”. *Physical Review Letters* **66**(21), p. 2689–2692. Cited page 5
- [20] Coentint CARREZ. “Étude de l’effet des distorsions du front d’onde dans un interféromètre atomique avec un condensat de Bose-Einstein” . Cited pages 6, 100, 131, 133, 140, and 145
- [21] P. CLADE, M. CADORET, E. DE MIRANDES, S. GUELLATI-KHÉLIFA, C. SCHWOB, F. NEZ, L. JULIEN & F. BIRABEN 2006. “Bloch Oscillations of Ultracold Atoms: A Tool for

- Metrological Measurements”. *JOURNAL DE PHYSIQUE IV* **135**, p. 3–7. Place: 17, AVE DU HOGGAR, PA COURTABOEUF, BP 112, F-91944 LES ULIS CEDEX A, FRANCE Publisher: EDP SCIENCES S A Type: Proceedings Paper.
Cited pages 42, 91, 97, and 98
- [22] Pierre CLADÉ, Saïda GUELLATI-KHÉLIFA, François NEZ & François BIRABEN 2009. “Large Momentum Beam Splitter Using Bloch Oscillations”. *Physical Review Letters* **102**(24), p. 240 402. Publisher: APS. Cited page 5
- [23] Ian CODDINGTON, Nathan NEWBURY & William SWANN 2016. “Dual-comb spectroscopy”. *Optica* **3**(4), p. 414. Cited page 11
- [24] Claude COHEN-TANNOUJDI, Jacques DUPONT-ROC & Gilbert GRYNBERG 2012. *Processus d’interaction Entre Photons et Atomes* (Edp Sciences). Cited page 92
- [25] Clément COURVOISIER 2016. *Condensat de Bose-Einstein Par Refroidissement Évaporatif Dans Un Piège Dipolaire Pour La Métrologie Par Interférométrie Atomique*. PhD Thesis Université Pierre et Marie Curie. Cited pages 103 and 107
- [26] Clément DEBAVELAERE, Cyrille SOLARO, Saïda GUELLATI-KHÉLIFA & Pierre CLADÉ 2024. “Atom interferometer using spatially localized beam splitters”. *Physical Review A* **110**(1), p. 013 310. Cited page 6
- [27] L. S. DREISSEN, C. ROTH, E. L. GRÜNDEMANN, J. J. KRAUTH, M. G. J. FAVIER & K. S. E. EIKEMA 2020. “Ramsey-Comb Precision Spectroscopy in Xenon at Vacuum Ultraviolet Wavelengths Produced with High-Order Harmonic Generation”. *Physical Review A* **101**(5). Publisher: American Physical Society (APS). Cited page 9
- [28] J. N. ECKSTEIN, A. I. FERGUSON & T. W. HÄNSCH 1978. “High-Resolution Two-Photon Spectroscopy with Picosecond Light Pulses”. *Physical Review Letters* **40**(13), p. 847–850. Publisher: American Physical Society (APS). Cited page 9
- [29] X. FAN & G. GABRIELSE 2021. “Driven One-Particle Quantum Cyclotron”. *Physical Review A* **103**(2), p. 022 824. Cited page 88
- [30] Hélène FLEURBAEY, Sandrine GALTIER, Simon THOMAS, Marie BONNAUD, Lucile JULIEN, François BIRABEN, François NEZ, Michel ABGRALL & Jocelyne GUÉNA 2018. “New Measurement of the 1 S - 3 S Transition Frequency of Hydrogen: Contribution to the Proton Charge Radius Puzzle”. *Physical Review Letters* **120**(18), p. 183 001. Cited page 14
- [31] Y. FUKUDA, J. HAYASHI, K. KONDO & T. HASHI 1981. “Synchronized Quantum Beat Spectroscopy Using Periodic Impact Excitations with CW Mode-Locked Laser Pulses”. *Optics Communications* **38**(5-6), p. 357–360. Publisher: Elsevier BV. Cited page 14
- [32] Alexey GRININ, Arthur MATVEEV, Dylan C. YOST, Lothar MAISENBACHER, Vitaly WIRTHL, Randolph POHL, Theodor W. HÄNSCH & Thomas UDEM 2020. “Two-Photon Frequency Comb Spectroscopy of Atomic Hydrogen”. *Science* **370**(6520), p. 1061–1066. Publisher: American Association for the Advancement of Science (AAAS). Cited pages 12, 13, 14, and 16
- [33] W. J. HUANG, Meng WANG, F. G. KONDEV, G. AUDI & S. NAIMI 2021. “The AME 2020

- Atomic Mass Evaluation (I). Evaluation of Input Data, and Adjustment Procedures”.
Chinese Physics C **45**, p. 030 002. Cited page 88
- [34] Theodor W HÄNSCH 2006. “Nobel Lecture: Passion for Precision”. *Reviews of Modern Physics* **78**(4), p. 1297. Publisher: APS. Cited page 9
- [35] Raphaël JANNIN, Pierre CLADÉ & Saïda GUELLATI-KHÉLIFA 2015. “Phase Shift Due to Atom-Atom Interactions in a Light-Pulse Atom Interferometer”.
Physical Review A **92**(1). Publisher: American Physical Society (APS). Cited page 103
- [36] Dominik Z. KANDULA, Christoph GOHLE, Tjeerd J. PINKERT, Wim UBACHS & Kjeld S. E. EIKEMA 2010. “Extreme Ultraviolet Frequency Comb Metrology”.
Physical Review Letters **105**(6), p. 063 001. Publisher: American Physical Society (APS). Cited page 12
- [37] M. KASEVICH, D.S. WEISS, E. RIIS, K. MOLER, S. KASAPI & S. CHU 1991. “Atomic Velocity Selection Using Stimulated Raman Transitions”. *Physical Review Letters* **66**, p. 2297. Cited pages 5 and 19
- [38] David W. KEITH, Christopher R. EKSTROM, Quentin A. TURCHETTE & David E. PRITCHARD 1991. “An Interferometer for Atoms”.
Physical Review Letters **66**(21), p. 2693–2696. Cited page 5
- [39] T. LÉVÈQUE, A. GAUGUET, F. MICHAUD, F. Pereira Dos SANTOS & A. LANDRAGIN 2009. “Enhancing the Area of a Raman Atom Interferometer Using a Versatile Double-Diffraction Technique”. *Physical Review Letters* **103**(8), p. 080 405. Publisher: APS. Cited pages 29, 60, and 61
- [40] Adela MARIAN, Matthew C. STOWE, John R. LAWALL, Daniel FELINTO & Jun YE 2004. “United Time-Frequency Spectroscopy for Dynamics and Global Structure”.
Science **306**(5704), p. 2063–2068. Publisher: American Association for the Advancement of Science (AAAS). Cited pages 9 and 12
- [41] léo MOREL 2019. *High Sensitivity Matter-Wave Interferometry: Towards a Determination of the Fine Structure Constant at the Level of 10^{-10}* . PhD Thesis Sorbonne Université. Cited pages 88, 90, 98, 104, 106, 107, 109, 113, 116, 121, 126, and 133
- [42] Léo MOREL, Zhibin YAO, Pierre CLADÉ & Saïda GUELLATI-KHÉLIFA 2020. “Determination of the Fine-Structure Constant with an Accuracy of 81 Parts per Trillion”. *Nature* **588**(7836), p. 61–65. Cited pages 5, 88, 99, 105, 110, 117, and 128
- [43] Léo MOREL, Zhibin YAO, Pierre CLADÉ & Saïda GUELLATI-KHÉLIFA 2020. “Determination of the fine-structure constant with an accuracy of 81 parts per trillion”. *Nature* **588**(7836), p. 61–65. Publisher: Springer Science and Business Media LLC. Cited page 99
- [44] Holger MÜLLER, Sheng-wei CHIOU, Sven HERRMANN & Steven CHU 2009. “Atom Interferometers with Scalable Enclosed Area”.
Physical Review Letters **102**(24), p. 240 403. Publisher: APS. Cited page 5
- [45] Holger MÜLLER, Sheng-wei CHIOU, Quan LONG, Sven HERRMANN & Steven CHU 2008. “Atom Interferometry with up to 24-Photon-Momentum-Transfer Beam Splitters”. *Physical Review Letters* **100**(18), p. 180 405. Publisher: APS. Cited page 19

- [46] Patrick MÜLLER, Kristian KÖNIG, Phillip IMGRAM, Jörg KRÄMER & Wilfried NÖRTERSCHÄUSER 2020. “Collinear Laser Spectroscopy of Ca^{I} Solving the Field-Shift Puzzle of the $4s^1 3d^2 \rightarrow 4p^1 3d^2$ Transitions”. *Physical Review Research* **2**(4), p. 043 351. Publisher: American Physical Society (APS). Cited page 5
- [47] D. PAGANO, S. AGHION, C. AMSLER, G. BONOMI, R. S. BRUSA, M. CACCIA, R. CARAVITA, F. CASTELLI, G. CERCHIARI, D. COMPARAT *et al.* 2020. “Gravity and Antimatter: The AEGIS Experiment at CERN”. *Journal of Physics: Conference Series* **1342**, p. 012 016. Cited page 15
- [48] Richard H. PARKER, Chenghui YU, Weicheng ZHONG, Brian ESTEY & Holger MÜLLER 2018. “Measurement of the Fine-Structure Constant as a Test of the Standard Model”. *Science* **360**(6385), p. 191–195. Publisher: American Association for the Advancement of Science. Cited pages 88 and 99
- [49] Nathalie PICQUÉ & Theodor W. HÄNSCH 2019. “Frequency Comb Spectroscopy”. *Nature Photonics* **13**(3), p. 146–157. Cited pages 9, 11, and 12
- [50] D. SAVOIE, M. ALTORIO, B. FANG, L. A. SIDORENKOV, R. GEIGER & A. LANDRAGIN 2018. “Interleaved Atom Interferometry for High-Sensitivity Inertial Measurements”. *Science Advances* **4**(12), p. eaau7948. Cited page 5
- [51] W. P. SCHLEICH, D. M. GREENBERGER & E. M. RASEL 2013. “A Representation-Free Description of the Kasevich-Chu Interferometer: A Resolution of the Redshift Controversy”. *New Journal of Physics* **15**(1), p. 013 007. Cited pages 49, 51, and 95
- [52] C. SOLARO, S. MEYER, K. FISHER, M. DEPALATIS & M. DREWSSEN 2018. “Direct Frequency-Comb-Driven Raman Transitions in the Terahertz Range”. *Physical Review Letters* **120**(25), p. 253 601. Publisher: American Physical Society (APS). Cited page 14
- [53] Cyrille SOLARO 2016. *Trapped Atom Interferometers: From Low to High Density Regime*. Theses Université Pierre et Marie Curie. Cited page 12
- [54] Cyrille SOLARO, Clément DEBAVELAERE, Pierre CLADÉ & Saïda GUELLATI-KHELIFA 2022. “Atom Interferometer Driven by a Picosecond Frequency Comb”. *Physical Review Letters* **129**(17), p. 173 204. Cited pages 6 and 29
- [55] Cyrille SOLARO, Steffen MEYER, Karin FISHER, Julian C BERENGUT, Elina FUCHS & Michael DREWSSEN 2020. “Improved Isotope-Shift-Based Bounds on Bosons beyond the Standard Model through Measurements of the $^2\text{D}_{3/2}$ - $^2\text{D}_{5/2}$ Interval in Ca^+ ”. *arXiv preprint arXiv:2005.00529* _eprint: 2005.00529. Cited page 12
- [56] A SOMMERFELD 1916. “The quantum theory of spectral lines”. *Annalen der Physik* **51**(17), p. 1–94. Place: PO BOX 10 11 61, D-69451 WEINHEIM, GERMANY Publisher: WILEY-VCH VERLAG GMBH Type: Article. Cited page 87
- [57] Pippa STOREY & Claude COHEN-TANNOUJDI 1994. “The Feynman Path Integral Approach to Atomic Interferometry. A Tutorial”. *Journal de Physique II* **4**(11), p. 1999–2027. Publisher: EDP Sciences. Cited pages 49 and 81

- [58] S STURM, K BLAUM, B SCHABINGER, A WAGNER, W QUINT & G WERTH 2010. “On g-Factor Experiments with Individual Ions”.
Journal of Physics B: Atomic, Molecular and Optical Physics **43**(7), p. 074 016.
Cited page 88
- [59] Eite TIESINGA, Peter J. MOHR, David B. NEWELL & Barry N. TAYLOR 2021. “CODATA Recommended Values of the Fundamental Physical Constants: 2018”.
Reviews of Modern Physics **93**(2), p. 025 010. Cited pages 87 and 88
- [60] Stefan WITTE, Roel Th ZINKSTOK, Wim UBACHS, Wim HOGERVORST & Kjeld S. E. EIKEMA 2005. “Deep-Ultraviolet Quantum Interference Metrology with Ultrashort Laser Pulses”. *Science* **307**(5708), p. 400–403. Publisher: American Association for the Advancement of Science (AAAS).
Cited pages 9 and 44
- [61] D. C. YOST, A. MATVEEV, A. GRININ, E. PETERS, L. MAISENBACHER, A. BEYER, R. POHL, N. KOLACHEVSKY, K. KHABAROVA, T. W. HÄNSCH *et al.* 2016. “Spectroscopy of the hydrogen1S-3S transition with Chirped Laser Pulses”.
Physical Review A **93**(4), p. 042 509. Publisher: American Physical Society (APS).
Cited page 9
- [62] Lin ZHOU, Shitong LONG, Biao TANG, Xi CHEN, Fen GAO, Wencui PENG, Weitao DUAN, Jiaqi ZHONG, Zongyuan XIONG, Jin WANG *et al.* 2015. “Test of Equivalence Principle At10-8 Level by a Dual-Species Double-Diffraction Raman Atom Interferometer”.
Physical Review Letters **115**(1), p. 013 004. Publisher: American Physical Society (APS).
Cited page 5

Sujet : Interférométrie atomique utilisant un peigne de fréquences et progrès sur la mesure du recul atomique

Résumé : Ma thèse s'est concentrée sur deux sujets dans le domaine des mesures de précision utilisant l'interférométrie atomique : le premier visait à développer un interféromètre atomique utilisant un peigne de fréquences, et le second visait à améliorer la précision de la mesure du recul atomique pour déterminer la constante de structure fine, α .

Tout d'abord, j'ai réussi à démontrer pour la première fois un interféromètre atomique basé sur des transitions Raman stimulées par un laser picoseconde, réalisant un gravimètre atomique avec une sensibilité relative de 10^{-7} en 5 minutes de temps d'intégration. Pour cela, il a fallu mettre au point un système de contrôle de la ligne à retard, permettant aux impulsions picosecondes de se superposer au nuage atomique en chute libre pendant 60 ms. Cela a permis la réalisation d'un nouvel interféromètre basé sur des impulsions $\pi/2 - \pi - \pi - \pi/2$, où les atomes peuvent être adressés localement dans chaque bras de l'interféromètre. Les résultats expérimentaux ont été complétés par des études théoriques et des simulations numériques.

Deuxièmement, j'ai étudié les effets systématiques limitant la précision de la mesure du rapport h/m entre la constante de Planck et la masse d'un atome de rubidium. Des expériences avec des condensats de Bose-Einstein (BEC) ont révélé une sensibilité aux fluctuations locales de l'intensité du laser, ce qui a conduit à une nouvelle méthode robuste pour sonder le profil d'intensité du faisceau laser à l'intérieur de la chambre à vide. J'ai conçu, fabriqué et caractérisé de nouveaux collimateurs pour les faisceaux Raman et Bloch. Une optimisation minutieuse des paramètres expérimentaux a permis de réduire l'incertitude d'une mesure de 30 %. De plus, grâce au BEC, nous avons observé un effet systématique lié à une réflexion parasite.

Différents schémas de verrouillage de phase pour les lasers Raman ont été mis en œuvre et comparés afin de mieux comprendre l'impact de cet asservissement sur la valeur mesurée.

Mots clés : Atomes froids, Interferometrie atomique, Peigne de fréquence, Métrologie quantique, Transition Raman

Subject : Atom interferometry using frequency comb and progress on atomic recoil measurement

Abstract:

My thesis focused on two topics within the field of precision measurements using atom interferometry: the first aimed to develop an atom interferometer using a frequency comb, and the second aimed to improve the measurement accuracy of atomic recoil for determining the fine structure constant, α .

Firstly, I successfully demonstrated for the first time an atom interferometer based on stimulated Raman transitions driven by a picosecond laser, achieving an atomic gravimeter with a relative sensitivity of 10^{-7} in 5 minutes of integration time. This involved developing a delay line control system that allowed picosecond pulses to overlap with the free-falling atomic cloud for 60 ms. This has enabled the realization of a new interferometer based on $\pi/2 - \pi - \pi - \pi/2$ sequence where atoms can be addressed locally in each arm of the interferometer. The experimental results were complemented by theoretical studies and numerical simulations

Secondly, I investigated the systematic effects limiting the accuracy of the h/m ratio measurement between Planck's constant and the mass of a rubidium atom. Experiments with Bose-Einstein Condensates (BEC) revealed sensitivity to local laser intensity fluctuations, leading to a new robust method for probing the laser beam intensity profile inside the vacuum chamber. I designed, fabricated, and characterized new collimators for Raman and Bloch beams. Careful optimization of experimental parameters reduced shot-to-shot uncertainty by 30%. Additionally, thanks to the BEC, we observed a systematic effect related to a parasitic reflection.

Different phase-locking schemes for the Raman lasers were implemented and compared to better understand the impact of this locking on the measured value.

Keywords : Cold atoms, Atom interferometry, Frequency comb, Quantum metrology, Raman transition
